In-vitro degradation of calcium phosphate bone substitutes : Coupled monitoring of the evolution of mechanical, microstructural and physico-chemical properties of DCPD and β-TCP samples

Marta Gallo

2015ISAL0107 Année 2015

MEMOIRE DE THESE

présenté devant

L'INSTITUT NATIONAL DES SCIENCES APPLIQUES DE LYON

pour obtenir

LE GRADE DE DOCTEUR

Formation Doctorale : Microstructure et comportement mécanique et macroscopique des matériaux – Génie des Matériaux

Ecole Doctorale : Ecole doctorale de Matériaux de Lyon

par

Marta Gallo

IN-VITRO DEGRADATION OF CALCIUM PHOSPHATE BONE SUBSTITUTES: COUPLED MONITORING OF THE EVOLUTION OF MECHANICAL, MICROSTRUCTURAL AND PHYSICO-CHEMICAL PROPERTIES OF DCPD AND B-TCP SAMPLES

Date de soutenance prévue le 26 novembre 2015

Commission d'Examen:

Professeur	Jean-Michel BOULER	Rapporteur
Professeur	Christèle COMBES	Rapporteur
Professeur	Aldo R. BOCCACCINI	Examinateur
Professeur	Marc BOHNER	Examinateur
Professeur	Jérôme CHEVALIER	Directeur de thèse
Maître de conférences	Solène TADIER	Co-directeur de thèse
Maître de conférences	Sylvain MEILLE	Co-directeur de thèse
Docteur	Rainer DETSCH	Invité

Université de Lyon
MATEIS – UMR CNRS 5510 – INSA de Lyon
7, Avenue Jean Capelle 69621 Villeurbanne cedex, France

INSA Direction de la Recherche - Ecoles Doctorales – Quinquennal 2011-2015

SIGLE	ECOLE DOCTORALE	NOM ET COORDONNEES DU RESPONSABLE
CHIMIE	**CHIMIE DE LYON** **http://www.edchimie-lyon.fr** Sec : Renée EL MELHEM Bat Blaise Pascal 3e etage 04 72 43 80 46 Insa : R. GOURDON secretariat@edchimie-lyon.fr	M. Jean Marc LANCELIN Université de Lyon – Collège Doctoral Bât ESCPE 43 bd du 11 novembre 1918 69622 VILLEURBANNE Cedex Tél : 04.72.43 13 95 directeur@edchimie-lyon.fr
E.E.A.	**ELECTRONIQUE, ELECTROTECHNIQUE, AUTOMATIQUE** **http://edeea.ec-lyon.fr** Sec : M.C. HAVGOUDOUKIAN Ecole-doctorale.eea@ec-lyon.fr	M. Gérard SCORLETTI Ecole Centrale de Lyon 36 avenue Guy de Collongue 69134 ECULLY Tél : 04.72.18 60.97 Fax : 04 78 43 37 17 Gerard.scorletti@ec-lyon.fr
E2M2	**EVOLUTION, ECOSYSTEME, MICROBIOLOGIE, MODELISATION** **http://e2m2.universite-lyon.fr** Sec : Safia AIT CHALAL Bat Atrium- UCB Lyon 1 04.72.44.83.62 Insa : S. REVERCHON Safia.ait-chalal@univ-lyon1.fr	M. Fabrice CORDEY Laboratoire de Géologie de Lyon Université Claude Bernard Lyon 1 Bât Géode – Bureau 225 43 bd du 11 novembre 1918 69622 VILLEURBANNE Cédex Tél : 04.72.44.83.74 Sylvie.reverchon-pescheux@insa-lyon.fr fabrice.cordey@ univ-lyon1.fr
EDISS	**INTERDISCIPLINAIRE SCIENCES-SANTE** **http://www.ediss-lyon.fr** Sec : Safia AIT CHALAL Bat Atrium – UCB Lyon 1 04 72 44 83 62 Insa : Safia.ait-chalal@univ-lyon1.fr	Mme Emmanuelle CANET-SOULAS INSERM U1060, CarMeN lab, Univ. Lyon 1 Bâtiment IMBL 11 avenue Jean Capelle INSA de Lyon 696621 Villeurbanne Tél : 04.72.11.90.13 Emmanuelle.canet@univ-lyon1.fr
INFOMATHS	**INFORMATIQUE ET MATHEMATIQUES** **http://infomaths.univ-lyon1.fr** Sec :Renée EL MELHEM Bat Blaise Pascal 3e etage infomaths@univ-lyon1.fr	Mme Sylvie CALABRETTO LIRIS – INSA de Lyon Bat Blaise Pascal 7 avenue Jean Capelle 69622 VILLEURBANNE Cedex Tél : 04.72. 43. 80. 46 Fax 04 72 43 16 87 Sylvie.calabretto@insa-lyon.fr
Matériaux	**MATERIAUX DE LYON** **http://ed34.universite-lyon.fr** Sec : M. LABOUNE PM : 71.70 –Fax : 87.12 Bat. Direction 1er et. Ed.materiaux@insa-lyon.fr	M. Jean-Yves BUFFIERE INSA de Lyon MATEIS Bâtiment Saint Exupéry 7 avenue Jean Capelle 69621 VILLEURBANNE Cedex Tél : 04.72.43 71.70 Fax 04 72 43 85 28 Ed.materiaux@insa-lyon.fr
MEGA	**MECANIQUE, ENERGETIQUE, GENIE CIVIL, ACOUSTIQUE** **http://mega.universite-lyon.fr** Sec : M. LABOUNE PM : 71.70 –Fax : 87.12 Bat. Direction 1er et. mega@insa-lyon.fr	M. Philippe BOISSE INSA de Lyon Laboratoire LAMCOS Bâtiment Jacquard 25 bis avenue Jean Capelle 69621 VILLEURBANNE Cedex Tél : 04.72 .43.71.70 Fax : 04 72 43 72 37 Philippe.boisse@insa-lyon.fr
ScSo	**ScSo*** **http://recherche.univ-lyon2.fr/scso/** Sec : Viviane POLSINELLI Brigitte DUBOIS Insa : J.Y. TOUSSAINT viviane.polsinelli@univ-lyon2.fr	Mme Isabelle VON BUELTZINGLOEWEN Université Lyon 2 86 rue Pasteur 69365 LYON Cedex 07 Tél : 04.78.77.23.86 Fax : 04.37.28.04.48 isavonb@dbmail.com

*ScSo : Histoire, Géographie, Aménagement, Urbanisme, Archéologie, Science politique, Sociologie, Anthropologie

Life is like riding a bicycle:

to keep your balance you must keep moving

Albert Einstein

Acknowledgment

I remember clearly the first time I stepped in Mateis: a sunny day of June and a lot of smiling French-speaking-faces. Three years have passed by then, but the same nice and warm feeling is still there thanks to all the people from the lab, always kind and helpful. Three years which have been possible thanks to **Jérôme**, which has given me the opportunity to start this Ph.D. and has always found time for me despite his super tight agenda. Thanks to **Sylvain**, which has been so much supportive: his "*on va y arriver*" and *crème de marrons* have been a fundamental fuel for me, mentally and physically. Thanks to **Solène**, which has been an incomparable source of advices professional and not. I'll make sure to write you only postal cards and letters in the future: I don't want to be responsible for the explosion of your mail-box.
In the years to come I will for sure remember all the meetings I've had with the three of you…and it will be a nice memory, don't worry! ;)

My gratitude goes also to Prof. **Aldo Boccaccini**, which has kindly hosted me in Erlangen, and Dr. **Rainer Detsch**, which has been of great help in my "initiation" to the "world of cell culture". Thanks also to Prof. **Marc Bohner** which has provided some of the samples I used as well as valuable advices.

I'd like to remember also all the people which has helped me with my experiments in these years. I'm sure the list could be longer, but I'd like to mention at least **Laurent Gremillard**, **Lucile Joly-Pottuz**, **Sandrine Cardinal**, **Jérôme Adrien**, **Florian Mercier**, **Delphine Farlay**, the groups of the mechanical and electronic atelier. A special thank also to **Antonia**, **Corinne, Erika, Liliane**: always present in case of need.

Three years in Mateis, three years of lunch-breaks: no matter how big the "*salle à caffée*" is, there will never be enough space to contain all **Laura**'s jokes, **Chole**'s amazing sweets, **Anouk**'s colorful cakes, **Malgo**'s chats in front of a warm cup of tea and everyone's cheerfulness. *Merci pour tout, les **gens du 5ème**!*
A special thought goes to my "brothers": **Abel** (Gebreegziabher Gebresilassie) and **Carlos** (ksiazece zlote pszeniczne), with whom I've shared this amazing experience.
I'd like to remember here also the "1st floor group" and in particular **Bérangère**, **Thierry**, **Lucian**: thanks for all the chats, and the professional and personal support. *Un très très gros merci!*

My gratitude goes also to **Alina**, which helped me a lot in my lab activities in Erlangen. Thanks also to the "**Henkestrasse team**" with whom I shared nice days and fruitful expeditions to Aldi. *Vielen Dank, ich hatte eine gute Zeit!*

I feel really lucky, because the BioBone program gave me the chance to meet great people from all over the world. I can't help but mentioning **Vale**, **Ana-Maria** and **Fra** with whom I shared so nice moments (no matter the country where we were): *gracias, mersi, grazie*. Furthermore, I'd like to thank all the **BioBone people**: we had a great "networking-time" together!

Thanks also to all my Italian friends: **PT**, **Chia**, **Roby**, **Cri**, **Ila**, **Gio**, **Ele**, **Andre**, **Cla**…You manage to keep in contact and hang out with me even if we live in different countries: that's real friendship! :)

Zia and **Diego**, the Wednesday's "ritual" skype calls have showed me how much you believe in me.

Ste, thank you for being as you are and for bearing me on a daily base (I'm aware it's a hard task). I don't know where we'll be in the future, but don't worry, there will be a Tatarko and a Gingembre with us. ;)

Ma' and **Pa'**, I'll never thank you enough for your support. The countless journeys to Lyon, the hours spent on Skype, all the messages you sent me in these years have erased the kilometers between us. *So che la ''famiglia dei pizzini'' mi seguirà e supporterà ovunque andrò*.

GLOSSARY

Once a material is implanted *in vivo* or undergoes tests *in vitro* its characteristics are likely to change. This evolution of properties can be induced by different phenomena, such as the dissolution of the crystals or the precipitation of new phases. For the present work specific words will be used in order to distinguish each of these phenomena. The choice of the terms, although arbitrary, is intended to simplify and clarify the comprehension. A list of the main terms with the respective meaning is given in the present section.

Bioactive: characterised by bioactivity

Bioactivity: specific effect on a living tissue caused by the exposure to a material or a substance. In the field of biomaterials for bone applications, bioactivity is often related to the formation of a calcium phosphate layer on the surface of the material upon immersion in simulated body fluids

Biocompatibility: “the ability of a material to perform with an appropriate host response in a specific application" (Williams' definition)

Biocompatible: characterised by biocompatibility

Cytocompatible: which is compatible with cells, opposite to cytotoxic.

DCPD: Dicalcium Phosphate Dihydrate, also known by the name of its mineral form “brushite”. In the present work the term “brushite” will not be used as a synonym of DCPD, while “brushite cement” will be employed to refer as DCPD

Degradation: change during time of a material implying the decrease of the properties of the material itself

Dissolution: physico-chemical process involving the formation of a solution composed by a solute and a solvent. In the present work the solute is represented by ceramic crystals and the solvent by the medium of immersion. The dissolution process can be induced also by cellular activity

Evolution: change of the properties of a material during time. The evolution of a sample can be induced by phenomena such those of dissolution and precipitation of new phases, implying or not a decrease of properties (degradation)

Inert: which has a limited interaction with the body. Inert ceramics for bone applications, for example, do not bond with bones after implantation

In vitro: test performed in conditions different from the normal biological ones (i.e. cellular tests made outside the body)

In vivo: test performed in a living organism

Osteoblasts: cells in charge of bone deposition

Osteoclasts: cells in charge of bone resorption

Osteoconduction: property of a material that allows natural bone to grow on its surface, possibly guiding it

Osteoconductive: characterised by osteoconduction

Osteoinduction: property of a material which induces osteogenesis, that is to say that stimulates undifferentiated cells to develop into bone-forming cells

Osteoinductive: characterised by osteoinduction

Osteointegration: process that leads to a rigid and long-lasting fixation of an implant in bone

NOMENCLATURE

DCPA: dicalcium phosphate anhydrous

DCPD: dicalcium phosphate dihydrate

HAp: hydroxyapatite

HBS: human body serum

MCPM: monocalcium phosphate monohydrate

µ-CT: micro computed tomography

OCP: octacalcium phosphate

PBS: phosphate buffered solution

PBS_d: PBS dynamic

RPMI: Roswell Park Memorial Institute medium

SBF: simulated body fluid

SEM: scanning electron microscopy

TCP: tricalcium phosphate

TCP_Mg: dense βTCP doped with magnesium (5% mol)

TCP_NoMg: dense pure βTCP

TCP_NaCl: dense βTCP immersed in NaCl solution (0.9% w/v)

TCP_RPMI: dense βTCP immersed in RPMI

TEM: transmission electron microscopy

TRIS_d: TRIS dynamic

TRIS_s: TRIS static

XRD: X-Ray diffraction

CHAPTER 1: STATE OF THE ART

CHAPTER 2: MATERIALS AND METHODS

CHAPTER 3: EVOLUTION OF DCPD SAMPLES IN SOLUTIONS

CHAPTER 4: EVOLUTION OF POROUS B-TCP SAMPLES IN SOLUTIONS

CHAPTER 5: EVOLUTION OF DENSE β-TCP SAMPLES IN PRESENCE OF OSTEOCLAST-LIKE CELLS

Preface

Although resorbable bone substitutes are currently used in surgery, the knowledge of their degradation process is still incomplete. However, only by knowing which parameters affect the degradation of these materials, it would be possible to tune their properties, and potentially match the resorption rate with the bone tissue regeneration.
The aim of this Ph.D. thesis was to establish and assess an experimental methodology to monitor the evolution of resorbable bone substitutes, **coupling the mechanical, microstructural and physico-chemical aspects**.

The results are presented in this manuscript in five chapters.

The **first chapter** contains a general overview on the context of the study. A bibliography research about the materials of interest for this work is presented (in particular, dicalcium phosphate dihydrate, DCPD, and beta tricalcium phosphate, β-TCP). Then, an introduction to the instrumented micro-indentation technique, which has been used for assessing the mechanical properties of the samples, is given. The chapter ends with the explanation of the experimental choices and the specificity of this study.

The **second chapter** details the processing of the samples, the experimental conditions as well as the characterisation techniques adopted in this work. In particular, it describes the techniques used to assess the evolution of the microstructure and of the physico-chemical features of the materials, together with their resulting mechanical properties.

The **third chapter** focuses on the results of the dissolution tests performed *in-vitro* with porous DCPD samples. The chapter highlights the effect of the dissolution media and of the dissolution conditions (static or dynamic) on the degradation rate and mechanisms. It also explores the different sequences of dissolution/precipitation occurring during the test and their effects on the microstructure and mechanical properties of the material.

The **fourth chapter** collects the outcomes of the dissolution tests carried out *in-vitro* with porous β-TCP samples and presents their discussion. In line with the previous chapter, it confirms the role of the testing conditions on the kinetics of dissolution. It also confirms the interest of coupling physico-chemical, microstructural and mechanical follow-up to get a full picture of the evolution of a given material. Even if β-TCP is generally considered as not dissolved, but resorbed, the present results show that its dissolution may occur, depending on testing conditions and initial microstructural features.

The **fifth chapter** is focused on the data collected during the cellular tests performed with osteoclastic cells on pure and magnesium-doped β-TCP dense samples. In the second part of the chapter these outcomes are discussed. The results confirm the cytocompatibility of both types of material, but suggest also that β-TCP could hinder the activity of osteoclasts. The addition of magnesium, finally, appears to alter the properties of the material, decreasing its dissolution rate.

The manuscript ends with a **general conclusion**, which collects the main results of this study. In particular, this work proves the strong correlation between the physico-chemical, micro-structural and mechanical properties of the samples. All these aspects should be considered when the evolution of a material is investigated. Moreover, the crucial influence of the immersion media, as well as of the set-up conditions, is showed. Moreover, the interest and the validity of using a local test such as instrumented micro-indentation rather than a method assessing the whole sample volume for monitoring the mechanical properties of degraded materials is confirmed. Finally, outlooks are suggested for the future, both to complete the investigation of the degradation process of DCPD and β-TCP samples, and to further develop the approach adopted in this study.

CHAPTER 1: STATE OF THE ART

Words labelled with an asterisk (*) are defined in the glossary

Bold type is used for key-words

1.1 Introduction

Accounting for 20% of the total weight of a human being, the skeleton represents one of the most important parts of our body [1]. Its crucial role is not only confined to a mere structural support, but it contributes also to organ protection (e.g. skull and thorax), production of blood cells (hematopoietic function of bone marrow) and storage of essential mineral elements and ions.
It appears therefore logical that many attempts of bone tissue engineering have been made since 1668, when the surgeon Job van Meek'ren (Holland) healed a cranium defect using a piece of bone harvested from the skull of a dog [2].
Todays this theme is still object of study and, actually, it is expected to concern more and more people due to the increase of the average life expectancy. At present around 2.2 million orthopaedic operations worldwide per year require the use of bone grafts as a consequence of fractures, tumours, bone infections and diseases [3].

It is possible to distinguish bone grafts in four main classes:

- Autograft: bone is harvested and transplanted from one part of the body to another location in the same body
- Allograft: from a human donor to another person
- Xenograft: from another species
- Synthetic

The first autologous graft was performed in the USA by the surgeon Frederick Albee [3] and it is still the "gold standard", because it represents no risk of rejection. However, its use is gradually decreasing because of its main drawbacks, i.e. the limited availability of material, the pain for the patient (two interventions generally required) and the possibility of morbidity (which can concern from 6 to 20% of patients [4]).

The main problem of allografts, instead, is due to treatment of the tissue. In order to minimize the possibility of transmission of diseases and rejection, the tissue is frozen or freeze-dried and sterilised: as a consequence, it loses its osteoinductive* potential [3].

Grafts derived from other species (i.e. xenografts) display almost the same disadvantages than allografts, requiring specific treatments to avoid any immune response, which deprive the tissue of its main potentialities [5].

In order to overcome all these inconveniences, more and more attention has been paid to the study and development of synthetic bone substitutes.
These materials are neither affected by limited availability nor by inconsistency and risk of morbidity [5]. On the other hand synthetic grafts often display poor mechanical properties (mostly brittleness) and, although some of them are osteoconductive, they are not usually considered as osteoinductive. For overcoming this last problem some studies have aimed to incorporate in synthetic bone grafts specific molecules, such as growth factors and bone morphogenetic proteins (BMP), to induce bone formation after implantation.
Among the eligible materials for the production of synthetic bone substitutes, the bioresorbable ones are attractive, thanks to their possibility of being replaced gradually by natural bone once implanted. This kind of bone substitutes, in fact, can fulfil the main requirements for a bone scaffolds, providing temporary support, stabilising the defect, resorbing progressively and allowing at the same time the ingrowth of new natural bone tissue. It is clear that, in order to achieve this goal, different aspects should be considered; in particular chemistry, architecture, mechanical properties and degradation rate of the material need to be carefully tailored. However, at present, there is still a lack of experimental tools to evaluate how resorbable materials evolve once implanted and how their mechanical properties are affected [6].

The aim of this work is to establish, validate and apply a protocol to study these evolution phenomena during time, their kinetics and mechanisms and their consequences on the material properties.

In the next paragraphs a short description of the physiological process of bone renewal will be given; a general list of possible bone substitutes will follow. Afterward, a more detailed description of a specific group of bone substitutes (calcium phosphates, CaP) will be presented. Finally the attention will be focused on the degradation process of these materials and a possible method (micro-indentation) to evaluate it from the mechanical point of view.

1.2 Bone Remodelling

It is well known from literature [6-9] that the degradation process occurring during the physiological remodelling of bone substitutes involves two different (but synergetic) phenomena: a physical one (dissolution and precipitation) and a biological one (cellular resorption and remineralisation).
While the first one is a purely physicochemical process linked to the properties of the material (such as the solubility in physiological fluids), the second one is caused by the cells activity (whose behaviour is influenced, in its turn, by the properties of the material as well). Once implanted, resorbable bone substitutes gradually disappear thanks to dissolution/precipitation and cellular resorption phenomena, leaving space to the new bone formed by the remodelling process.
On the overall, this study will be mainly focused on the dissolution/precipitation process, but, nevertheless, we will try to investigate, at least partially, some of the resorption aspects too (while remineralisation will not be further addressed). The present paragraph is therefore aimed to give a brief description of bone remodelling and in particular resorption phenomena, which take place in physiologic conditions and may account for the degradation processes of bone substitutes.

Bone remodelling is a physiological process, which allows the cyclic renewal of bones and the healing of small defects. This process consists of several steps, which are cyclically repeated, leading to a complex equilibrium between resorption and deposition of bone.

The bone tissue hosts 4 typical types of cells: osteoblasts, pre-osteoblasts, osteocytes and osteoclasts. While the first three all derive from mesenchymal cells (multipotent cells of connective tissues), the osteoclasts result from the differentiation of hematopoietic cells (responsible for the production of blood cells).
Osteoblasts are usually gathered together in proximity of sites where new bone is deposited; some studies hypothesise that osteoblasts promote bone formation by regulating the concentration of calcium and phosphate ions [10]. These cells present a globular shape, with dimensions of around 20 μm, and are characterised by a life-span of up to 3 months [10].

Pre-osteoblasts are, as suggested by the name, precursor of osteoblasts. These cells are located above all in the periosteum and turn into osteoblasts upon specific hormonal signals.

Osteocytes are the cells typical of the mature bone tissue, where they are located in spaces called *lacunae*, they display a star-shape and have an average life of 25 years. These cells originate from osteoblasts "trapped" in the bone matrix that they have produced and, although spread in the tissue, they can communicate one with the other thanks to long cytoplasmic extensions.

Osteoclasts are cells in charge of bone resorption; at present there is no knowledge of other kinds of cells capable to resorb mineralised bone. Osteoclasts are polykarios cells (they have more than one nucleus) originated from the fusion of precursors (hematopoietic stem cells, [11, 12]); they can reach dimensions of more than 100 μm and generally have a lifespan of 2 weeks [10]. Osteoclasts usually display more than one nucleus (5-8 nuclei) when they are active, which leads to believe that the

fusion takes place just before the resorption process starts [13]. When active, osteoclasts exhibit typical morphological characteristics such as a ruffled border, an actin ring and a functional secretory domain (Figure 1). Moreover, active osteoclasts highly express tartrate resistance acid phosphatase (TRAP), an enzyme often used as a phenotypic marker of this kind of cells [13, 14].

In conjunction with osteoblast, osteoclasts are responsible of the phenomenon of bone remodelling. Some theories claim that healthy osteocytes normally send messages to osteoclasts to prevent resorption. On the other hand, in case of micro-cracks some osteocytes can be damaged and, thus, stop sending the "not to resorb" signal. As a consequence osteoclasts precursor are "recruited" and migrate through the blood stream towards the area where remodelling is needed [13].
Once on the resorption site, the precursors undergo fusion, originating multinucleated cells (osteoclasts). These latter strongly attach to the surface: within the cell a reorganisation of the actin filaments (a protein linked to cell structure and motion) leads to the appearance of an actin ring at the base of the osteoclast. This process results in the formation of a sealed zone at the interface between the cell and the surface. At the same time, a polarisation of the cell takes place: the part of membrane encompassed by the actin ring take the characteristic aspect of ruffled border, while on top of the cell another domain, called functional secretary domain, appears [8].
The resorption can, therefore, start: acid and proteolytic enzymes are released by means of vesicles under the sealed zone (lacuna). At the same time proton pumps move protons (obtained by carbonic anhydrase, $H_2O + CO_2 \rightarrow HCO^-_3 + H^+$) from the cytoplasm to the lacuna, decreasing the pH in the sealed zone (around 3.3-4.2) and enhancing, thus, bone resorption. The products resulting from the degradation of apatite crystals (Ca^{2+}, PO_4^{3-}, CO_3^{2-}, H_2O) and collagen fibrils are endocytosed in the osteoclast, transferred across the cell and finally released into the extracellular fluids through the functional secretary domain (Figure 1). At this point the osteoclast can either migrate towards another zone where resorption is needed or undergo apoptosis [8, 13].
At the same time the process of bone resorption implies the release of growth factors which induce the action of osteoblasts: after osteoclasts have executed their resorption function, in fact, osteoblasts can start the deposition of new bone tissue, maintaining, thus, the crucial balance between old and new bone [13].

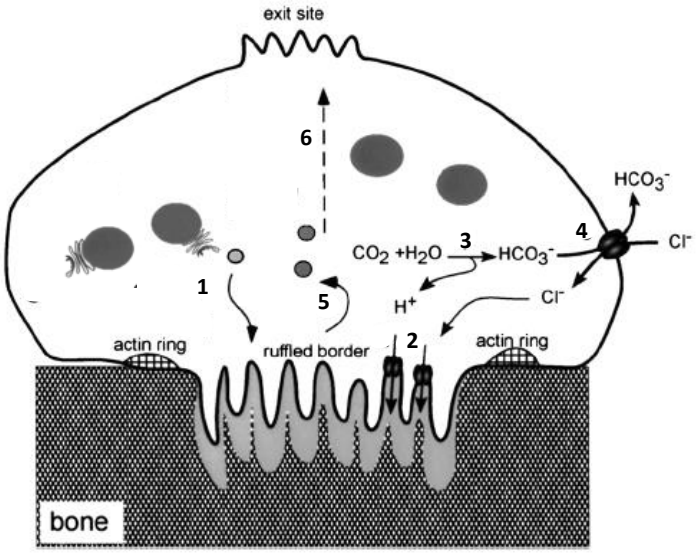

Figure 1: Cross-section of bone resorbing osteoclast. The principal steps of the process are listed from 1 to 6 (moving of vesicles, acidification of extracellular space, carbonic anhydrase generates protons, chloride-bicarbonate exchange, endocytosis of organic matrix, expulsion of degradation products through the secretary domain) [8]

1.3 Synthetic bone substitutes

Among synthetic calcium phosphate-based bone substitutes, ceramics play for sure an important role, thanks to their good biocompatibility* and similarity to the inorganic component of natural bones. Big scientific efforts have been spent for improving ceramics for bone applications in the last decades (the first bioresorbable bone filler, TCP*-based, was proposed in 1920, [15]). One of the main results of this process has been a shift in the use of bioceramics from an inert* to a bioactive* form [16]. It is possible to distinguish, at present, three generations of ceramics [16]:

- 1st generation: inert ceramics, such as alumina or zirconia, characterised by high mechanical properties and perfect for load-bearing applications (e.g. hip prosthesis)
- 2nd generation (since 1980's): ceramics that can be resorbed and bond with natural bone (e.g. hydroxyapatite, tricalcium phosphate)
- 3rd generation (end of 20th century): characterised by a high bioactivity* and aimed to foster tissue regeneration. These materials often consist of ceramics of the 2nd generation produced in highly porous form so that they can be "seeded" with cells and biochemical factors (tissue engineering).

1.3.1 Resorbable bone substitutes

Resorbable ceramics can be divided in several groups, but the present overview will be focused just on four: calcium carbonates (CC), calcium sulfates (CaS), bioglass-glass ceramics (BG) and calcium phosphates (CaP) [16]. In particular, the present study dealt with the last group of ceramics (CaP); for this reason calcium phosphates will be discussed more extensively in paragraph 1.4.

Calcium Carbonates (CC)

Calcium carbonates ($CaCO_3$) present 6 different allotropic forms, depending on their solubility (in increasing order: calcite, aragonite, vaterite, monohydrated $CaCO_3$, hexahydrated $CaCO_3$, amorpous $CaCO_3$) [17]. In nature the most common forms are calcite and aragonite, which can be found in pearl, coral and shells. Also the most soluble metastable form, i. e. amorpous $CaCO_3$, is quite widespread, acting as a stock of CC during the biomineralisation of some sea organisms. Moreover, calcium carbonate is one of the main impurities/substitutions in bone mineral. For this reason since many years CC are employed as bone graft materials. Natural calcium carbonates (mainly coral and nacre) are used in form of powder, granules and gel [18, 19]. Thanks to their intrinsic porosity (e.g. the porosity of coral is around 50%) these materials favour bone ingrowth. Once implanted, in fact, they dissolve and cause the formation of a carbonated apatite layer which links to the surrounding bone [20]. *In-vivo* studies both in animals and humans have confirmed the biocompatibility, bioactivity and resorbability of calcium carbonates [21]. Current researches are focused on the production of synthetic CC, in order to avoid problems typical of natural materials, such as the limited availability and the possibility of contaminations. In this perspective CC pure or in combination with other phases (i.e. calcium phosphates) have been proposed [22, 23].

Calcium Sulfates (CaS)

This group consists of hydrated calcium sulfate, that is to say gypsum, either in form of cements or of solid, with the formula: $CaSO_4 \cdot 2H_2O$.
Although usually produced starting from the α hemihydrate powder, which leads to the formation of a stronger material compared to the β one [24], CaS displays the most rapid degradation process (3-8

weeks) among resorbable ceramics. Its degradation is mainly due to dissolution phenomena more than cellular degradation ones [6].
Because of this characteristic rapid degradation, different studies on the production of biphasic composites (with HAp granules), which could tune the resorption rate of CaS are still ongoing [6].

Boactive Glasses (BG) and glass ceramics

This class of materials is highly reactive and induces the quick formation of bonds with bone [16, 25].
After the creation in 1969 of the first BG (the silica-based 45S5) by Hench [26], several BG compositions have been studied and the mechanism of the so-called "bioactivity" of Bioglass® has been fully documented in literature [3].
BGs have been also proved to be resorbable (mainly by dissolution process, in 1-2 years *in-vivo*) and are currently used for dental and middle-hear surgeries. Future applications of BGs could be in the soft tissue domain [16, 25, 27].

For the sake of briefness, in this work glass ceramics have been here coupled with bioactive* glasses, but they could represent a separate category.
Glass ceramics are made of a crystalline phase (mostly apatite-wollastonite, A-W, $Ca_{10}(PO_4)_6(OH)_2$ - $CaO \cdot SiO_2$) and a glassy one ($MgO\text{-}CaO\text{-}SiO_2\text{-}P_2O_5$) [16]. Thanks to the presence of a crystalline phase, the A-W glass-ceramic displays mechanical properties higher than those of BGs and can be used, therefore, in load-bearing implants (in vertebrae and long bones). This material exhibits a good bioactivity*, whereas almost no resorption has been observed even after years of implantation [16].

1.4 Calcium Phosphates

One of the most interesting characteristics of this class of materials is their chemical composition. CaPs, in effect, have a composition really close to the inorganic component of bone (apatite).
Stoichiometric hydroxyapatite is a mineral compound with the following formula: $Ca_{10}(PO_4)_6(OH)_2$. However, the most common form of HAp in the human body is not stoichiometric and presents some ionic substituents, such as carbonate and magnesium ions [28]. For sake of clearness, from here on, stoichiometric apatite will be named "HAp" while the non-stoichiometric one will be called "apatite".
Although different from the apatite present in bone tissue (for example in terms of microstructure), synthetic calcium phosphates display optimum biocompatibility* and they are often resorbable, offering, thus, a good option for bone replacement.
The CaPs group includes different materials, either obtained at high temperature, e.g. by sintering, or at low temperature, e.g. by means of precipitation in aqueous medium [16, 28]. The main calcium phosphate phases are listed in Table 1.
In the next pages a brief description of the process of these materials and an introduction to some CaPs of interest in respect to this work will be given. Therefore, special attention will be devoted to β-TCP (β-tricalcium phosphate) and DCPD (dicalcium phosphate dihydrate), which belong, in our case, to the family of sintered ceramics and cements respectively.

Table 1: example of calcium phosphates (first five synthesised at room temperature, the other four by thermal treatment) (adapted from [28]*)*

name	acronym	formula	Ca/P
Monocalcium phosphate monohydrate	MCPM	$Ca(H_2PO_4)_2 \cdot H_2O$	0.5
Dicalcium phosphate (anhydrous)	DCPA	$CaHPO_4$	1.00
Dicalcium phosphate dihydrate	DCPD	$CaHPO_4 \cdot 2H_2O$	1.00
Octacalcium phosphate	OCP	$Ca_8H_2(PO_4)_6 \cdot 5H_2O$	1.33
Precipitated hydroxyapatite	pHA or apatite	$Ca_{10-x}(HPO_4)_x(PO_4)_{6-x}(OH)_{2-x}$	1.50-1.67
α-Tricalcium phosphate	α-TCP	$\alpha\text{-}Ca_3(PO_4)_2$	1.50
β-Tricalcium phosphate	β-TCP	$\beta\text{-}Ca_3(PO_4)_2$	1.50
Sintered hydroxyapatite	HAp	$Ca_5(PO_4)_3OH$	1.67
Tetracalcium phosphate	TTCP	$Ca_4(PO_4)_2O$	2.00

1.4.1 Synthesis and processing

Most of the materials used for medical applications are obtained by reaction at high temperature (such as hydroxyapatite and tricalcium phosphate) [28]. Nevertheless low-temperature CaPs, which were initially used only as reagents for obtaining high-temperature CaPs [28], are more and more used in the biomedical field. After the discovery of calcium phosphate cements (CPC), in fact, low-temperature CaPs have experienced a large diffusion. The main compounds of this class are: MCPM, DCPA, DCPD, OCP, pHA (see Table 1 for definitions).

Many calcium phosphates can be processed at high temperature, for example through sintering procedures. In particular the initial powders can be shaped (in the so called “green body”), thanks to the addition of binders or after simple mechanical compaction, and then treated at high temperature (and pressure in some cases) [29]. At high temperatures, diffusion processes lead to necks formation between particles and consolidation; the final result is a solid body. Traditionally this technique has been used to obtain dense samples. Nevertheless if the thermal treatment is performed at a temperature inferior to the one of sintering (sub-sintering), or if partial particle packing in the green state is preserved, porous materials can be obtained.
In the case of sub-sintering, the particles create links between each other, but the process of sintering is stopped before they can merge completely. As a consequence, some porosity is left in the final material.
Other techniques for obtaining a final material, which displays the desired degree of porosity, imply some simple changes in the elaboration of the green body. For example the addition of a porogenic agent in the suspension of the initial powders (slurry) will result once sintered in a porous body [30]. In the same way, organic particles (such as oil or polymeric beads) can be mixed to the powders and then burnt out during the thermal process leaving porosities [31, 32]. Finally a polymeric sponge can be dipped in a calcium phosphate slurry and afterwards eliminated through the sintering treatment; in this case, the sponge acts as a template, leaving open porosities in the final material [33]. Additive manufacturing technologies are expanding fast in the ceramic community, and this applies also in the field of bone substitute applications. These techniques also allow creating a well-controlled architecture and porosity network.

Some other CaPs can be processed at low temperature through a setting reaction, simultaneously to their synthesis. This process is typical of cements and the resulting material, thus, is often referred to as CPC (Calcium Phosphate Cement).

The elaboration of CPC consists in mixing one (or more) CaPs and an aqueous solution. During the reaction the CaP dissolves and consequently precipitates in form of crystals of a less soluble calcium phosphate. Finally the crystals grow and get entangled leading to the formation of the microstructure of the cement. The setting reaction can be either of acid-base type (one acidic and one basic CaP are mixed in order to obtain a neutral CaP) or characterised by the fact that both the reagent and the resulting CaP have the same Ca/P molar ratio [28].
The CPC class can be further divided into two subgroups depending on the end-product of the setting reaction: the cement obtained can be, in fact, either an apatite CPC or a brushite CPC.
Whatever the production method is, the final product is always quite fragile (with a tensile strength largely lower than the compression strength), this is why CPC are generally used only for non-load-bearing applications such as maxillofacial surgeries [16].
Nevertheless, the main advantage of these materials is that they are obtained by setting reaction at low temperature and can be injected and let cure directly in the body of the patient without the problems of necrosis induced by exothermic reactions typical of other materials such as PMMA cements [34]. Finally, the setting process permits to obtain porous samples. In fact, if the amount of solution is in excess compared to the stoichiometric quantity, the liquid will evaporate during the drying step leaving porosities inside the material.

1.4.2 CaPs of interest for this work

In the next pages the main features of some calcium phosphates compounds will be presented. The phases are the ones of interest for the present study, either because they represent the main initial component of the samples used in this work or because they appear on the samples during the tests performed. While these latter phases will be described quite briefly, the former (namely DCPD and β-TCP) will be illustrated more profusely.

Hydroxyapatite

This section will first be devoted to the stoichiometric form of calcium phosphate hydroxyapatite (HAp) and then to its non-stoichiometric forms, which will be denoted “apatite” throughout this manuscript.

In fact, synthetic hydroxyapatites can be obtained both at low temperature, by a precipitation process, or at high temperature. The stoichiometric form ($Ca_{10}(PO_4)_6(OH)_2$, HAp), obtained at high temperature, has an atomic calcium to phosphorus ratio of 1.67 [28] and an hexagonal lattice, where tetrahedra of calcium phosphate surround columns of hydroxides (Figure 2). HAp is highly crystalline and is characterised by the lowest solubility among all CaPs in physiological conditions.

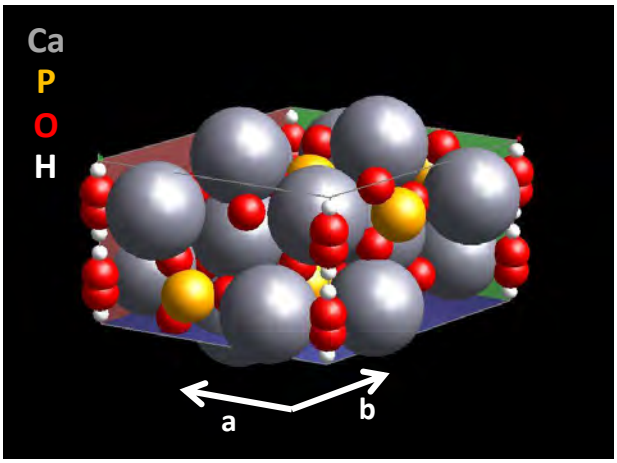

Figure 2: Crystallographic structure of hydroxyapatite

The stoichiometric form of hydroxyapatite is never present in biological systems, but it is commonly used as a model biomaterial for bone and dental applications. Either of synthetic or of natural origin, HAp is characterised by excellent biocompatibility*, which means that it induces an appropriate reaction of the body after implantation [16].
It has been documented how synthetic HAp can induce the formation of an apatite layer *in-vitro* [16]. This phenomenon is often identified as an evidence of the bioactivity* of a material. However this point of view is also debated [35, 36]. Although well tolerated by the organism, as proved with *in-vivo* tests [37-40], synthetic HAp seems to require a very long time to degrade. In certain cases, it has been shown that HAp substitutes were still present and integrated in the new bone after periods as long as 10 years [41]. Several *in-vitro* tests with osteoclasts (cells in charge of bone resorption), in addition, have shown little resorption on pure HAp surfaces [7, 42]. Because of its low solubility, HAp is dissolved and resorbed at a much slower rate than that of other CaPs.
To overcome this problem, HAp is often mixed with β-TCP (β-tricalcium phosphate); the aim is to obtain materials (called BCP, Biphasic Calcium Phosphates) with a dissolution rate and a bioactivity* that represent a good compromise between those of HAp and β-TCP [14, 42].
An alternative solution is the use of non-stoichiometric form, also called biomimetic nanocrystalline apatite, obtained at low temperature. This is characterised by a low crystallinity with crystals of sub-micron dimension [43, 44]; as a consequence, its solubility is relatively high compared to the one of HAp obtained at high temperature and could, therefore, help to overcome the problem of the too slow degradation of stoichiometric apatites.
Nanocrystalline apatite displays characteristics similar to those of the biological one, which accounts for the main part of the inorganic components of bones [3], dentine and dental enamel [45]. Legros [46] has described the bone mineral apatite by the following formula:

$$Ca_{8.3}\,\square_{1.7}\,(PO_4)_{4,3}(CO_3)_{1,0}(HPO_4)_{0,7}(CO_3,OH)_{0,3}\square_{1,7}$$

It is to be noted that this global formula does not take into account all possible variations, which differ depending on parameters such as the part of tissue sampled, age, gender, diet…
As seen in this formula, the apatite lattice allows many substitutions to occur. For example, carbonate and hydrogenophosphate ions are often encountered and present in the biological tissues. The non-stoichiometric composition and the presence of a hydrated layer on the crystal surface of these biological apatites are also found in synthetic nanocrystalline apatites [44, 47, 48]. The presence of a metastable hydrated layer, which contains labile ions, has been shown to ease the ionic exchange between nanocrystals and the surrounding medium as well as the absorption of proteins and biological molecules at their surface. It has been proved that, during ageing, the composition and the thickness of the hydrated layer of apatite nanocrystals evolve [43]. For these reasons, nanocrystalline apatite presents a very high surface reactivity, which permits the tuning of their biological properties.
Few works have investigated the osteoclastic resorption of such biomimetic apatite, with different conclusions about the influence of the hydrated layer and its degree of maturation on the osteoclastic resorption [49, 50].

Octacalcium Phosphate (OCP)

Octacalcium phosphate, OCP ($Ca_8(HPO_4)_2(PO_4)_4 \cdot 5H_2O$), is considered to be the solubility-controlling phase in living bone [6] and seems to be the main precursor of apatite in physiologic conditions [39, 51]. Its stoichiometric composition displays a Ca/P ratio equal to 1.33, but this ratio often differs in nature.
The structure of OCP consists of apatite layers alternated with hydrated layers (where also some calcium ions and phosphate groups are located) (Figure 3) [52, 53].
The conversion of OCP into HAp involves the release of phosphates and the incorporation of calcium ions as showed by *in-vitro* tests performed both in culture medium and TRIS-buffer solution [54]. The conversion starts with the formation of an amorphous layer, which later turns into HAp. This phenomenon, as proved both by *in-vitro* and *in-vivo* tests [54], is topotaxial, which means that it is

based on the diffusion of ions in the lattice and not on a dissolution-precipitation process; as a consequence the final shape of HAp crystals is really close to the one of the initial OCP particles. OCP has been suggested, at present, in form of granules for healing critical-size bone defects, but also as coating on metallic implants, in order to increase their osteoconductivity* [54].

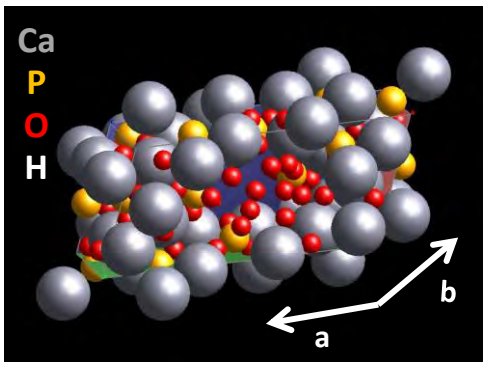

Figure 3: Crystallographic structure of OCP

OCP has been proved to be biocompatible*, biodegradable and osteconductive* [28]. An OCP layer seems to precipitate on almost all bioceramics during *in-vitro* tests in SBF (Simulated Body Fluid) and it is proposed, thus, by some authors, as an index of bioactivity* more significant than HAp precipitation [39, 40]. Another study has given evidences that OCP, *in-vitro*, fosters the differentiation of cells responsible for bone deposition (osteoblasts) and, *in-vivo*, eases bone regeneration [54]. Moreover the newly-formed bone in presence of OCP displays a structure, composed by non-collagenous filaments and CaP granules, which is very similar to the one of the initial *loci* of mineralisation found in physiologic bone formation processes [54]. Finally, the change in calcium concentration due to the conversion of OCP into HAp, seems to be linked to the differentiation of osteoclasts (cells in charge of bone resorption) [54].

Dicalcium Phosphate Anhydrous (DCPA)

Dicalcium phosphate anhydrous (DCPA or DCP, $CaHPO_4$) is also named monetite in its mineral form. DCPA crystallises in a triclinic unit cell and its structure consists of rows of $CaHPO_4$ mutually linked by Ca-O bonds [55] (Figure 4).
One way for obtaining DCPA is to produce DCPD (the dihydrated form of DCPA presented below) and convert it into DCPA by thermal hydrolysis (>60°C). DCPA can also be synthesised directly through setting reaction in very acid conditions (pH<4-4.5) or in water-deficient environments [56]. At present, DCPA finds its applications in the field of bone regeneration, in not-load-bearing zones, both in form of injectable paste and blocks [28].

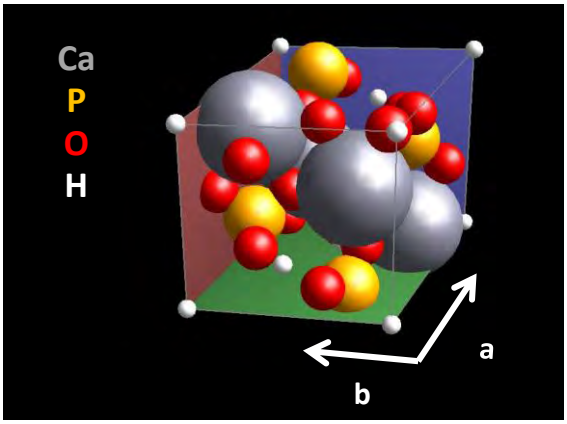

Figure 4: Crystallographic structure of DCPA

Although rarely present in physiologic conditions (DCPA has been found in fracture callus, [28]), DCPA is biocompatible* and biodegradable. *In-vivo,* it displays properties of osteoconduction* and osteoinduction* has been reported in some cases [56]. *In-vitro* experiments, finally, have given evidences that DCPA could stimulate osteoblasts activity [56].

Dicalcium Phosphate Dihydrate (DCPD)

Dicalcium phosphate dihydrate (DCPD), also named brushite in its mineral form, is a ceramic with chemical formula $CaHPO_4 \cdot 2H_2O$ and Ca/P ratio equal to 1.
DCPD is structured in non-centrosymmetrical monoclinic crystals with plate-like shape [56], composed of rows of Ca^{2+} and HPO_4^{2-} ions spaced out by layers of water molecules (Figure 5) [52].

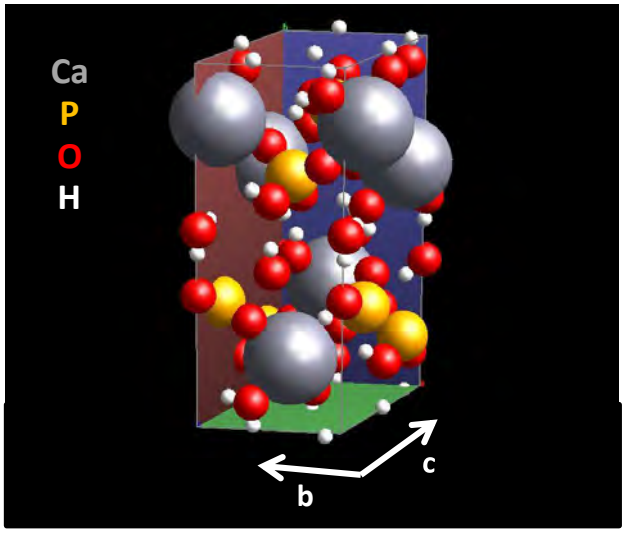

Figure 5: Crystallographic structure of DCPD

DCPD can be obtained, among different processes, through setting reaction at room temperature, in the form of cements. CaP cements (CPC) are obtained by mixing one (or more) CaP powder with an aqueous liquid phase; the result can be either an apatite or a brushite cement. Since the production of the first CPC by Brown and Chow[1] in 1986 [28, 57] scientific interest has been focused mainly on apatitic cements. However, the need of improving CPC resorption rate arisen in recent years has shifted the attention towards cement compositions including a metastable phase in physiological conditions such as DCPD which is hydrolysed in apatite once implanted leading especially to the development of brushite CPCs which degrade faster than apatitic ones.
In order to obtain a brushite CPC, it is necessary to mix an alkaline Ca source (often tricalcium phosphate, given its large availability) with a phosphate acidic source (mainly phosphoric acid, PA) and water. Given that the alkaline source is always characterised by a Ca/P ratio higher than 1, the phosphate acidic source has to have a ratio inferior to 1, so that the final product of the reaction has a Ca/P = 1, typical of DCPD. This necessary condition leads to a limited range of possible phosphate sources: besides phosphoric acid, in fact, only MCPM (monocalcium phosphate monohydrate, $Ca(H_2PO_4)_2 \cdot H_2O$) and MCPA (monocalcium phosphate anhydrous, $Ca(H_2PO_4)_2$) display a Ca/P < 1 (0.5 precisely). Moreover MCPM is usually preferred to its anhydrous form because it provides already one of the two water molecules required for the setting reaction of DCPD. Consequently, brushite cements are usually obtained by means of one of the following formulae [28, 58, 59] (where TTCP refers to tetracalcium phosphate, $Ca_4(PO_4)_2O$):

[1] Brown and Chow reaction: $Ca_4(PO_4)_2O + CaHPO_4 \rightarrow Ca_5(PO_4)_3OH$ (TTCP + DCPA → HA) [21]

$$\beta - TCP + MCPM + H_2O \rightarrow DCPD$$
$$\left(Ca_3\left(PO_4\right)_2 + Ca\left(H_2PO_4\right)_2 \cdot H_2O + 7H_2O \rightarrow 4CaHPO_4 \cdot 2H_2O\right) \quad (1)$$

$$\beta - TCP + PA + H_2O \rightarrow DCPD$$
$$\left(Ca_3\left(PO_4\right)_2 + H_3PO_4 + 6H_2O \rightarrow 3CaHPO_4 \cdot 2H_2O\right) \quad (2)$$

$$TTCP + MCPM + CaO + H_2O \rightarrow DCPD$$
$$\left(Ca_4\left(PO_4\right)_2 O + 3Ca\left(H_2PO_4\right)_2 \cdot H_2O + CaO + 11H_2O \rightarrow 8CaHPO_4 \cdot 2H_2O\right) \quad (3)$$

Whatever the above mentioned ways to prepare brushite cements, the reaction is of acid-base type and causes the formation of an acidic paste; this particular condition is essential, given that DCPD precipitates at pH<6.
One of the simplest reactions for obtaining DCPD is the one proposed by Lemaître and Mirtchi in 1989 (Eq.(1)). The reaction can be summarised in the following 4 main stages. Dissolution of the reagents: in this case MCPM dissolves first, causing a pH decrease (Eq.(4)); then β-TCP dissolution takes place (Eq.(5)), thanks to the acidic environment. Once the solution is saturated with respect to calcium and phosphate ions, nucleation of a more stable CaP compound (DCPD, Eq.(6)) occurs, followed by crystal growth and entanglement leading to the formation of the cement microstructure.

$$Ca\left(H_2PO_4\right)_2 \cdot H_2O \rightarrow Ca^{2+} + 2H_2PO_4^- + H_2O \quad (4)$$

$$\beta - Ca_3\left(PO_4\right)_2 + 4H^+ \rightarrow 3Ca^{2+} + 2H_2PO_4^- \quad (5)$$

$$Ca^{2+} + H_2PO_4^- + 2H_2O \rightarrow CaHPO_4 \cdot 2H_2O + H^+ \quad (6)$$

$$\text{Full equation: } \beta - Ca_3\left(PO_4\right)_2 + Ca\left(H_2PO_4\right)_2 \cdot H_2O + 7H_2O \rightarrow 4CaHPO_4 \cdot 2H_2O \quad (7)$$

While the dissolution of MCPM is an endothermic reaction, the one of β-TCP is exothermic. Also DCPD precipitation releases energy, so, on the overall, the full equation (Eq.(7)) is exothermic [56, 60] nevertheless the amount of heat released is quite low (< 50°C in the conditions reported in [61] and it is not likely to induce any damage in case of injection in the human body. This aspect and the fact that the setting reaction takes place at room temperature are some of the characteristics of DCPD cement, which make it an excellent candidate for biomedical applications.

Once the reagents for the production of the cement have been chosen, other important parameters must be considered. In fact, preparation of the initial CaP powders, use of additives, ratio powder-to-liquid (P/L) can strongly affect the setting reaction and the final product (both in terms of structure and mechanical properties).
Being interested in the present work at the system β-TCP - MCPM - H_2O (Eq.1(1)), only this one will be analysed in detail, while the others (Eq.(2)-(3)) will not be mentioned further. For any additional information, however, it is advisable to consult the work of Bohner [59].
In the case of β-TCP - MCPM - H_2O system, one of the parameters to carefully control is the preparation of **β-TCP** and in particular its **grinding**. As previously reported by Bohner [59], during grinding of the β-TCP powder, its specific surface increases and its "plasticity limit" (= volume of liquid needed to obtain a workable paste) decreases (Figure 6). As a consequence it is possible to obtain a more liquid paste (although more reactive, Figure 7). All the other characteristics of the final product, such as porosity and mechanical properties, however, remain unaltered [59].

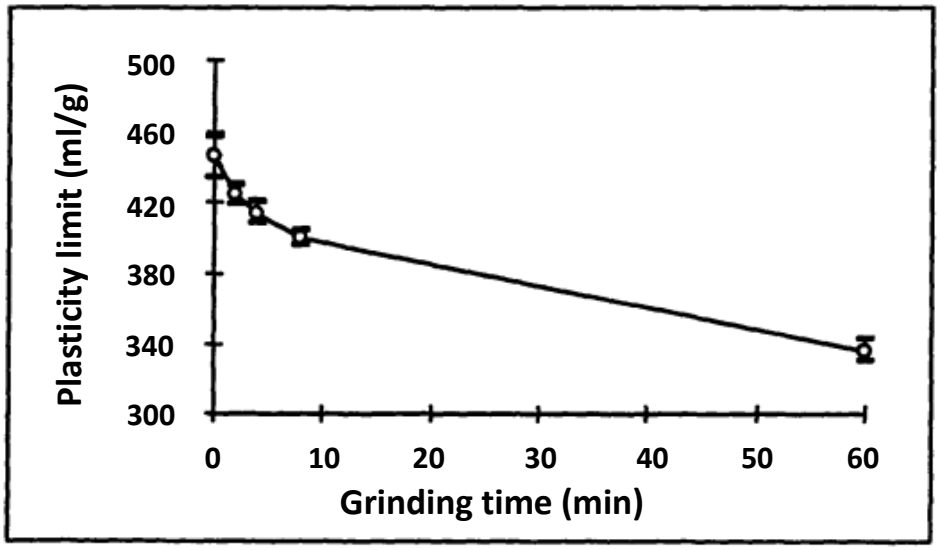

Figure 6: Plasticity limit vs grinding time of β-TCP powder (bars = 90% confidence level) [59]

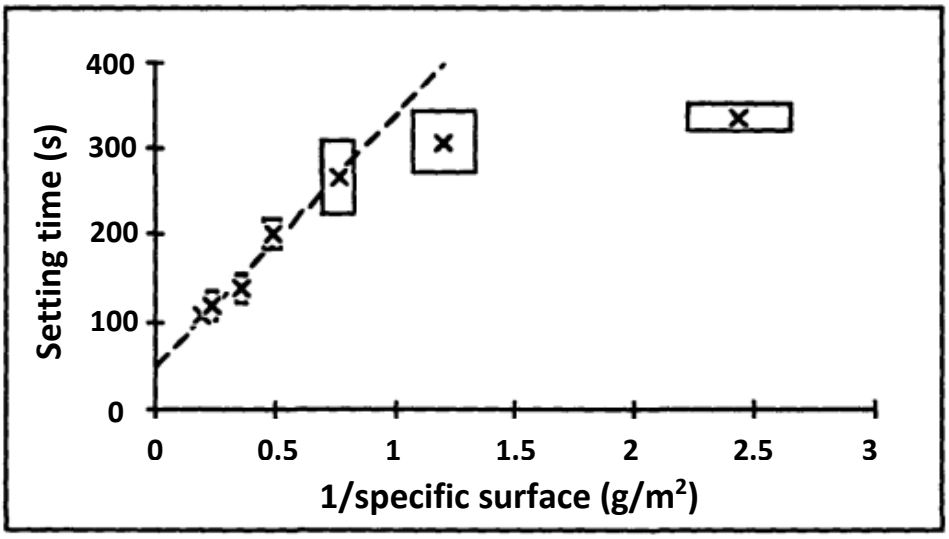

Figure 7: Setting time vs inverse ratio of the specific surface of β-TCP powder (squares = 90% confidence level). Cement composition: 1.5 g β-TCP, 1.2 ml solution 2M phosphoric acid and 0.1M sulphuric acid [59]

As far as **additives** are concerned the main interest is arisen by retardants. In case of bone substitutes, for example, it is crucial to obtain cements with a setting time compatible with the surgical process. For this reason, additives are frequently used to slow down the too fast setting reaction of DCPD cements. Retardants can act either slowing the rate of dissolution of β-TCP or delaying the precipitation of DCPD. The most used ones are sulfate, citrate and pyrophosphate ions (listed in order of increasing effect, Figure 8). All of them inhibit DCPD crystal growth, but, while citrates and pyrophosphates also decrease the rate of dissolution of β-TCP, sulfates slightly increase it [59].

When choosing the retardant, one should also consider its consequences on the properties of the cement. On this regard, sulfates strengthen the final material, by causing the formation of a finer microstructure of the cement. On the other hand pyrophosphates and citrates do not seem to affect either the porosity or the mechanical properties of the cement in a significant way (Table 2).

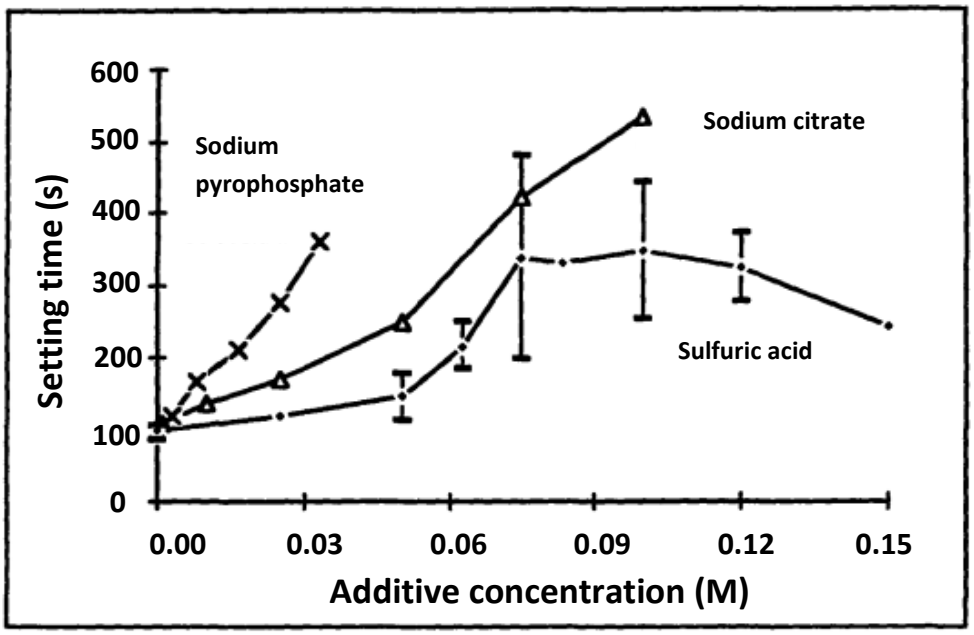

Figure 8: Effect of retardant concentration on setting time. Retardants: $Na_4P_2O_7$, $C_6H_5O_7Na_3$, H_2SO_4 (only for sulfuric acid, bars = 90% confidence level). Cement composition: 1.5 g β-TCP, 1.2 ml solution 2M phosphoric acid and the retardant [59]

Table 2: Influence of additives on the final properties of the cement (confidence interval = 90%) CPP = calcium pyrophosphate, $Ca_2P_2O_7$ [59]

	Setting time (s)	Resistance, traction (MPa)	Porosity (%)
No additives	112 ± 5	0.9 ± 0.3	51.6 ± 0.2
0.03M pyrophosphate	190 ± 10	0.8 ± 0.4	52.4 ± 0.8
0.03M citrate	148 ± 6	0.8 ± 0.3	52.2 ± 0.6
20%wt CPP ($Ca_2P_2O_7$)	128 ± 6	0.7 ± 0.2	54.2 ± 0.2

Finally the choice of the **powder to liquid phase ratio** (P/L) can strongly influence both the mechanical and the microstructural properties of the cement. By decreasing P/L, in fact, setting time and porosity increase, while the resistance (in compression and traction) decreases [57, 59]. This last effect can be explained not only by the above mentioned augmentation of porosity, but also by the increase in the average size of the crystals [59].

To conclude, it is clear that even slight changes in the choice of the initial parameters can lead to very different cements; for sure this can be a tough challenge for the reproducibility of samples, but at the same time it offers the possibility to tune the properties of the final cement in a wide range, making it suitable for different applications [56]. At present, DCPD is produced in form of pastes or blocks, alone or in combination with other materials (i.e. β-TCP, BG…) and it is mainly used for dental and orthopaedic applications (in maxillofacial, cranial and vertebroplastic surgery). Studies currently ongoing, however, are exploring the possibility of exploiting DCPD for drug delivery system, for cancer therapy and in the field of biosensors [56].

β-Tricalcium Phosphate (β-TCP)

Tricalcium phosphate, abbreviated TCP, is a ceramic with chemical formula $Ca_3(PO_4)_2$. TCP has three polymorphs (β, α and α') depending on the temperature. At low temperature β is the stable allotropic form; between 1180°C and 1400°C [62] α is stable, while at temperature above 1470°C the dominant polymorph is α'.
While the α form is monoclinic, the β one displays a rhombohedral structure with cell parameters: $a = b = 10.4352$ Å, $c = 37.4029$ Å, $\alpha = \beta = 90°$, $\gamma = 120°$. In the α crystals, columns of Ca^{2+} are alternated with columns composed by calcium and phosphates; the β structure is similar, but consists of two types of Ca-P columns and none containing only calcium (Figure 9, [63]). This difference leads to a looser structure in the case of α-TCP (volume per unit formula = 180 $Å^3$ for α-TCP, 168 $Å^3$ for β-TCP, [64]), also reflected in a lower density (2.86 g/cm^3 for α-TCP, 3.07 g/cm^3 for β-TCP).

Among the three allotropic forms the β one tends to be preferred, because of its higher mechanical strength compare to the α one, its biocompatibility* and its lower rate of solubility [62]. In this perspective the next parts of this work will be focused only on the β form of TCP.

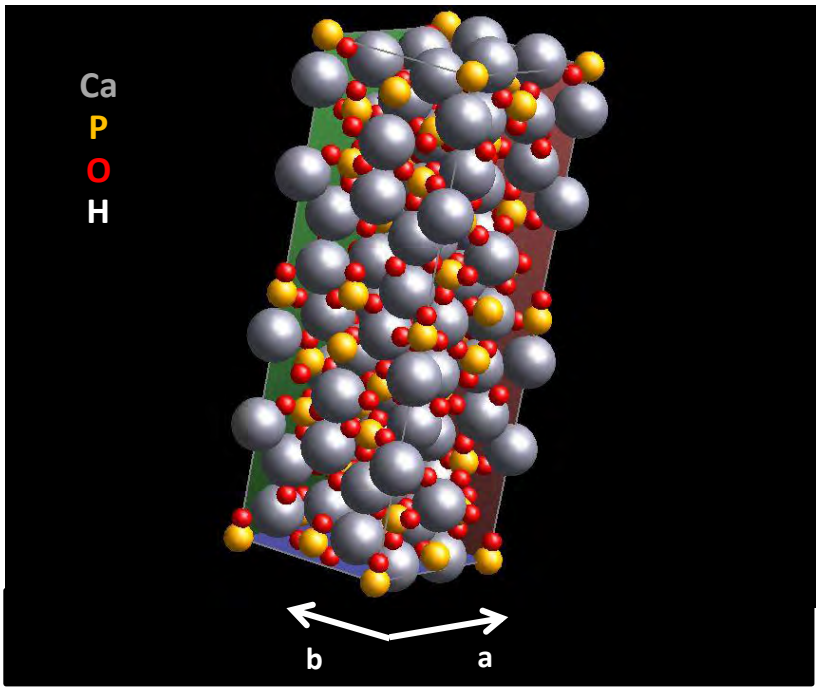

Figure 9: β-TCP crystallographic structure

In order to synthetize β-TCP, different routes can be followed, which can all be classified in three main categories:

- Pechini/wet chemical technique
- Aqueous precipitation
- Mechano-chemical method

The Pechini method is based on the preparation of a liquid solution whose homogeneity is retained in the solid state. For such a purpose, specific salts ($Ca(NO_3)_2 \cdot 4H_2O$ and $H_2NH_4PO_4$, calcium nitrate tetrahydrate and dihydrogen ammonium phosphate) are dissolved in 0.2M citric acid aqueous solution; after heating (60-70°C), ethylene glycol is added. Citric acid induces the formation of chelates, which are then polymerised thanks to the presence of ethylene glycol. The result is a

viscous solution (resin), characterised by high homogeneity; after a thermal treatment of calcination, finally, pure β-TCP is obtained [65, 66].

The wet chemical technique is quite similar to the Pechini method, but neither chelating (i.e. citric acid) nor gelling agents (i.e. ethylene glycol) are used. In practice, $(NH_4)_2HPO_4$ (diammonium hydrogen phosphate) is drop-wise added to $Ca(NO_3)_2{\cdot}4H_2O$ (calcium nitrate tetrahydrate) and mixed in order to obtain a precipitate, while the pH is maintained constant by adding NaOH [67], HNO_3 [68] or NH_4OH [31]. Finally the precipitate is calcined, turning into β-TCP.

In the aqueous precipitation method a suspension of calcium hydroxide ($Ca(OH)_2$) is mixed with a phosphoric acid solution (H_3PO_4) [69, 70]. The resulting precipitated compound consists of Ca-deficient hydroxyapatite (CDHA) that, upon appropriate thermal treatment, converts into β-TCP, following the equation (Eq.(8), [71]:

$$\begin{gathered} CDHA \rightarrow \beta - TCP + H_2O \\ Ca_9\left(HPO_4\right)\left(PO_4\right)_5\left(OH\right)_3 \rightarrow Ca_3\left(PO_4\right)_2 + H_2O \end{gathered} \tag{8}$$

Finally, for the solid state reaction a powder source of calcium and another source of phosphate are mixed in stoichiometric proportions to obtain β-TCP and milled before undergoing a thermal treatment of calcination. Different combinations of reagents are possible and among those some of the most diffused ones are:

$$DCPA + CC \tag{9}$$

$$DCPD + CC \tag{10}$$

$$DCPD + CaO \tag{11}$$

$$DCPD + HAp \tag{12}$$

$$CPP + CC \tag{13}$$

Where: DCPA = dicalcium phosphate anhydrous ($CaHPO_4$), DCPD = dicalcium phosphate dihydrate ($CaHPO_4{\cdot}2H_2O$), CC = calcium carbonate ($CaCO_3$), HAp = hydroxyapatite ($Ca_5(PO_4)_3(OH)$), CPP = calcium pyrophosphate ($Ca_2P_2O_7$).

A deep analysis of the phase evolution during the synthesis of β-TCP through the system DCPD+CC (Eq.(10)) has been developed by Jinlog et al. [72]. As explained, the thermal treatment of the mixed powders involves different steps, which lead to the formation of TCP.
At first DCPD undergoes a dehydration process, turning into DCPA at around 200°C (from here after the described steps are valid also for the reaction showed in Eq.(9)). Then DCPA condensates into calcium pyrophosphate at 450-500°C following the equation (14). At 800°C calcium carbonate is converted into calcium oxide (CaO) upon the release of carbon dioxide (Eq.(15)). The calcination of CC seems to be the rate-controlling step of the whole reaction: once CaO is formed, in fact, the final phase can take place and CPP and CaO can react forming β-TCP (Eq.(16)), [72].

$$2CaHPO_4 \rightarrow Ca_2P_2O_7 + H_2O\uparrow \tag{14}$$

$$CaCO_3 \rightarrow CaO + CO_2\uparrow \tag{15}$$

$$Ca_2P_2O_7 + CaO \rightarrow \beta - Ca_3\left(PO_4\right)_2 \tag{16}$$

All the solid-state reaction processes, whatever the reagents are, can be either performed in dry or wet condition before the thermal treatment (meaning, by “wet”, that water or ethanol are added

during the milling step). Although the addition of a liquid phase should homogenise and simplify the grinding process, it has been proved that the reaction rate is slowed down and the risk of pollution might increase [73]. This is why dry grinding is often preferred to the wet one.

One of the key passages during the elaboration of β-TCP samples is the thermal treatment that the powder undergoes. When it is necessary to sinter fully dense specimen, in fact, problems arise from the phase transition β→α and its reverse transition during cooling which, causing a decrease in volume, induces the formation of cracks. Therefore many efforts have been focused on increasing the temperature of the transition phase of TCP (1180°C for pure phases). This goal can be reached, for example, by the addition of **dopants**: different studies have proved magnesium to be a good solution for this purpose [62, 74, 75]. By adding Mg (in form of MgO, up to 5 wt.%), the transition temperature of TCP is increased up to 1500°C enabling the sintering of denser samples without β→α transition [29, 62]. A similar effect, although weaker, can be obtained by adding calcium pyrophosphates (CPP, $Ca_2P_2O_7$) [62] or zinc (Zn, [76]). Moreover also the use of NaF (sodium fluoride) has been proved to improve the densification of the final material [77].
Nevertheless the doping process can also induce important changes other than the mere increase of density. For example an augmentation of grain size has been observed when using NaF [77]: this can be explained both by the increase of vacancies induced by the substitutional Na ions (which are likely to change the kinetics of grain boundaries migration) and the formation of a liquid phase which helps the sintering process.
In the same way the dissolution rate of the sintered material can also be affected; in particular the substitution of Ca^{2+} by smaller ions (such as Mg^{2+}, Mn^{2+}, Zn^{2+}), decreasing the bonding distance between cation and oxygen, stabilises the lattice and hinders the dissolution process [52].
Finally the biological properties of the material can be influenced by the addition of dopants [25]: several studies, indeed, are presently aimed at the assessment of the consequences of ions substitution on cell proliferation [52, 76, 77].
To conclude, it is worthy to remember that at present β-TCP is commercially available in different forms (blocks, granules…) and it is used as bone substitute for non-load-bearing applications, such as maxillo-facial reconstructions [16, 28].

1.5 Evolution of calcium phosphates

As mentioned, the evolution of an implanted material can be due both to cellular activity and to physico-chemical phenomena of dissolution and re-precipitation. The current paragraph focuses on this second aspect; the results of *in-vitro*, *in-vivo* and cellular tests performed on β-TCP and DCPD will be briefly summarised. Basic information about the evolution upon implantation of other kinds of CaPs (such as HAp, OCP and DCPA) has been already provided in paragraph 1.4.2 and will not be further investigated.

Already back in 1991 LeGeros [78] suggested the influence of the physico-chemical properties of materials on their biodegradation process, underlining, in particular, the importance of solubility and dissolution. As proposed by Bohner [6] it seems that the evolution of properties of implanted materials depends on their solubility (influenced by composition and crystal size), kinetics (depending on geometry) and *in-vivo* conversion, as confirmed also by other authors [16].
In particular, in physiological conditions (37°C, pH 7.4), the threshold of **solubility** is represented by OCP (octacalcium phosphate $Ca_8H_2(PO_4)_6 \cdot 5H_2O$). If a CaP phase is more soluble than OCP (e.g. MCMP, DCPD, DCPA, MCP, see Figure 10) it is likely that, once implanted, it will dissolve; this kind of materials are usually defined as “biosoluble”. On the other hand, CaPs, which are less soluble than OCP, such as β-TCP and HAp, will be resorbed mainly (if not only) through cellular activity (either by macrophages or osteoclasts) and can be named “bioresorbable”.

As far as **kinetics** of dissolution is concerned, size, shape and porosity of the implant seem to play an important role. The observation of dissolution and precipitation of phases, which are not thermodynamically predicted, could be justified by the influence of the implant geometry on the kinetics of its dissolution. For example, some studies showed that DCPD samples after implantation underwent dissolution/re-precipitation phenomena just at core or on their whole volume depending, probably, on the location of the specimen and its volume [79, 80].
Finally, while dissolving, "biosoluble" CaPs release ions that can interact with the surrounding medium and **precipitate** in form of other compounds which are less soluble (mainly apatite, given that this compound is the most stable in physiological conditions). This process clearly alters the dissolution process; this is why some authors stated that the solubility of CaP is not primarily leaded by their solubility products, but rather by the transformations that take place on their surface [81].

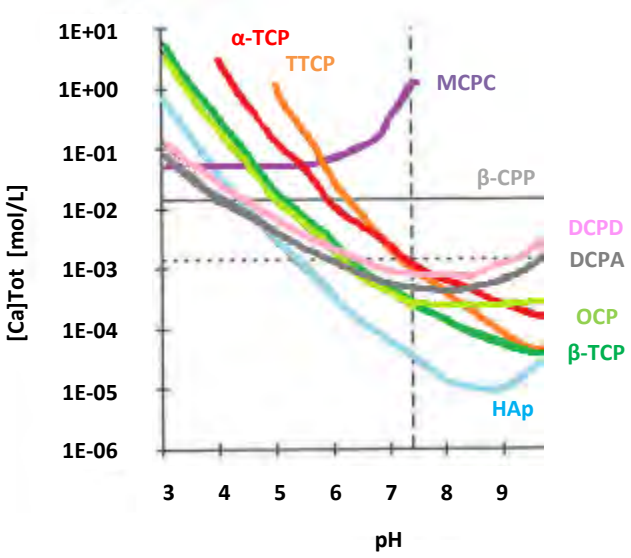

Figure 10: Isotherm curves of solubility of CaP (in water, 25°C). From top to bottom: MCPM, β-CPP (flat line), α-TCP, TTCP, DCPD, DCPA, OCP, β-TCP, HAp. The solubility is expressed as the total concentration of calcium ions dissolved in solution. Dotted line: Ca ions concentration in human serum/blood. Dashed line: pH of human serum [6, 45, 82, 83]

1.5.1 Dicalcium phosphate dihydrate (DCPD)

As far as the biomedical applications are concerned, DCPD has been proved to be a very good candidate for resorbable bone grafts. It is important, then, to know how this material reacts once implanted.
As reported in previous studies [57, 84], once in contact with an aqueous solution, DCPD can be stable, dissolve (if the medium is undersaturated in Ca^{2+} and HPO_4^{2-}) or hydrolyse to apatite.
Tang [85] suggests a mechanism of **dissolution** for brushite cements analogous to the one of crystallisation: as during crystallisation embryo formation takes place when critical conditions are reached, during dissolution only the pits bigger than a critical size seem to grow, while the smaller ones disappear. Moreover the dissolution (and hydrolysis) implies the release of H^+ ions, which, by decreasing the pH, speeds up the dissolution itself. At the same time, given that Ca^{2+} and HPO_4^{2-} are released by DCPD, the concentration of calcium and phosphate ions in the solution increases, slowing down the dissolution process. If the medium reaches the values of saturation with respect to HAp, finally, this latter can precipitate.
On this regard, Kanzaki [86] observed the dissolution kinetics of DCPD at 25°C, in a pseudophysiological solution (TRIS, NaCl, $CaCl_2$, $K_2HPO_4 \cdot 3H_2O$) containing the same calcium and phosphorus concentration as human body fluids. Kanzaki proved, by means of atomic force

microscopy (AFM) observations, that HAp precipitates after DCPD dissolution and that there are no evidences of a direct structural transformation of this latter in HAp.
Several studies, moreover, have attested the precipitation of octacalcium phosphate (OCP) rather than hydroxyapatite [51], [69]. However OCP is a thermodynamically metastable phase with respect to HAp: this means that, once precipitated, it is supposed to further hydrolyse to hydroxyapatite. As a consequence OCP is considered as a precursor of apatite phases (also in physiological conditions such as during bone formation and enamel mineralisation). Mandel [51], for example, has observed the formation of OCP upon immersion of DCPD in Dulbecco's Modified Eragle's Medium (DMEM) already after 7 days and hypothesised that whenever the pH of the medium can drop to values around 7 (6.8-7.2) OCP nucleates rather than HAp (according to Eq.(17)).

$$10CaHPO_4 \cdot 2H_2O \rightarrow Ca_8\left(HPO_4\right)_2\left(PO_4\right)_4 \cdot 5H_2O + 2Ca^{2+} + 4H_2PO_4^- + 15H_2O \qquad (17)$$

The same phenomenon was observed by Juhasz [69] on samples immersed in SBF* and Human Blood Serum (HBS*): an early precipitation of OCP (above all in SBF) was followed by the appearance of a carbonated-apatite layer. The difference between the kinetics in SBF and HBS could be linked to the presence of proteins, which could hinder the phenomena of dissolution and precipitation. With this regard, Grover [87], having observed a more pronounced loss of mass for DCPD samples immersed in PBS (Phosphate Buffered Saline solution) than in bovine serum, supposed that some proteins contained in the serum inhibit the formation of the apatite layer that appears, instead, in PBS and that is responsible of the slowing down of the dissolution phenomenon (Figure 11).

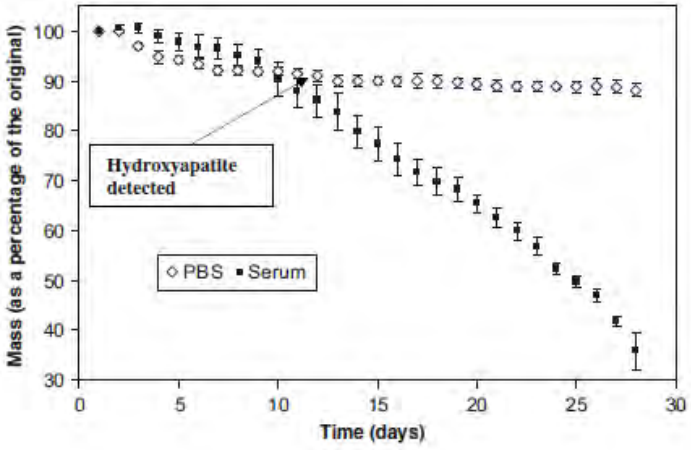

Figure 11: Mass loss of brushite cement in PBS or serum with daily refresh and liquid to cement volume ratio LCVR = 60 [87]

Few studies have been focused on the assessment of the **mechanical properties** of DCPD; Charrière and others have performed compression, traction and torsion tests on moist porous brushite cements (40% of porosity, samples wrapped in paper soaked with distilled paper and kept sealed until the test). Their findings have showed that the compressive Young's Modulus for this material is around 16% higher than the tensile one (see Table 3) and that the elastic properties are strain-rate dependant in humid conditions. Finally, they concluded that, although displaying much lower strength than HAp, DCPD can be compared, to a certain extent, to cancellous bone in terms of mechanical properties and can be applied for bone filling applications (see Figure 12) [1].
Other groups focused on the analyses of the evolution of the mechanical properties of brushite cements after **immersion in different media**. Huan and Chang [88], for example, compared the properties (in humid conditions) of DCPD aged in water and in PBS: while the compressive strength of the samples immersed in water slightly decreased all along the duration of the test (up to 28

days), the properties of those in PBS decreased for the first 15 days and then increased, as found also in dynamic conditions by Grover (wet tests, [57]) (see Figure 13).
This last author, moreover, also analysed the influence of the experimental set-up on the evolution of a porous brushite cement (43% porosity and solid phase made of 34% DCPD and 66% β-TCP). Different media (serum or PBS), aging regimes (static or with daily refresh) and liquid to cement volume ratio (LCVR) were applied. The outcomes showed an increased loss of mass with a higher LCVR (see Figure 14), in dynamic conditions (after 28 days in PBS with LCVR = 60, ΔW = -12% in dynamic and ΔW = -8% in static) and in serum. Finally an earlier appearance of HAp was observed in case of high LCVR, probably because in these conditions a higher rate of dissolution was maintained for a longer time.

Table 3: Brushite mechanical properties in humid conditions, 40% of porosity [1]

Tension		Compression		Shear	
Modulus (GPa)	**Strength (MPa)**	**Modulus (GPa)**	**Strength (MPa)**	**Modulus (GPa)**	**Strength (MPa)**
6.6 ± 0.4	1.3 ± 0.3	7.9 ± 0.3	10.7 ± 2.0	2.7 ± 0.4	2.9 ± 0.4

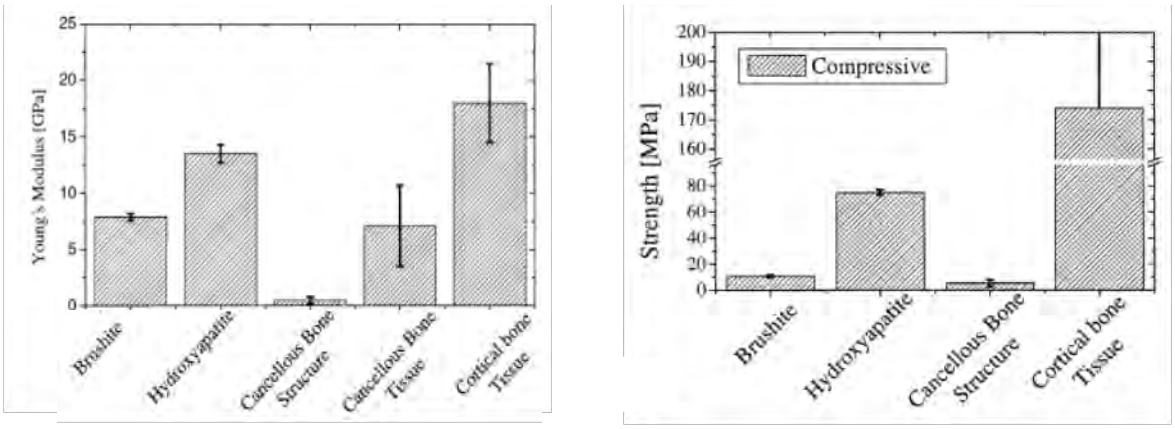

Figure 12: Young's Modulus and compressive strength of brushite cement, hydroxyapatite and bone [1]

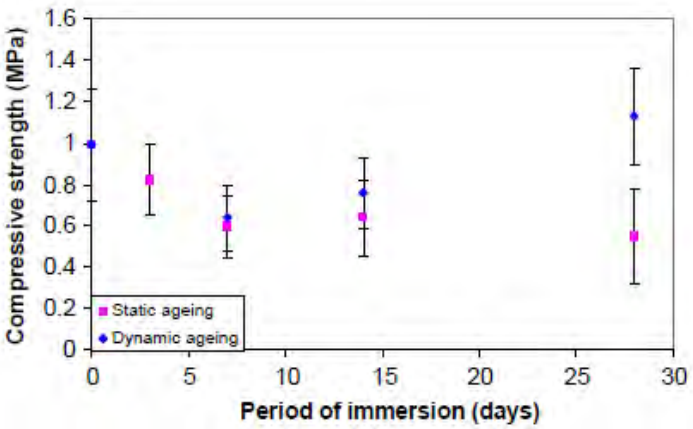

Figure 13: Compressive strength of brushite cement after immersion in PBS in static or dynamic (daily refresh) conditions (LCVR = 60) [57]

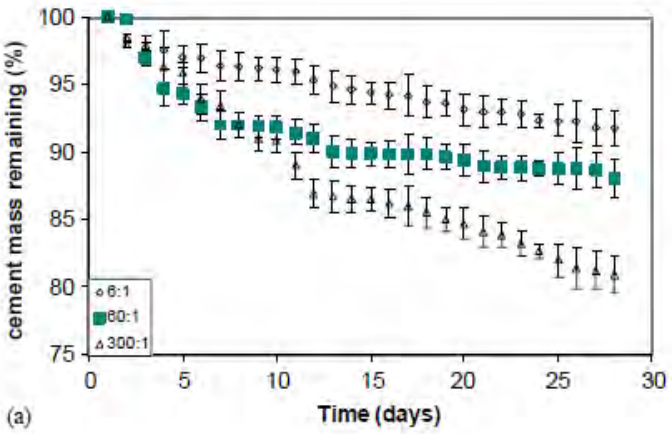

Figure 14: Mass loss of brushite cement in PBS (daily refresh) - effect of LCVR [57]

As far as ***in-vitro*** interaction between brushite cements and **cells** is concerned, Xia and others [89] have grown murine RAW 264.7 cells (with the addition of growth factors RANKL and MCSF) on DCPD for up to 14 days. Having observed the differentiation of some of the cells to osteoclast-like cells, the authors stated a potential role of cells in the degradation process of brushite cements. Nevertheless they also hypothesised that osteoclasts may not resorb DCPD as quickly as HAp, given that at acidic pH (pH around 3.3-4.2, like the one present in the sealed compartment under osteoclasts) DCPD is more stable than HAp (see Figure 10).

In-vivo, the dissolution of brushite would be expected to be slow, given that the physiological fluids are supersaturated with regards to calcium phosphates (apatite in particular). Instead, studies have generally documented the opposite [90, 91]. This apparent contradiction can be explained by the fact that *in-vivo* other elements also play a key role and must be considered, such as the continuous renewal of body fluids and the action of cells, like macrophages and osteoclasts, which can resorb the implanted material.

A brushite cement matrix enriched with β-TCP granules implanted in sheep femurs has shown the appearance of new bone after just 6 weeks accompanied by the preferential dissolution of DCPD and the phagocitosis of β-TCP particles, but without particular signs of inflammation [90].

Longer *in-vivo* experiments were reported by Penel [92]: in this case residues of brushite cement implanted in sheep femurs were detected for up to 6 months. After one year, however, all the material had been converted into carbonated-apatite and new trabecular bone could be observed.

Also brushite cements implanted in rabbit femurs displayed a rapid degradation characterised by a decrease of volume from the periphery to the centre and the formation of particles. This last phenomenon can be considered responsible for the presence of macrophages in the surroundings of the implant [38]. The cellular response to brushite cements, therefore, is linked to the disintegration of the material and can vary strongly depending on particles size and number [56].

To conclude, DCPD has been proven to be biocompatible*, biodegradable and osteoconductive* [28], even if the initial decrease of pH induced by its degradation can cause a slight inflammation.

1.5.2 β-Tricalcium phosphate (β-TCP)

Dissolution mechanisms of β-TCP have been analysed in details in several papers [93-95]. Although different media and experimental setup have been used, common results can be found in these works. Ducheyne and others [93] stated that the dissolution process of β-TCP seems to start with the release of Ca^{2+} and PO_4^{3-} with a Ca/P ratio slightly higher than 1.5 at the beginning and a rate that gradually slows down. This decrease during time of the dissolution rate was confirmed also by other authors [94] and can probably be explained by the theory of Bohner and Lemaître [95]. According to their work, in conditions of low saturation the dissolution of β-TCP is controlled by the diffusion of H^+ (and it is, as a consequence, function of the pH), while with higher saturation of the medium the rate decreases, a layer of apatite is likely to precipitate on the surface of the material and, as a consequence, the dissolution phenomena depend no more on diffusion but rather on the saturation of the liquid towards apatite.

Other authors have focused their attention on the influence of several experimental **parameters of the setup**, such as the kind of medium used and its pH, the presence of proteins, the refresh (or not) of the medium and its stirring, on the evolution of the immersed material. The experimental conditions vary significantly from one study to the other, but some general conclusions can be drawn.

For example, the presence of proteins in the medium does not seem to alter the dissolution and precipitation phenomena but rather influences the size and distribution of the precipitates [96]. Moreover both Rohanizadeh [96] and Juhasz [69] observed an ambivalent role of proteins: these molecules, in fact, can either slow down the precipitation of new phases acting as chelating agents of calcium ions or, once adsorbed on surface of the material, behave as nucleation sites.

As far as the pH is concerned, no obvious influence on weight changes of the immersed samples was observed by Hsu [97]. On the other hand, the same study showed a strong effect of sample composition (in case of biphasic materials) and, to a certain extent, of the medium. In particular the comparison between immersion in water and Ringer's solution brought to the conclusion that while in the first medium the material starts dissolving (as testified by a decrease in weight), in the second one, which is richer in ions, phenomena of precipitation of new phases could intervene causing an increase in weight.

Another experiment by Sánchez-Salcedo [98], investigating the structural changes of biphasic HA/β-TCP scaffolds (27/73% wt), compared static conditions (without stirring) and orbital stirring of the medium (SBF). The results have showed how the evolution of the sample structure is logically accelerated in case of orbital stirring. In this configuration, in fact, the pore volume diminishes more than in static conditions because of precipitation processes; such a phenomenon can probably be explained by the fact that both the dissolution of the material and the homogenization of the medium are favoured by shaking the fluid. The same study has offered also a useful insight on the evolution of ion concentration (calcium and phosphate) and pH of the fluid (SBF) versus time. As can be observed in Figure 15 after a strong initial decrease of Ca^{2+} and PO_4^{3-}, explained by the precipitation of an apatite-like phase, the ion concentration reaches a plateau. According to the authors, in this "quasi-equilibrium" the consumption of ions due to the precipitation of new phases is compensated by the release of calcium and phosphates due to the dissolution of β-TCP (testified also by an increase of the pH, Figure 15).

Finally, regarding the precipitation of new phases, the works of Leng and others [39, 40] showed how for bioceramics immersed in SBF, either without or with refresh of the medium, the formation of octacalcium phosphate (OCP) is induced more than that of apatite. Moreover one of the two papers [39], comparing HAp, β-TCP, α-TCP, BG (Bioglass®) and A-W glass ceramics (Apatite-Wollastonite) immersed in SBF for up to 14 days, displayed the precipitation of OCP an all types of bioceramics except on β-TCP.

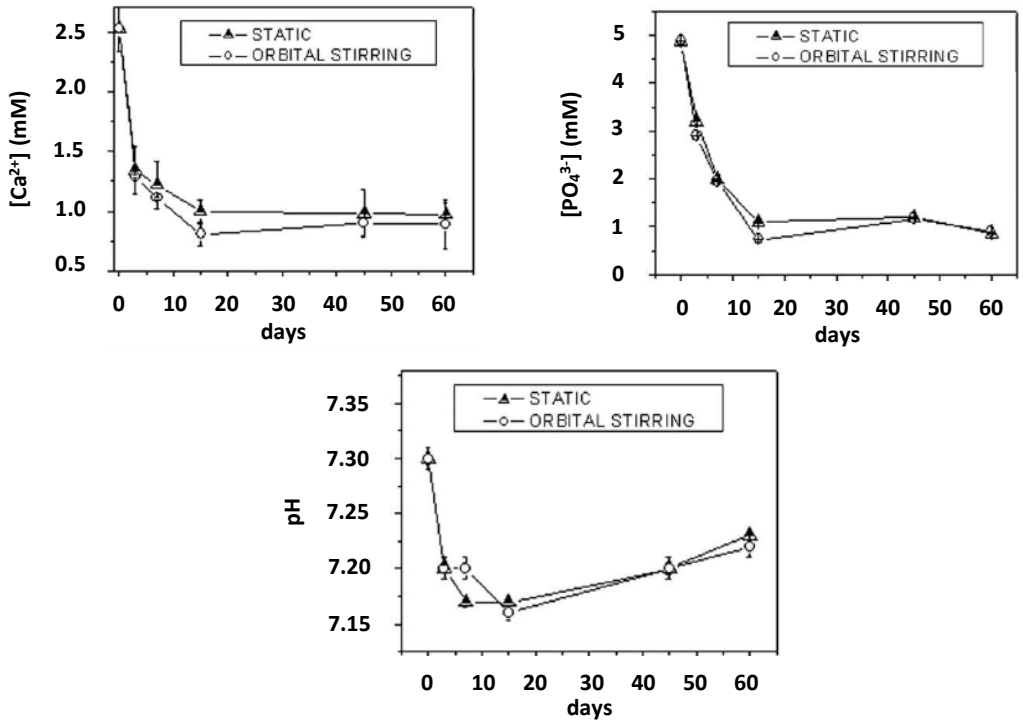

Figure 15: Evolution of ion concentration and pH of SBF with immersion of biphasic HA/β-TCP scaffolds in static and orbital stirring conditions [98]

Few studies, instead, have been focused on the **mechanical properties** of the samples and in these cases uniaxial compression has been mainly adopted as the standard method.
For example the work by Santos [99] aimed to assess the mechanical properties of porous β-TCP scaffolds, has showed the correlation between porosity and strength of the samples (determined by uniaxial compression test). In particular increasing the porosity of the material from 46% to 54% led to a drastic decrease of compressive strength, namely from 8.6 MPa to 2.4 MPa.
Other studies, instead, have gone further in the investigation of the mechanical properties of CaP ceramics trying to analyse their evolution as a function of immersion time of the material in a medium. In the paper of Hsu [97], three different composites of HAp, α-TCP and β-TCP (COMP1, COMP2 and COMP3) were immersed in water at pH 4 and 7.2 and in Ringer's solution (a solution containing calcium ions but no phosphates) for up to 26 weeks. The mechanical properties were assessed before and after immersion (on dried samples) by means of four-point bending and uniaxial compression. While this latter technique did not show any correlation between time of immersion and evolution of mechanical properties, the four-point bending test displayed some trends. In particular the properties of the material with the higher HAp content (COMP1 = 76% HAp, 2% α-TCP, 22% β-TCP) seemed to increase during the immersion both in water and Ringer's solution, while the samples with the highest β-TCP content (COMP3 = 3% HAp, 97% βTCP) exhibited a slight decrease of strength after immersion in water, but no significant changes in Ringer's solution (Figure 16). The authors concluded that the sample composition has more effect on the mechanical properties than the immersion conditions (kind of fluid and pH) and no evident decrease of strength was observed although the materials were immersed for several weeks.
On the opposite the work of Dong-Yun [100] has showed how the compressive strength of porous HAp/β-TCP (60%/40%) scaffolds decreases after immersion in Hank's balanced salt solution (containing both calcium and phosphates) in dynamic conditions (refresh every 2 days). After 8 weeks of immersion a drop of 30% in compressive strength was observed for samples with 46% of porosity and of 40% for samples with 43% of porosity (Figure 17). However no information on the

evolution of the porosity and the weight of the samples is given; as a consequence trying to depict the phenomena that take place appears to be a hard task.

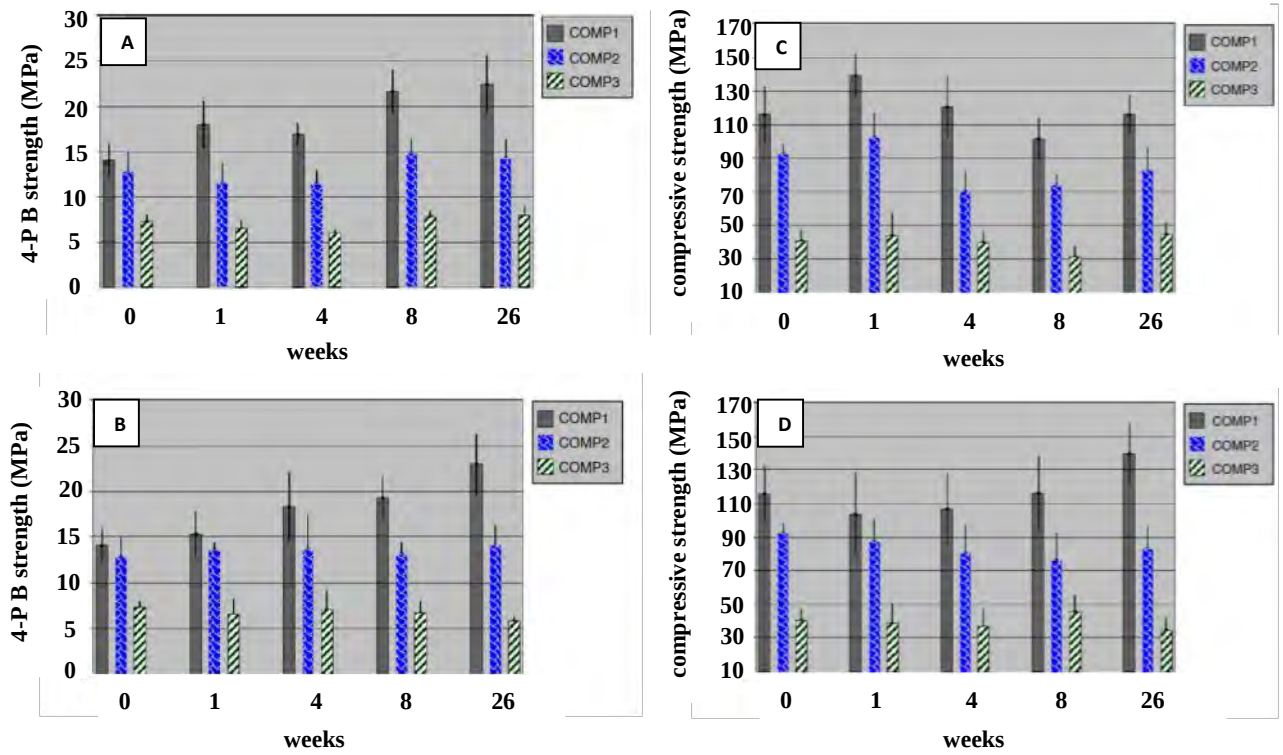

Figure 16: 4-point bend (on the left) and compression strength (on the right) of composite materials after immersion in Ringer's solution at pH 7.2 (A and C) or water at pH 4 (B and D) [97]

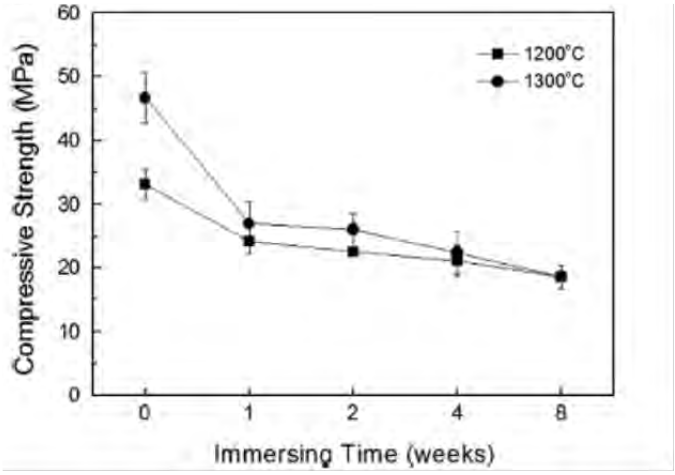

Figure 17: Compressive strength of HAp/β-TCP scaffolds after immersion in Hank's balanced salt solution (1200°C = 46% initial porosity, 1300°C = 43% initial porosity) [100]

Other groups have focused their attention on the interaction between β-TCP and **cells *in-vitro***.
The work of Detsch, in particular, has been aimed to the evaluation of the resorption process by osteoclasts [7, 101]. In these studies osteoclast precursors (human monocytes or murine RAW 264.7) were grown with stimulating factors on HAp, β-TCP and biphasic calcium phosphate (BCP). The results show a cell proliferation comparable for all materials, but little (if none) resorption on β-TCP when compared to HAp and BCP. The authors hypothesized that this difference in resorption could

be linked to the faster dissolution rate of β-TCP and its higher release of calcium, which could inhibit osteoclasts activity.
These results corroborate also the outcome of a previous study by Yamada [42] in which neonatal rabbit bone cells, cultured on HAp, β-TCP and BCP, resorbed mainly biphasic ceramics and created just small and discontinuous lacunae on β-TCP. This material, because of its high solubility in acidic environments, is supposed to be resorbed more extensively by osteoclasts (which operate through the acidification of the sealed zone), but apparently its solubility rate is too high for fostering cellular resorption. As a consequence β-TCP is suggested by Detsch [102] to be a good candidate for applications in which a fast degradation (mainly induced by dissolution) is required, while HAp represents an alternative for sites in which slow remodelling (by means of cells) is desired.
At the same time, as pointed out in the study of Lange [103], β-TCP, inducing less differentiation of cells towards osteoclast compared to HAp, is a safer material, given that its debris are likely to cause less inflammation and bone resorption.
In fact, although *in-vitro* studies have attested that no apatite-like phases precipitate on surface of β-TCP and that this material is hardly resorbed by osteoclasts, several ***in-vivo*** studies have proved the osteconductive* property of β-TCP.
Porous scaffolds made of globular or rod-shaped particles [38, 104] were implanted in rabbit femurs: although the activity of bone cells seems to be affected by the microstructure of the material, in all cases bone ingrowth was observed after few weeks (8 weeks, [38]) and the grafts were partially resorbed after 12 weeks [104].
An even faster resorption was observed by Kondo [105] in whose study β-TCP beads implanted in rat femurs started to be resorbed and replaced by bone already after 7 days.
Moreover, although with longer timing, *in-vivo* studies in human sinus cavities have also proved similar results: in these cases β-TCP started to be resorbed and substituted after few months (≈3) following the implantation [106, 107] and it almost totally disappeared within one year [108].
On the contrary the study by Handschel [109] showed that TCP granules implanted in calvaria (skullcap) of mice displayed no degradation after 6 months and induced the author to state that the application of loads is necessary if resorption of TCP is desired.
On the other hand, in another of his works, Kondo [110] has showed that porous β-TCP scaffolds in dog dorsal muscles were replaced by new bone after 56 days, proving that this material displays, in some conditions, properties of osteoinductivity*.

To sum up, although the bioactivity* of TCP is still debated, its biocompatibility* is commonly recognised. The initial increase of pH caused by β-TCP dissolution ($Ca_3(PO_4)_2 \rightarrow 3Ca^{2+} + 2PO_4^{3-}$, [98, 111]) appears to be too small to cause any negative *in-vivo* reaction and, on the overall, all the experiments on animals have obtained good results both in terms of compatibility, osteoconduction* and resorption. Further tests on humans have drawn similar conclusions, suggesting the use of β-TCP for non-load-bearing applications, such as mandibular, periodontal and maxillary sinus defects. β-TCP has been proved to be non-cytotoxic; its relatively high solubility (>HAp) leads to a degradation rate higher than that of HAp and mainly induced by dissolution.
Further considerations, moreover, have been done on the importance of the microstructure of the bone substitute. This, in fact, plays and important role in the degradation process and, sometimes, it can override the chemistry of the material leading to “unexpected” results. For example, in the case of β-TCP degradation, dissolution is a fundamental part, but if the material has a high micro-porosity it is likely that some particles are released and, then, phagocytated by macrophages (cells in charge of eliminating debris and foreign substances), increasing, in this way, the cellular contribution to the degradation process [104, 112-114].

To conclude, as it always happens when it comes to materials in contact with the body, several parameters (chemistry, micro-structure, doping…) must be taken into account in order to assess the benefits of β-TCP. Anyway, it is possible to state that this material represents a very good option for bone grafting and it is, then, worthy of further studies.

1.6 Local assessment of mechanical properties

As explained in the previous paragraph, several studies have been carried out both on DCPD and β-TCP, mainly with a strong focus on their dissolution and their behaviour once implanted.
All these studies, although very exhaustive from the physical or chemical point of view, do not usually investigate the consequences of these phenomena on the evolution of the mechanical properties.
In the works more focused on the mechanical aspect, on the other hand, almost only the compression technique has been exploited. Just a few papers involve the use of different tests (such as 4 point bending, tension, torsion); in all cases, nevertheless, the mechanical tests employed involve the whole volume of the sample in the assay, providing, then, a global measurement of the mechanical properties.
In the present study, instead, the interest is of evaluating the mechanical properties of the samples on a local scale. The idea is to assess the properties of different parts of each sample, given that there are evidences that the degradation phenomena do not proceed in a homogeneous way, but affect in a different way various portions (e.g. surface, core) of the sample. For this purpose, the micro-indentation technique has been chosen.
At present, to the best knowledge of the authors, only one study [115] has been published on this kind of local analyses and the assessment of the evolution of the mechanical properties in relation to the changes in the physico-chemical and micro-structural aspects. This subject, therefore, appears worthy to further investigations.

The following pages contain a brief introduction of the micro-indentation technique, followed by the description of the theories adopted for the calculation of two important mechanical parameters: hardness and Young's Modulus.

1.6.1 Micro-Indentation: introduction

Since its first use by Brinell in 1900 the indentation technique has not changed in its fundamental idea: a load is applied on an indenter in contact with the sample and the trace left on the material is analysed afterwards in order to calculate the hardness of the material.
However several improvements have been made along the years and, among these, one of the most important is the possibility to record the force and displacement values throughout the duration of the test. The technique thus modified is called "instrumented indentation". The recorded data can be plotted in a load-displacement graph as the one displayed in Figure 18 [116].

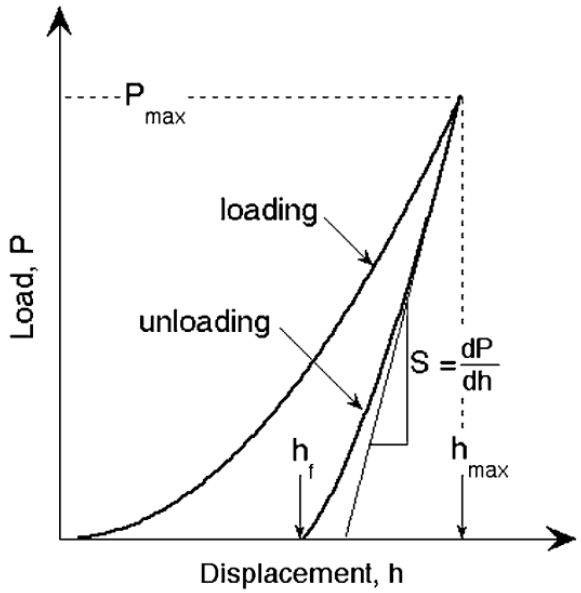

Figure 18: Typical curve load (P) versus displacement (h) obtained by indentation. S: unloading stiffness. h_{max}: maximum depth of penetration. h_f: final residual depth. [116]

Different shapes of indenter can be used; the most common are conic, Vickers and Berkovich indenters, especially at low applied loads in the so-called “nano-indentation” (showed in Figure 19), and spherical ones.
In any case, the fundamental prerequisite of the indenter is having high hardness and Young’s Modulus, so that its deformation during the test is reduced as much as possible and is purely elastic. For this reason indenters are mainly made of diamond, sapphire or tungsten carbide.

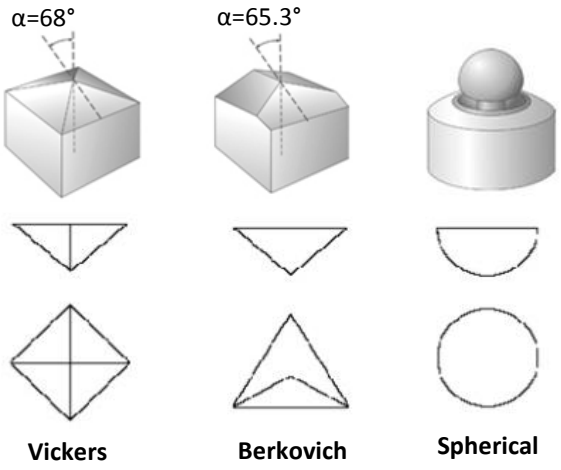

Figure 19: Main geometries of tips used for indentation and the correspondent traces left on samples (cross and horizontal section) [3]

1.6.2 Hardness

As mentioned, the indentation technique allows the measurement of the hardness of a material, that is to say its resistance to plastic deformation. The generic formula used for calculating the hardness (*H*) of a sample is the following:

$$H = \frac{P_{max}}{A} \tag{18}$$

Where P_{max} is the maximum load applied and *A* is the contact area. This latter can be either the actual surface of the residual impression left on the material or the projection of the impression in the plane of the sample surface. Different types of Hardness are then defined (Vickers, Brinell, etc…). The definition of the contact area and the shape of the indenter can therefore strongly affect the final values of hardness obtained. In general, however, in case of instrumented indentation the projected area is preferred to the real one.
Knowing the shape of the indenter, it is possible to calculate the contact area as a function of the depth (h_c) along which there is an actual contact between the indenter and the sample. As can be seen in Figure 20 [116], h_c is the difference between the maximum depth of penetration (h_{max}) and the sink-in, h_s, which, in case of negligible pile-up (see also Figure 21), corresponds to:

$$h_s = \dot{o} \frac{P_{max}}{S} \tag{19}$$

Where ε is a constant linked to the geometry of the indenter (ε = 0.75 for a sphere) and *S* is the so-called “unloading stiffness”, that is to say the slope (d*P*/d*h*) of the initial part of the unloading curve (Figure 18). As a consequence, h_c can be obtained as [116]:

$$h_c = h_{max} - \dot{o} \frac{P_{max}}{S} \tag{20}$$

To sum up, starting from the recorded data of load and displacement it is possible to calculate the slope (*S*) of the initial part of the unloading curve and with this (through Eq.(20)) the value of h_c. This latter allows calculating the contact area with simple mathematical formula, which depends on the geometry of the indenter. Finally, dividing the maximum load by the area (Eq.(18)) the hardness of the material can be obtained.

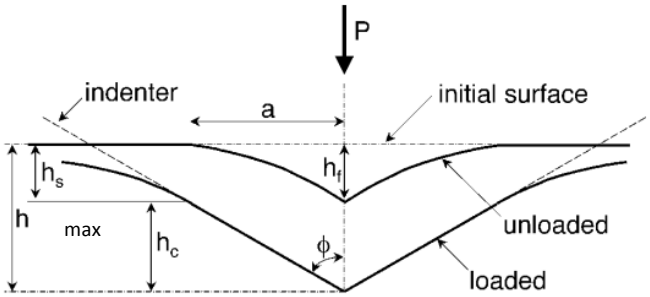

Figure 20: Scheme of the unloading process (cross section). h_{max}: maximum depth of penetration. h_s: sink-in. h_c: depth of contact. h_f: final indentation depth. [116]

1.6.3 Young's Modulus

The major advantage of the instrumented indentation is that this technique provides not only the value of hardness, parameter representative of the plastic or damageable character of the material, but also that of Young's Modulus (*E*), parameter representative of its elastic behaviour.
The method for quantifying *H* and *E* here reported was reviewed in 1992 by Oliver and Pharr [116] and is nowadays widely spread thanks to the fact that it avoids the need of imaging the indentation impression.
The calculation of the elastic modulus is based on the assumption that the unloading phase is purely elastic. Based on previous works by Hertz [117] and Sneddon [118], the equation showed in eq.(21) allows the calculation of the Young's modulus. For this purpose it is necessary to know the initial unloading stiffness *S*, the projected contact area *A* and a correction factor β, which takes into account the non-axisymmetry of the most common used tips ($1.0226 \leq \beta \leq 1.085$, for pyramidal tips [116]). These values are linked by the equation:

$$S = \beta \frac{2}{\sqrt{\pi}} E_{eff} \sqrt{A} \tag{21}$$

E_{eff} is the effective elastic modulus which takes into account the fact that elastic displacements are present both in the sample (with Young's modulus *E* and Poisson's ratio *v*) and the indenter (with Young's modulus E_i and Poisson's ratio v_i).
The effective elastic modulus is defined as:

$$\frac{1}{E_{eff}} = \frac{1-\nu^2}{E} + \frac{1-\nu_i^2}{E_i} \tag{22}$$

In conclusion, knowing the values of load and displacement throughout the test, it is possible to calculate the unloading stiffness (*S*) and, by applying Eq.(20), to obtain the depth of contact (h_c). Once h_c is known, it is possible, knowing the geometry of the indenter, to calculate the contact area *A* necessary for solving the Eq.(21) and obtaining, then, E_{eff} and, finally, the Young's modulus of the material (*E*).

It is worthy underlining how much this method is robust. Eq.(21), in fact, is a very general formula that can be used for all kinds of axisymmetric indenter [119, 120] and has been proved to be

unaffected by small deviation from pure axisymmetric geometry. Moreover the relation is valid not only for elastic contact, but also in the elasto-plastic domain and does not seem to be influenced by sink-in phenomena (showed in Figure 21).

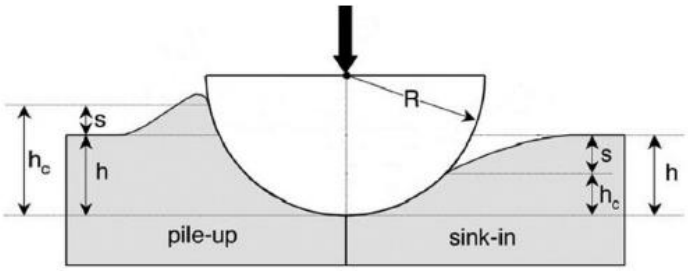

Figure 21: Pile-up and sink-in phenomena showed in the cross section of an indentation profile ($s = h_s$) [121]

1.6.4 Spherical indentation

As explained in the introductive paragraph (paragraph 1.6.1), indentation tips can present different geometries (Figure 19). In the present work, however, we will focus only on the spherical one.
For spherical indentations the initial part of the loading curve is purely elastic, given that there are no geometric singularities at the tip of the indenter, and it can be associated, thus, to the famous theory proposed by Hertz [117].
The spherical geometry is commonly used because it offers the following advantages:

- Possibility to identify the transition from the elastic to the plastic domain,
- Theoretical existence of a unique solution (set of elasto-plastic parameters) for each load-displacement curve,
- Easy modelling in a finite element method.

Furthermore, given that the plastic deformation (ε) in the spherical case is proportional to the applied load (P), it is possible to calculate the average pressure (p_0) as a function of the contact radius (a) and the radius of the sphere (R) eq.(23). The graphs representing $p_0 = f(a/R)$ are sometimes defined as "indentation stress-strain" curves and can provide interesting information such as the passage between the elastic and the plastic domain [122].

$$p_0 = \frac{P}{\pi a^2} = f\left(\frac{a}{R}\right) \tag{23}$$

As mentioned, during an instrumented indentation test the values of load (P) and displacement (h) are recorded. These data can be later used to calculate the hardness of the material eq.(18) and, thanks to Oliver and Pharr's method (eq.(24)), the elastic modulus (E). It is worthy to underline that H and E obtained by micro-indentation provide information on two different depths of the material. The hardness, in fact, is affected by a volume of material included in a hemisphere with a radius of around 10 times the maximum penetration depth reached during the test, while for the elastic modulus the radius is up to 20 times the penetration depth [115].

$$S = \beta \frac{2}{\sqrt{\pi}} E_{eff} \sqrt{A} \rightarrow E_{eff} = \frac{S\sqrt{\pi}}{2\beta\sqrt{A}} \tag{24}$$

Where $A = \pi a^2 = 2\pi R h_c - \pi h_c^2$ and $\beta=1$ in case of spherical indentation

Previous works have already followed this approach. In particular, Clement et al. [123] proved the suitability of spherical micro-indentation for the characterisation of porous materials (such as those used in the present thesis). In their work the authors performed micro-indentation tests on samples of gypsum with different porosities (32% and 56%) and on a brushite cement (porosity of 54%). This study showed how porous materials (with porosity superior to 20%) when indented, undergo a damaging process more than a real plastic deformation. Both gypsum and brushite cement, in fact, displayed a densification of the material in the volume under the indenter tip. Moreover, no signs of macro-cracks (typical of dense ceramics) were noticed. A really similar behaviour was observed also for other porous ceramics, such as alumina, as reported in the work of Staub et al. [124].

All these works, moreover, showed the importance of the choice of the indentation parameters and in particular of the **applied load** and the **diameter of the tip**. The load, in fact, should be high enough to minimise the influence of the roughness of the sample surface, but not too high, in order to avoid an excess of damage in the material. At the same time the tip should be big enough to involve in the test a representative volume of sample, in order to obtain an "average" behaviour of the material, which encompasses both the ceramic grains and the pores. On the other hand, a too big tip limits the number of indentations that can be performed on the same surface.

Keeping in mind the several advantages and the few constraints just listed, spherical micro-indentation was chosen for the assessment of the mechanical properties of the materials studied in the present thesis. In particular, this choice was dictated by two main reasons:

- The volume tested by spherical micro-indentation is relatively important and can offer, as a consequence, an average value of the properties of the material. Therefore, this seems to be an appropriate choice in case of porous samples (such as those studied in this thesis)
- The tendency to cause cracks is reduced by spherical tips compare to other geometries. Cracks are localisations of deformations and they reflect, thus, a local behaviour. Given that in this work the average response of the material was sought, the tip geometry which reduces as much as possible the formation of cracks was preferred.

1.7 Aims and scientific approach

As previously mentioned, although resorbable bone substitutes are really promising, at present there is still a lack of knowledge regarding certain aspects of their ageing process. Some tools for experimentally evaluate their evolution upon immersion or implantation exist, but the general approaches usually tend to evaluate separately each aspect of the material (physico-chemistry, microstructure, mechanics), rather than study their interconnections. However, only by knowing how the evolution of each of these properties affects the others, it would be possible to understand how to tune the characteristics of the present materials and obtain even better bone substitutes.
It appears clear, consequently, how useful and important it can be to find a way to enrich our knowledge of these dissolution/resorption phenomena.
The aim of the present work is exactly to develop such a method, to assess and apply it on calcium phosphate materials.

The peculiarity of this study lies in the effort to establish a holistic protocol, which encompasses different fundamental aspects of the characterisation of materials, such as physico-chemistry, microstructure and mechanics. The aim is to understand how changes in one of these aspects are affected and affect the others.

1.7.1 Experimental strategy

Regarding the choice of the materials targeted in this work, resorbable calcium phosphate samples were preferred. As the resorption of an implanted material can be due to both cellular activity and physico-chemical phenomena of dissolution and re-precipitation, both aspects need to be investigated: therefore, a part of this *in-vitro* study has been dedicated to assess the evolution of calcium phosphate phases in solution (chapter 3 and 4) while another one has been devoted to osteoclastic cells driven resorption (chapter 5).

Calcium phosphate phases show quite different processes of dissolution/resorption. In particular, DCPD and β-TCP were considered of interest, because, in physiological conditions, the former is known to undergo dissolution and re-precipitation phenomena, while the latter is generally considered non soluble. As a consequence, DCPD is defined as "biosoluble" and β-TCP as "bioresorbable" (cf. section 1.5). These two CaP phases can thus be used as "model" materials for the investigation of the two different aspects of the *in-vivo* resorption process.

In addition, both DCPD and β-TCP are known materials and are already employed in bone graft substitutes for commercial applications. Therefore, a further investigation of their behaviour in conditions close to physiological ones could shed a bit more light on their evolution upon implantation and be of practical importance.

As far as material characteristics are concerned, the purpose was to process the samples so that their evolution kinetics was neither too slow nor to rapid, so that it remained possible to study separately all aspects involved in dissolution processes on one hand and in re-precipitation on the other hand.
For the dissolution tests, porous specimens were preferred to dense ones, so to increase the rate of degradation and to observe a significant evolution in reasonable times. For cellular resorption experiments, instead, dense samples were chosen; too rough surfaces might hinder the cell growth [125] and make it more difficult to identify the possible resorption pits made by osteoclasts on sample surfaces.

Although it is clear that *in-vitro* tests are limited and, for several aspects, far from the real *in-vivo* situation, this kind of experiments exhibits nevertheless incomparable advantages: a good way of validating hypotheses, and, as written previously, of separating dissolution processes from re-precipitation ones. This might be done, for example, by choosing a solution, which would foster one of these phenomena rather than the other one. In this perspective, TRIS-buffered solution, which contains neither calcium nor orthophosphate ions, was preferred to other media cited in literature, because it should favour the dissolution process. In addition, a phosphate buffered saline solution was also used because, containing phosphate ions, it should, on the opposite, promote the precipitation of CaP phases.
Finally, to get closer to real *in-vivo* conditions and observe a significant evolution in a reasonable time, it was decided to periodically refresh the immersion solution. In parallel, some samples were also dipped in solutions which were not refreshed at all, to highlight the influence of fluids circulation on the kinetics, and possibly to get more insight on the very first resorption phenomena, which, in dynamic conditions, could occur in a too short time to be observed.

1.7.2 Specificity of this study

As highlighted in the previous paragraphs, one of the aims of this study was the evaluation of the evolution of the mechanical properties due to dissolution/resorption phenomena that occurs on the samples. The novelty of this work is linked to the choice of a non-conventional technique for the assessment of the mechanical properties of the specimen, that is to say spherical micro-indentation.

Although usually applied on dense materials, in the present study this tool has been chosen for being used on porous samples because it displays several advantages. In particular the micro-indentation technique:

- is quasi-non destructive: the samples can be used for other analyses after they have undergone the micro-indentation test,
- involves in the test a larger volume of material if compared to nano-indentation: the information obtained is an average and not just the value of a single phase (or crystal) of the material. This “average value” is by far more representative and important in the case of porous samples, because it includes both the material and the porosity,
- requires small amounts of material: it can be applied even on small specimen such as those typical of biomedical applications. Moreover, it provides information on a local scale: it is possible to assess the mechanical properties of different parts of the same sample.

This latter point, in particular, results to be very interesting and useful in the case of the present study. Performing micro-indentation tests on different regions (such as outer and inner part) of the same immersed sample, in fact, it is possible to assess the possible presence of a gradient of properties and to better understand, as a consequence, how the evolution process progresses. The hope (and believe) is, finally, to be able to answer questions such as: Where does the dissolution/precipitation start? How does it proceed? How does it influence the mechanical properties of the material? And by adding this information to the one obtained by means of more conventional analyse techniques (i.e. SEM, XRD…) shed a bit more of light on how the evolution upon implantation of resorbable bone grafts takes place.

References

1. Charrière, E., et al., *Mechanical characterization of brushite and hydroxyapatite cements.* Biomaterials, 2001. **22**(21): p. 2937-2945.
2. Hernigou, P. and Y. Homma, *Tissue bioengineering in orthopedics.* Clin Cases Miner Bone Metab, 2012. **9**(1): p. 3.
3. ; Available from: http://www.doitpoms.ac.uk/tlplib/bones/structure.php.
4. Blokhuis, T.J., et al., *Properties of Calcium Phosphate Ceramics in Relation to Their In Vivo Behavior.* Journal of Trauma and Acute Care Surgery, 2000. **48**(1): p. 179.
5. Zhang, J., et al., *Calcium phosphate cements for bone substitution: Chemistry, handling and mechanical properties.* Acta Biomaterialia, 2014. **10**(3): p. 1035-1049.
6. Bohner, M., *Bioresorbable ceramics*. Degradation rate of bioresorbable materials - Prediction and evaluation, ed. F. Buchanan2008, Boston: Woodhead publishing in Materials.
7. Schaefer, S., et al., *How degradation of calcium phosphate bone substitute materials is influenced by phase composition and porosity.* Advanced Engineering Materials, 2011. **13**(4): p. 342-350.
8. Detsch, R.B., A. R., *The role of osteoclasts in bone tissue engineering.* J Tissue Eng Regen Med., 2014.
9. Chow LC, M.M., Takagi S., *A dual constant-composition titration system as an in vitro resorption model for comparing dissolution rates of calcium phosphate biomaterials.* J Biomed Mater Res B Appl Biomater., 2003. **65**: p. 245-251.
10. Manolagas, S.C., *Birth and Death of Bone Cells: Basic Regulatory Mechanisms and Implications for the Pathogenesis and Treatment of Osteoporosis.* Endocrine Reviews, 2000. **21**(2): p. 115-137.
11. Udagawa, N.T., N.; Akatsu, T.; Tanaka, H.; Sasaki, T.; Nishihara, T.; Koga, T.; Martin, J.; Suda, T., *Origin of osteoclasts: mature monocytes and macrophages are capable of differentiating into osteoclasts under a suitable microenvironment prepared by bone marrow-derived stromal cells.* Proc Natl Acad Sci, 1990. **87**(18): p. 7260–7264.
12. Vignery, A., *Macrophage fusion: the making of osteoclasts and giant cells.* The Journal of Experimental Medicine, 2005. **202**(3): p. 337-340.
13. Väänänen, K., *Mechanism of osteoclast mediated bone resorption—rationale for the design of new therapeutics.* Advanced Drug Delivery Reviews, 2005. **57**: p. 959– 971.
14. Detsch, R., et al., *In vitro-Osteoclastic Activity Studies on Surfaces of 3D Printed Calcium Phosphate Scaffolds.* JOURNAL OF BIOMATERIALS APPLICATIONS, 2010.
15. Rieger, W., *Ceramics in orthopedics — 30 years of evolution and experience.* World tribology forum in arthroplasty, 2001.
16. Gremillard, L., et al., *Degradation of Bioceramics*. Degradation of implant materials, ed. N. Eliaz2012: Springer.
17. Tadier, S., *Étude des propriétés physico-chimiques et biologiques de ciments biomédicaux à base de carbonate de calcium : apport du procédé de co-broyage.* Ph.D. Thesis, 2009.
18. Demers, C.N., et al., *Effect of experimental parameters on the in vitro release kinetics of transforming growth factor beta1 from coral particles.* J Biomed Mater Res, 2002. **59**(3): p. 403-10.
19. Berland, S., et al., *Nacre/bone interface changes in durable nacre endosseous implants in sheep.* Biomaterials, 2005. **26**(15): p. 2767-73.
20. Oudadesse, H., *Étude des phénomènes physiques dans la transformation du corail implanté « in-vivo » par radioactivation nucléaire, par diffraction des rayons X et par spectrométrie infrarouge.* Ph.D. Thesis, Uniersité Clermont II 1989.
21. Chatainier, S., *Évaluation de ciments à base de carbonate de calcium synthétique en comblement osseux : étude expérimentale chez le rat.* Thèse d'exercice, faculté de chirurgie dentaire de Toulouse, 2007.
22. Combes, C., et al., *Preparation, physical-chemical characterisation and cytocompatibility of calcium carbonate cements.* Biomaterials, 2006. **27**(9): p. 1945-54.

23. Combes, C., R. Bareille, and C. Rey, *Calcium carbonate-calcium phosphate mixed cement compositions for bone reconstruction.* J Biomed Mater Res A, 2006. **79**(2): p. 318-28.
24. Koh, I., et al., *The compressive modulus and strength of saturated calcium sulphate dihydrate cements: Implications for testing standards.* Journal of the Mechanical Behavior of Biomedical Materials, 2014. **34**(0): p. 187-198.
25. Hoppe, A., N.S. Güldal, and A.R. Boccaccini, *A review of the biological response to ionic dissolution products from bioactive glasses and glass-ceramics.* Biomaterials, 2011. **32**: p. 2757-2774.
26. Hench, L.L., *Bioceramics.* Journal of the American Ceramic Society, 1998. **81**(7): p. 1705-1728.
27. Miguez-Pacheco, V., et al., *Bioactive glasses in soft tissue repair.* American Ceramic Society Bulletin, 2015. **94**(6): p. 5.
28. Bohner, M., *Calcium orthophosphates in medicine: from ceramics to calcium phosphate cements.* Injury, 2000. **31, Supplement 4**(0): p. D37-D47.
29. Famery, R., N. Richard, and P. Boch, *Preparation of α- and ß-tricalcium phosphate ceramics, with and without magnesium addition*. Vol. 20. 1994, Kidlington, ROYAUME-UNI: Elsevier.
30. Salma-Ancane, K., et al., *Development of Mg-containing porous ß-tricalcium phosphate scaffolds for bone repair.* Ceramics International, 2015. **41**(3, Part B): p. 4996-5004.
31. Koç, N., M. Timuçin, and F. Korkusuz, *Fabrication and characterization of porous tricalcium phosphate ceramics.* Ceramics International, 2004. **30**(2): p. 205-211.
32. Stergioudi, F., et al., *Novel production and characterization of porous calcium phosphate suitable for bone tissue engineering applications.* Ceramics International, 2015. **41**(3, Part A): p. 3822-3832.
33. Bellucci, D., A. Sola, and V. Cannillo, *Bioactive glass-based composites for the production of dense sintered bodies and porous scaffolds.* Materials Science and Engineering, C, 2013.
34. Vallet-Regí, M. and J.M. González-Calbet, *Calcium phosphates as substitution of bone tissues.* Progress in Solid State Chemistry, 2004. **32**(1–2): p. 1-31.
35. Bohner, M. and J. Lemaitre, *Can bioactivity be tested in vitro with SBF solution?* Biomaterials, 2009. **30**(12): p. 2175-2179.
36. Pan, H., et al., *Apatite-formation ability--predictor of "bioactivity"?* Acta Biomater, 2010. **6**(11): p. 4181-8.
37. Yuan, H., et al., *Material-dependent bone induction by calcium phosphate ceramics: a 2.5-year study in dog.* Biomaterials, 2001. **22**(19): p. 2617-2623.
38. Lu, J., et al., *The Biodegradation Mechanism of Calcium Phosphate Biomaterials in Bone.* Journal of Biomedical Materials Research Part B: Applied Biomaterials, 2002. **63**: p. 408–412.
39. Xin, R., et al., *A comparative study of calcium phosphate formation on bioceramics in vitro and in vivo.* Biomaterials, 2005. **26**(33): p. 6477-6486.
40. Leng, Y., J. Chen, and S. Qu, *TEM study of calcium phosphate precipitation on HA/TCP ceramics.* Biomaterials, 2003. **24**(13): p. 2125-2131.
41. Beekmans, H.C.S., et al., *The hydroxylapatite-bone interface : 10 years after implant installation*. Int. J. Oral Maxillofac. Surg. Vol. 37. 2008, Kidlington, ROYAUME-UNI: Elsevier. 5.
42. Yamada, S., et al., *Osteoclastic resorption of calcium phosphate ceramics with different hydroxyapatite / beta-tricalcium phosphate ratios.* Biomaterials, 1997. **18**: p. 1037-1041.
43. Rey, C., et al., *Surface properties of biomimetic nanocrystalline apatites; applications in biomaterials.* Progress in Crystal Growth and Characterization of Materials, 2014. **60**(3–4): p. 63-73.
44. Rey, C., et al., *Physico-chemical properties of nanocrystalline apatites: Implications for biominerals and biomaterials.* Materials Science and Engineering: C, 2007. **27**(2): p. 198-205.
45. Elliott, J.C., *Structure and chemistry of the apatites and other calcium orthophosphates, Studies in Inorganic Chemistry.* Ed. Elsevier, 1994. **18**.
46. Legros, R., *Apport de la physico-chimie à l'étude de la phase minérale des tissues calcifiés.* Thèse de doctorat, Institut National Polytechnique de Toulouse, 1984.
47. Rey, C., et al., *Resolution-enhanced Fourier transform infrared spectroscopic study of the environment of phosphate ion in the early deposits of a solid phase of calcium phosphate in*

bone and enamel and their evolution with age. I : Investigation in the υ4 PO4 domain. Calcif. Tissue INT. , 1990(46): p. 384-394.

48. Rey, C., et al., *Bone mineral: update on chemical composition and structure.* Osteoporosis international : a journal established as result of cooperation between the European Foundation for Osteoporosis and the National Osteoporosis Foundation of the USA, 2009. **20**(6): p. 1013-1021.
49. Kim, H.M., et al., *Dissolution of poorly crystalline apatite crystals by osteoclasts determined on artificial thin-film apatite.* J Biomed Mater Res, 2001. **56**(2): p. 250-6.
50. Pascaud, P., *Apatites nanocristallines biomimétiques comme modèles de la réactivité osseuse: Etude des propriétés d'adsorption et de l'activité cellulare d'un biphosphonate, le tiludronate.* Thèse de doctorat, Université de Toulouse, 2012.
51. Mandel, S. and A.C. Tas, *Brushite (CaHPO4·2H2O) to octacalcium phosphate (Ca8(HPO4)2(PO4)4·5H2O) transformation in DMEM solutions at 36.5 °C.* Materials Science and Engineering: C, 2010. **30**(2): p. 245-254.
52. Boanini, E., M. Gazzano, and A. Bigi, *Ionic substitutions in calcium phosphates synthesized at low temperature.* Acta Biomaterialia, 2010. **6**(6): p. 1882-1894.
53. Xin, R., Y. Leng, and N. Wang, *In situ TEM examinations of octacalcium phosphate to hydroxyapatite transformation.* Journal of Crystal Growth, 2006. **289**(1): p. 339-344.
54. Suzuki, O., *Octacalcium phosphate: Osteoconductivity and crystal chemistry.* Acta Biomaterialia, 2010. **6**(9): p. 3379-3387.
55. Dickens, B., J.S. Bowen, and W.E. Brown, *A refinement of the crystal structure of CaHPO4 (synthetic monetite).* Acta Crystallographica Section B, 1972. **28**(3): p. 797-806.
56. Tamimi, F., Z. Sheikh, and J. Barralet, *Dicalcium phosphate cements: Brushite and monetite.* Acta Biomaterialia, 2012. **8**: p. 474-487.
57. Grover, L.M., et al., *In vitro ageing of brushite calcium phosphate cement.* Biomaterials, 2003. **24**: p. 4133–4141.
58. Peters, F. and D. Reif, *Functional Materials for Bone Regeneration from Beta-Tricalcium Phosphate.* Materialwissenschaft und Werkstofftechnik, 2004. **35**(4): p. 203-207.
59. Bohner, M., *Propriétés physico-chimiques et ostéogéniques d'un biociment hydraulique à base de phosphates de calcium*, 1993, Ecole Polytechnique Fédérale de Lausanne. p. 196.
60. Hofmann, M.P., et al., *Real-time monitoring of the setting reaction of brushite-forming cement using isothermal differential scanning calorimetry.* (1552-4973).
61. Rousseau, S., M. Bühler, and J. Lemaître, *Thermometric study of brushite cements.* European Cells and Materials, 2002. **3**(1): p. 2.
62. Ryu, H.-S.Y., Hyuk-Joon; Hong, Kug Sun; Chang, Bong-Sun; Lee, Choon-Ki; Chung, Sung-Soo, *An improvement in sintering property of b-tricalcium phosphate by addition of calcium pyrophosphate.* Biomaterials, 2002. **23**: p. 909-914.
63. Yashima, M.S., Atsushi; Kamiyama, Takashi; Hoshikawa, Akinori, *Crystal structure analysis of β-tricalcium phosphate Ca 3(PO 4) 2 by neutron powder diffraction.* Journal of Solid State Chemistry, 2003. **175**(2): p. 272-277.
64. Matherw, M., et al., *The crystal structure of a-Ca3(PO4)2.* Acta Cryst., 1977. **B33**: p. 8.
65. Vallet-Regì, M., J. Pena, and I. Izquierdo-Barba, *Synthesis of b-tricalcium phosphate in layered or powdered forms for biomedical applications.* Solid State Ionics, 2004. **172**: p. 445-449.
66. Peña, J. and M. Vallet-Regí, *Hydroxyapatite, tricalcium phosphate and biphasic materials prepared by a liquid mix technique.* Journal of the European Ceramic Society, 2003. **23**(10): p. 1687-1696.
67. Bahman Mirhadi, B.M., Nayereh Askari, *Synthesis of nano-sized β-tricalcium phosphate via wet precipitation.* Processing and Application of Ceramics, 2011. **5 [4] (2011) 193–198**.
68. Soon-Ho Kwon, Y.-K.J., Seong-Hyeon Hong, Hyoun-Ee Kim, *Synthesis and dissolution behavior of b-TCP and HA/b-TCP composite powders.* Journal of the European Ceramic Society, 2003. **23**: p. 1039-1045.

69. Juhasz, J., et al., *Biological control of apatite growth in simulated body fluid and human blood serum.* Journal of Materials Science: Materials in Medicine, 2008. **19**(4): p. 1823-1829.
70. Atsuo Ito and Koji Senda and Yu Sogo and Ayako Oyane and Atsushi Yamazaki and Racquel, Z.L., *Dissolution rate of zinc-containing β-tricalcium phosphate ceramics.* Biomedical Materials, 2006. **1**(3): p. 134.
71. GIBSON, I.R.R., I.; BEST, S.M.; BONFIELD, W., *Characterization of the transformation from calcium-deficient apatite to b-tricalciumphosphate.* JOURNAL OF MATERIALS SCIENCE: MATERIALS IN MEDICINE, 2000. **12**: p. 799-804.
72. Jinlong, N., Z. Zhenxi, and J. Dazong, *Investigation of Phase Evolution During the Thermochemical Synthesis of Tricalcium Phosphate.* Journal of Materials Synthesis and Processing, 2001. **9**(5): p. 235-240.
73. El Briak-BenAbdeslam, H., et al., *Wet or dry mechanochemical synthesis of calcium phosphates? Influence of the water content on DCPD–CaO reaction kinetics.* Acta Biomaterialia, 2008. **4**(2): p. 378-386.
74. Olsson, M., *Chemical stability of grain boundaries in b-tricalcium phosphate ceramics.* Master Thesis, 2012.
75. Ando, Y., *Phase Diagrams of Ca3 (PO4) 2-Mg3 (PO4)2 and Ca3(PO4)2-CaNaPO4 Systems.* 1957.
76. Xue, W., et al., *Synthesis and characterization of tricalcium phosphate with Zn and Mg based dopants.* Journal of Materials Science: Materials in Medicine, 2008. **19**(7): p. 2669-2677.
77. Seeley, Z., A. Bandyopadhyay, and S. Bose, *Tricalcium phosphate based resorbable ceramics: Influence of NaF and CaO addition.* Materials Science and Engineering: C, 2008. **28**(1): p. 11-17.
78. LeGeros, R., *Biodegradation and bioresorption of calcium phosphate ceramics.* Clin Mater, 1993. **14**: p. 65-88.
79. Bohner, M., et al., *Compositional changes of a dicalcium phosphate dihydrate cement after implantation in sheep.* Biomaterials, 2003. **24**(20): p. 3463-3474.
80. Penel, G., et al., *Raman microspectrometry studies of brushite cement: in vivo evolution in a sheep model.* Bone, 1999. **25**(8756-3282 (Print)).
81. Driessens, F.C.M., ECERS, Maastricht, 1989.
82. Salimi, *Systematic investigations of calcium phosphates produced by wet chemistry method and supercritical processing techniques (Ph.D. thesis).* 2013.
83. Hofmann, M.P., *Physikalische Charakterisierung von Calciumphosphat-Pulvern zur Einstellung von Prozessparametern für die Herstellung von Knochenzement/Physical characterisation of calcium phosphate powders for the adjustment of processing parameters for the fabrication of bone cement*, 2003.
84. Xia, Z., et al., *In vitro biodegradation of three brushite calcium phosphate cements by a macrophage cell-line.* Biomaterials, 2006. **27**(26): p. 4557-4565.
85. Tang, R., C. Orme, and G.H. Nancollas, *A new understanding of demineralization: the dynamics of brushite dissolution.* J. Phys. Chem., 2003. **B**(107): p. 5.
86. Kanzaki, N., et al., *Dissolution kinetics of dicalcium phosphate dihydrate under pseudophysiological conditions.* Journal of Crystal Growth, 2002. **235**(1–4): p. 465-470.
87. Grover, L.M., et al., *Biologically mediated resorption of brushite cement in vitro.* Biomaterials, 2006. **27**: p. 2178–2185.
88. Huan, Z. and J. Chang, *Novel bioactive composite bone cements based on the b-tricalcium phosphate-monocalcium phosphate monohydrate composite cement system.* Acta Biomaterialia, 2009. **5**(4): p. 1253-1264.
89. Xia, Z., et al., *In vitro biodegradation of three brushite calcium phosphate cements by a macrophage cell-line.* Biomaterials, 2006. **27**: p. 4557–4565.
90. FelixTheiss, et al., *Biocompatibility and resorption of a brushite calcium phosphate cement.* Biomaterials, 2005. **26**: p. 4383–4394.
91. Apelt, D., et al., *In vivo behavior of three different injectable hydraulic calcium phosphate cements.* Biomaterials, 2004. **25**(7–8): p. 1439-1451.

92. Penel, G., et al., *Raman Microspectrometry Studies of Brushite Cement: In Vivo Evolution in a Sheep Model.* Bone, 1999. **25**(2 S): p. 81S–84S.
93. Ducheyne, P., S. Radin, and L. King, *The effect of calcium phosphate ceramic composition and structure on in vitro behavior. I. Dissolution.* J Biomed Mater Res, 1993. **27**(1): p. 25-34.
94. Tang, R.K., et al., *Kinetics of dissolution of beta-tricalcium phosphate.* Langmuir, 2001. **17**(11): p. 3480-3485.
95. Bohner, M., J. Lemaître, and T.A. Ring, *Kinetics of Dissolution of β-Tricalcium Phosphate.* Journal of Colloid and Interface Science, 1997. **190**(1): p. 37-48.
96. Rohanizadeh, R., et al., *Apatite precipitation after incubation of biphasic calcium-phosphate ceramic in various solutions: influence of seed species and proteins.* 1998(0021-9304 (Print)).
97. Hsu, Y.H., I.G. Turner, and A.W. Miles, *Mechanical properties of three different compositions of calcium phosphate bioceramic following immersion in Ringer's solution and distilled water.* Journal of Materials Science: Materials in Medicine, 2009. **20**(12): p. 2367-2374.
98. Sanchez-Salcedo, S., et al., *In vitro structural changes in porous HA/Î²-TCP scaffolds in simulated body fluid.* Acta Biomaterialia, 2009. **5**(7): p. 2738-2751.
99. Santos, C.F.L., et al., *Design and production of sintered β-tricalcium phosphate 3D scaffolds for bone tissue regeneration.* Materials Science and Engineering: C, 2012. **32**(5): p. 1293-1298.
100. Kim, D.-H., et al., *In vitro biodegradable and mechanical performance of biphasic calcium phosphate porous scaffolds with unidirectional macro-pore structure.* Ceramics International, 2014(0).
101. Detsch, R., et al., *The resorption of nanocrystalline calcium phosphates by osteoclast-like cells.* Acta Biomaterialia, 2010. **6**: p. 3223–3233.
102. Detsch, R., H. Mayr, and G. Ziegler, *Formation of osteoclast-like cells on HA and TCP ceramics.* Acta Biomaterialia, 2008. **4**(1): p. 139-148.
103. Lange, T., et al., *Proinflammatory and osteoclastogenic effects of beta-tricalciumphosphate and hydroxyapatite particles on human mononuclear cells in vitro.* Biomaterials, 2009. **30**(29): p. 5312-5318.
104. Okuda, T., et al., *The effect of the microstructure of β-tricalcium phosphate on the metabolism of subsequently formed bone tissue.* Biomaterials, 2007. **28**(16): p. 2612-2621.
105. Kondo, N., et al., *Bone formation and resorption of highly purified b-tricalcium phosphate in the rat femoral condyle.* Biomaterials, 2005. **26**(28): p. 5600-5608.
106. Coelho, et al., *Physico/chemical characterization and preliminary human histology assessment of a β-TCP particulate material for bone augmentation*. Vol. 29. 2009, Amsterdam, PAYS-BAS: Elsevier. 7.
107. Chappard, D.G., Bernard; Mallet, Romain; Pascaretti-Grizon, Florence; and M.L. F. Basle, Helene, *Sinus lift augmentation and b-TCP: A microCT and histologic analysis on human bone biopsies.* Micron, 2010. **41**: p. 321-326.
108. Horch, H.S., R.; Pautke, C.; Neff, A.; Deppe, H.; Kolk, A., *Synthetic, pure-phase betatricalcium phosphate ceramic granules (Cerasorb1) for bone regeneration in the reconstructive surgery of the jaws.* Int. J. Oral Maxillofac. Surg., 2006. **35**: p. 708-713.
109. Handschel, J., et al., *TCP is hardly resorbed and not osteoconductive in a non-loading calvarial model.* Biomaterials, 2002. **23**(7): p. 1689-1695.
110. Kondo, N., et al., *Osteoinduction with highly purified b-tricalcium phosphate in dog dorsal muscles and the proliferation of osteoclasts before heterotopic bone formation.* Biomaterials, 2006. **27**(25): p. 9-9.
111. Zou, C., et al., *Characterization and dissolution-reprecipitation behavior of biphasic tricalcium phosphate powders.* Journal of Alloys and Compounds, 2011. **509**(24): p. 6852-6858.
112. Jarcho, M., *Calcium Phosphate Ceramics as Hard Tissue Prosthetics*, in *Classic Papers in Orthopaedics*, P.A. Banaszkiewicz and D.F. Kader, Editors. 2014, Springer London. p. 419-421.
113. Heymann, D., G. Pradal, and M. Benahmed, *Cellular mechanisms of calcium phosphate ceramic degradation.* Histology and Histopathology, 1999. **14**: p. 871-877.

114. Müller, K.H., et al., *The effect of particle agglomeration on the formation of a surface-connected compartment induced by hydroxyapatite nanoparticles in human monocyte-derived macrophages().* Biomaterials, 2014. **35**(3): p. 1074-1088.
115. Clement, P., *Détermination des proprietés mécaniques de céramiques poreuses par essais de micronindentation instrumenée sphérique.* Ph.D. Thesis, 2013.
116. Oliver, W.C. and G.M. Pharr, *Measurement of hardness and elastic modulus by instrumented indentation: Advances in understanding and refinements to methodology.* Journal of Materials Research, 2004. **19**(01): p. 3-20.
117. Hertz, *Ueber die Berührung fester elastischer Körper.* Journal für die reine und angewandte Mathematik 1881(92): p. 156-171.
118. Sneddon, I.N., *The relationship between load an penetration in the axisymmetric Boussinesq problem for a punch of arbitrary profile.* Int J Eng Sci 1965(3): p. 47-57.
119. Pharr, O., *An improved technique for determining hardness and elastic modulus using load and displacement sensing indentation experiments.* J. Mater. Res., 1991. **7**(6).
120. Cheng, Y.-T. and C.-M. Cheng, *Relationships between hardness, elastic modulus, and the work of indentation.* Applied Physics Letters, 1998. **73**(5): p. 614-616.
121. Pintaude, G. and A.R. Hoechele, *Experimental analysis of indentation morphologies after spherical indentation.* Materials Research, 2014. **17**: p. 56-60.
122. Lawn, B.R., *Indentation of Ceramics with Spheres: A Century after Hertz.* Journal of the American Ceramic Society, 1998. **81**(8): p. 1977-1994.
123. Clément, P., et al., *Mechanical characterization of highly porous inorganic solids materials by instrumented micro-indentation.* Acta Materialia, 2013. **61**(18): p. 6649-6660.
124. Staub, D., *Propriétés mécaniques des céramiques en alumine de forte porosité pour les supports de catalyseurs.* Thèse INSA LYON, 2014.
125. Davison, N.L., et al., *Osteoclast resorption of beta-tricalcium phosphate controlled by surface architecture.* Biomaterials, 2014. **35**(26): p. 7441-7451.

CHAPTER 2: MATERIALS AND METHODS

In the present chapter materials, methods and protocols used during this work are presented. The three materials chosen for the tests (two types of β-tricalcium phosphate and one of dicalcium phosphate dihydrate) were obtained by means of different elaboration processes which are described in the following sections. Then, the tests of dissolution (in solutions but without cells) and of resorption (materials in contact with cells) which have been performed are explained in detail. Finally the techniques used to characterise the samples, both before and after ageing are described.

2.1 Samples fabrication

The present paragraph is divided in three sections: the first deals with the fabrication of DCPD porous samples, while the second and the third one with β-TCP porous and dense specimens respectively.
All the samples, regardless their composition, were produced in cylindrical shape. This geometry is characterised by the presence of two surfaces flat and parallel, which are one of the main requirements for performing indentation tests. Moreover, this shape is also suitable for cellular tests: cylindrical specimens can easily fit cell culture pits and can be seeded on one of the flat surfaces.

2.1.1 Synthesis of DCPD samples

As already mentioned in Chapter 1, in the present work, DCPD samples were obtained via a setting reaction, as suggested by Lemaître and Mirtchi [1](eq.(1)).

$$\begin{gathered} \beta - TCP \; + \; MCPM \; + \; H_2O \; \rightarrow \; DCPD \\ \beta - Ca_3\left(PO_4\right)_2 + \; Ca\left(H_2PO_4\right)_2 \cdot H_2O \; + \; 7H_2O \; \rightarrow \; 4CaHPO_4 \cdot 2H_2O \end{gathered} \tag{1}$$

To obtain pure DCPD samples, β-TCP was not purchased, but produced, in order to avoid as much as possible any contaminations which could alter the setting process and the final composition of the cement.

The synthesis of β-TCP was carried out mixing stoichiometric quantities of DCPA and calcium carbonate (CC), according to the following solid-state reaction ([2], eq.(2)):

$$\begin{gathered} DCPA \; + \; CC \rightarrow \beta - TCP \\ 2CaHPO_4 + \; CaCO_3 \rightarrow \beta - Ca_3\left(PO_4\right)_2 + \; CO_2 \uparrow \; + \; H_2O \uparrow \end{gathered} \tag{2}$$

In particular, commercial powders of DCPA (Sigma Aldrich, purity > 98%, Lot 051M0120V, M=136.06 g/mol) and calcium carbonate (Sigma Aldrich, purity > 98.5%, Lot SZBC0590V, M=100.09 g/mol) were dried overnight at 55 °C in order to eliminate any possible adsorbed water and then let cool in a vacuum chamber. The reagents were weighed so to have a molar ratio of 2:1 and mixed with the aid of zirconia beads of 0.75-1.5 mm of diameter (weight powder to beads ratio of 1.5) for 25 minutes in a Turbula Shaker-Mixer (Glen Milles, NJ, USA). After this step the powder was sieved, in order to retrieve all the ZrO_2 beads, placed in alumina crucibles and calcined according to the thermal treatment described in Figure 1 (HT 40/17, Nabertherm, Germany).

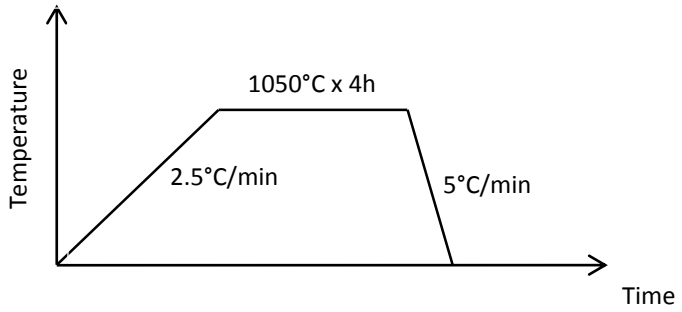

Figure 1: Thermal treatment used for the solid-state synthesis of β-TCP powder

After the thermal treatment, the final powders were characterised by means of XRD. The resulting diffractogram, shown in Figure 2, displays peaks, which all perfectly match with the reference pattern of β-TCP (JCPDF file #01-070-2065). Traces of HAp could be present, but in negligible amount (≤ 2 wt.%).

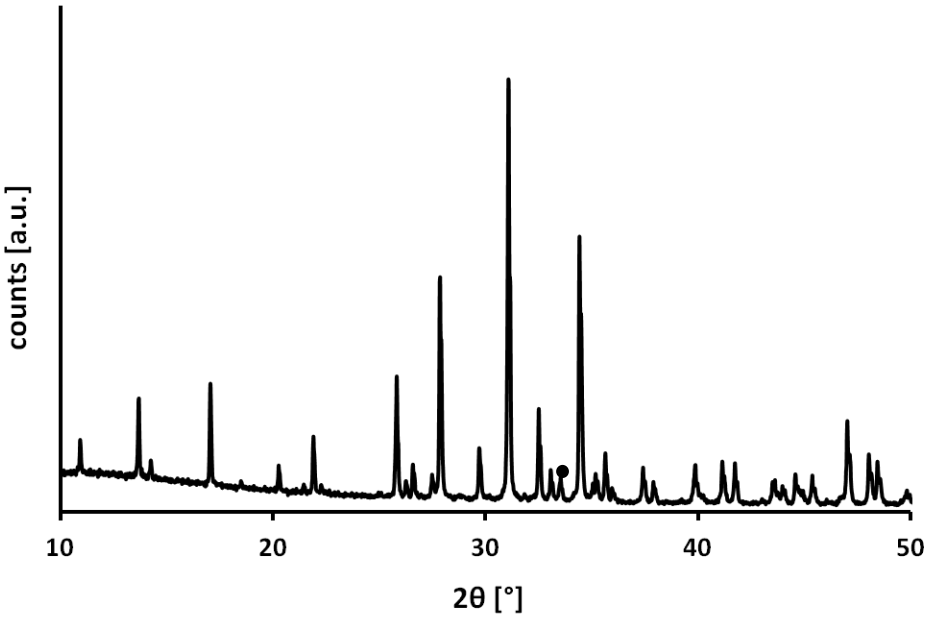

Figure 2: XRD of β-TCP powders synthesised by solid state reaction. All the unlabelled-peaks belong to β-TCP, while the small dot signals a possible peak of HAp

Once produced, the powder was ground with Al_2O_3 beads (0.9-2 mm) with a powder to beads ratio of 0.3 in weight and successively sieved (<315 µm). The purpose was to obtain a fine powder in order to minimize the time required for the complete dissolution of β-TCP to make the DCPD cement and, therefore, to avoid residual β-TCP particles in the final product. The grain size distribution of the powders, before and after grinding, was assessed by means of a laser granulometer (Mastersizer 2000, Malvern, UK) in the dry-state configuration (Scirocco 2000). The results (reported in Figure A.a.1 and Table A.a.1 in Annex) displayed how the initial powder ("not ground") was characterised by a bimodal distribution with a median size of 4.7 µm. The best compromise was obtained after 22 minutes of grinding: at this point, the biggest particles had been crushed, but the smallest ones had not started yet to gather into big agglomerates. Therefore, the values of d_{10}, d_{50} and especially d_{90}

(that is to say the 10°, 50° and 90° percentile) were particularly low, i.e. equal to 1.3, 3.2 and 9 µm respectively (cf. Figure A.a.1 and Table A.a.1 in Annex).

The as-obtained powder was ready to be mixed with MCPM for the DCPD cement production.
As far as MCPM is concerned, the powder (Sigma Aldrich, purity>85%, Lot BCBC9399V, M=252.07 g/mol) was dried overnight at 55 °C to eliminate any possible presence of adsorbed water.

For optimising the final DCPD material, prepared by a setting reaction according to equation (1), different tests were performed changing the nature and concentration of additive and powder to liquid ratio (P:L). The influence of these parameters on the knife setting time was evaluated. The knife setting time is here defined as the time needed to have a cement paste enough cohesive so that when it is cut in two pieces by a thin spatula, the cut does not heal itself and the two parts remain clearly separated. As expected, in terms of retardants, the effect of sulphates (AS) appeared weaker than that of the same concentration of citrates (AC) (cf. paragraph 1.4.2, [3]) (Figure A.a.2 in Annex). Moreover, the delay of the setting time was directly proportional to the concentration of additive (both for AC and AS) and inversely proportional to the P:L ratio.

Considering the final porosity desired for the samples (around 60%, in order to observe an evolution of the material in a reasonable time), the powder to liquid ratio was set equal to 0.95. With such an excess of water the cement displayed a quite low viscosity; the addition of 0.05 M of citrate was enough, thus, to obtain a setting time of around 4 min 30 s. The use of sulphates was excluded, given that the setting-time obtained with citrates was considered appropriate for the casting process. Moreover, in this way, possible changes in the microstructure, such as refinements of grains, which can be induced by the addition of sulphates (but not of citrates, as reported in literature [3]), were avoided.

For the final composition of DCPD samples, 5.2408 g of β-TCP and 4.2592 g of MCPM were weighed respecting a molar ratio of 1:1. At the same time, 10 mL of 0.05 M citric acid solution was measured so to have a final P:L of 0.95 g/mL, where P is the total weight of MCPM plus β-TCP. The MCPM powder was first mixed with the liquid phase for 30 seconds, then the β-TCP powder was added and the dough was continuously stirred for another 3 minutes. After this time the cement was poured into cylindrical moulds (height = 12 mm, diameter = 12 mm) composed of polyoxymethylene (POM) (Figure 3). The lower flat surface of the moulds was maintained in contact with an acetate film in order to obtain samples with at least one very smooth flat surface, to ease characterisations such as indentation measurements. The moulds were left into closed plastic bags to avoid drying and let at room temperature for 24 h. After this time, the samples were de-moulded and immersed in distilled water for 30 minutes, in order to eliminate the possible residual acidity due to the setting process; this time expired, the specimen were let dry at 37 °C until constant weight was reached. Finally, the dimensions and weight of the samples were measured with a calliper and their apparent density was computed (ratio between the weight of the specimen and its external volume).

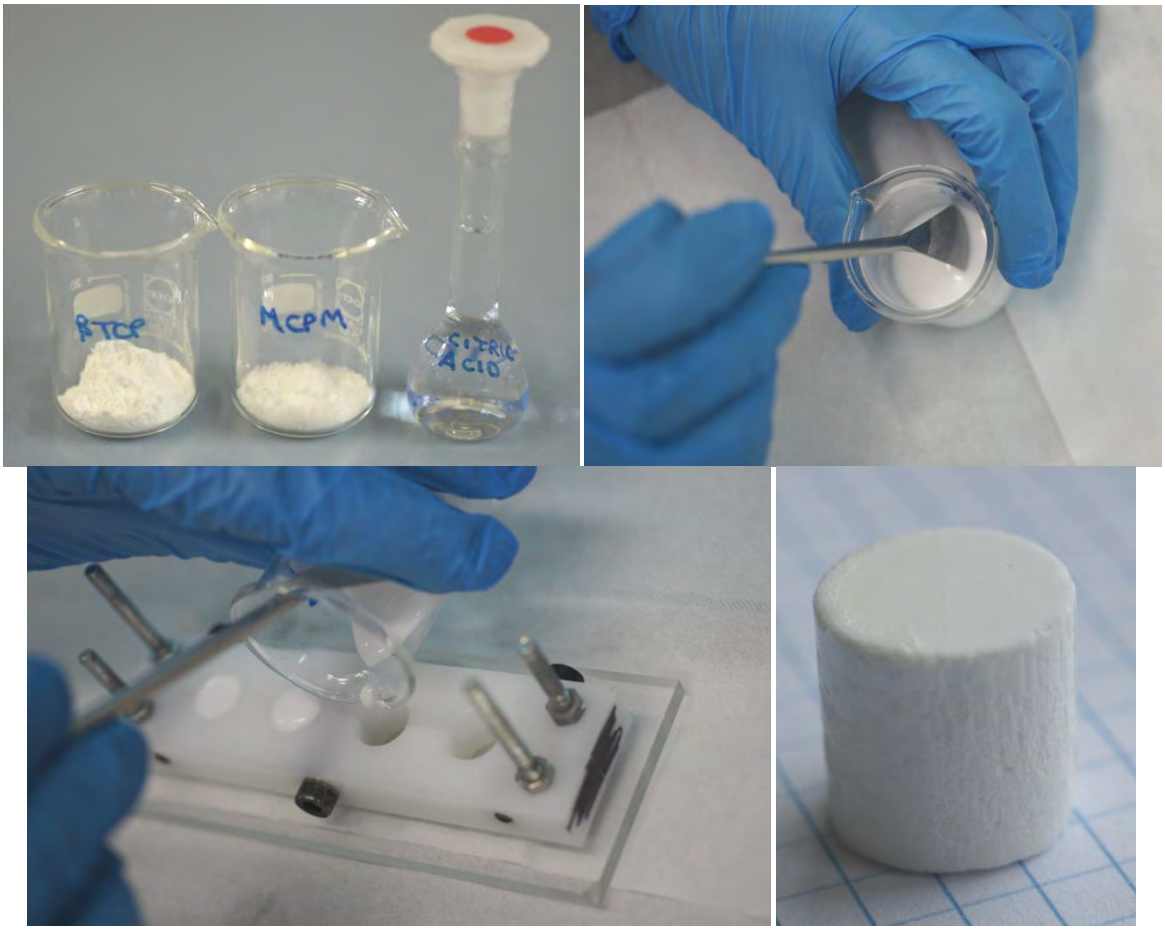

Figure 3: Reagents, mixing, moulding and final result of DCPD cement preparation (h= 12 mm, Ø = 12 mm)

The samples which were obtained with this protocol will be referred to as "DCPD samples" throughout the whole manuscript.

No further preparation of the specimens was required for their characterisation before immersion; all the analyses (micro-indentation comprised) were performed on the smooth flat surface.

2.1.2 Synthesis of porous β-TCP samples

Porous samples were kindly provided by Prof. Marc Bohner (RMS Foundation, Bettlach, Switzerland). The adopted elaboration technique consisted in first producing a cylindrical sample composed of calcium deficient hydroxyapatite using a cement route and then calcining the Ca-deficient apatite (CDHA) in order to obtain β-TCP. To obtain porous samples, the CDHA cement paste was emulsified before its moulding and its setting.

Briefly, for the production of the CDHA cement, α-TCP powder (<10 µm) was mixed for 2 minutes at 2000 rpm in a blade mixer with an emulsifying solution (made of 2.8 wt.% Na_2HPO_4, 1 wt.% emulsifier Cremophor EL (BASF, Germany) and 96.2 wt.% water) and paraffin oil (total P:L ratio = 0.84 g/g). The so obtained emulsion was put into a syringe and then injected into cylindrical Teflon® moulds (9.5 x 9.5 mm), which were then tapped so to avoid the presence of large air bubbles in the final samples. The specimens set while incubated at 60 °C and 100% humidity for 72 h (see eq.(3), [4]); they were then demoulded and soaked into Petroleum ether (Rectapur grade, VWR) for 48 h to remove as much paraffin as possible.

Finally, specimens were sintered at 800 °C with a heating and cooling rate = 2.5 °C/min and a 1h-plateau to obtain the β-TCP phase (eq.(4).

$$3\alpha - Ca_3(PO_4)_2 + H_2O \rightarrow Ca_9(HPO_4)(PO_4)_5(OH) \quad (3)$$

$$Ca_9(HPO_4)(PO_4)_5(OH) \rightarrow 3Ca_3(PO_4)_2 + H_2O \quad (4)$$

Once received, and before being immersed for the dissolution tests, the porous β-TCP samples were cut at low speed with a diamond blade (0.5 mm of thickness), so to obtain a cylinder with two parallel and flat surfaces (Figure 4), and polished with diamond lapping films (Buehler, ref.156802, 156796 and 156792). This last passage was performed manually, without water or lubricants and in several steps, gradually decreasing the roughness of the abrasive paper (1-0.5-0.1 µm).

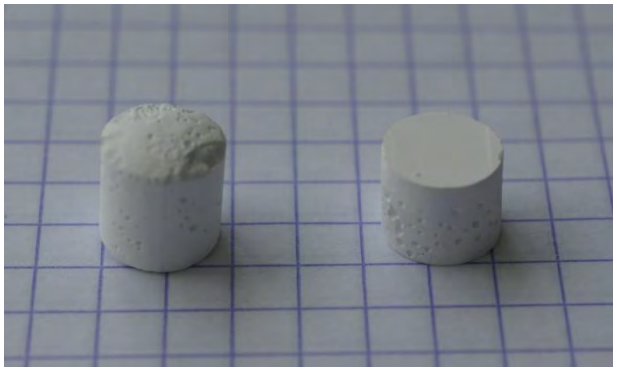

Figure 4: Porous β-TCP samples as received (on the left) and after cut (on the right, h= 9.5 mm, Ø = 9.5 mm)

2.1.3 Synthesis of dense β-TCP samples

For the production of dense samples, pure β-TCP and magnesium-doped β-TCP (referred in the whole manuscript as TCP_NoMg and TCP_Mg respectively) powders, provided by Prof. Marc Bohner (RMS Foundation, Bettlach, Switzerland), were used.
As descripted elsewhere [5], for the synthesis of TCP_NoMg (pure β-TCP), powders of DCP (GFS Chemicals) and HAp (Budenheim) were mixed, thermally treated at 1300 °C for 4 h, crushed to 0.5 mm and then ground in a planetary mill for 1 h at 400 rpm with the addition of fumaric acid (10%wt) (Fluka Analytical) and ethanol (2 mL/100 g) to prevent agglomeration.
For the TCP_Mg powder, the same process was followed, but magnesium phosphate octahydrate ($Mg(PO_4)_2 \cdot 8H_2O$, Fluka) was added to the initial powder mixture. The final molar content of Mg was 5% and the ratio between the sum of moles of magnesium and calcium and those of phosporus was kept equal to 1.5 ((Mg+Ca)/P = 1.5).

The powders of TCP_NoMg and TCP_Mg were placed in a cylindrical die (Ø = 10 mm), pressed in a uniaxial press at 130 MPa for 45 s (Figure 5) and further isostatically pressed at 400 MPa for 40 s (Cold Isostatic Pressing, Nova Swiss, France). The obtained discs were finally sintered following the thermal treatment showed in Figure 6 (resulting in cylinders of 8.5 mm in diameter and 4 mm in height). A 20 h long plateau at 800 °C was aimed to eliminate all traces of fumaric acid, which were still left after the powder synthesis as testified by the grey colour of the samples prior to thermal treatment (Figure 7). Note that calcined samples were also not completely white (Figure 7), as will be discussed in chapter 5.

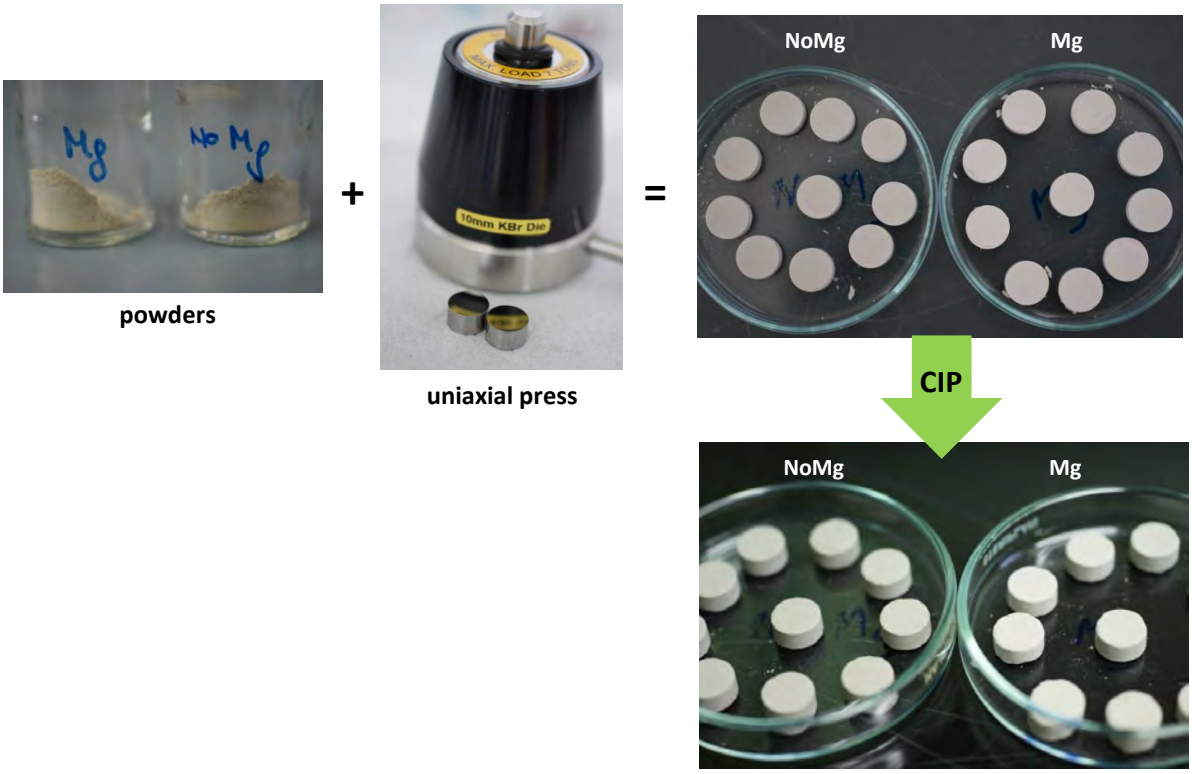

Figure 5: Production of dense β-TCP samples - uniaxial press

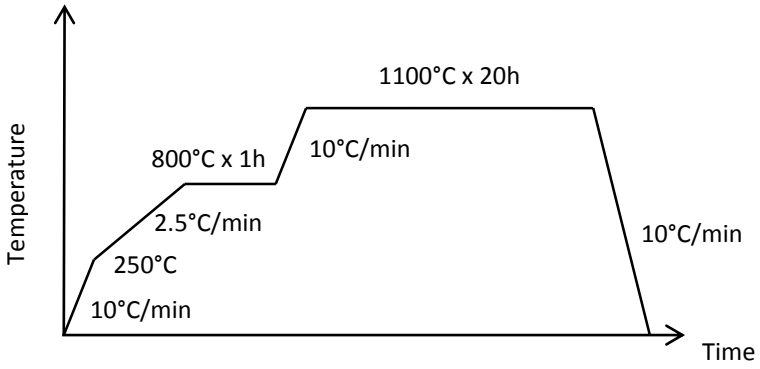

Figure 6: Production of dense β-TCP samples - thermal treatment

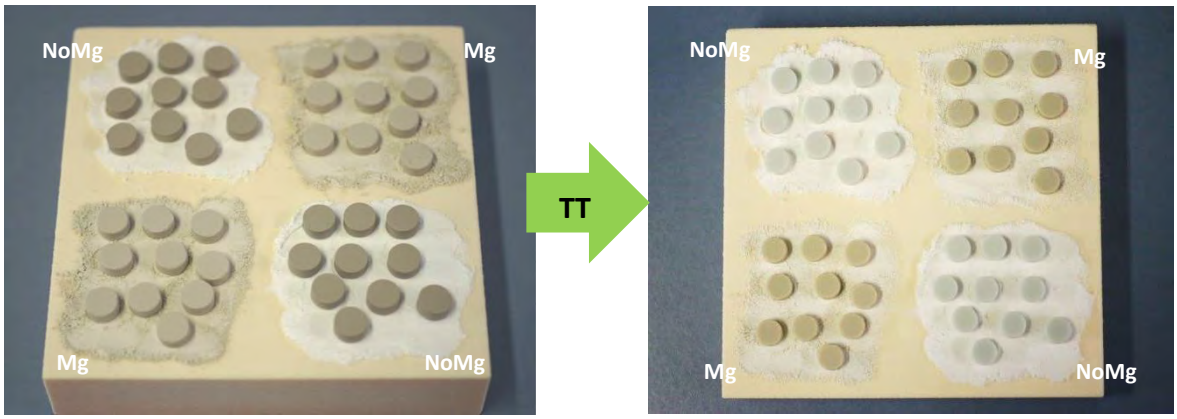

Figure 7: Production of dense β-TCP samples - samples before and after thermal treatment (TT). Specimens were placed on a layer of powder with the same chemical composition as the samples to hinder diffusion.

2.2 Dissolution tests

Dissolution tests were performed only with porous samples (DCPD and β-TCP), in different solutions and without cells. The specific conditions are explained in detail in the following pages.

2.2.1 Immersion solutions

As explained in paragraph 1.7.1, two different solutions were chosen for performing the dissolution tests: tris(hydroxymethyl)aminomethane (denoted TRIS in the manuscript) and phosphate buffered saline solution (PBS). While the first medium does not contain calcium and phosphate ions, the second one is characterised by the presence of some phosphates. Therefore, TRIS should foster dissolution phenomena whereas PBS should promote the precipitation of calcium phosphate phases.

For the present work, 0.1 M TRIS solution was prepared by dissolving 12.114 g of tris(hydroxymethyl)aminomethane ($(HOCH_2)_3CNH_2$) powder (Sigma Aldrich, purity >99.8%, M=121.14 g/mol, Lot BCBN1573V) in 1 L of deionised water, with a pH adjusted to 7.4 by the drop-by-drop addition of HCl (Fisher Chemical, 37% code H/1200/PC15, Lot 1531899). 0.01 M PBS solution was prepared by dissolving one pouch of commercial powder (Sigma Aldrich, Lot SLBH8322V) in 1 L of deionised water, leading to the following composition: NaCl 137 mM, KCl 2.7 mM, Na_2HPO_4 10 mM, KH_2PO_4 1.8 mM.

2.2.2 Static conditions

In the present work, dissolution tests are considered “static” when the solution was not periodically renewed. In other words, a sample was immersed at t0 in a given solution and remained inside of it for the whole duration of the test.
In this study, dissolution experiments in static conditions were performed with the aid of an incubator (Innova 40, New Brunswick Scientific, Germany, Figure 8) in the conditions given in Table 1. Briefly, the temperature (37 °C) and the pH (7.4) were chosen to be as close as possible to physiological conditions. For simplicity, this kind of tests was performed only in TRIS medium.
The ratio between the weights of samples and the volume of the TRIS solution, in which they were immersed, depended on the sample composition (DCPD or β-TCP). Indeed, the liquid-to-sample weight ratio was chosen in order to be high enough to facilitate the degradation of the samples in reasonable times [6, 7], but still employing a total amount of liquid which could be contained into the

vessels. As a consequence, given that DCPD specimens presented a higher density, their final liquid-to-sample ratio was lower than the one adopted for β-TCP specimens.
Finally, a light shaking was adopted in order to homogenise the solution throughout the test.

Figure 8: Incubator used for static dissolution tests

Table 1: Chosen conditions for the static and dynamic dissolution tests

	Static conditions	Dynamic conditions	
Fluid	TRIS-buffered solution	TRIS-buffered solution	PBS solution
Solution renewal (amount, rate, frequency)	No	100mL in 1min, every 24h	100mL in 1min, every 24h
Solution pH	7.40 ± 0.15	7.40 ± 0.15	7.40 ± 0.10
Temperature	37 °C	37 °C	37 °C
Stirring	Orbital shaking, 50 rpm	Blade stirrer, 50 rpm	Blade stirrer, 50 rpm
Liquid volume/ sample weight ratio	130 mL/g (DCPD) 430 mL/g (β-TCP)	130 mL/g (DCPD) 430 mL/g (β-TCP)	130 mL/g (DCPD) 430 mL/g (β-TCP)
Test duration	30min - 14 days (DCPD) 1 - 8 weeks (β-TCP)	1 day - 14 days (DCPD) 1 - 8 weeks (β-TCP)	30min*, 1 d - 14 days (DCPD) 1 - 8 weeks (β-TCP)

** Note that for the 30 minutes test, static and dynamic conditions were considered as being equivalent (no solution renewal in either case); therefore 30 minutes tests were in fact all performed following the protocol described for static conditions (including for PBS).*

For DCPD samples, time-points were equal to 30min, 1 day, 4, 8 and 14 days, whereas β-TCP samples were immersed longer, i.e. 1 week, 2, 4 and 8 weeks.

2.2.3 Dynamic conditions

In this work, dissolution tests are considered to be “dynamic” when the immersion solution was refreshed every 24 h.
For tests in dynamic conditions, the dissolution tester PTWS 1210 (Pharmatest, Germany) was used (Figure 9). Two independent peristaltic pumps linked to the instrument allow to set an automatic periodic refresh of the medium: the first pump is used to withdraw a pre-set amount of liquid in a determined time, while the second one is used to introduce the new medium into the vessels. All during the test, the temperature of the samples was kept constant at 37 °C thanks to a thermostatic bath (Figure 9). Moreover blade stirrers, with adjustable speed, constantly mix the medium inside the vessels. The amount of liquid to remove, the rate and the delay between one refresh and the next can be set by the user. For dissolution tests in dynamic conditions both TRIS and PBS solutions were used. The experimental conditions which were chosen are reported in detail in Table 1.

In *in-vivo* conditions, body fluids maintain their pH and composition constant within time. Given the difficulty to reproduce such a constant environment in an *in-vitro* set-up designed to test several samples in parallel for long periods, a compromise was reached by periodically renewal of the immersion medium. The delay between two consecutive solution renewals was set equal to 24 hours, because previous studies have proved this time to be adequate for maintaining the pH of the solution confined in a limited range of values (namely 7.40 ± 0.40 [7]).

Figure 9: Equipment used for dynamic dissolution tests (from http://www.pharma-test.de/ptws-1210/)

It is worthy to underline that for the 30-minute test, TRISs and TRISd were considered equivalent: thus, this time-point was performed only static conditions.

2.3 Resorption tests

As explained in Chapter 1, the evolution of an implanted material can be affected by two main phenomena: dissolution/precipitation and cellular-driven resorption. While the former process has been mimicked in this study through static and dynamic immersion tests, for the latter some cellular tests were performed in collaboration with Prof. Aldo Boccaccini and Dr. Rainer Detsch, at the Biomaterial Department of FAU University (Erlangen, Germany).
In particular, given that the cells in charge of bone resorption in a physiological context are osteoclastic cells, it seemed logical to study the resorption of calcium phosphate materials by this type of cells.
After preliminary tests, the results obtained on β-TCP showed that this material was more promising and could offer more interesting insights than DCPD on the resorption process; a lower cellular activity and a poorer differentiation of osteoclasts was observed, in fact, on DCPD. That is why the final assays were performed on β-TCP only. In particular both pure (TCP_NoMg) and doped (TCP_Mg) β-TCP were used (cf. paragraph 2.1.3), with the aim of evaluating the influence of magnesium doping on the resorption process.

Before being tested, all samples underwent a sterilisation procedure in autoclave (Systec DX 23, Microbiology International, USA) consisting in a treatment in 100% relative humidity at 121 °C and 200 kPa for 20 min.

In terms of cell-type, murine RAW 264.7 monocytes were chosen as osteoclast precursors. The cell culture protocol was established after some preliminary tests and included an initial differentiation phase in cell culture plates (without samples) and, after having moved the cells, a second phase of growth on the surface of the specimens. In detail, RAW 264.7 monocytes were thawed, seeded in 6-well culture plates and fed with Roswell Park Memorial Institute medium (RPMI) 1640 medium (Life Technologies, ref.21875, Lot 1317076) with the addition of streptomycin (sp, 1%) and foetal bovine serum (FBS, 20%) for the first 8 days. Then they were split and grown for one week with RPMI medium enriched not only with streptomicin and foetal bovine serum (+sp 1% + FBS 10%), but also with MCSF (Macrophage Colony Stimulating Factor) in the concentration of 25 ng/ml. After this period, RANKL factor was added (40 ng/ml) to the medium and the cells were cultured for another 10 days. Once the differentiation phase was ended, the cells were scratched, centrifuged and seeded on TCP_NoMg, on TCP_Mg samples and on glass discs which were used as control (100 000 cells/sample, 1 mL/sample), where they were let for 48 hours, 4 days and 7 days respectively.
At the end of the tests, cells and samples were fixed and treated with specific procedures depending on the planned analyses; further details about these protocols are provided in the section “Characterisation: resorption tests” (par. 2.5).

In parallel to resorption tests some dissolution assays were performed, in order to evaluate the ion release from dense samples. For this purpose, TCP_NoMg and TCP_Mg specimens were immersed in cell culture medium (RPMI) or in physiological saline reference NaCl aqueous solution (0.9% w/v). The samples were treated exactly as described previously for resorption tests (i.e. same amount of medium, same refresh) and let immersed for 48h, 4d, 7d respectively. After these times, they were retrieved, washed with deionised water and let dry at room temperature. All the solutions of immersion were kept to be further analysed.

2.4 Characterisation: dissolution tests

In order to follow the evolution of porous DCPD and β-TCP samples during their immersion in TRIS and PBS solutions, several complementary analyses were performed both on surface and at core of the specimens.

In particular, after having been retrieved from the immersion solutions, the samples were rinsed with deionised water, dried at 37 °C until constant weight and then store in dry conditions until tested. The same surface already used for the analyses at time zero underwent all the characterisations performed on the outer part of the samples after immersion. For the inner part (core), instead, specimens were cut at low speed with a diamond blade (0.5 mm of thickness); a low speed of rotation was imparted to the blade so to avoid the formation of scratches on the surface of the cut. Any polishing procedure was avoided, in order to reduce the risk of pollution of the material.
All the used techniques, described in the following pages, are classified according to whether they permit to gain insight on morphological, physico-chemical, micro-structural or mechanical properties of the materials.

2.4.1 Morphological and chemical properties

X-ray diffraction

For the current study X-ray diffraction (XRD) analyses were performed with a diffractometer Bruker D8 Advance (Germany) with a copper anticathode (λ = 1.54 Å) and configuration θ-θ. Each scan was acquired between 4° and 90°, with a step equal to 0.02° and a time/step of 0.4 s. The samples were generally turned during the analyses (rpm = 30) so to scan a larger surface and obtain an average value. Specimen were analysed both on surface (left untouched) and at core; for this last part the samples were cut in two parts at mid-height with a diamond blade (0.5 mm thick).

The resulting diffractograms were interpreted with the aid of the software DiffracPlus EVA and the relative database.

XRD patterns used for the identification of the crystalline phases were the following:

- DCPD: JCPDF file#01-072-0713
- DCPA: JCPDF file#00-009-0080
- MCPM: JCPDF file#00-009-0347
- Apatite: JCPDF file#01-073-1731
- OCP: JCPDF file#01-074-1301
- β-TCP: JCPDF file#01-070-2065
- NaCl: JCPDF file#01-075-0306

In addition, some of the XRD scans were treated using Rietveld refinement method with the Topas 4 software (Bruker D8 Advance, Germany). The peaks shape was described by a modified Thompson-Cox-Hastings pseudo-Voigt function. The starting structures were obtained from the Cristallography Open Database (see table Table 2) (http://cod.ibt.lt/, accessed in July 2015). Only the peak shape parameters, scale factor, lattice parameters and preferential orientations (using Sperical harmonics) were adjusted.

Table 2: CIF files used for the initial structures of the phases identified by Rietveld refinement

phase	CIF file #
MCPM	2310630
HAp	9002213
DCPD	9007305
DCPA	9007619
OCP	7217893

pH

During the present study the pH value of solutions, where the samples were immersed, was measured with a pH-meter, calibrated on 3 points (pH=4.00±0.02; pH=7.00±0.02; pH=9.20±0.02 at 37 °C). The pH was monitored on a daily base (immediately before the refreshment of the medium in case of dynamic tests).

In parallel, the pH of reference solutions was also registered. For static conditions, the reference solution corresponded to the initial TRIS solution, which was kept at the same temperature in the same apparatus (orbital shaking), but without samples dipped inside. For dynamic conditions, the pH of the new solution which was used for the daily refresh was measured just before being introduced into the vessels and was used as a reference.

2.4.2 Microstructural properties

Scanning Electron Microscope

In the present work, scanning electron microscopy (SEM) analyses were performed mainly with the aim of evaluating the sample's surface topography and the crystal morphologies. Specimens were glued to a specific sample-holder with a silver conductive paint and scanned with the equipment Supra55VP (Zeiss) at low voltage (1 kV); in this way it was possible to avoid any samples' metallisation, which could "conceal" the morphology at the nano level. The working distance was always between 4.5 mm and 5.5 mm.

Roughness assessment

Specimen roughness was assessed by means of a digital microscope (Hirox KH-7700, USA). This equipment works by varying the focal distance of its lens: for each focal distance just the parts of the sample located on the focal plan are on focus, while all the others are blurred. Knowing the distance of the focal plan it is possible, therefore, to calculate the distance of the parts of the sample which are on focus. As a result, a three-dimensional reconstruction of the surface of the specimen is obtained and the parameters relative to its roughness can be calculated.

Several parameters of roughness can be calculated depending on the formula adopted; in the present study the root mean squared (or R_{RMS}, eq.(5)) value has been chosen. Although it is clear that the use of just one parameter is not sufficient for a complete characterisation of a surface, it can provide, nevertheless, useful information when a comparison between different samples is needed. Moreover, the RMS value was preferred to the average roughness (R_a, eq.(6)), because it is slightly more affected by single peaks and valleys and it provides, therefore, a "safer" measurement (Figure 10).

$$R_{RMS} = \sqrt{\frac{1}{N}\sum_{i=1}^{N}\left(Y_i - \bar{Y}\right)^2} \tag{5}$$

$$R_a = \frac{1}{N}\sum_{i=1}^{N}\left|Y_i - \bar{Y}\right| \tag{6}$$

$$\bar{Y} = \frac{1}{N}\sum_{i=1}^{N} Y_i \tag{7}$$

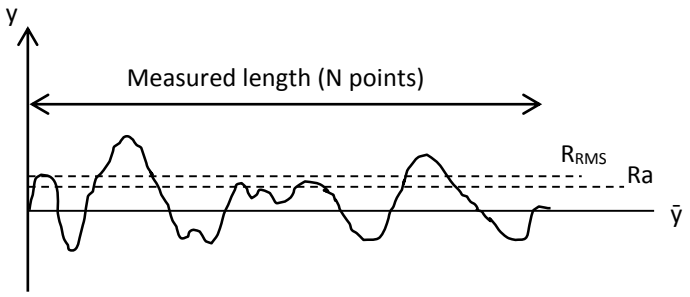

Figure 10: Two parameters of roughness (Ra and R_{RMS})

Note that, for their observation with the digital microscope, DCPD and β-TCP samples had to be metallised with a thin layer of gold (around 12 nm thick) in order to enhance the contrast on their surface.

X-ray computed tomography technique

The X-Ray computed tomography technique (µ-CT) is based on the same principle than a regular X-ray radiography. The object of the analysis is invested by an X-ray beam; this latter, by crossing the sample, is attenuated on an extent which depends on the characteristic of the material (composition, density). The transmitted beam is collected by a detector placed behind the sample and converted in a digital image. The obtained picture (in greyscale) displays parts more or less brilliant depending on the attenuation coefficient of the corresponding part of the sample (the highest the attenuation the brighter the tone).
The peculiarity of the CT technique is that the specimen is rotated during the analyses so that several images are acquired at different angles (Figure 11). These radiographs, then, can be reconstructed with the aid of a software and give birth to a 3D representation of the sample. The major and evident advantage of this technique is that it allows the observation of the inner part of an object in a non-destructive way, i.e. without the need of cutting it. Another important benefit is the possibility to get information on the three dimensional microstructure of the sample (e.g. pores interconnection,…) whereas usual observation tools provide only 2D information.

In the present study a micro-tomographer (µ-CT) Phoenix v|Tome|x (General Electric, USA) equipped with a Varian Paxscan detector (1920x1536 pixels) and an X-ray source of 1-4 µm was used for analysing the inner part of the samples before and after immersion (Figure 12). The resolution, variable between 1 and 100 µm/voxel, was usually set equal to 10 µm/voxel. For few specific samples, when it was necessary to investigate the microstructure in more detail, the resolution was set to 2 µm. To be able to reach such a resolution in the lab apparatus, samples had to be cut (typical size of scanned sample: 2 mm x 2 mm x 4 mm); this is why such a high resolution imaging could not be performed prior to immersion.

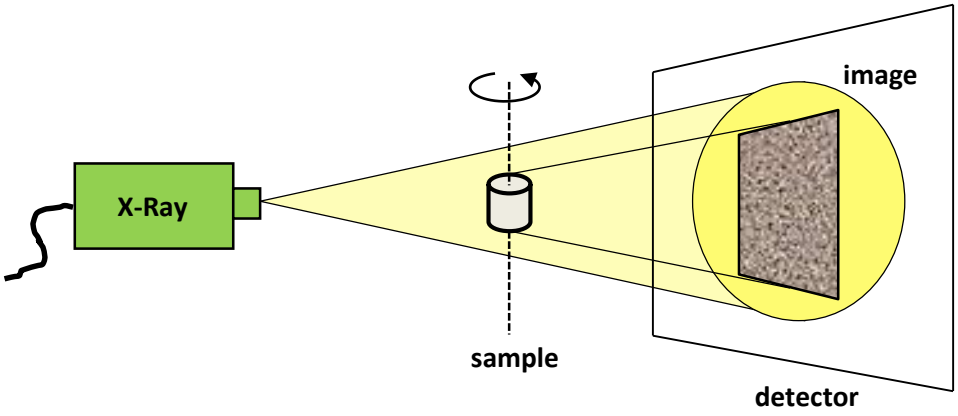

Figure 11: Schematic representation of a X-Ray tomography system

Figure 12: X-Ray tomographer Phoenix v|Tome|x

Finally, some of the acquired 3D volumes were further analysed by means of the public domain ImageJ/Fiji shareware [8] in order to obtain quantitative measurements.
In particular, for β-TCP porous samples immersed in certain conditions, an outer ring composed of two layers was noticed on µ-CT reconstructions: the external part was made of a bright crown and its inner part of a darker one (named "superficial crown" and "porous crown" respectively, Figure 13-A). Quantitative evaluation of the thickness of these layers was performed by the ImageJ/Fiji shareware. Briefly, a median 3D filter was applied to the whole 3D volumes, in order to soften the differences of grey levels between the zones. The radial reslice function, which creates orthogonal reconstructions of an image stack by rotating a reference line around one of its ends, was applied (Figure 13-B); in this way, the cylindrical geometry of the sample was converted into a parallelepiped one. After the radial reslice, the outer ring was isolated and binarised through a threshold, in order to clearly discriminate the darker zones (in red in Figure 13-C). The value of each pixel corresponding to the porosity was set equal to 1, while the one corresponding to the material was set equal to 0. The sum of all the pixels values along the *z*-axis (i.e. proceeding from the surface towards the core of the specimen, Figure 13-C) multiplied by the resolution gave the average thickness of the porous crown for each radial slice. The histogram function, finally, permitted to calculate the mean value and the standard deviation of the thickness of the porous layer (Figure 13-D). For the external crown the

same procedure was followed, but during the threshold step the bright layer was selected instead of the porous one.
The thicknesses of the "superficial crown" and of the "porous crown" were assessed at different immersion times. For β-TCP porous samples immersed in TRISs and in PBSd, only one sample was analysed for each time-point, whereas for TRISd, two samples were used.

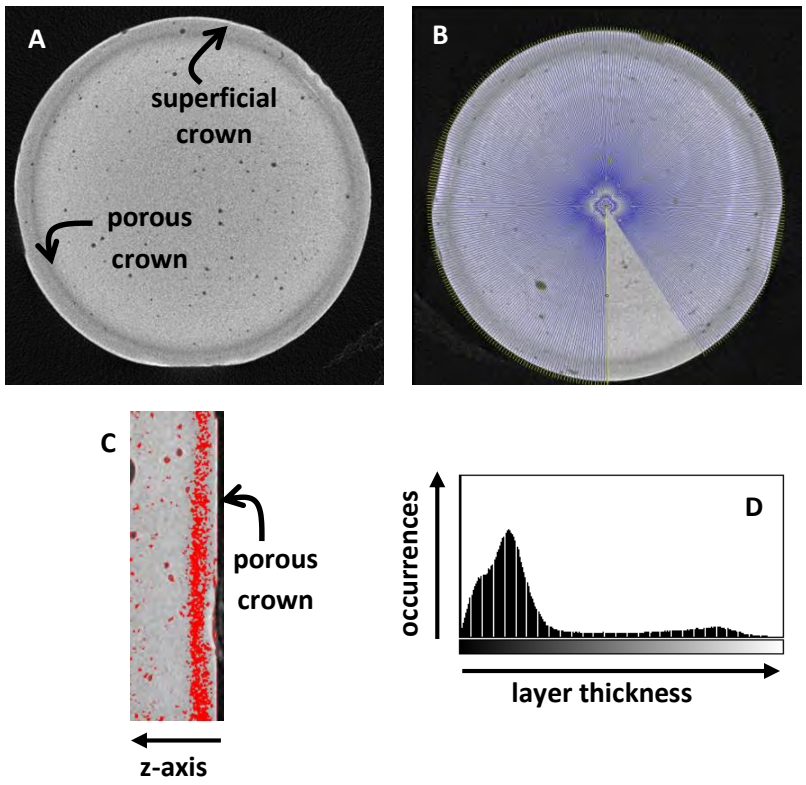

Figure 13: Main steps of the image analysis procedure performed on µ-CT data

Mercury intrusion porosimetry

Mercury intrusion porosimetry is commonly used for measuring pore size, volume, density, distribution of a material. Since mercury does neither wet most of the materials nor enter spontaneously in capillaries, it must be forced to enter pores. The required pressure to cause mercury intrusion is inversely proportional to the pore entrance size. Therefore, knowing the applied pressure (*P*), the contact angle (θ) between the surface and mercury and its surface tension (*γ*) it is possible to deduce the pore "diameter" (*D*) (or, more exactly the entrance diameter and/or the diameter of interconnections between pores) according to Washburn's equation:

$$D = -4\gamma \cos\theta / P \qquad (8)$$

In the present work, mercury intrusion porosimetry was mainly used to obtain the pore size distribution of samples before and after immersion.

2.4.3 Mechanical properties

µ-indentation technique

The main principles of indentation have already been presented in Chapter 1. As said, for the present study, among the different tip geometries, the spherical one was preferred.

Two different pieces of equipment have been used for performing indentation tests.
The first one is a universal testing machine Electroforce® 3200 (BOSE, USA) equipped with a load cell (22 N max, resolution of 2 mN) and a capacitive displacement sensor (max ±0.5 mm, resolution of 50 nm) (Figure 14). This instrument, thanks to its wide range of displacement, was preferred for testing DCPD samples, where, after degradation, problems of saturation of the displacement sensor could appear using other machines with a narrower displacement range. During all the tests (before and after immersion), the different parameters were set as follows:

- Spherical tip of WC, Ø = 1 mm
- Maximum load = 1.5 N
- Head speed = 0.3 N/s
- Dwell at maximum load of 10 s

The sphere diameter and the load were chosen after several preliminary tests aimed to maximise the number of indentations on each sample, reduce as much as possible the influence of surface roughness on results and involve in the test a volume of specimen big enough to be representative of the material.
The head speed was set equal to 0.3 N/s as reported in a previous study [7] and the dwell was applied in order to diminish viscous effects during the unloading process. Any possible movement of the specimen during the indentation tests was avoided by using a sample holder which acted as a vise.

All the indentations “on surface” were performed on the smoother of the two flat surfaces of each DCPD sample, i.e. the one which was in contact with the acetate film when the cement was moulded (cf. paragraph 2.1.1).

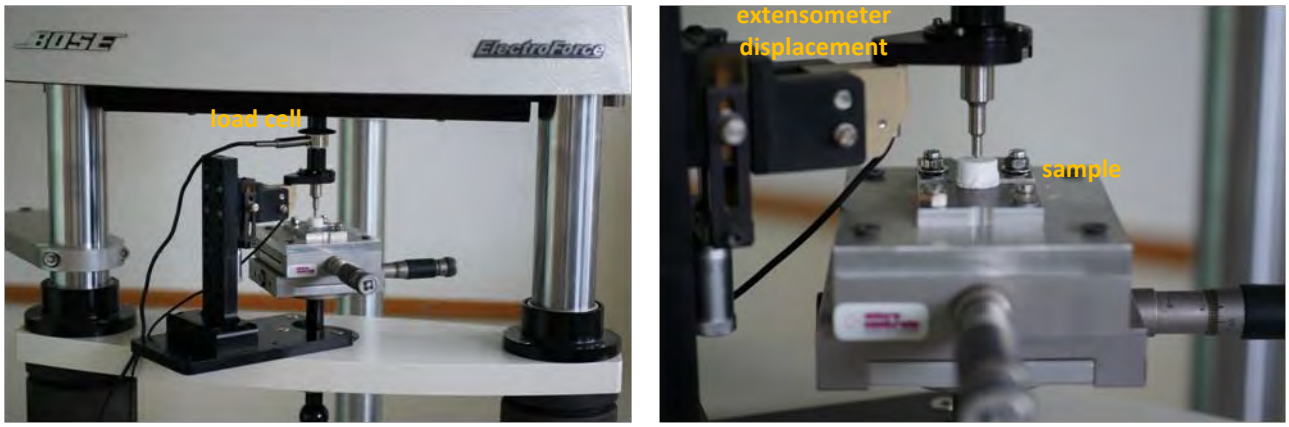

Figure 14: Electroforce® 3200 testing machine

The second instrument, was used for β-TCP porous samples: a G 200 nano-indenter (Agilent Technologies, USA).
One of the main advantages of the nano-indenter machine consists in the possibility of using a Continuous Stiffness Measurement (CSM) mode. This configuration overlaps small periodic oscillations to the main loading-unloading curve and allows, as a consequence, to constantly

calculate the values of hardness and elasticity of the specimen. Moreover the nano-indenter is equipped with an optical microscope, so that it is easier to see possible bubbles/defects on the surface of the sample and to avoid them during the test.
It must be underlined that, although the machine is called a nano-indenter, the tests performed on β-TCP can be anyway considered as micro-indentation technique: the point and the load applied, in fact, lead to a depth of penetration of the order of magnitude of microns.
In particular the following conditions were chosen for the tests:

- Spherical tip of Al_2O_3, Ø = 2 mm (Figure 15)
- Max load = 0.5 N
- CSM: 2 nm, 45 Hz
- Deformation speed = 0.05 1/s

The calibration of the tip was performed by direct measurement of the radius with a digital microscope. Moreover, the stiffness of the machine was evaluated through tests on reference samples (i.e. fused silica).
The indentation tests were performed “on surface” (preparation of samples detailed in paragraph 2.1.2), while for the measurements “at core” the samples were simply cut (at low speed) with a diamond blade and not polished.

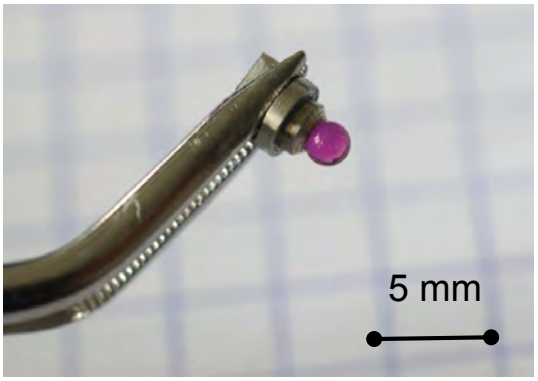

Figure 15: Indentation tip (or ball) used for β-TCP samples

Compression tests

Compression tests were performed using an Instron equipment coupled with a micrometer precise extensometer (LVDT). Samples were compressed using a 10 kN Instron Load cell, placed between two resurfaced alumina plates, to ensure a good parallelism (as displayed in Figure 16). For some samples, the compression process involved several charge/discharge cycles to obtain the Young’s modulus of the samples during the different regimes (before and after the dwell). The whole process was filmed using a Canon camera, placed in the plan of the sample to correlate the visible deformation with the obtained curves.

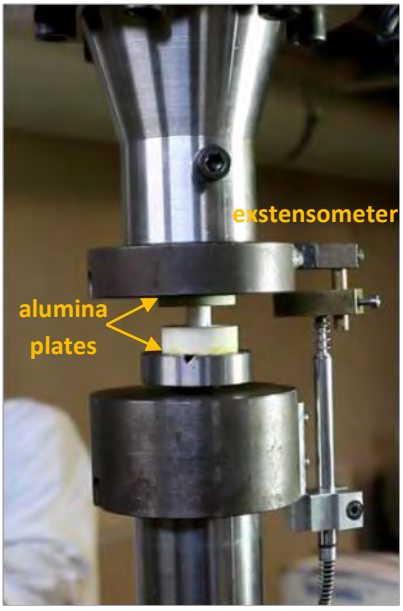

Figure 16: Set up for compression tests

2.5 Characterisation: resorption tests

In order to evaluate if the RAW cells differentiate into osteoclast-like cells, several biological aspects have to be considered. In particular, the morphology should be that of a giant-multinucleated cell, which spreads and creates a sealed chamber between itself and the surface, displaying the formation of the typical "actin ring" on its border (Figure 1 in Chapter 1). Moreover, if the osteoclast-like cells are in their active form, resorption pits should be visible on the surface of the material where the cells were grown. Finally, osteoclasts express some enzymes, which are peculiar and can be used, therefore, as markers of their activity.

In the present study, different techniques were exploited to analyse the resorption process both from the material perspective (section 2.5.1) and from the cells one (section 2.5.2); a detailed list is presented in the following pages.

2.5.1 Material characterisations

X-ray diffraction

XRD analyses were performed before and after immersion on some dense samples which underwent dissolution tests (in RPMI and NaCl, cf. paragraph 2.4) and on some others used for resorption assays (after having removed the cells with trypsin).

The program followed was the same as used for the porous samples of the dissolution tests (4°-90°, step = 0.02°, time/step = 0.4'') (see "X-ray Diffraction" in paragraph 2.4.1).

Transmission Electron Microscopy

In the present study, samples were cut, mechanically polished and then furtherly thinned through argon ion bombardment by means of a Gatan Precision Ion Polishing System (PIPS). A transmission

electron microscope (TEM) (JEOL 2010F, USA) was then used on thin slices of TCP_NoMg and of TCP_Mg for assessing the presence of magnesium ions and their location.

Ion titration

The release of calcium ions was evaluated both in the solutions where dense samples were immersed without cells (i.e. dissolution tests in RPMI and NaCl) and with cells (i.e. resorption tests).
The calcium ion concentration was measured by means of a calcium colorimetric assay kit (MAK022, Sigma Aldrich, lot B9A09380V). Briefly, the Ca^{2+} concentration is assessed by determining the quantity of the chromogenic complex formed between calcium ions and o-cresolphthalein. In fact, the colour of the liquid, spectrophotometrically measured at 575 nm, is proportional to the calcium ions present in it.
In the present study, according to the producer instructions, an aliquot of immersion solution was mixed with the chromogenic reagent and the calcium assay buffer, and incubated at room temperature for 10 minutes. The absorbance was then measured at 575 nm and compared to standard curves previously calculated with known concentrations of calcium ions.

2.5.2 Biological characterisations

Scanning Electron Microscope

Cells morphology was investigated by scanning electron microscopy analyses. Moreover, β-TCP dense samples were observed by SEM before and after both dissolution and resorption tests.

The observation protocol and the apparatus have been described previously (see “Scanning Electron Microscope” in paragraph 2.4.2).

The specimen retrieved from dissolution tests (in RPMI and NaCl) were observed at low voltage (1 kV), in secondary electron mode (SE) without any further treatment (i.e. without metallisation).
The ones obtained after resorption assays were treated to fix the cells on the surface. In particular, for the fixation, the cell culture medium was removed and the samples were covered with a fixer solution *I* (0.1% glutaraldehyde, 2% paraformaldehyde, 5% sucrose, 0.2M sodium cocodylate trihydrate) for 15 min. After the fixer solution *I* was removed, a fixer solution *II* (0.3% glutaraldehyde, 3% paraformaldehyde, 0.2% sodium cocodylate trihydrate) was poured on the specimen and let stay for 15 min. This time elapsed, the samples were covered with ethanol 30% for 30 min and, then, underwent a sequence of immersions (each of 30 min) in solutions with increasing content of ethanol (namely 50-70-80-90-95-100%). Once the samples were completely dehydrated, they were super-critically dried at 35 °C and 79 bars (EM CPD 300, Leica, Germany).

After being observed at SEM, some samples were treated in order to remove the cells on their surface. For this purpose, the samples were immersed in SDS (sodium dodecyl sulfate, Carl Roth, Lot 2326.2) for 15 min in ultrasound and then rinsed with deionized water.

Fluorescence

Cells nuclei and actin were stained with sytox (Life Technologies, ref.S7020, lot 1325713) and rhodamine phalloidin (Life Technologies, ref.R415, lot 1321031) respectively. For this purpose, the cells were fixed with a FluoFix solution (0.1 M PIPES, 1 mM EGTA, 4% PEG, 3.7% paraformaldehyde, PBS, NaOH) for 15 min, washed with PBS (DPBS, Life Technologies), permeabilised (0.1% Triton X-100, 5% sucrose, PBS) for 5 min then covered with a phalloidin solution (8 µl of phalloidin each ml of PBS) for 1 h. After this time samples were washed with PBS, the nuclei were stained with a sytox solution (1 µl of sytox each ml of PBS) for 5 min, washed again and left covered with PBS until the

observation at the fluorescence microscope (wavelength ≈ 560 nm for phalloidin and ≈ 520 nm for sytox) (AxioCam ICc1, Scope A1, Zeiss, Germany).

Analysing the images obtained by fluorescence staining, several parameters were calculated such as cell density and diameter, number of multinucleated cells and nuclei. For evaluating the cell density for each sample different fluorescence images were analysed by means of the ImageJ/Fiji shareware [8] (for a total area of about 1 mm^2). Only the pictures of sytox staining were used; in this way, after a binarisation of the image, the number of nuclei was automatically counted and associated to the number of cells. Overestimation of cell density due to the presence of multinucleated cells was avoided by manually excluding double counting of cells with more than one nucleus. The size of cells was calculated with a semi-automatic procedure of ImageJ on fluorescence images (both sytox and phalloidin) on a total area of about 0.2 mm^2. In particular the cells were assimilated to circular or slightly elliptical shapes and their Feret's diameter was calculated. Finally, the amount of multinucleated cells and the number of nuclei was manually counted on a total area of about 0.6 mm^2.

Viability

Cell proliferation and viability were assessed by WST (Water Soluble Tetrazolium) assay. In this test the tetrazolium salt is reduced by specific enzymes (whose number is considered proportional to viable cells) into an insoluble formazan dye. This last one is characterised by a bright purple color and can thus be detected by a spectrophotometer. In the present case, when performing the assay, the supernatant was retrieved, samples were washed with PBS and then immersed in a "master solution" (1 mL for each sample) composed by 1% vol. of WST and 99% vol. of RPMI. After an incubation of 2 hours in this solution, the intensity of the dye was assessed with a spectrophotometer (Specord 40, Jena Analytik, Germany) set at a wavelength of 450 nm. For each material, three samples were analysed and for each sample three repetitions were performed. The value obtained for the reference after 48 h was set equal to 100% and all the other measurements were normalised as a consequence.

TRAP staining

TRAP (Tartrate Resistance Acid Phosphatase) is known to be a phenotypic marker for osteoclasts; this enzyme, in fact, is particularly produced by osteoclasts and represents, therefore, a common method to distinguish osteoclast-like cells from undifferentiated ones [9].
The TRAP-staining procedure was carried out using a commercial kit (Sigma Aldrich, ref.387A, lot SLBJ8585V). In detail, cells were fixed with a TRAP-Fixer solution (25% citrate solution, 64% acetone, 11% formaldehyde) for 15 min, the rinsed with de-ionised water and immersed in a second solution (91% water, 1% Garnet, 1% sodium nitrate, 1% naphtal, 4% acetate solution, 2% tartar solution) for 1 hour. After this time the samples were washed with water, let dry and then observe at the optical microscope (AxioCam ERc5s, PrimoVert, Zeiss, Germany).

Lactase dehydrogenase

The lactase dehydrogenase (LDH) assay is a means of measuring the number of living cells: LDH, in fact, is a protease enzyme active only in healthy cells. For quantifying the amount of active LDH, a substrate (NAD) is used: the reduction of the substrate by LDH results in a change of color that can be spectrophotometrically measured (490 nm).
In the present study, in particular, samples were rinsed with PBS, in order to remove the floating cells, therefore the remaining adherent cells were lysed (by adding 10 vol.% of LDH Assay Lysis

Solution), incubated for 45 min and centrifuged, in order to discharge the debris. The liquid was then used for the enzymatic analysis which was carried out according to the producer instruction (Sigma Aldrich, TOX7). The absorbance of the liquid was finally measure by spectrophotometric analysis at 490 nm (Specord 40, Jena Analytik, Germany).

Acid phosphatase

Acid phosphatase (SAP) is an enzyme used as marker of monocytes' activity. In the present case SAP was measured through the colorimetric assay based on the yellow end-product of the hydrolysation of pNPP substrate (p-nitrophenyl phosphate) by acid phosphatase enzyme. In practice, cells were lysed, the liquid was centrifuged and mix (2.5:1) with a solution composed of 9 mM p-NPP and 0.09 M citrate buffer (CS0740 kit, Sigma Aldrich). The liquid was then incubated for 4 hours; at this time the reaction was stopped by adding a solution of NaOH (1 N). The absorbance of the liquid was finally spectrophotometrically read at 405 nm and 690 nm (Specord 40, Jena Analytik, Germany).

References

1. Bohner, M., *Calcium orthophosphates in medicine: from ceramics to calcium phosphate cements.* Injury, 2000. 31, Supplement 4(0): p. D37-D47.
2. Peters, F. and D. Reif, *Functional Materials for Bone Regeneration from Beta-Tricalcium Phosphate.* Materialwissenschaft und Werkstofftechnik, 2004. 35(4): p. 203-207.
3. Bohner, M., *Propriétés physico-chimiques et ostéogéniques d'un biociment hydraulique à base de phosphates de calcium*, 1993, Ecole Polytechnique Fédérale de Lausanne. p. 196.
4. Bohner, M., *New hydraulic cements based on α-tricalcium phosphate–calcium sulfate dihydrate mixtures.* Biomaterials, 2004. 25(4): p. 741-749.
5. Olsson, M., *Chemical stability of grain boundaries in b-tricalcium phosphate ceramics.* Master Thesis, 2012.
6. Bisschop, J., et al., *In situ AFM study of the dissolution and recrystallization behaviour of polished and stressed calcite surfaces.* Geochimica et Cosmochimica Acta, 2006. 70: p. 1728–1738.
7. Clement, P., *Détermination des proprietés mécaniques de céramiques poreuses par essais de micronindentation instrumenée sphérique.* Ph.D. Thesis, 2013.
8. M. Abramoff, M. and P. Magalhaes, *Image processing with ImageJ.* J. Biophotonics Int., 2004(11): p. 7.
9. Detsch, R.B., A. R., *The role of osteoclasts in bone tissue engineering.* J Tissue Eng Regen Med., 2014.

CHAPTER 3: EVOLUTION OF DCPD SAMPLES IN SOLUTIONS

3.1. Characterisation of DCPD samples before immersion

The cylindrical samples (h= 12 mm, Ø = 12 mm), produced with the elaboration protocol described in paragraph 2.1.1, displayed an average porosity of 61% (apparent density of 0.9 g/cm^3). As explained in chapter 2, the specimens were analysed both at the surface and in the core. The smoothest of the two flat surfaces (casted in contact with an acetate film during the fabrication of the samples) was chosen to be the one to be systematically investigated, while for analysing the inner part (core) of the specimens, the cylinders were transversally cut with a diamond blade and the centre part of the new surface was considered as being representative from the bulk of the material. The composition at time zero, assessed by a Rietveld refinement of X-ray Diffraction patterns, was of 92% DCPD with 8% of remaining MCPM at the surface (Figure 1) (JCPDF file #01-072-0713 and #00-009-0347 respectively) and 100% DCPD in the core. Moreover, the DCPD crystals present at the surface were characterised by a certain preferential orientation; in particular the relative intensity of the peaks at 2θ=11.7° (hkl (0,2,0)) and 2θ=29.3° (hkl (1,1,-2)) were higher than expected, while this was not observed in the core. This characteristic was most probably due to the elaboration process.

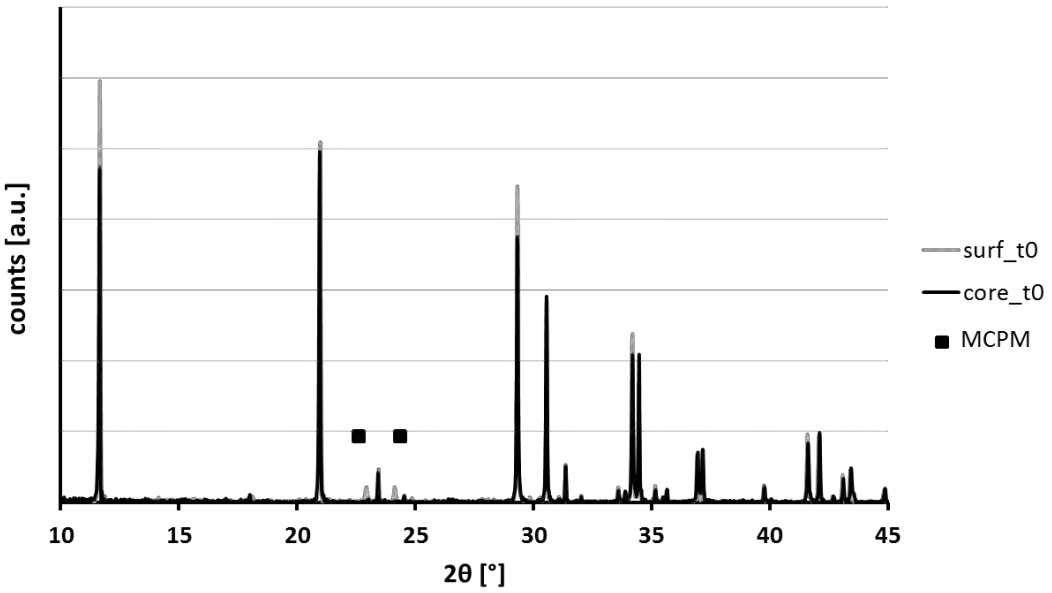

Figure 1: XRD patterns of DCPD at the surface (in grey) and in the core (in black) before immersion

On the overall, the samples macrostructure was homogeneous, as showed by micro-tomography (µ-CT) observations (Figure 2). Porosities of different size were noticed, but neither big bubbles nor defects were observed. The slightly brighter layer close to the surface of the samples visible in Figure 2-A was interpreted as a further sign of platelets alignment leading to a denser surface layer. To exclude that this brighter layer was due to edges artefacts, a cylinder was cut into half and scanned (Figure 2-C). The brighter zone (around 100-200 µm thick) was present only along the original surface and not all over the edges, confirming that its origin was linked to a real denser layer and not a digital artefact (Figure 2-C).

DCPD crystals, observed by scanning electron microscope, appeared in shape of platelets about 10 µm long, 2-4 µm wide and 300-500 nm thick (Figure 3). SEM images confirmed the hypothesis of a preferential orientation: while in the core platelets formed water lily-shaped clusters, at the surface they were quite aligned parallel to the surface (Figure 3).

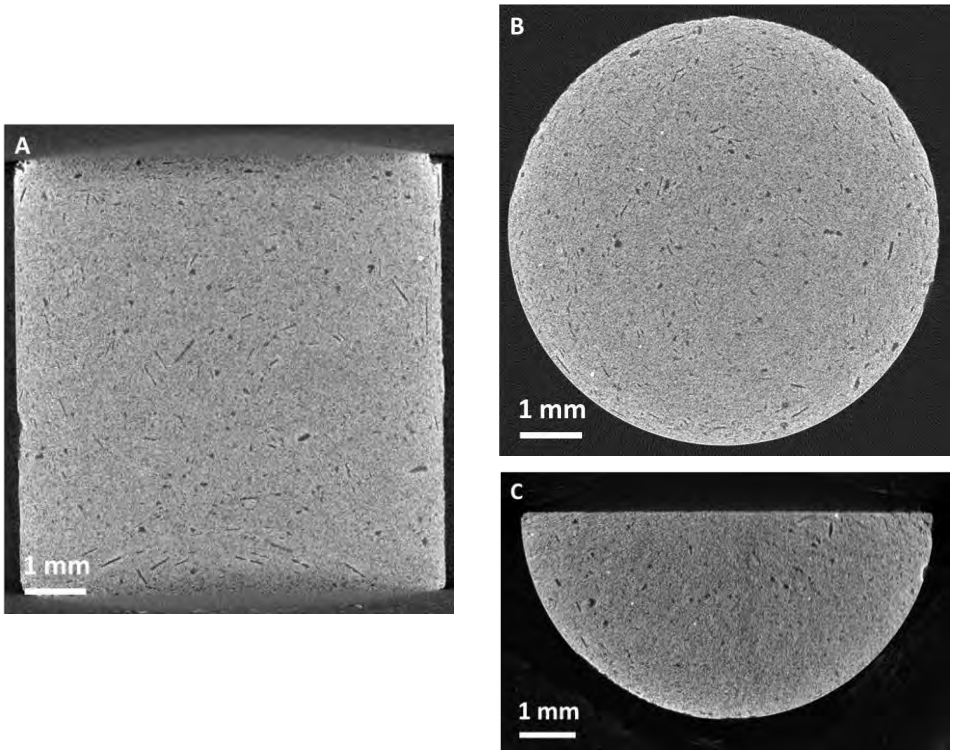

Figure 2: Frontal (A) and transverse (B) µ-CT images of an entire cylinder and transverse µ-CT image of a half-cylinder (C) of DCPD before immersion (resolution of 10 µm/voxel)

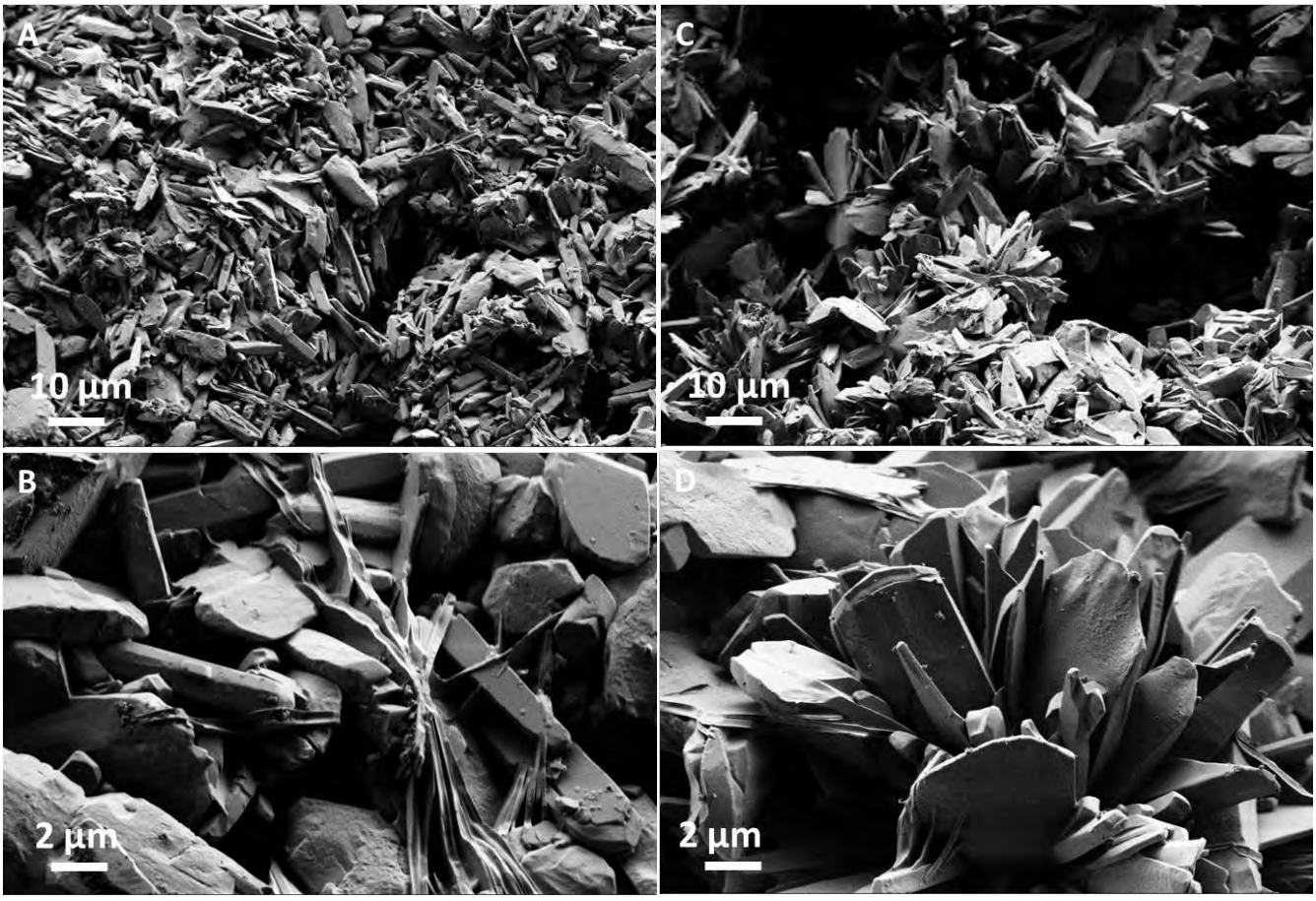

Figure 3: SEM micrographs of DCPD samples at the surface (A-B) and in the core (C-D) before immersion

The initial samples were also characterised in terms of mechanical properties by means of micro-indentation (for detailed experimental conditions cf. paragraph 2.4.3, “micro-indentation” section). All the specimens underwent 4 indentations on the smoothest surface before immersion, while 3 samples, used as reference for the inner part, were indented in the core (10 indentations each). Data summed up in Table 1 show the average values and standard deviation of hardness and elastic modulus obtained for DCPD samples at time zero. At the surface, *H* was just below 10 MPa and *E* of around 1100 MPa, while in the core *H* and *E* were around 6 MPa and 900 MPa respectively. Despite the relatively high dispersion of data (above all at the surface, Figure 4-Figure 5), both hardness and Young’s modulus resulted to be significantly lower at the core (Figure 6-Figure 7).

To conclude, the roughness (RMS), measured by digital microscopy, was equal to 1.15 ± 0.12 µm at the surface (standard deviation of multiple measures on one sample) and 1.07 ± 0.19 µm in the core. The maximum depth of penetration reached during micro-indentation tests before immersion was around 70 µm for the surface and 90 µm for the core, and was, therefore, deep enough to avoid a significant influence of the surface roughness (significant till a depth equal to 5 times the roughness, cf. chapter 2 [1]).

Table 1: Average values and standard deviation of hardness and Young’s modulus of DCPD samples at t0 (n=148 at the surface and n=30 in the core, n being the number of indentations)

	avg H_{std} [MPa]	avg E_{std} [MPa]
surface	$9.2_{3.8}$	1101_{400}
core	$6.1_{1.0}$	882_{113}

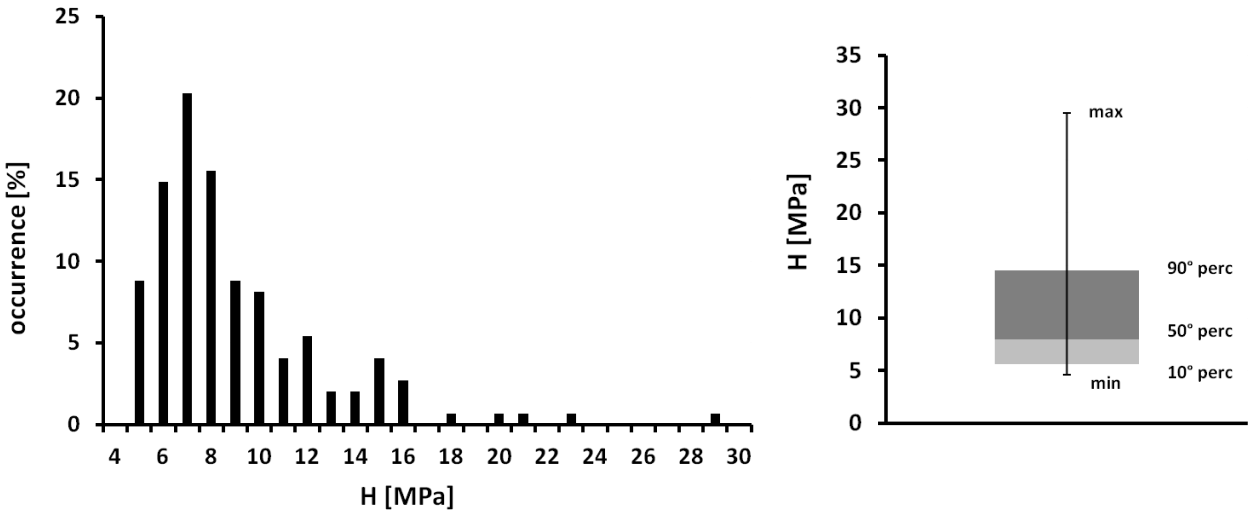

Figure 4: Distribution of hardness values obtained at the surface for all DCPD samples at t0 (n=148)

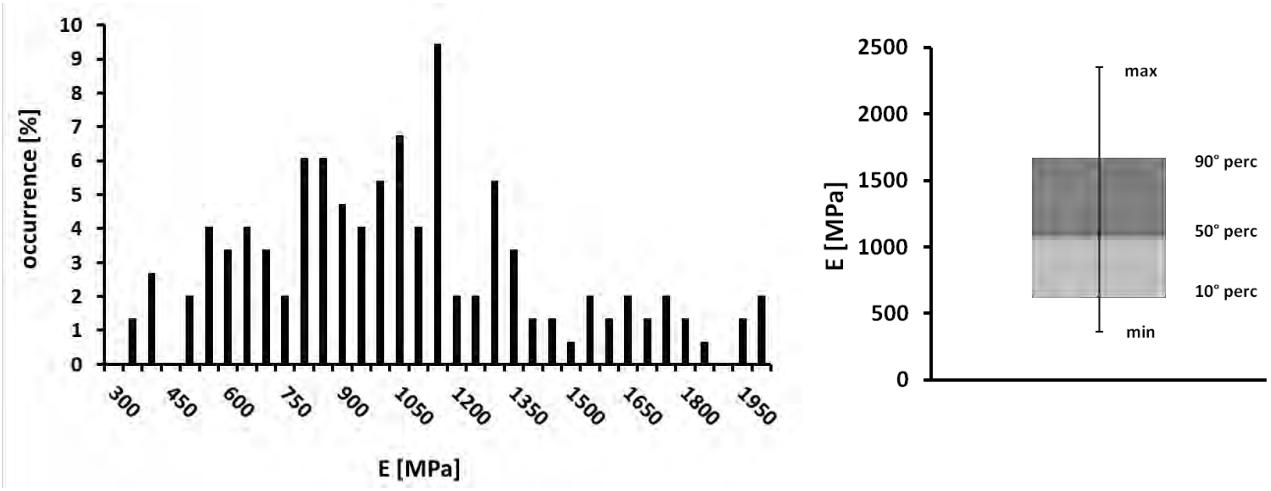

Figure 5: Distribution of values of Young's Modulus obtained at the surface for all DCPD samples at t0 (n=148)

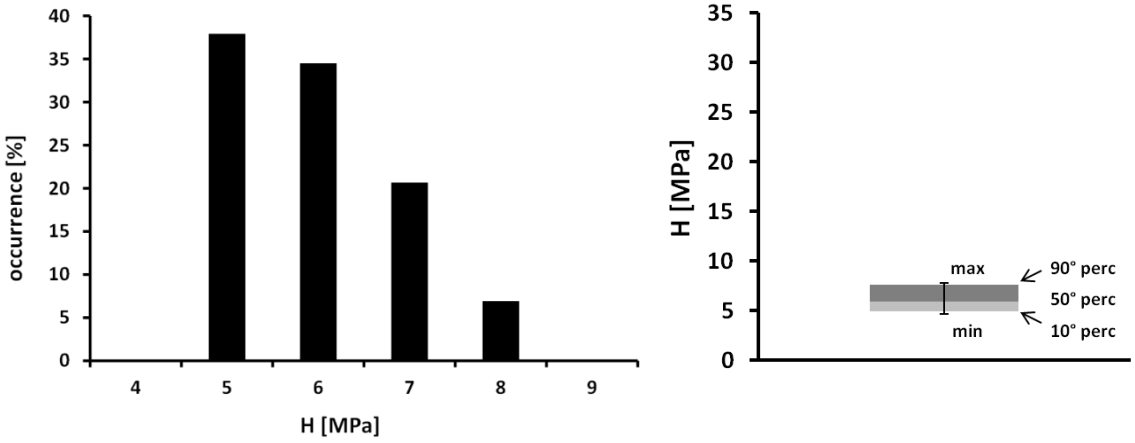

Figure 6: Distribution of hardness values obtained in the core for DCPD reference samples at t0 (n=30)

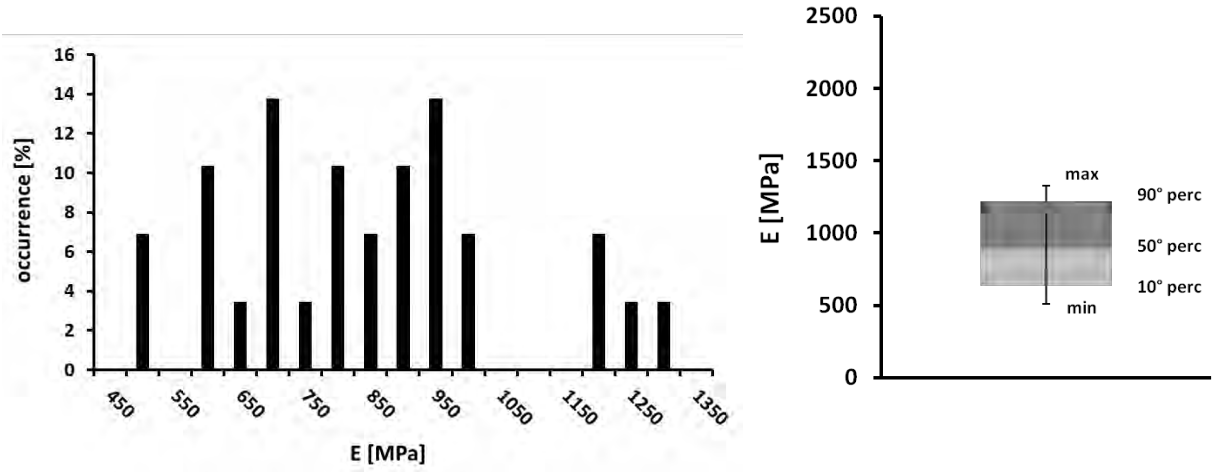

Figure 7: Distribution of values of Young's Modulus obtained in the core for DCPD reference samples at t0 (n=30)

3.2 Dissolution tests of DCPD samples: Results

As reported in Chapter 2, DCPD samples were immersed in TRIS-solution in static conditions hereafter denoted at TRISs, in dynamic conditions with periodical renewal of the solution (TRISd), and in PBS in dynamic conditions only (PBSd). Time-points were equal to: 30 minutes, 1-4-8-14 days. The results of the dissolution tests are presented in the following sections.

3.2.1 Morphological changes

Measurement of mass (±0.1 mg) and dimensions (± 0.01 mm) of the samples before and after immersion allowed the monitoring of changes in volume, weight, and apparent density all along the duration of the tests. The results are presented as variation in percentage compared to the initial value. For a certain parameter X, thus, the variation was calculated as:

$$\Delta X\,(\%) = \frac{X_{fin} - X_{in}}{X_{in}} * 100 \qquad (1)$$

where X_{in} and X_{fin} are the values of the parameter before and after immersion respectively.

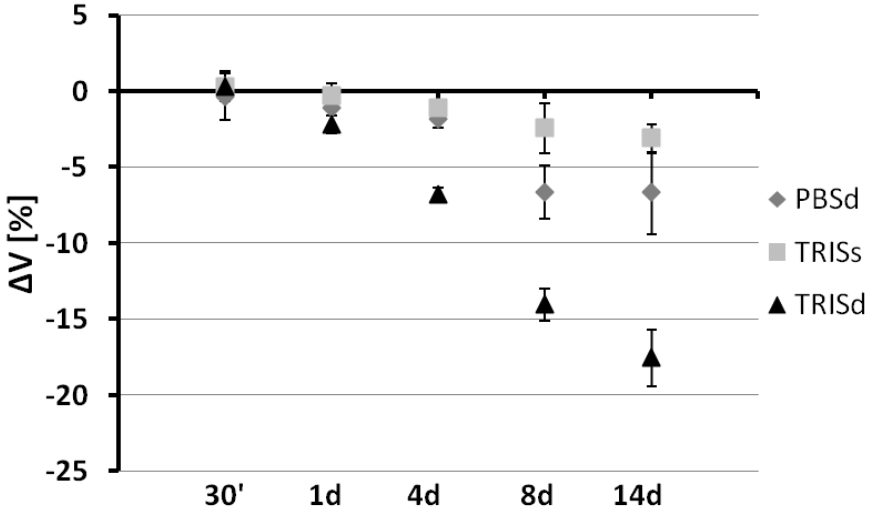

Figure 8: Percent variation of samples volume after immersion (average volume at t_0 = 1.37 ± 0.03 cm^3), n=3 (n being the number of samples per condition)

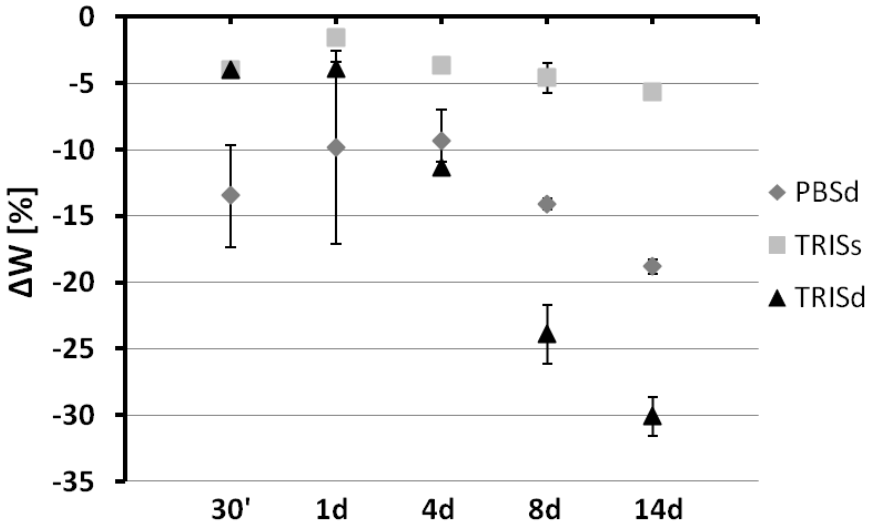

Figure 9: Percent variation of weight of samples after immersion (average weight at t_0 = 1.25 ± 0.03 g), n=3

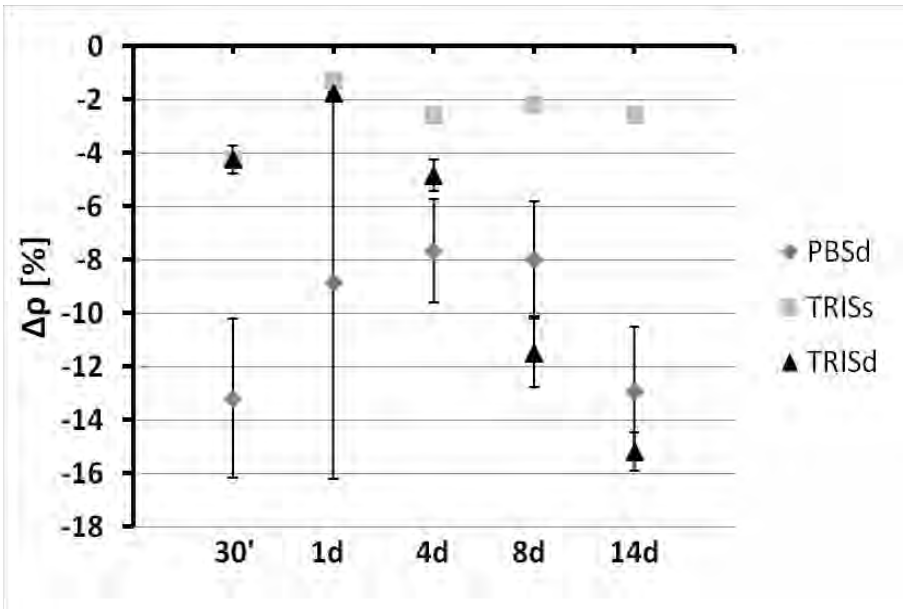

Figure 10: Percent variation of apparent density of samples after immersion (average density at t_0 = 0.91 ± 0.01 g/cm^3), n=3

The data collected showed some clear trends. As far as volume is concerned, all samples underwent a decrease of dimension along time (Figure 8). This was especially marked for samples immersed in TRISd, which reached a loss of 17.5% after 14 days. At the same time-point, the volume of samples in PBSd decreased of 6.5%, while the one of samples in TRISs exhibited the smallest changes (ΔV = -3%). The evolution of weight (Figure 9) displayed a first quick loss of mass, observed after 30 minutes of immersion, followed by an increased at day 1 (also at day 4 in PBSd) and then a progressive decrease till the end of the test. The maximum change was observed after 14 days, when samples in TRISs, PBSd, and TRISd displayed a loss of weight of 5.5%, 19%, and 30% respectively. It is worthy to notice that samples in PBSd underwent the largest changes till day 1 and, then, they were surpassed by those in TRISd. Finally, the evolution of apparent density was quite similar to that of weight (Figure

10): samples in TRISs displayed the smallest changes, while samples in PBSd evolved first more (till day 4) and then less than those in TRISd.

Figure 11 displays the appearance of the samples after different immersion times in PBSd. Starting from day 8, the surface appeared clearly rougher than at the beginning. This appears even clearer in the picture of the section of a sample immersed for 14 days in PBSd (the dots in the inner part of the section are traces left by the indentation tests), where a significant difference is noticed between the external ring of the sample and its inner part. The external layer was quite fragile, making it difficult to handle and analyse the specimens; for this reason, longer immersion times were avoided.
In the case of samples immersed in TRISs (Figure 12), differently from what observed after immersion in PBSd, no superficial layer was observed in the core around the section of the specimen.
The macroscopic aspect of the samples immersed in TRISd, finally, is reported in Figure 13. The section of a specimen immersed for 14 days displays quite well the presence of an outer layer, which differs from the inner part of the sample. This is consistent with the modification of the aspect of the external surface, which is clearly visible from day 8.

Figure 11: Pictures of samples after immersion in PBSd (dots in the inner part of the section are traces left by the indentation tests)

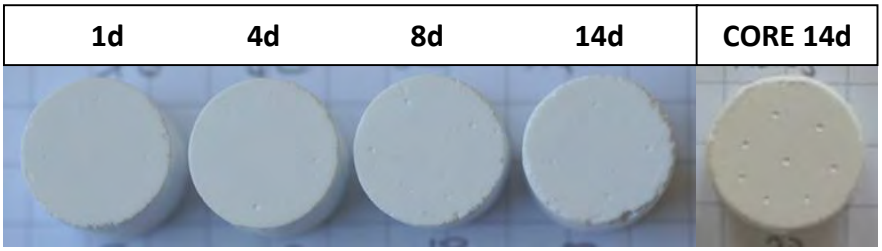

Figure 12: Pictures of samples after immersion in TRISs (dots in the inner part of the section are traces left by the indentation tests)

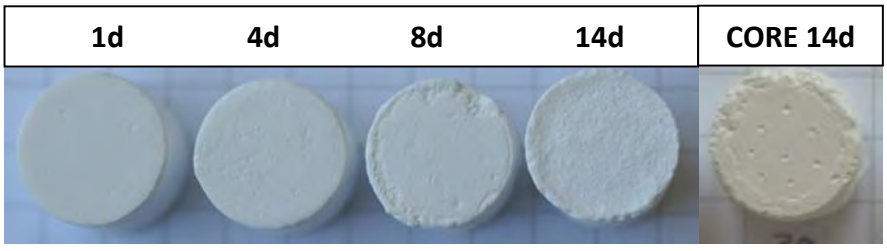

Figure 13: Pictures of samples after immersion in TRISd (dots in the inner part of the section are traces left by the indentation tests)

3.2.2 Chemical changes

The evolution of crystalline phases in the samples was followed by XRD. The results are divided into analyses of the surface and analyses of the core; each group, moreover, includes the three different conditions of tests (PBSd, TRISs, and TRISd).

3.2.2.1 X-ray diffraction: evolution of the sample surface

PBSd

After 30 minutes of immersion in PBSd, diffraction patterns displayed a complete disappearance of MCPM peaks (at 2θ=22.9° and 24.1°) and the appearance of DCPA (peaks at 2θ=26.4°, 26.6°, 30.2°) as can be seen in Figure 14. Rietveld refinements performed on this XRD pattern permitted to show that the sample surface was composed of 35 wt.% DCPA (the remaining phase being DCPD). At day 1, however, the DCPA disappeared too, leaving place to pure DCPD. No further changes were noticed at day 4, while a strong diminution of DCPD, coupled with the appearance of OCP (92 wt.%), was observed at day 8. The presence of OCP was testified by peaks at 25.9°, 31.3-31.8° and, above all, by the characteristic peak at 2θ=4.7° (Figure 15). At the end of the longest time-point (14d), finally, DCPD had completely disappeared from the XRD pattern, while OCP was the preponderant phase (95 wt.%) in conjunction with a small amount of apatite (<5 wt.%). The percentage of each phase as calculated by Rietveld refinements is listed in Table 2, while the whole XRD patterns collected can be consulted in Annex (Figure A.b.1 and A.b.2).

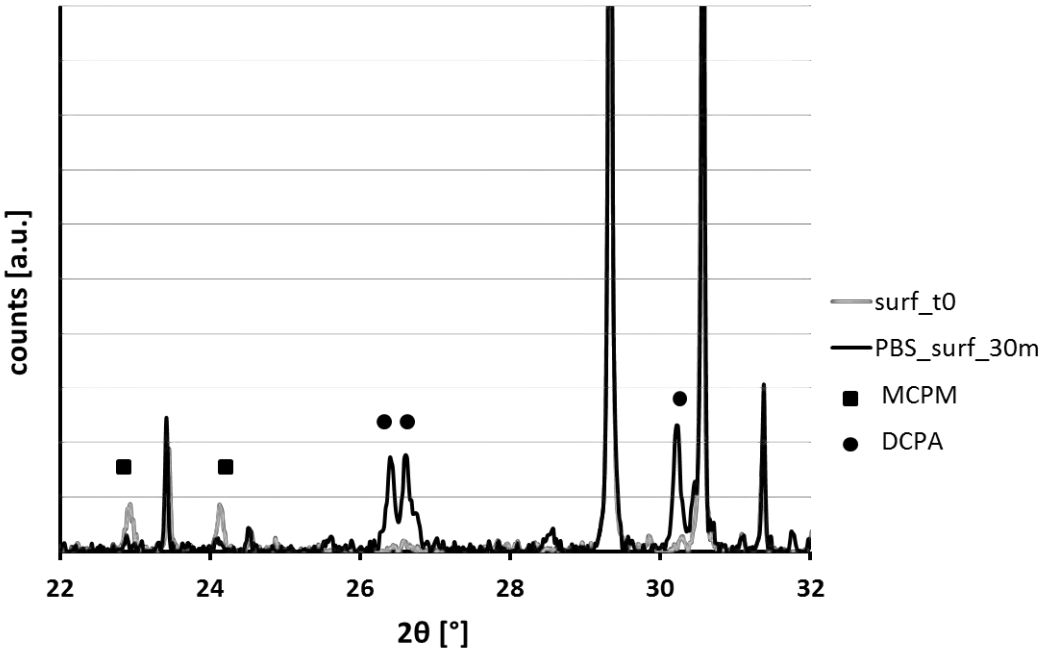

Figure 14: XRD patterns of the surface of DCPD samples at time 0 and after 30 minutes in PBSd. Peaks, which are not marked, correspond to the DCPD phase. For clarity purposes the y-axes is showed till half the height of the highest peak

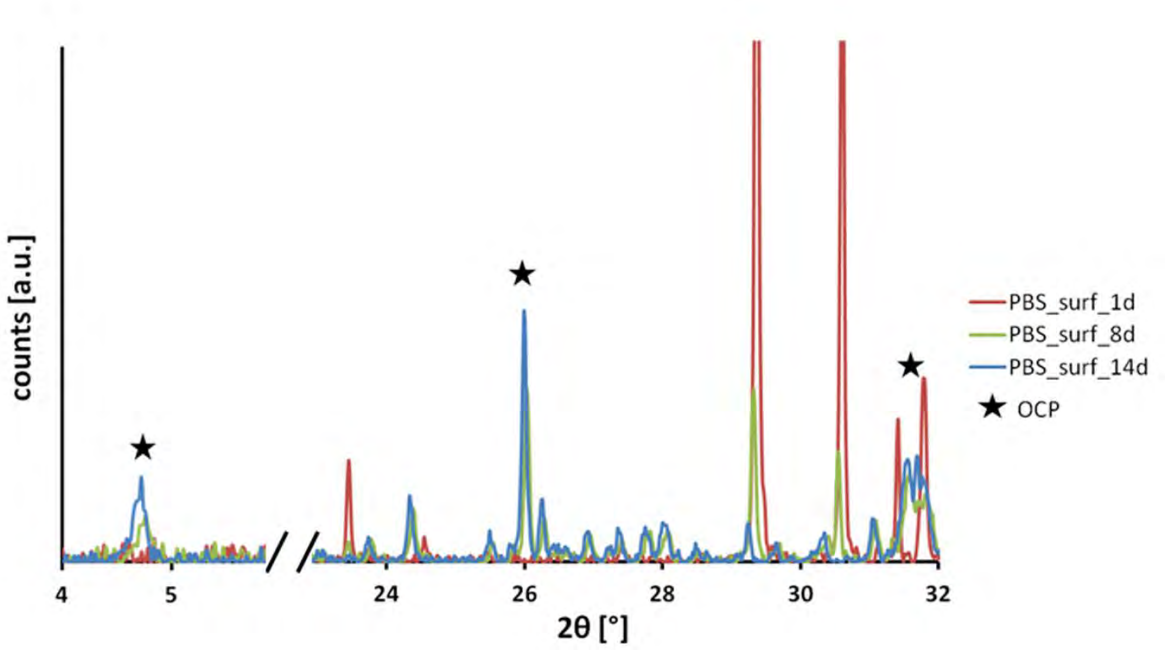

Figure 15: XRD patterns of surface of DCPD samples after 1-8-14 days in PBSd. Peaks of apatite (identified by Rietveld refinements are not marked on the XRD pattern, because they overlap OCP ones). For clarity purposes the y-axes is showed till half the height of the highest peak and non-indexed peaks correspond to DCPD phase.

Table 2: Percentage of phases (in wt.%) detected at the surface of DCPD samples immersed in PBSd (as calculated by Rietveld refinements, uncertainty = ± 2%)

phase	t0	30m	1d	4d	8d	14d
MCPM	8	-	-	-	-	-
DCPA	-	35	3	-	-	-
DCPD	92	65	97	100	8	-
OCP	-	-	-	-	92	95
apatite	-	-	-	-	-	5

TRISs

Samples immersed in TRISs displayed only few changes along time. After 30 minutes of immersion, MCPM disappeared, while a small quantity of DCPA was detected (< 9 wt.%). This latter phase almost completely disappeared by day 1; after that time only DCPD was detected. The characteristic peaks observed for each phase were the same as already listed in the previous paragraph. The most significant time-points and the percentage of each phase are presented in Figure 16 and Table 3 respectively, while the complete evolution along time is reported in Annex (Figure A.b.3).

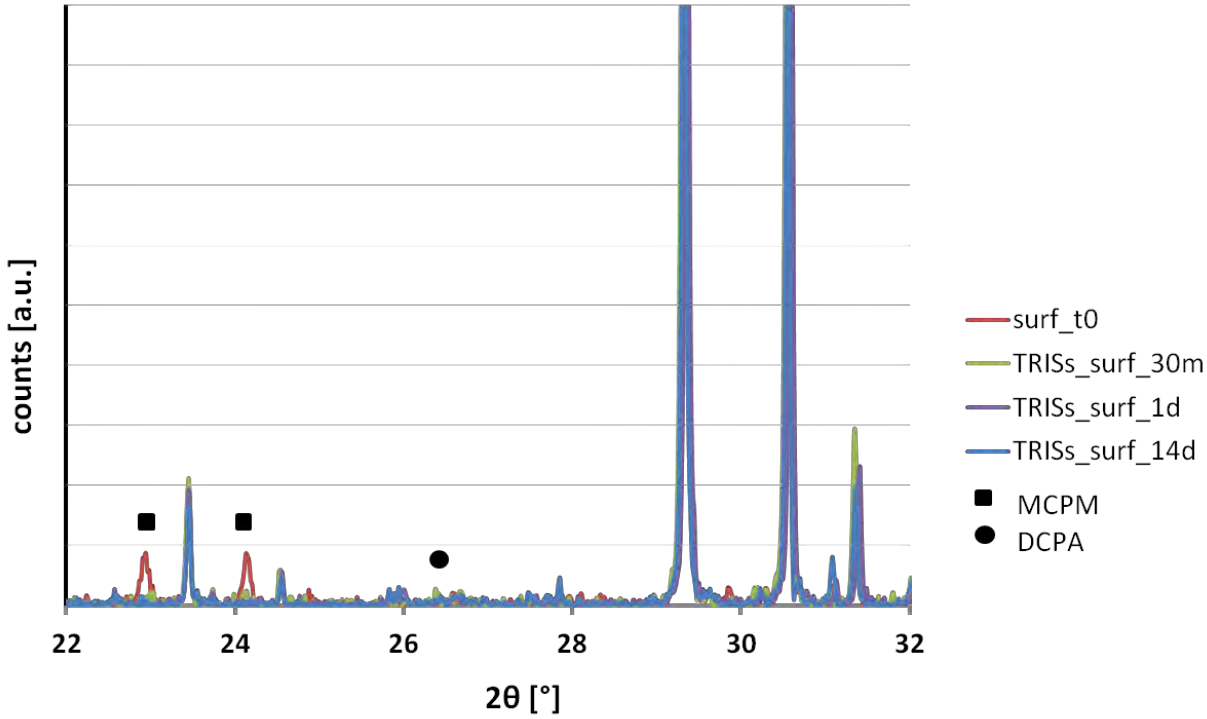

Figure 16: XRD patterns of surface of DCPD samples at time 0, after 30minutes, 1 day, and 14 days in TRISs. For clarity purposes the y-axes is showed till half the height of the highest peak and non-indexed peaks correspond to DCPD phase.

Table 3: Percentage of phases (in wt.%) detected at the surface of DCPD samples immersed in TRISs (as calculated by Rietveld refinements, uncertainty = ± 2%)

phase	t0	30m	1d	4d	8d	14d
MCPM	8	-	-	-	-	-
DCPA	-	9	-	-	-	-
DCPD	92	91	100	100	100	99
OCP	-	-	-	-	-	1
apatite	-	-	-	-	-	-

TRISd

The dissolution and precipitation processes that took place on samples immersed in TRISd were similar to those observed in PBSd, the main difference being that in TRISd the appearance of OCP was delayed compared to PBS. In particular, after 30 minutes MCPM had disappeared leaving place to around 9 wt.% of DCPA (less than the 35 wt.% observed in PBSd for the same time-point). DCPA peaks were not observed anymore at day one (as in PBSd) and between day 1 and 4, thus, only DCPD was detected. At day 8, an amount of around 18 wt.% of apatite was detected by Rietveld refinements. Finally, after 14 days, almost all DCPD had disappeared, while OCP and apatite represented the main phases (accounting for 64 wt.% and 36 wt.% respectively). Figure 17 reports only the most significant time-points (0-30m-1d-14d), percentage of phases are summarised in Table 4, while all the XRD patterns along time are represented in Annex (Figure A.b.4).

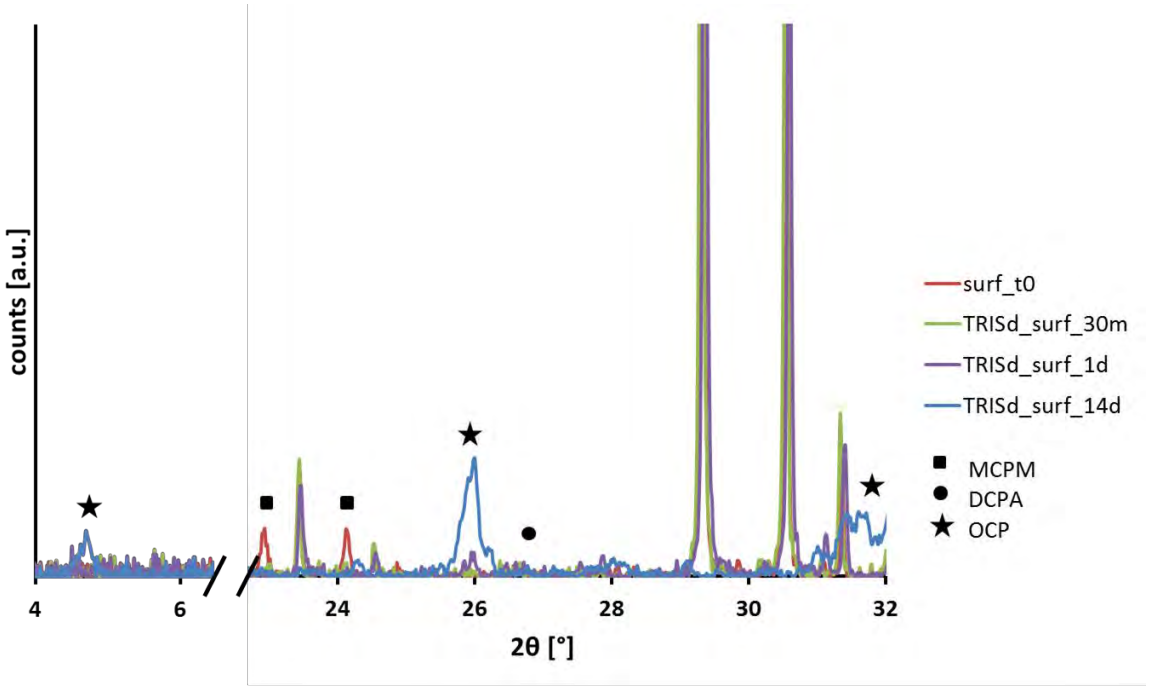

Figure 17: XRD patterns of surface of DCPD samples at time 0, after 30minutes, 1 day, and 14 days in TRISd. Peaks of apatite (identified by Rietveld refinments are not marked on the XRD pattern, because are overlapped to OCP ones. For clarity purposes the y-axes is showed till half the height of the highest peak and non-indexed peaks correspond to DCPD phase.

Table 4: Percentage of phases (in wt.%) detected at the surface of DCPD samples immersed in TRISd (as calculated by Rietveld refinements, uncertainty = ± 2%)

phase	t0	30m	1d	4d	8d	14d
MCPM	8	-	-	-	-	-
DCPA	-	9	-	-	-	-
DCPD	92	91	100	100	82	-
OCP	-	-	-	-	-	64
apatite	-	-	-	-	18	36

3.2.2.2 X-ray diffraction: evolution of the sample core

After having been immersed for different times in the solutions, cylindrical were cut in halves and X-ray Diffraction measurements were also performed on the inner surface, which is denoted as “core” throughout this manuscript.

As already said, the core of initial samples was composed of pure DCPD, differently from the surface, where traces of MCPM were found.

PBSd

Although the initial composition was slightly different between surface and core of samples, an important precipitation of DCPA (73 wt.%) was also observed in the core after only 30 minutes of immersion in PBSd. However, this phase did not dissolve then as quickly as it did at the surface, and was present till day 4 (55 wt.%). At this time point, moreover, also some OCP appeared (5 wt.%). The amount of this last phase increased between 4 and 8 days and then remained constant till the end of the test (9 wt.%). All the changes just described can be observed in Figure 18, Table 5 and in Annex (Figure A.b.5).

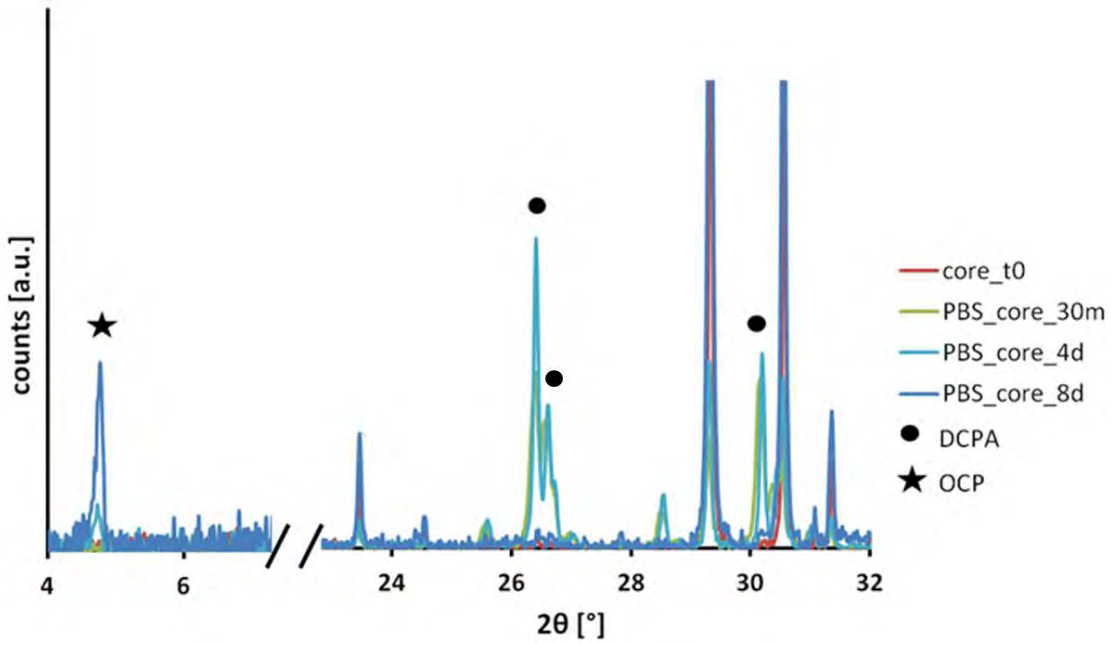

Figure 18: XRD patterns of DCPD samples in the core at time 0, after 30minutes, 4 and 8 days in PBSd. For clarity purposes the y-axes is showed till half the height of the highest peak and non-indexed peaks correspond to DCPD phase.

Table 5: Percentage of phases detected in the core of DCPD samples immersed in PBSd (as calculated by Rietveld refinements, uncertainty = ± 2%)

phase	t0	30m	1d	4d	8d	14d
MCPM	-	-	-	-	-	-
DCPA	-	74	81	55	-	-
DCPD	100	26	19	40	91	92
OCP	-	-	-	5	9	8
apatite	-	-	-	-	-	-

TRISs

Samples immersed in TRIS in static conditions displayed a quite simple evolution in the core. After the first minutes of immersion, in fact, a relevant quantity of DCPA (around 48 wt.%) appeared; after another day it diminished, reaching a value of around 10 wt.%, then it stayed stable till day 14, when only DCPD was detected. The percentages of each phase as a function of time are listed in Table 6, the most significant time-points are reported in Figure 19, while further details can be found in Annex (Figure A.b.6).

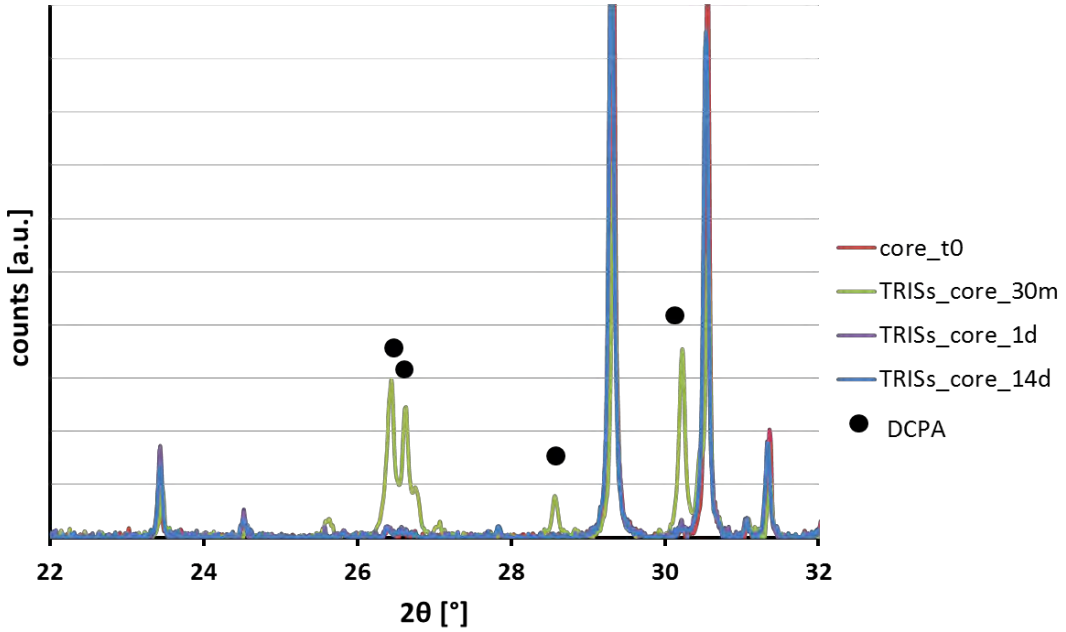

Figure 19: XRD patterns of DCPD samples in the core at time 0, after 30minutes, 1 and 14 days in TRISs. For clarity purposes the y-axes is showed till half the height of the highest peak and non-indexed peaks correspond to DCPD phase.

Table 6: Percentage of phases detected in the core of DCPD samples immersed in TRISs (as calculated by Rietveld refinements, uncertainty = ± 2%)

phase	t0	30m	1d	4d	8d	14d
MCPM	-	-	-	-	-	-
DCPA	-	49	10	8	11	-
DCPD	100	51	90	92	89	100
OCP	-	-	-	-	-	-
apatite	-	-	-	-	-	-

TRISd

Samples in TRIS in dynamic conditions underwent, in the core, a first appearance of DCPA after 30 minutes of immersion; this phase lasted, in a smaller amount, till day 1 and it afterwards disappeared leaving space to pure DCPD (day 4). After 8 days, beside DCPD, around 17 wt.% of OCP was detected. The percentage of this phase, finally, increased till the end of the test (14d), when it reached an amount of almost 75 wt.%. Figure 20 reports the XRD patterns obtained in the core after 30 minutes, 4 days, and 8 days of immersion in TRISd; the complete data are showed in Annex (Figures A.b.7 and A.b.8). Moreover, Table 7 reports the percentages of phases calculated by Rietveld refinements.

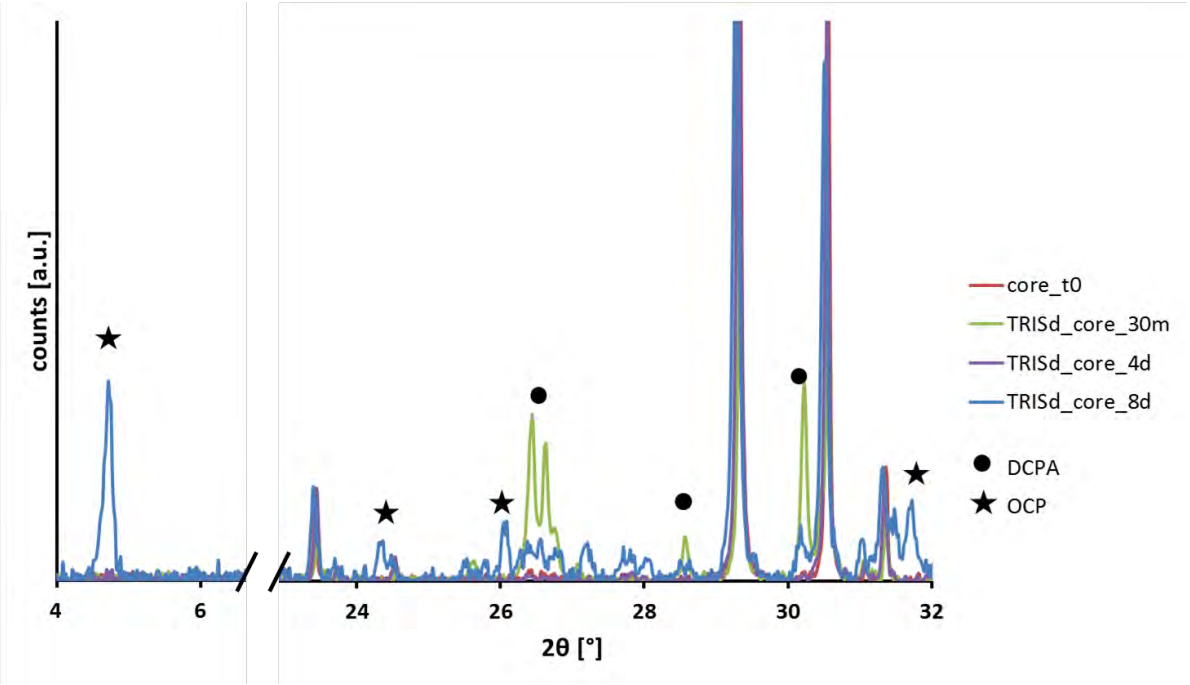

Figure 20: XRD patterns of DCPD samples in the core at time 0, after 30minutes, 4 and 8 days in TRISd; For clarity purposes the y-axes is showed till half the height of the highest peak and non-indexed peaks correspond to DCPD phase.

Table 7: Percentage of phases detected in the core of DCPD samples immersed in TRISs (as calculated by Rietveld refinements, uncertainty = ± 2%)

phase	t0	30m	1d	4d	8d	14d
MCPM	-	-	-	-	-	-
DCPA	-	49	9	-	-	-
DCPD	100	51	91	100	83	25
OCP	-	-	-	-	17	75
apatite	-	-	-	-	-	-

3.2.2.3 X-ray diffraction analyses: summary

The following table (Table 8) and figure (Figure 21) sum up all the data concerning XRD analyses of DCPD samples. The table lists the phases present at the surface and in the core after immersion in different solutions and for different time-points. Phases written in a smaller font are those found in smaller amount (<10 wt.%). The quantitative evaluation of the different phases is represented, instead, in Figure 21, where the percentages obtained by Rietveld refinements are displayed as a function of time.

Table 8: Summary of phases detected on DCPD samples (surface and core) after immersion

time	SURFACE			CORE		
	PBSd	**TRISs**	**TRISd**	**PBSd**	**TRISs**	**TRISd**
0	DCPD + MCPM	DCPD + MCPM	DCPD + MCPM	DCPD	DCPD	DCPD
30m	DCPD + DCPA	DCPD + DCPA	DCPD + DCPA	DCPD + DCPA	DCPD + DCPA	DCPD + DCPA
1d	DCPD	DCPD	DCPD	DCPD + DCPA	DCPD + DCPA	DCPD + DCPA
4d	DCPD	DCPD	DCPD	DCPD + DCPA + OCP	DCPD + DCPA	DCPD
8d	OCP + DCPD	DCPD	DCPD + apatite	DCPD + OCP	DCPD + DCPA	DCPD + OCP
14d	OCP + apatite	DCPD	OCP + apatite	DCPD + OCP	DCPD	DCPD + OCP

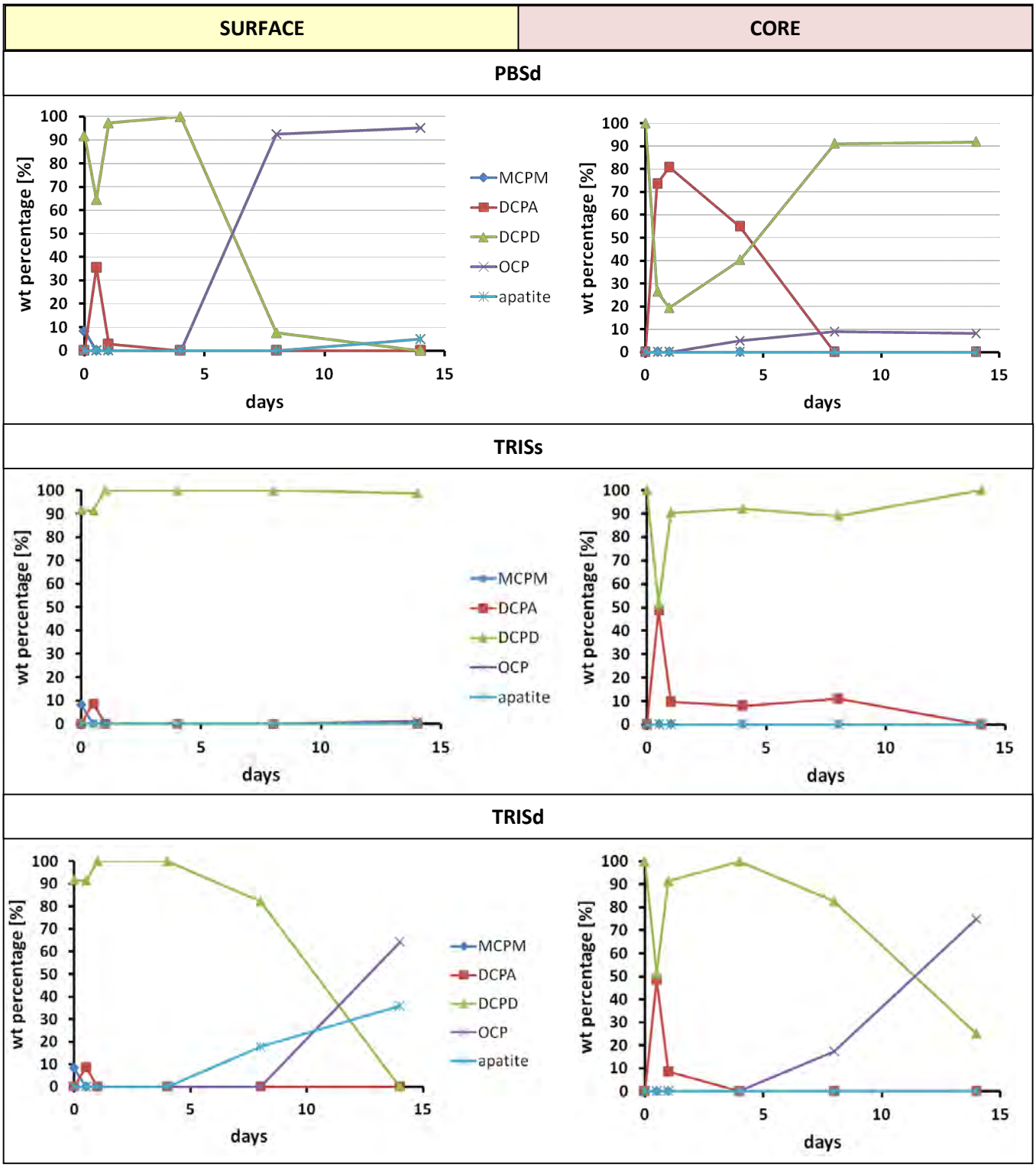

Figure 21: Evolution of weight percentage of crystalline phases obtained by Rietveld refinements versus immersion time at the surface (left) and in the core (right) of DCPD samples

3.2.2.4 pH evolution

All along their immersion, the pH of the solutions where samples were dipped was monitored. In parallel, the pH of reference solutions was also registered and plotted in dotted lines in Figure 19. For static conditions, the reference solution corresponded to the TRIS solution, which was kept at the same temperature in the same apparatus (orbital shaking), but without samples dipped inside. For dynamic conditions, the pH of the reference solutions was measured in the media which were used for the daily refresh. All pH measurements (both for reference solutions and for solutions containing samples) were performed prior to the renewal of the media.

The following graph reports the average values calculated from the measurement done on all the samples. The first figure (Figure 22) shows the evolution of pH along all the duration of the test, while the second one (Figure 23) is an enlargement of the initial part of the Figure 22 and represents only the values of the pH during the initial 30 minutes of immersion. Given that in the dynamic set-up, the refresh of the medium was repeated every 24 hours, TRISs and TRISd conditions were considered as equivalent for the time-point of 30 minutes. Therefore 30-minute samples were only immersed in PBSd and TRISs (see Figure 23 and Chapter 2, section 2.2 for more detail).

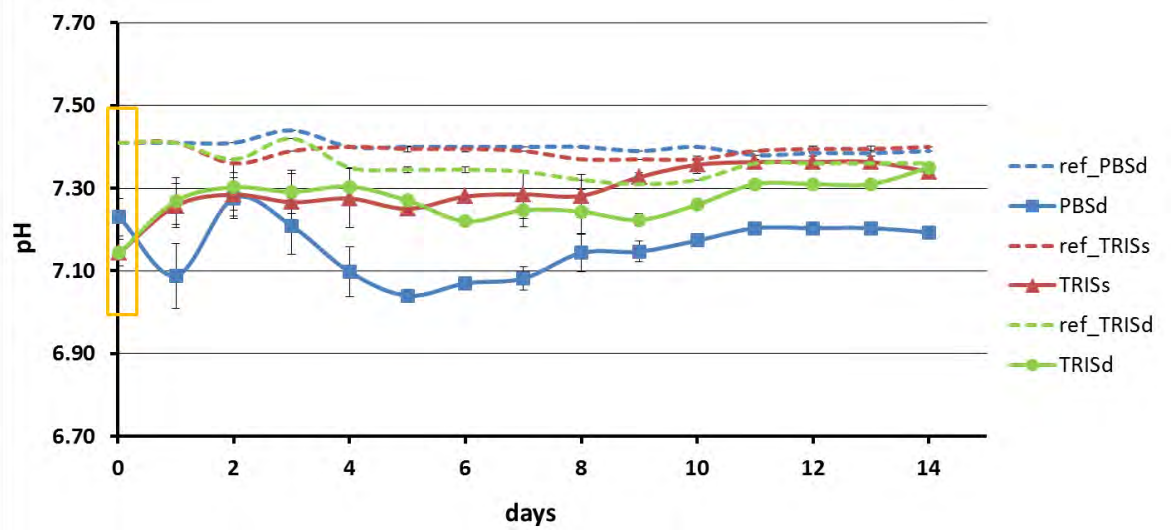

Figure 22: Evolution of pH of the immersion solutions all along the 14 days

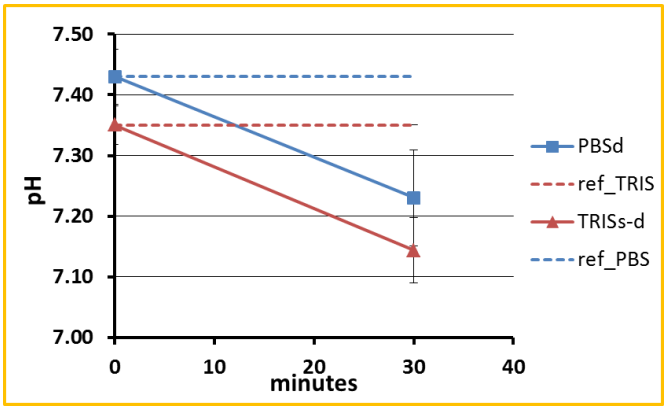

Figure 23: Evolution of pH of the solutions, first 30 minutes of immersion

The pH of the reference solutions was set around 7.4, which is the value of body fluids in physiological conditions. Comparing the values measured in the solutions containing the samples and those of the reference solutions, some differences were clearly visible; in particular, the pH of the solutions in presence of the samples was always lower than the one of the references.

In PBSd, a quick drop of pH was observed during the first hours of immersion (till day 1). After an increase at day 2, the pH decreased again, then, starting from day 5, it increased slowly. Finally a sort of equilibrium was reached around day 10.
As far as TRISs is concerned, after a first drop in the first 30 minutes, the pH value increased till day 1. After this period the pH stayed almost stable, except for a slight further increase around day 9.
Finally, TRISd displayed values quite close to those of TRISs till day 4. Starting from the fourth day, however, the pH value of TRISd slightly decreased. Finally, from day 9, the pH further increased.

3.2.3 Microstructural changes

Changes in the morphology of the samples were observed both at a macroscopic level, by means of X-ray tomography, and at a microscopic scale, by SEM analyses. The present paragraph collects the results of those observations.

3.2.3.1 Micro-computed tomography

As showed at the beginning of this chapter (paragraph 3.1.2), DCPD samples before immersion were characterised by a quite homogeneous structure, without big cracks and bubbles (Figure 2). The only inhomogeneity was the slightly denser layer, visible at the surface.

Figure 24 reports the evolution of the microstructure of DCPD samples after immersion in PBSd. Watching from left to right the image of the frontal sections and clockwise the image of the transversal section, it is possible to notice the microstructural changes that took place between day 1 and day 14. Given that no significant changes were observed after 30 minutes of immersion, the corresponding images are not reported here, but they can be consulted in Annex (Figures A.b.9 and A.b.10). No visible changes were detected for samples immersed in PBSd till day 4, when some brighter precipitates were noticed close to the surface in µ-CT images. The layer of precipitates became thicker and thicker along time (700 µm at 8d and 800 µm at 14d, according to measurements done using the public domain ImageJ/Fiji shareware). It is noteworthy to observe that the brighter precipitates seemed not to show much adhesion between one another, and that the surrounding layer seemed to be more porous than the original DCPD microstructure. At the last time-point, the superficial layer was still characterised by a poor inner cohesion and a low adhesion to the core of the sample. Even after 14 days, no clear changes could be detected in the bulk of the samples: all the observed changes took place on the surface of the specimens, while the inner microstructure remained comparable to the initial one.

Since it was evidenced from Figure 22, that a thin layer of precipitates was already present after 4 days of immersion in PBSd, a scan of the surface after 4 days of immersion was performed with higher resolution (2 µm per voxel) to get more insight in this layer and in its location (Figure 25). In parallel, a sample was embedded in an epoxy resin, sliced and observed by SEM (Figure 26). The images show that the layer of precipitates was around 350 µm thick and did not lay directly on the surface, but some hundreds of microns (≈300 µm) below it (Figure 25-B). Moreover the precipitates, which appear whiter than the bulk of the sample in µ-CT scans, were generally located in bigger porosities (Figure 25-C, Figure 26). This was consistent with the porous layer surrounding the precipitates, as already observed at a lower resolution after 8 and 14 days (Figure 24).

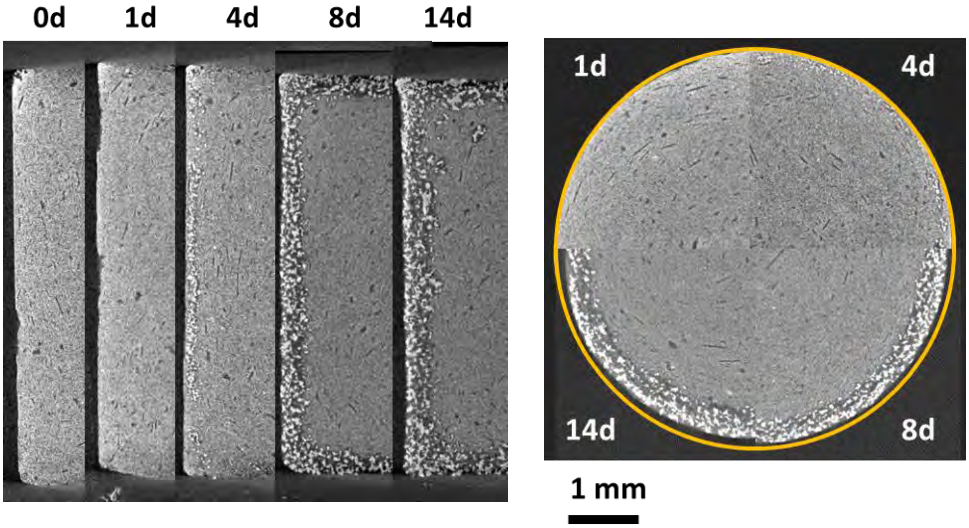

Figure 24: Frontal (left) and transverse (right) µ-CT images of DCPD samples after different times of immersion in PBSd (resolution of 10 µm/voxel). The circle in yellow (transverse section) represents the circumference of the sample at t0

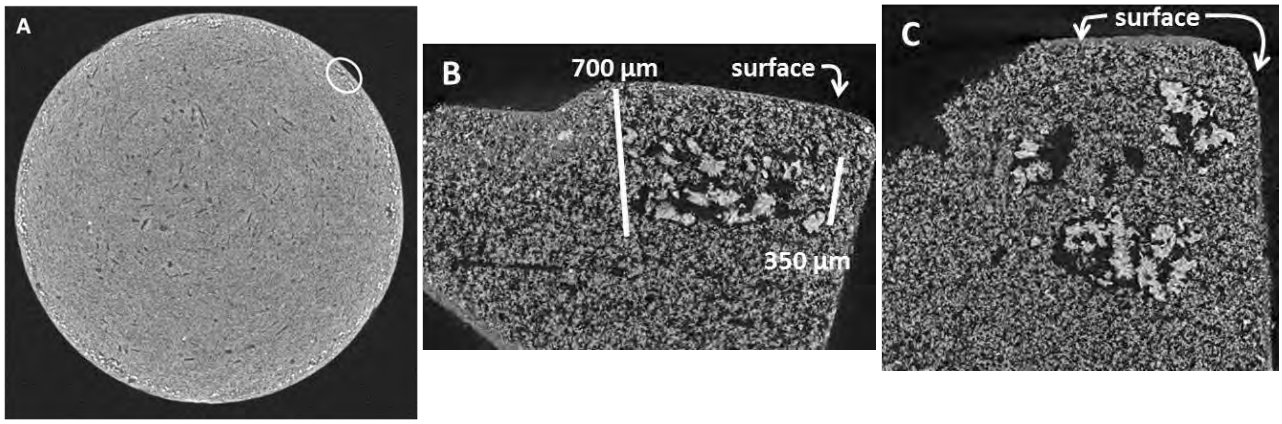

Figure 25: transverse µ-CT image of DCPD after 4 days in PBSd (A) (resolution of 10 µml/voxel). Higher resolution images of the circled area in A (transverse B, frontal C), resolution of 2 µm/voxel

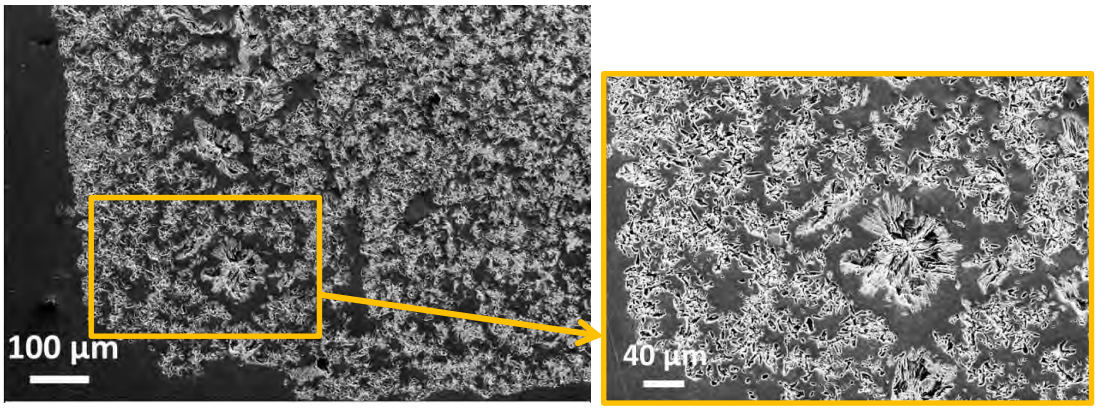

Figure 26: Micrographs of a DCPD sample immersed for 4 days in PBSd and embedded in an epoxy resin before SEM observation

Samples immersed in TRISs did not show relevant changes in their morphology all along the duration of the test (Figure 27). Also, the changes in diameter were too small (-1%) to be represented on the µ-CT image, as done for the samples, which were immersed in PBSd (Figure 24).

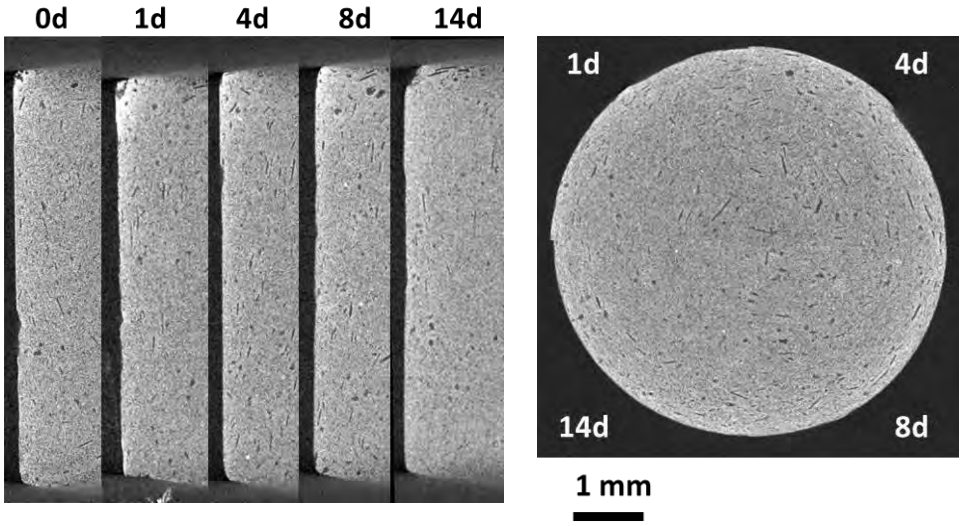

Figure 27: Frontal (left) and transverse (right) µ-CT images of DCPD after different times of immersion in TRISs (resolution of 10 µm/voxel)

When immersed in TRISd (Figure 28), DCPD samples did not undergo visible morphological changes till day 8. At this time-point, a denser layer close to the surface and some globular precipitates below it were noticed. For longer times of immersion (14d), the thickness of the layer of precipitates increased, reaching a value of 900-1100 µm. All along the length of the immersion no visible changes were observed in the inner part of the specimens.

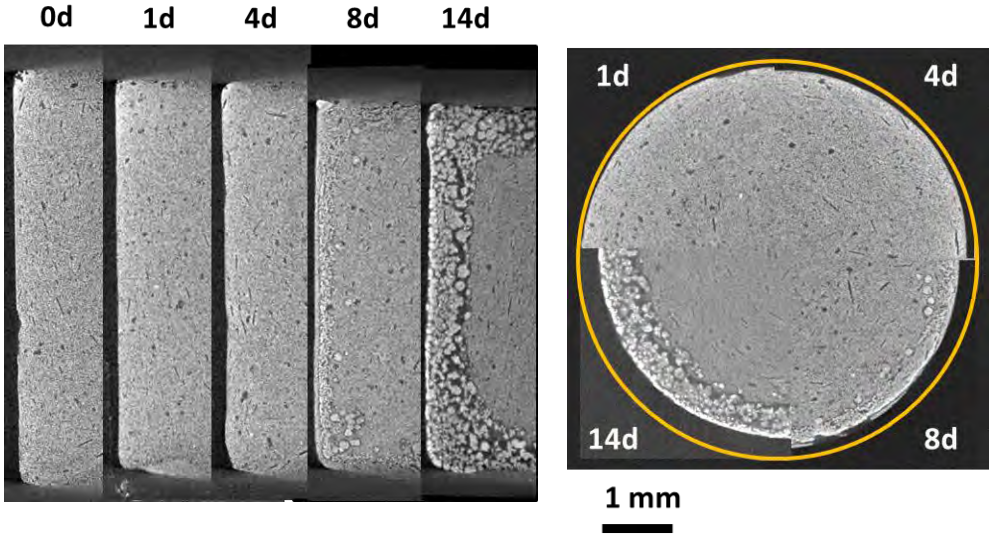

Figure 28: Frontal (left) and transverse (right) µ-CT images of DCPD after different times of immersion in TRISd (resolution of 10 µm/voxel). The circle in yellow (transverse section) represents the circumference of the sample at t0

3.2.3.2 Scanning Electron Microscopy

After immersion both the surface and the core of the specimens were observed by means of a Scanning Electron Microscope. The obtained images are presented in the following pages; the first section concerns the surface, while the second one the core.

Evolution of the samples surface

Samples surfaces were observed by SEM after different immersion times. No changes were observed after 30 minutes; images referring to this time-point, thus, are not reported here, but can be found in Annex (Figure A.b.11).

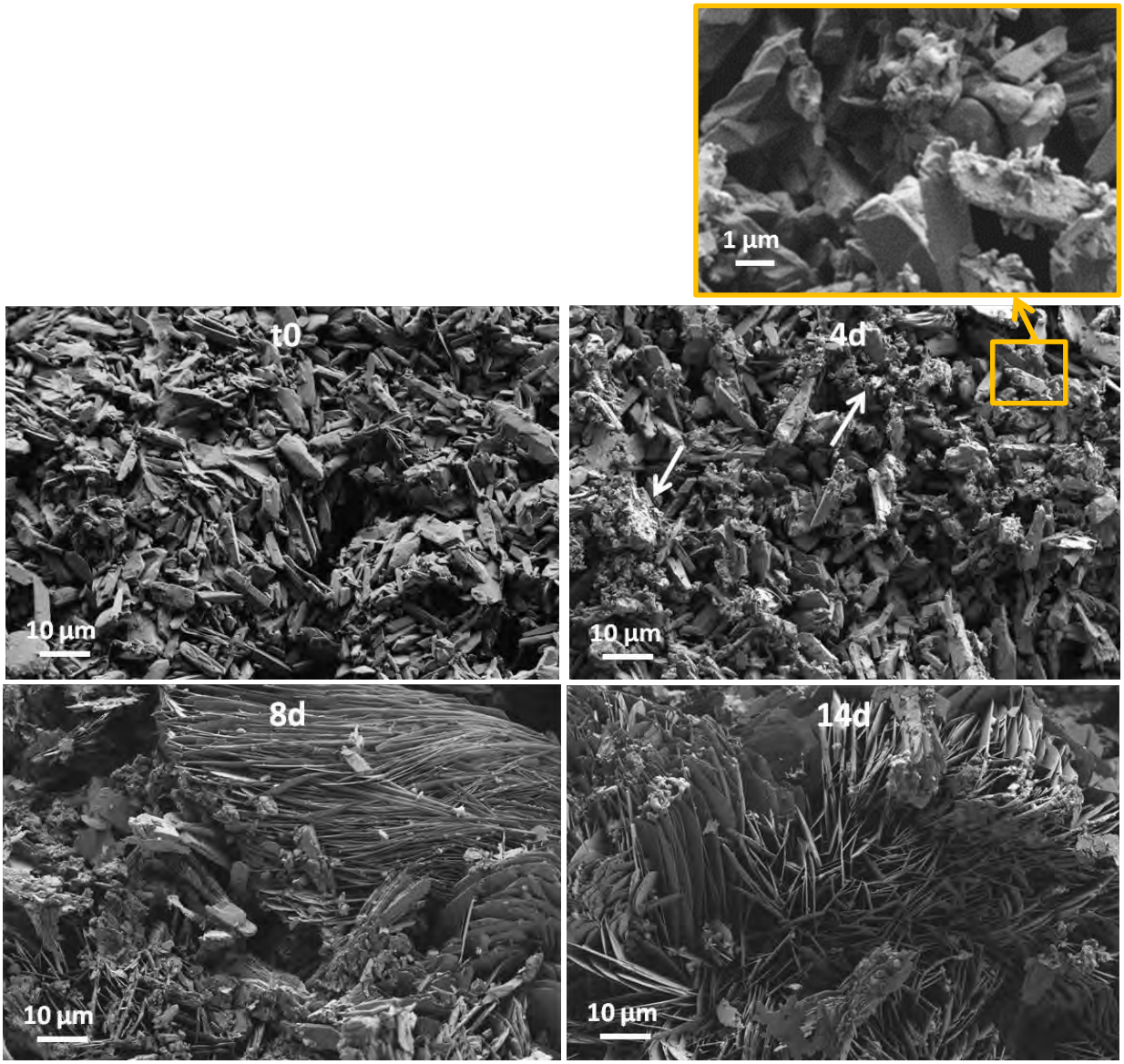

Figure 29: SEM micrographs of surfaces of DCPD samples after immersion in PBSd for different times

After 4 days of immersion in PBSd, some small precipitates were present on DCPD platelets at the surface of the samples (cf. arrows and enlargement in Figure 29); apart from this, however, no significant changes were noticed. On the contrary, an evident modification of crystal morphology was observable at day 8. At this time, the surface of the specimen was mainly covered with thin sheet-like platelets (200-300 nm thick and 10-20 µm long) aligned more or less in parallel and gathered into

bunches (Figure 29). These formations resembled the precipitates already observed in the DCPD sample immersed for 4 days in PBSd and embedded in epoxy resin (Figure 26). After 14 days, finally, all the surface of the samples was covered with this kind of platelets and no DCPD crystals could be identified anymore.

The morphology of the crystals observed on the surface of samples immersed in TRISs did not undergo any visible change all along the immersion period (Figure 30).

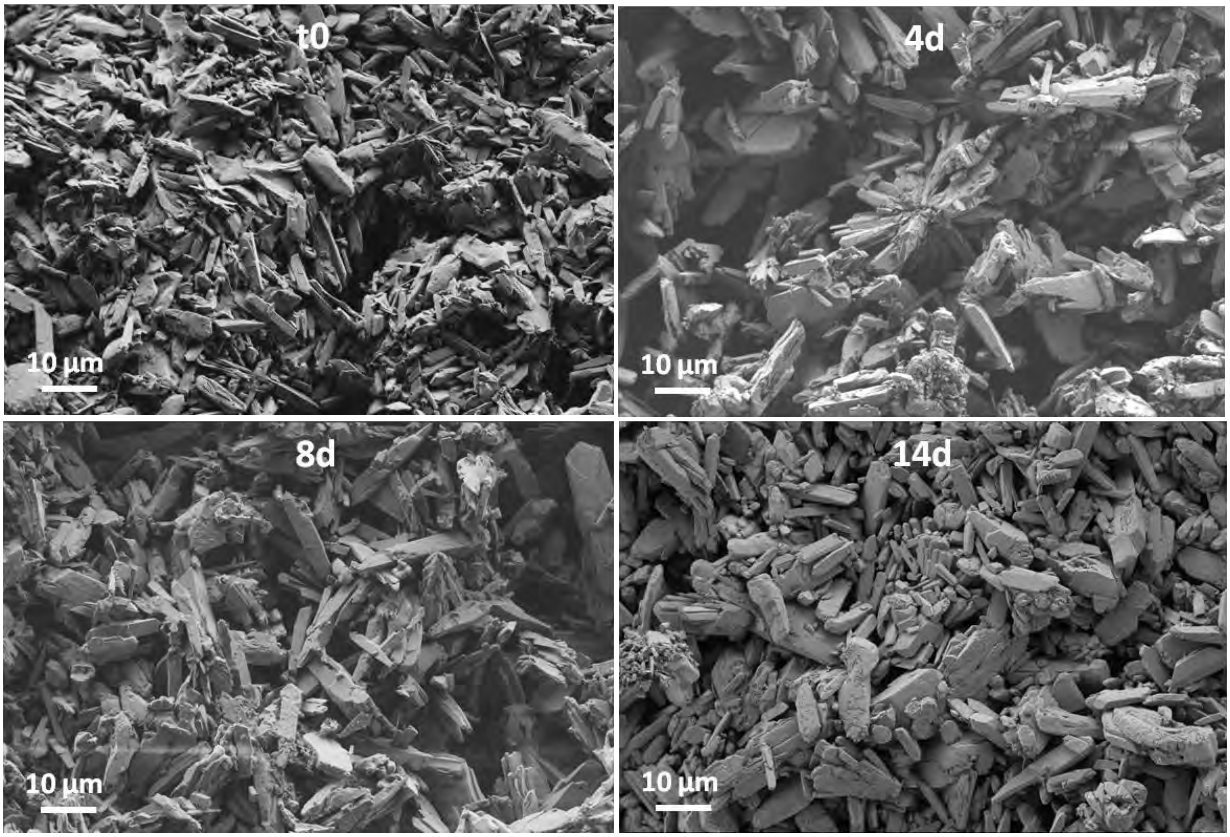

Figure 30: SEM micrographs of surfaces of DCPD samples after immersion in TRISs for different times

The morphology of crystals present on the surface of samples immersed in TRISd appeared almost unchanged till day 8 (Figure 31). At this time-point, some small fragments and or/precipitates were observed at the surface (cf. white arrows in Figure 31-8d), but DCPD crystals were still well visible. After 14 days, however, the morphology appeared greatly altered: DCPD was no more visible and the surface was covered with sheet-like platelets, small (200-300 nm thick and 5-10 µm long) and tightly packed. Moreover a layer of "spongy" precipitates, with pores of 300-500 nm and walls of around 100 nm (as measured by image analysis through ImageJ/Fiji shareware), was spread on most of the surface Figure 31-14d).

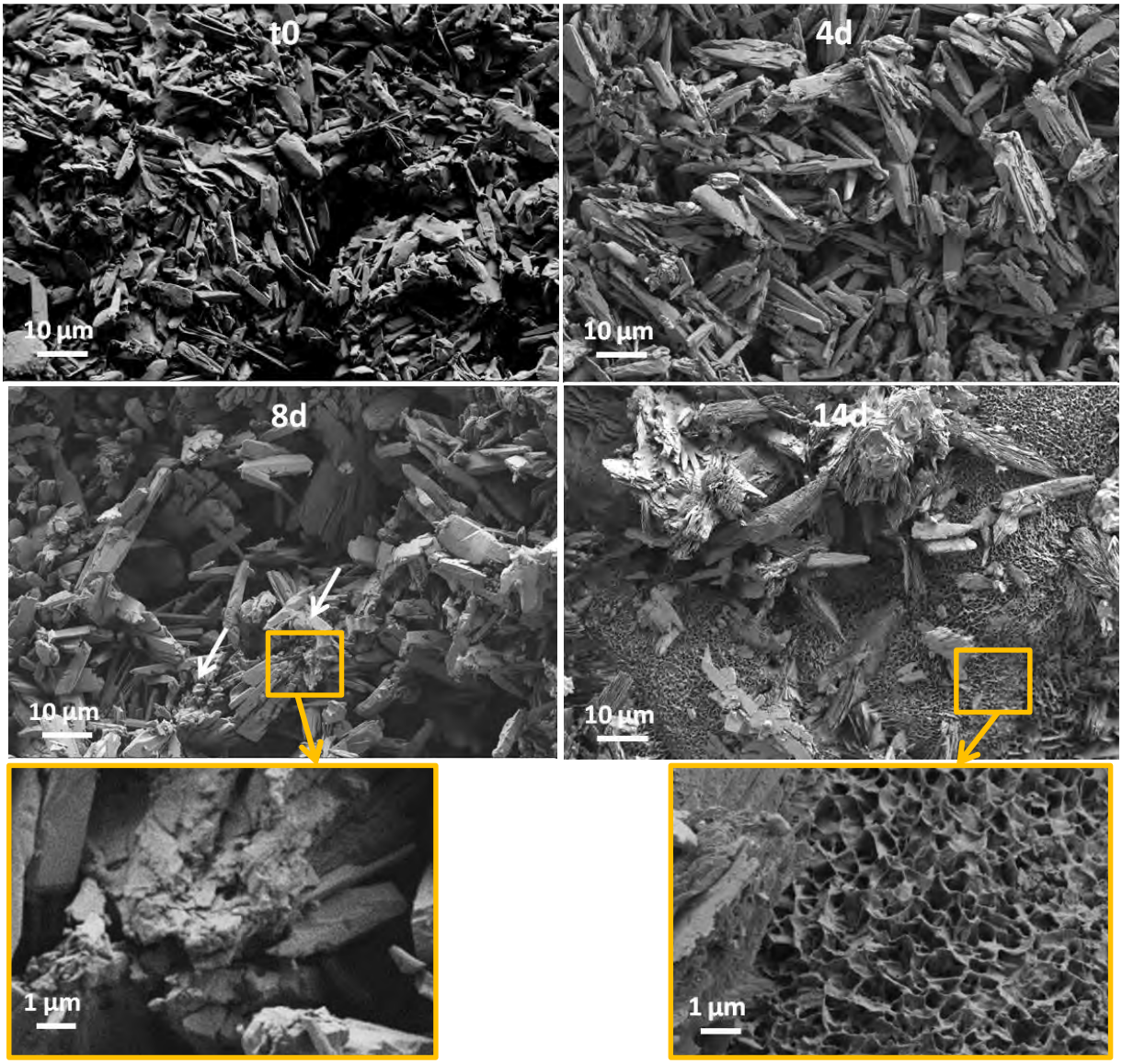

Figure 31: SEM micrographs of the surfaces of DCPD samples after immersion in TRISd for different times

Evolution of the samples core

Images of DCPD samples in the core are displayed only for 1 day and 14 days of immersion. At these time-points, in fact, the micrographs displayed the major changes observed in the core. Images related to the other time-points, however, can be found in Annex (A.b.12-A.b.14).

After 1 day in PBSd, some new crystals were noticed in the core of the samples. The single crystals appeared more porous and made of thinner layers but they were assembled in clusters of shape similar to the morphology of the initial DCPD (water lily-shaped) (cf. white arrows in Figure 32-1d). After 14 days, these more porous crystals, which were observed at day 1, were not visible anymore. On the other hand, the core appeared to be uniquely composed of the initial DCPD crystals, although most of them showed a rougher surface compared to the one at t0 (cf. enlargement of image at 14d in Figure 32 compared to Figure 3).

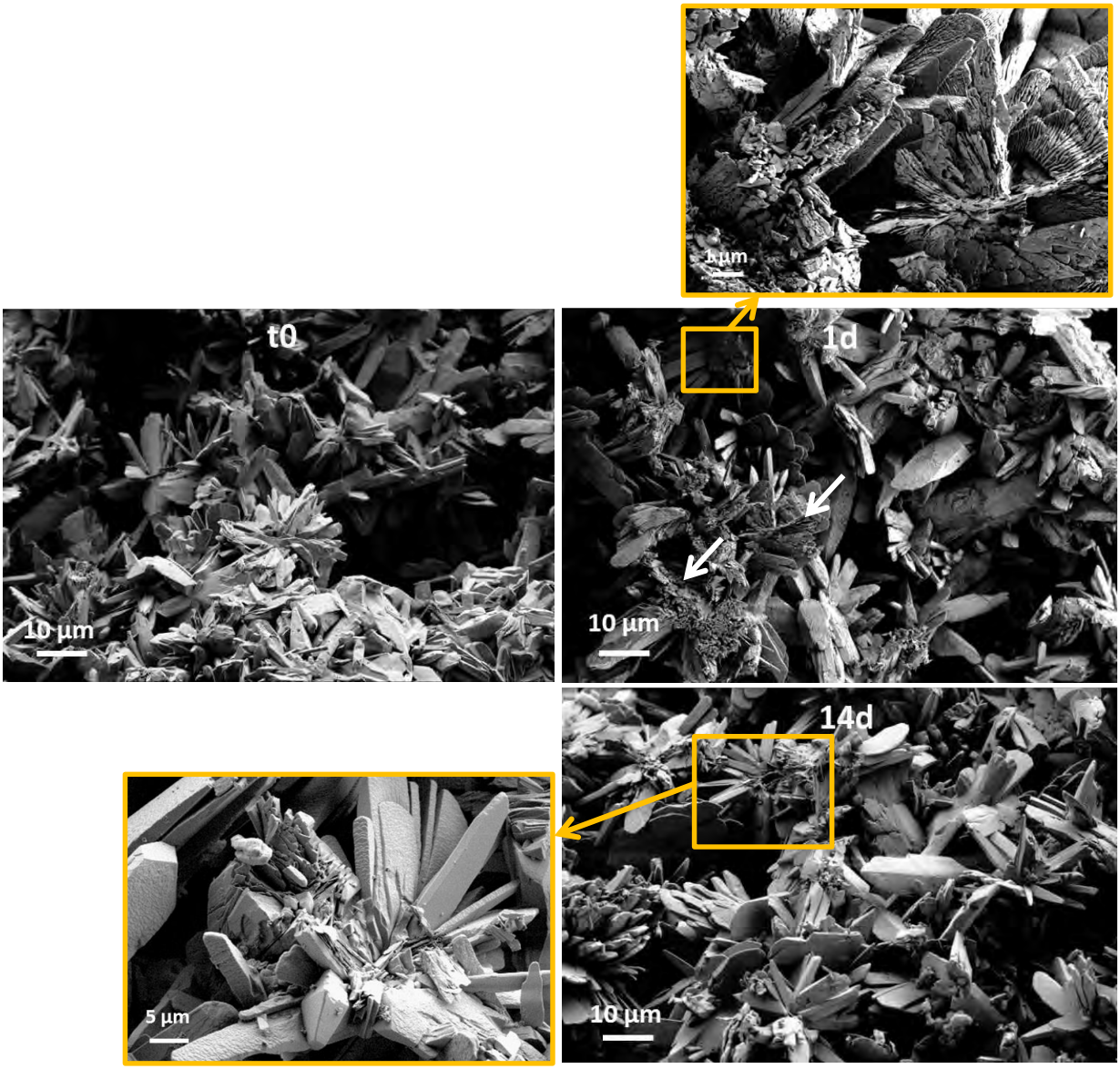

Figure 32: SEM micrographs of the core of DCPD samples after immersion in PBSd for different times

After 1 day in TRISs some of the crystals in the inner part of the specimens appeared more porous (cf. arrows in Figure 33-1d); however, the morphology was on the overall unchanged. After 14 days no visible changes could be noticed.

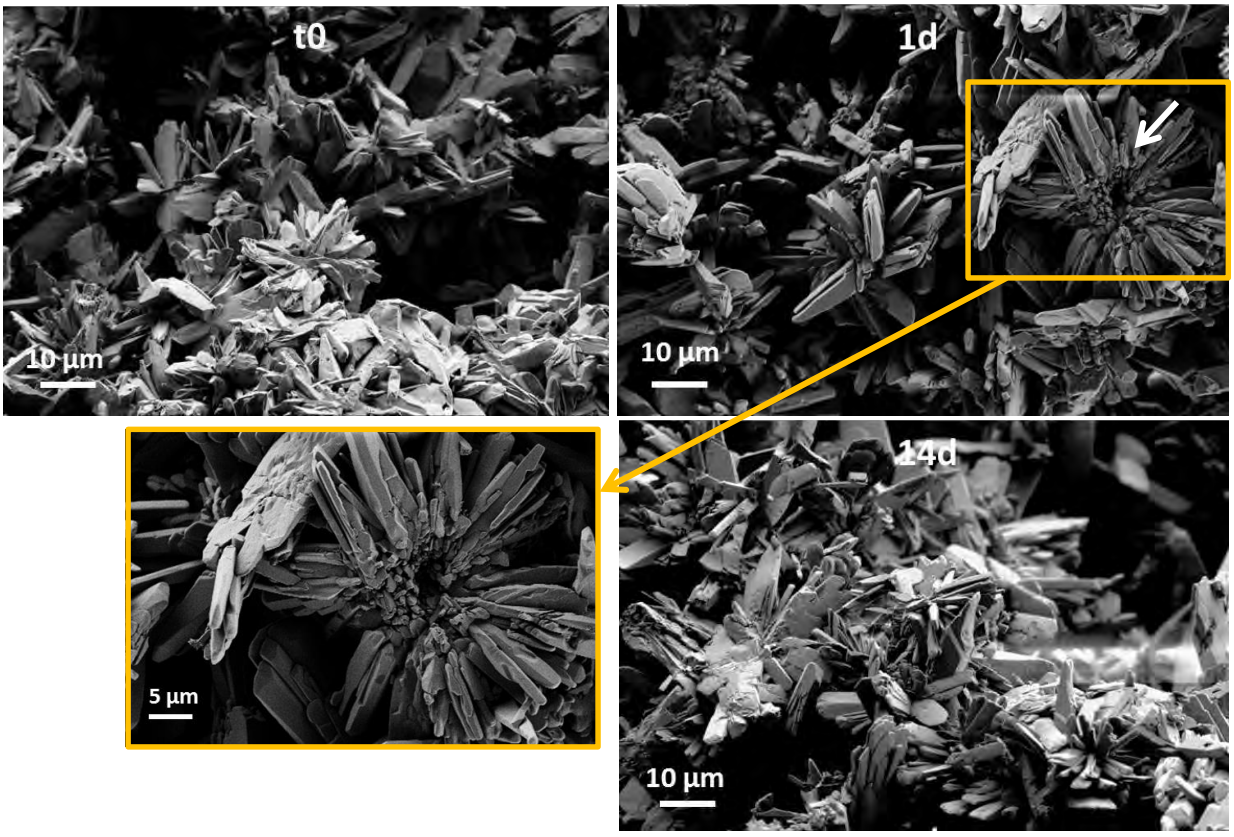

Figure 33: SEM micrographs of the core of DCPD samples after immersion in TRISs for different times

After 1 day in TRISd, the surface of some DCPD crystals was rougher than at time zero, but also in this case the typical water-lily-shaped morphology was still unaltered (Figure 34). At 14d, the single crystals were even rougher and some of them appeared as made of thinner layers.

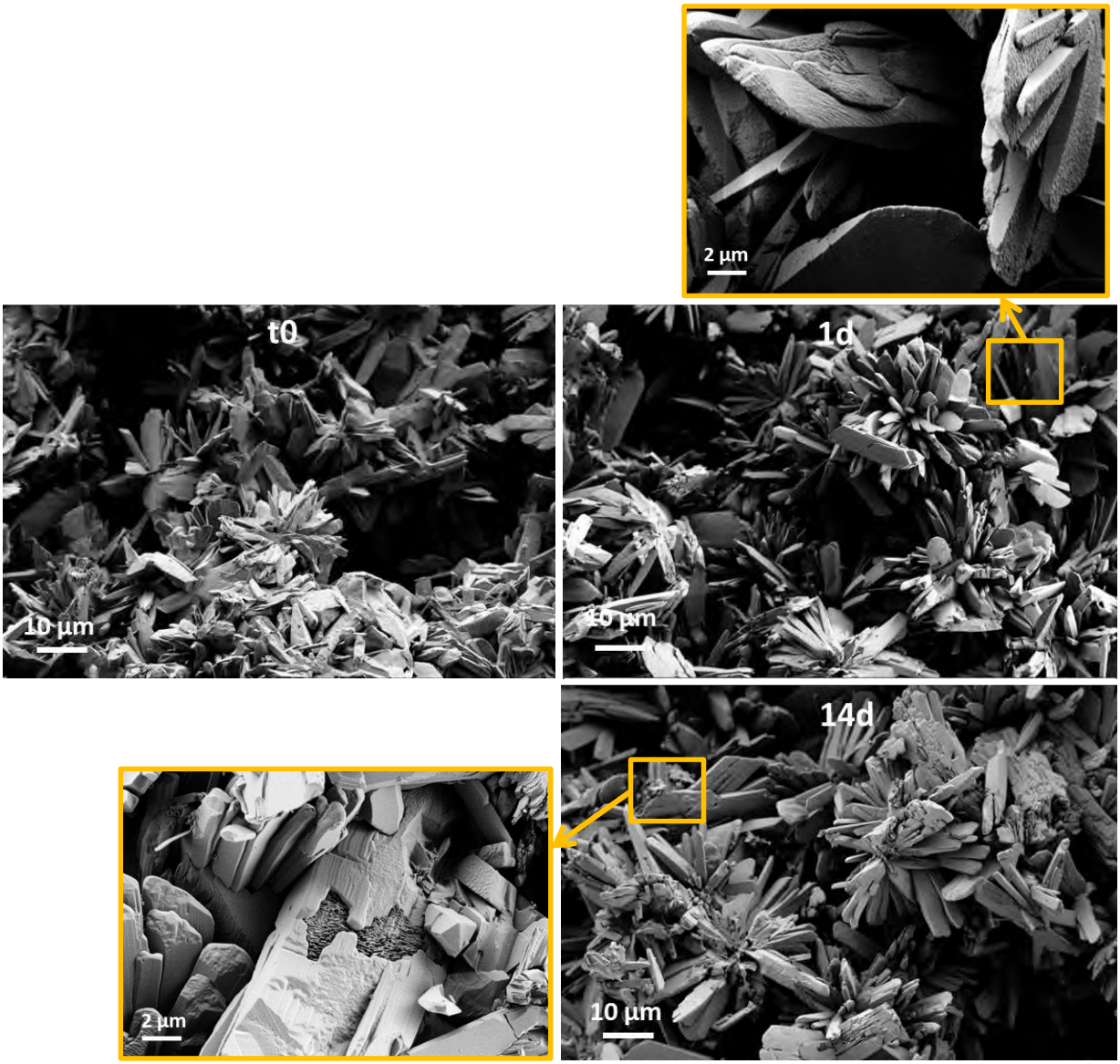

Figure 34: SEM micrographs of the core of DCPD samples after immersion in TRISd for different times

3.2.4 Mechanical changes

For the assessment of the evolution of their mechanical properties due to immersion, samples were tested both at the surface and in the core by micro-indentation tests, as described in chapter 2 (paragraph 2.4.3).

Due to the differences between the values of properties at time zero at the surface and in the core (Table 1), two separate references were used. For the surface, samples were indented before (4 indentations) and after (8 indentations) immersion; in this way, the evolution of *E* and *H* was assessed by comparing their values at time zero and after immersion of the very same sample. For performing the indentations, the smoothest plane surface of the cylindrical samples was preferred, that is to say the one casted in contact with the acetate film (cf. paragraph 2.1.1).

Regarding the core, given the impossibility to test the inner part of the samples before immersion and the limited dispersion of data at initial time (Figure 6 and Figure 7), a value of reference at time zero was obtained by testing the core of 3 samples (10 indentations each) chosen randomly among all the specimens and not used for further immersion. The mechanical properties after immersion

were assessed directly on the core of each sample that underwent dissolution test. The evolution of *E* and *H*, thus, was obtained comparing the values recorded after immersion to those of the calculated reference at time zero.

For each time-point, after immersion, three samples were tested at the surface (8 indentations per sample) and two in the core (8 indentations per sample). The results are presented in the following tables and graphs in form of average raw values and average percentage variations compared to the average initial values (cf. Eq.(1)). Variations in percentage of the properties of each single sample are reported in Annex (A.b.15-A.b.20). Moreover, some representative curves of indentation (load vs. displacement) are plotted. For sake of order, graphs and comments are divided according to the corresponding dissolution medium.

PBSd

Observing the values of hardness and Young's modulus obtained at the surface (Table 9 and Figure 35-left), a quite important dispersion was noticed for the first time-points (30m-1d), exactly as already noted for samples before immersion. Starting from day 4, however, *H* and *E* both tended to clearly decrease at the surface, with diminutions between 58% and 68% at day 8, and ranging from 61% to 72% at day 14.
All these remarks can apply also on the raw curves load vs. displacement of the indentation tests (Figure 36). The well visible variations in the depth of penetration, in fact, correspond to changes in hardness, while the modifications of the slope of the unloading part of the curves (a bit less evident on the graphs, though) are signs of variation of Young's modulus. Moreover, the profile of the loading segment of the curves reflects the state of the indented surface. For example, the violent decreases of load which can be observed on the loading curves obtained at 8 and 14 days show that some "collapse" phenomena of the porous structure took place during the test (as already observed in literature for highly porous materials [2, 3]).

Table 9: Average values and standard deviations of hardness and Young's modulus after different immersion times in PBSd

t	**H [MPa] avg $_{std}$**		**E [MPa] avg $_{std}$**	
	SURF	**CORE**	**SURF**	**CORE**
0	$9.2_{3.8}$	$6.1_{1.0}$	1101_{399}	882_{213}
30 min	$6.6_{4.5}$	$2.6_{0.2}$	738_{404}	311_{7}
1d	$5.0_{2.9}$	$2.7_{0.5}$	722_{410}	361_{110}
4d	$4.9_{1.9}$	$2.9_{0.6}$	619_{238}	418_{156}
8d	$2.5_{0.2}$	$6.3_{0.3}$	423_{43}	679_{68}
14d	$2.3_{0.4}$	$3.9_{2.3}$	355_{63}	420_{163}

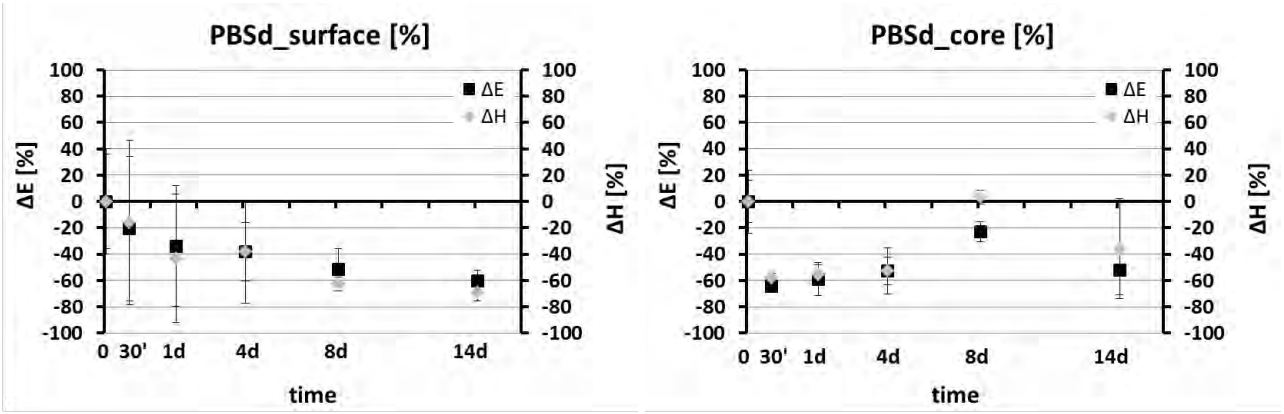

Figure 35: Variation of H and E at the surface (left) and in the core (right) after different times of immersion in PBSd

As far as the inner part of the samples is concerned, a strong decrease of *H* (around -55%) and *E* (between -50% and -65%) was already noticed after 30 minutes of immersion (Table 9 and Figure 35-right). At day 1 the values were quite similar to 30 minutes, while the mechanical properties started to slightly re-increase after 4 days. At day 8 the properties of the material significantly increased, reaching a value of hardness almost equal to the initial one ($\Delta H \approx 0$) and an elastic modulus around 22% lower than the original one. Between 8 and 14 days, finally, a further decrease of properties was observed.

The load-displacement curves condense quite well the information just exposed and also display that the surface state did not change significantly from one time-point to the others (Figure 37).

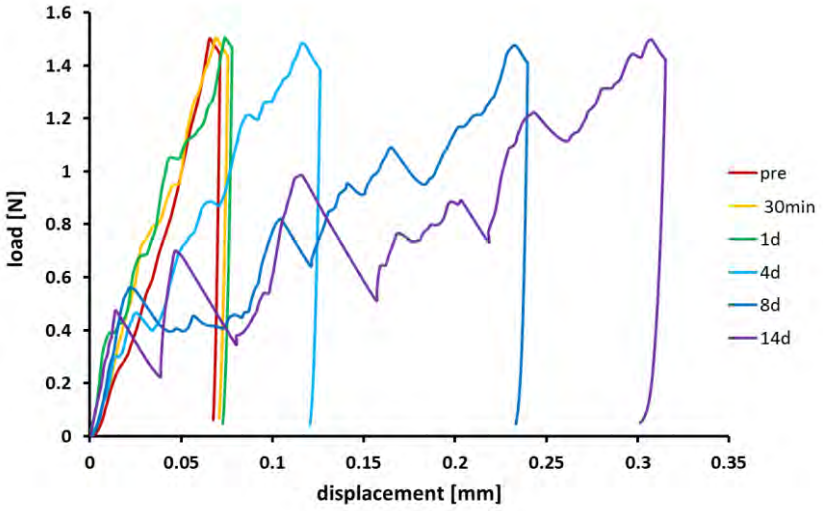

Figure 36: Representative load-displacement curves obtained when indenting DCPD samples at the surface after different immersion times in PBSd

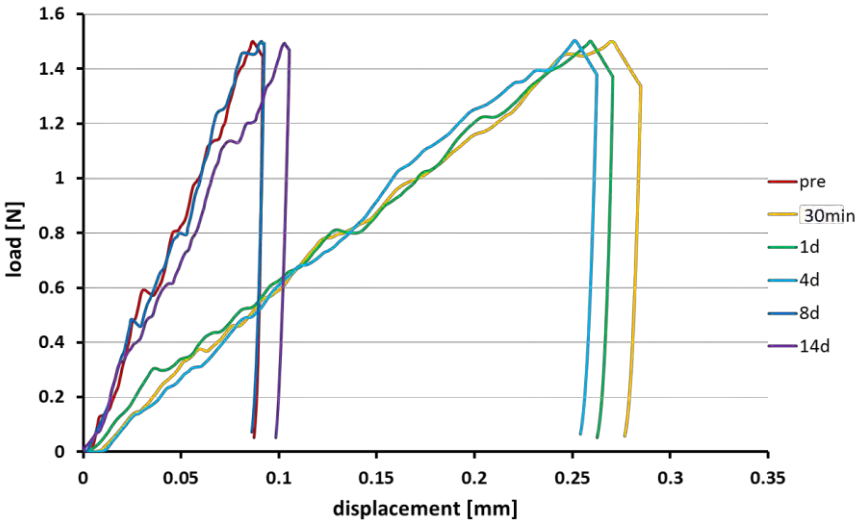

Figure 37: Representative load-displacement curves obtained when indenting DCPD sample in the core after different immersion times in PBSd

TRISs

The dispersion of *E* and *H* already noted at t0 affected the results obtained for samples immersed in TRISs for a longer period, compared to what was observed in the other solutions. No clear evolution was noticed for hardness and Young' modulus values neither at the surface nor in the core (Table 10 and Figure 38). The only relevant change was observed in the core for initial time-points: after 30 minutes of immersion, both *H* and *E* decreased significantly (-38% and -45% respectively, Figure 38-right) and then reached again their initial value, as measured at day 1.

Table 10: Average values and standard deviations of hardness and Young's modulus after different immersion times in TRISs

t	H [MPa] avg std		E [MPa] avg std	
	SURF	CORE	SURF	CORE
0	$9.2_{3.8}$	$6.1_{1.0}$	1101_{399}	882_{213}
30 min	$9.7_{0.9}$	$3.8_{1.6}$	1249_{73}	485_{37}
1d	$12.1_{2.4}$	$6.6_{0.5}$	1485_{309}	980_{25}
4d	$7.9_{1.3}$	$6.1_{0.7}$	1081_{132}	789_{37}
8d	$7.5_{1.3}$	$6.2_{0.6}$	1086_{179}	917_{56}
14d	$7.6_{0.8}$	$5.9_{0.2}$	1060_{234}	750_{1}

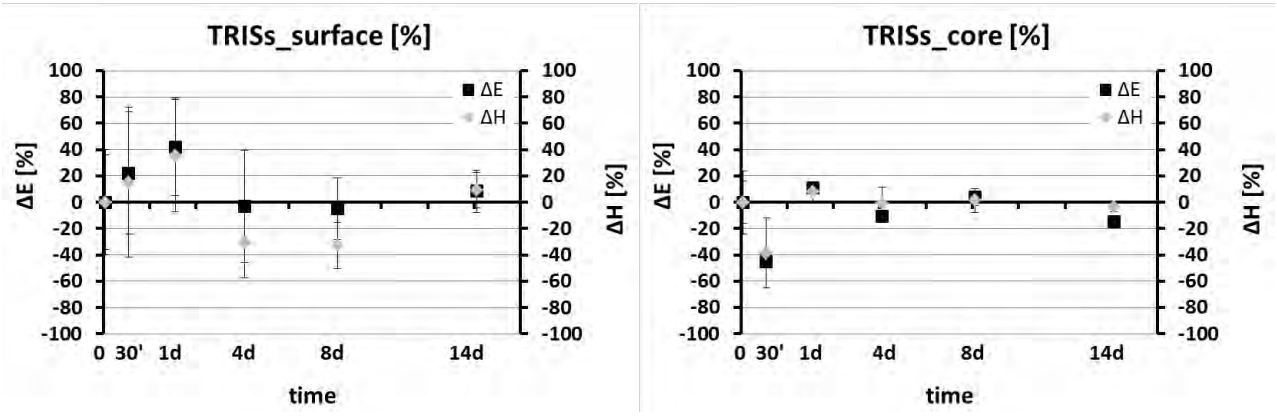

Figure 38: Variation of H and E at the surface (left) and in the core (right) after different times of immersion in TRISs

Indentation curves confirm what was just observed (Figure 39 and Figure 40); all the curves, in fact, appear quite similar to those at time zero, with the exception of the curve from the core at 30 minutes, which shows a much higher penetration depth.

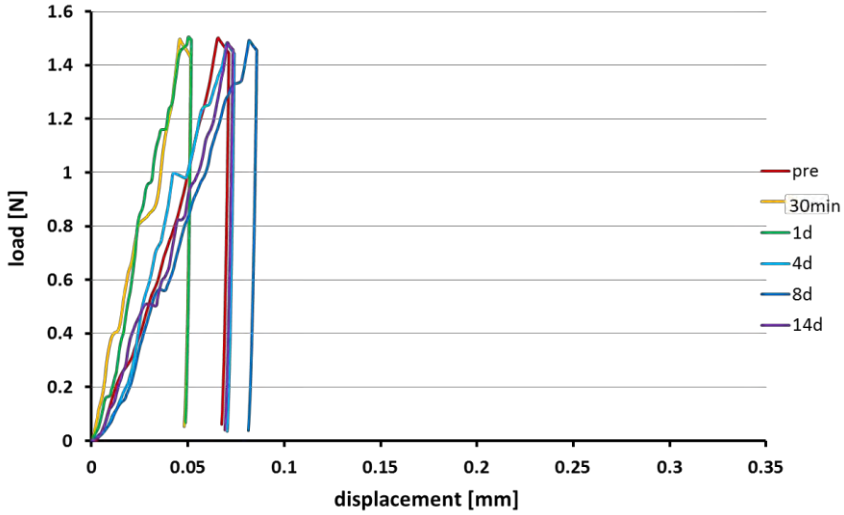

Figure 39: Representative load-displacement curves obtained when indenting DCPD samples at the surface after different immersion times in TRISs

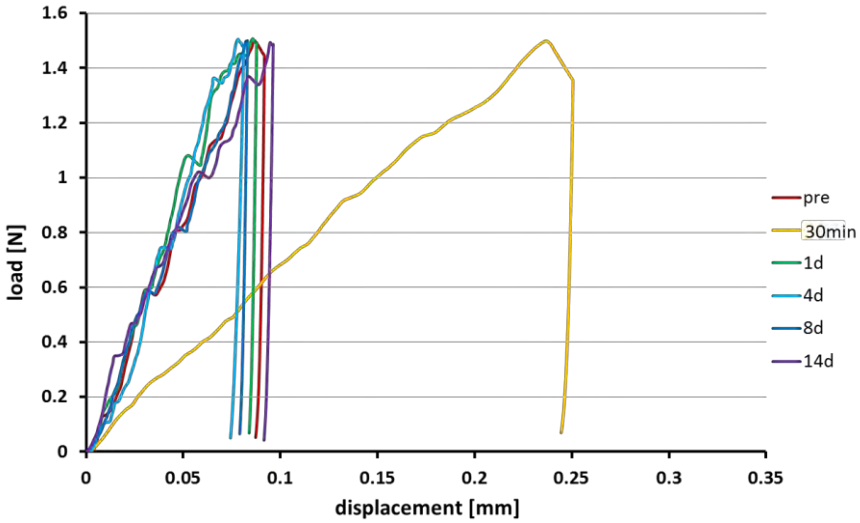

Figure 40: Representative load-displacement curves obtained when indenting DCPD sample in the core after different immersion times in TRISs

TRISd

As for all the other samples, measurements performed at the surfaces of specimens immersed in TRISd displayed an important dispersion along the first time-points (30 minutes and 1 day) (Table 11 and Figure 41-left). After 4 days, at the surface, a decrease of *H* (between 25% and 50%) was noticed, while *E* did not show a clear reduction trend. After 8 days, however, at the surface both hardness and Young's Modulus underwent a strong decrease (-57% and -53% respectively). Finally, between 8 and 14 days, the elastic modulus increased slightly (Δ*E* reached -40%); a similar trend was also noticed for the hardness values, which, although quite dispersed, reached after 14 days an average value comparable the initial one .
This was also seen from the indentation curves (Figure 42), which display an increase of penetration depth during the first 8 days followed by its decrease at day 14. It is also worth to notice that the curves appeared much "smoother" than those obtained after immersion in PBSd, suggesting that few "collapse" phenomena occurred during the indentation tests.

As far as the inner part of the samples is concerned, the most evident change was after 30 minutes, when a decrease of *H* and *E* took place (Table 11 and Figure 41-right). Between 30 minutes and 1 day, the properties reached again values close to the initial ones, and, during the following time-points (4 and 8d) no relevant changes were noticed. After 14 days, a slight decrease of properties (-4% for *H* and -30% for *E* on average) was observed.
Slight signs of "collapses" of the structure were visible on the indentation curves (Figure 43); moreover a specifically high depth of penetration was noticed for the samples that underwent a 30 minutes-immersion.

Table 11: Average values and standard deviations of hardness and Young's modulus after different immersion times in TRISd

t	H [MPa] avg std		E [MPa] avg std	
	SURF	CORE	SURF	CORE
0	9.2 3.8	6.1 1.0	1101 399	882 213
30 min	9.7 0.9	3.8 1.6	1249 73	485 37
1d	9.2 1.2	6.7 0.4	1387 236	820 135
4d	6.2 0.7	6.7 0.4	1071 73	816 85
8d	3.9 1.5	6.7 0.3	579 193	834 125
14d	8.0 2.9	5.7 0.3	578 174	598 369

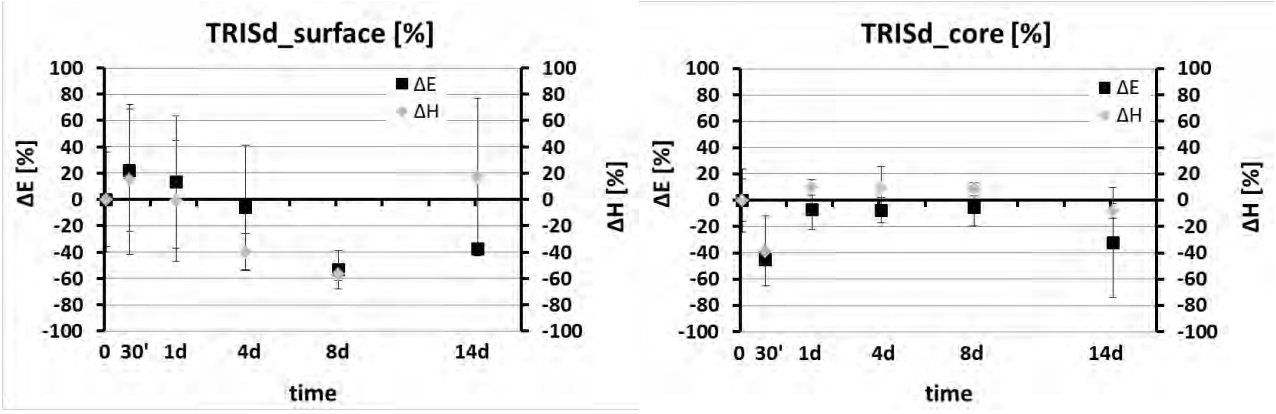

Figure 41: Variation of H and E at the surface (left) and in the core (right) after different times of immersion in TRISd

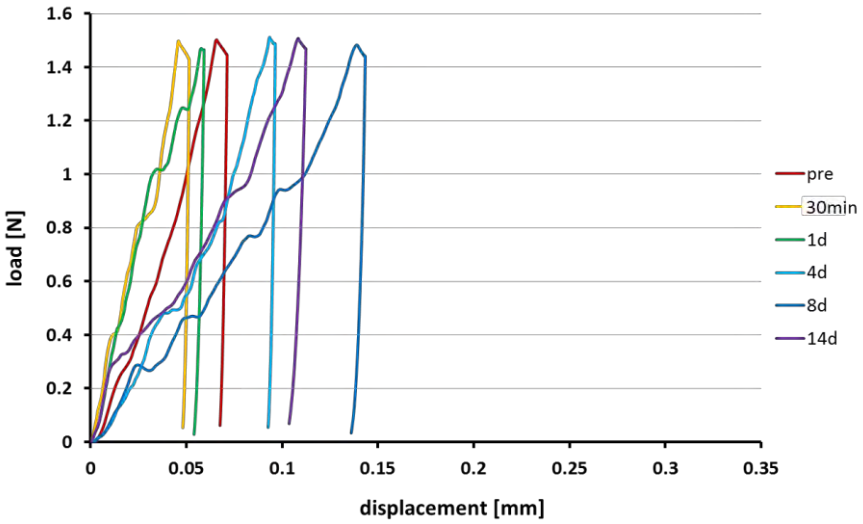

Figure 42: Representative load-displacement curves obtained when indenting DCPD sample at the surface after different immersion times in TRISd

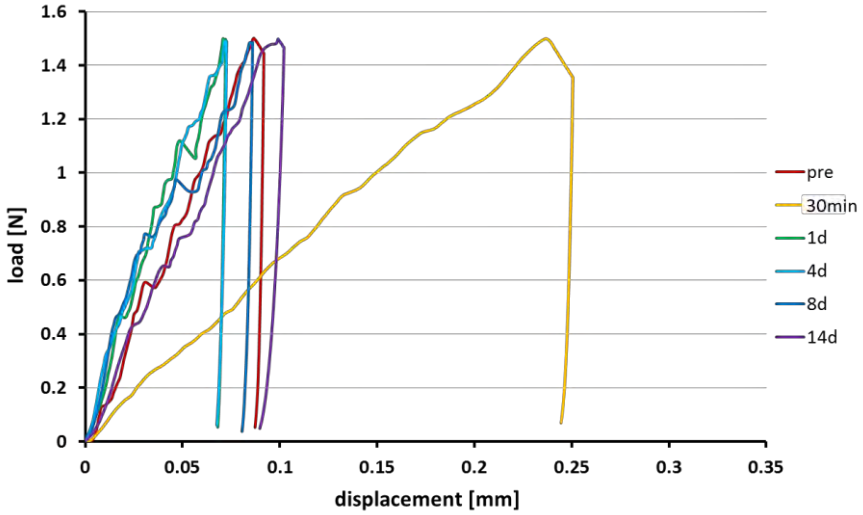

Figure 43: Representative load-displacement curves obtained when indenting DCPD sample in the core after different immersion times in TRISd

Mechanical tests performed in humid conditions

As detailed in Chapter 2 (section 2.4), the tests described above were performed on samples, which were dried after having been removed from the immersion solutions.

To simulate more closely the physiologic conditions and to validate the possible use of *in-situ* indentation (i.e. mechanical test directly performed on the sample, while it is still in the immersion solution), preliminary tests were performed in humid conditions: one specimen was tested at the surface when still humid, just after having been taken out of the immersion medium.

For this purpose, the specimen was indented at time zero in dry conditions (4 indentations), immersed for 30 minutes in TRISs and tested again, in order to have a reference at "time close to zero" in humid conditions, and then immersed for 14 days in TRISs. Once withdrawn, it was immediately indented (condition "post_humid"), let dry and further indented (condition "post_dry").

The Figure 44 reports the absolute values of hardness and Young's Modulus obtained in dry and humid conditions before and after immersion. The error bars derive from the different indentations performed on the sample in each condition.

As can be noticed, the presence of humidity did not influence the evolution of the mechanical properties: *H* and *E*, in fact, were higher after the 14 days-immersion both when the sample was

tested in dry and humid conditions. However, the presence of water had a strong influence on the absolute values. In particular, the hardness measured in humid conditions (both at time zero and after 14 days) displayed much lower values than in dry conditions, while the elastic modulus was only slightly affected. The differences of hardness in presence and absence of water, finally, are particularly evident in the load-displacement curves reported in Figure 45.

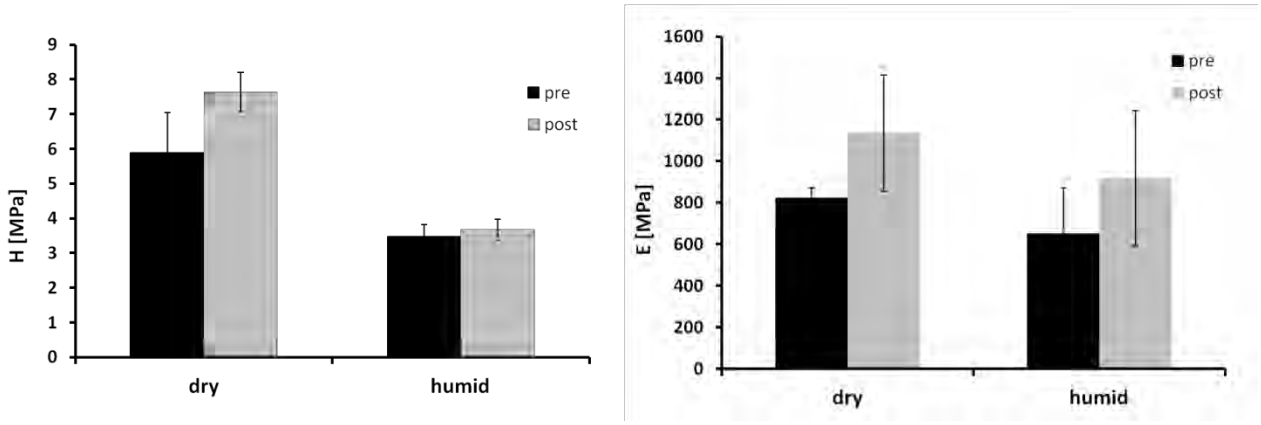

Figure 44: Values of hardness (left) and elastic modulus (right) in dry and humid conditions before (denoted as "pre", in black) and after (denoted as "post", in grey) immersion (14d in TRISs)

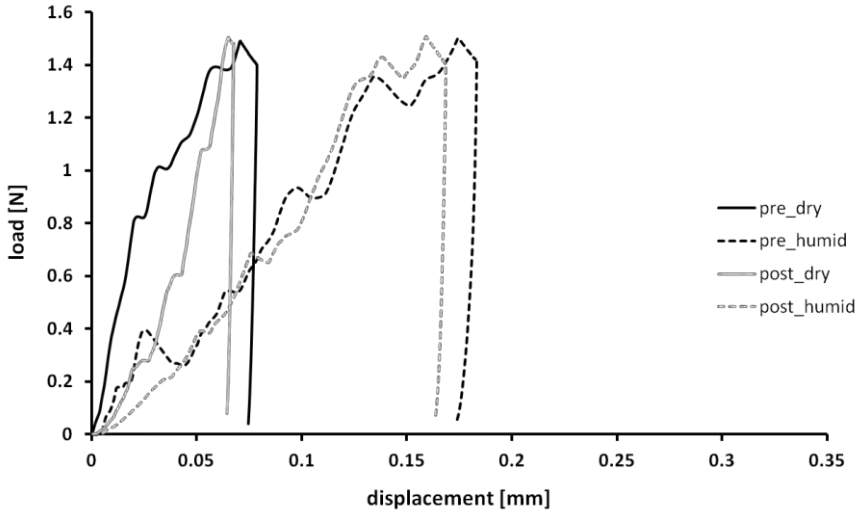

Figure 45: Indentation curves obtained in dry (in black) and humid (in grey) conditions before (solid lines) and after (dotted lines) immersion (14d TRISs)

3.3 Discussion

The first paragraph of this section will be dedicated to the DCPD samples before immersion. Then, the discussion will be devoted to the *in-vitro* evolution of DCPD samples immersed in the three different conditions. Comparing and correlating all the data collected about morphological, physico-chemical, microstructural and mechanical changes during the tests, the discussion will then focus on the influence of the immersion conditions on the samples evolution.

Finally, the last section will discuss the new methodology, which was set up in this work and will focus more particularly on the validity of the instrumented micro-indentation technique as a tool to evaluate the *in-vitro* evolution of DCPD samples.

3.3.1 Initial DCPD samples

As described in the result section (paragraph 3.1), the DCPD samples at time zero presented some differences between their surface and their bulk.
In the core, they were composed of 100% DCPD, crystallized in shape of platelets about 10 µm long, 2-4 µm wide and 300-500 nm thick (Figure 3), arranged in water-lily clusters without any specific orientation (Figure 1). This morphology is consistent with what is usually observed for DCPD crystals [4].
At the surface, instead, they presented a denser layer, which appeared brighter on the µ-CT images (Figure 2-A). This was interpreted as a sign of platelets alignment due to the elaboration process: during the casting of the cement, platelets of DCPD tended to align parallel to the walls of the mould. This was also confirmed by the XRD pattern of the surface (Figure 1), where the relative intensity of the peaks at 2θ=11.7° (hkl (0,2,0)) and 2θ=29.3° (hkl (1,1,-2)) were higher than expected, suggesting a preferential orientation. It should be noticed that 8 wt.% of the surface was composed by MCPM, which came from the setting reactants (cf. Chapter 2). This amount seems, however, too small to justify the observation by µ-CT of a brighter layer; moreover, being both DCPD and MCPM made of calcium and phosphate they would probably appear in the same grey level in tomography images (unless they strongly differed in terms of density). By the way, after 30 minutes of immersion, the MCPM initially present at the surface had completely dissolved (Table 2-Table 4), while the bright layer was still well visible (Figure A.b.9-A.b.10 in Annex).
The excess of MCPM found at the surface suggested that the cement had still a low internal pH when it was dried, despite the 30 minutes immersion stage in distilled water, which was aimed to eliminate this residual acidity (cf. Chapter 2). Interestingly, it is known from the literature that the DCPD phase generally tends to transform into DCPA in such acidic conditions [5, 6]. Here, no DCPA was detected, which could be related to the presence of citrate ions introduced to increase the setting time of the cements. Indeed, it has been reported that the presence of citrate ions could prevent the conversion of DCPD into DCPA [5].
In terms of mechanical properties, both hardness and Young's modulus resulted to be significantly higher at the surface than in the core (Table 1). This characteristic was probably due to the already mentioned preferential orientation of crystals at the surface and was consistent with a previous study [2]. Moreover, the higher dispersion of data observed on sample surfaces (Figure 4- Figure 7) reflected the inhomogeneity of composition (MCPM and DCPD) and surface structuration of the denser outer-layer, while the measurements in the core were less scattered, given that they were always done on a cut-surface (cf. Chapter 2).
When comparing the mechanical properties measured here with those found in literature for brushite cements, several parameters have to be considered. First of all, only few works focused on the analysis of the mechanical characteristics of brushite cements and, secondly, the conditions of these tests often differed from the ones of the present study. For example, Charrière et al. [7] performed compression, traction and torsion tests on moist porous brushite cements (40% of porosity, samples wrapped in paper soaked with distilled paper and kept sealed until the test) (cf. paragraph 1.5.1). The values of Young's modulus obtained by compression can be assimilated, to a certain extent, to our results of *E* assessed by micro-indentation. In particular Charrière et al. reported a Young's modulus of 7.9 ± 0.3 GPa, which is by far higher than the 1.1 ± 0.4 GPa that we measured at the surface at time zero for our specimens. It should be taken into consideration, however, that the samples tested by Charrière and his co-workers presented a much lower degree of porosity (40%) compared to the specimens used for the present study (61%). Since the porosity is highly detrimental for the mechanical properties of a material, the lower elastic modulus of the samples described in this thesis could be justified, thus, by the high degree of porosity of the cement, appearing, therefore, coherent with the literature.

3.3.2 Evolution of samples immersed in TRISs

During the first **30 minutes** in TRISs, the pH of the solution dropped from 7.35 to 7.15 (Figure 23). Simultaneously, the MCPM initially present at the surface dissolved and DCPA was detected by XRD both at the surface and in the core (Figure 16, Figure 19, Table 3, Table 6). It was logical that the dissolution of MCPM in an aqueous solution at initial pH 7.4 tended to cause a pH decrease. It should be noted that the lower pH, the more soluble the DCPD (Chapter 1, Figure 10). This medium acidification was also most probably responsible for the conversion of DCPD into the more stable DCPA phase (Chapter 1, Figure 10).

Between 30 minutes and **1 day**, the pH value increased from 7.15 to 7.3 (Figure 22). As seen on XRD patterns, no more MCPM remained to be dissolved after the first half-hour of immersion. Concomitantly, the amount of DCPA detected by XRD measurements decreased: no more DCPA was found at the surface while only 9.7 wt.% was detected in the core (Figure 21, Table 3, Table 6). This evolution was unexpected since DCPA is less soluble than DCPD (Chapter 1, Figure 10) and hence should not dissolve. A probable explanation arises when one takes into consideration that the XRD measurements were performed after drying of the samples (cf. Chapter 2). Even if the drying stage was performed in mild conditions at 37°C, it is probable that the formation of DCPA took place during sample drying rather than during their stay in solution.
This hypothesis seemed to be confirmed by the results obtained during a preliminary *in-situ* test: a DCPD sample was cut and then dipped in TRIS solution at 37°C for more than 4 days. Its crystalline composition was continuously assessed by *in-situ* XRD. No DCPA was detected at any time (experimental details and results are reported in Annex, Figure A.b.21 and A.b.22). However, it should be noted that, due to experimental constraints, the conditions in which this preliminary test was performed, were slightly different from the *ex-situ* tests presented in this chapter. In particular, the liquid to cement ratio was lower (35.7 mL/g vs. 130 mL/g). However, this smaller liquid volume resulted in a lower pH in the solution (final pH = 7.00). This should have theoretically fostered the conversion of DCPD into DCPA. Therefore, the absence of DCPA peaks on XRD patterns furtherly strengthens the assumption of DCPA arising from the drying step.
Moreover, this hypothesis is consistent with previous studies. Indeed, it is known that the decomposition of DCPD into DCPA is favoured by a low pH, the presence of moisture, an elevation of temperature and the time spent by the sample in these conditions [5, 8]. For example, Martin and Brown observed that "*Equilibration of any sample containing the metastable phase DCPD above 36°C resulted in the conversion of DCPD to DCPA. Under acidic conditions in the presence of MCPM, DCPD readily converted to DCPA below 37°C*" [6]. Due to the microporous nature of the cements, the composition of the immersion solution was certainly different inside and outside the block: when the MCPM phase dissolved, it might be assumed that the pH decreased more significantly locally, close to and inside the sample, whereas the important volume of solution around the cements (liquid volume to sample weight = 130 mL/g) limited the pH decrease "seen" by the surface. Moreover, the complete drying of the inner part of the sample likely required more time than the drying of its surface. Thus, the conditions described by Martin and Brown [6] as leading to the conversion of DCPD to DCPA could have been reached in the specimen during its drying, and particularly in the core of the sample, where both a lower pH and a slower drying rate might have been experienced than at its surface. This could explain why at 30 minutes, there was 9 wt.% of DCPA at the surface, while 49 wt.% were found in the core. After 1 day, instead, since the pH of the TRIS solution had increased, the formation of DCPA during drying was less favoured and led to the absence of DCPA at the surface and only 9.7 wt.% DCPA in the core.
It is planned to carry on further experiments to confirm this explanation.

In parallel with these physico-chemical changes, the apparent density of the samples decreased of 4% between t0 and 30 minutes (Figure 10). This variation entirely corresponded to a weight loss since no significant volume change was detected (Figure 8). The dissolution of MCPM constituting only 8 wt.% of the sample surface would not lead to any significant weight variation (loss estimated

to less than 5 wt.‰ on the total weight of the specimen). Therefore, this loss was mainly attributed to the loss of crystallisation water during the decomposition from DCPD to DCPA. However, this variation should account for 21 % of the weight of DCPD converting to DCPA and should lead to a weight loss around 10%. The gap between the expected and the experimented mass losses might be linked to the formation of phases, which could not be detected by XRD, either because they precipitated in too low amounts or because they were amorphous. For example, the presence of an amorphous phase was detected by Fulmer and Brown when studying the DCPD hydrolysis in distilled water [9]. Also, it is reported that the presence of citrate ions has an inhibitory effect on calcium phosphates crystallisation [10]. In this view, FT-IR spectrophotometry measurements would help clarifying this question and verify the presence of citrates inside the cements [11].
DCPA, localised mainly in the core, seemed to cause a strong decrease of mechanical properties: while at the surface *H* and *E* appeared almost unchanged, in the inner part of the samples they underwent a clear diminution (-38% and -45% respectively, Figure 38). The conversion from DCPD to DCPA is indeed known to be detrimental to the mechanical properties of this type of cements since the recrystallization tends to lower the strength of each single crystal [8, 12].

Assuming that all these observations made at 30 minutes were caused by the drying process, it seems logical to compare the samples properties at 1 day with those at t0 rather than at 30 minutes. In this perspective, the small change in density (-2 wt.%) matched roughly the expected weight loss due to the conversion of DCPD into DCPA observed in the core. This latter phase was indeed identified by XRD (Figure 21) and could correspond to the porous crystals noticed by SEM in the inner part of the specimens (cf. arrows in Figure 33). The increase of porosity and the amount of DCPA were however too low to affect significantly the mechanical properties, which remained close to the initial ones (Figure 38).

From **day 1 to day 9**, the pH value stayed almost stable around 7.3 (Figure 22), leading to a constant amount of DCPD converting into DCPA during the drying stage (Figure 21). The volume and the mass seemed to decrease at a slow but constant rate (Figure 8, Figure 9), suggesting a dissolution of the DCPD phase during immersion. However the apparent porosity (Figure 10) and the mechanical properties (Figure 38) were not significantly affected by these changes.
Around day 9, a slight pH increase (to 7.4) was noticed in the TRIS solution and from this point onwards, no more DCPA was detected by XRD (Figure 21). It seemed that 9 days were required for the complete elimination of the internal acidity and the equilibration of the internal pH of the microporous cement with the surrounding TRIS solution. This might also be linked to the end of the slow diffusion out of the cement of residual citric acid, as reported previously by Hofmann et al. and Cama et al. [11, 13].

Until **day 14**, it seemed that the DCPD phase continued to dissolve slowly (Figure 8, Figure 9) but no evident changes were noticed both at the macro and micro level (Figure 12, Figure 27, Figure 30, Figure 33). Regarding the mechanical properties, the average values of *H* and *E* did not evolve significantly. However, the dispersion of the data observed at the surface at t0 decreased all along the duration of the test (Figure 38), maybe because the dissolution of the DCPD crystals rendered the sample surfaces more homogeneous. This last phenomenon appeared to have, therefore, a higher influence on the scattering of the measurements than the increase of surface roughness noticed after immersion (Figure 12).

3.3.3 Evolution of samples immersed in TRISd

For the **30 minutes** immersion test, the static and dynamic conditions were considered equivalent; as a consequence only the tests in static conditions were performed (cf. Chapter 2, section 2.2) and the results are already discussed in the previous section.

For **day 1**, both conditions (static and dynamic) were tested. Since the samples were retrieved just before the first solution renewal, the only differences between these two conditions could be due to the apparatus and the stirring method (cf. Chapter 2). Results obtained in the TRISs and in the TRISd conditions were completely similar: the pH increased to 7.3 (Figure 22), a small amount of DCPA was detected in the core (Figure 21), leading to a slight decrease of mass and apparent density (Figure 9, Figure 10), without affecting the mechanical properties (Figure 41). It can thus be concluded that differences between samples immersed in TRISs and TRISd, arisen on later time-points, were more probably induced by the refresh (in TRISd) than by the setup.

Starting from day 1, two thirds of the TRIS solution were renewed every 24h. It is necessary to keep in mind, that the observed values of pH were thus also influenced by the pH of the fresh solution introduced during the refresh. As a reference, the pH of the fresh medium is plotted in green dotted lined in Figure 22.

Between t0 and **4 days**, the samples mass decreased of 11% (Figure 9). Given that no more DCPA was detected at day 4 (Figure 21), this change was most probably related to a partial dissolution of the DCPD phase. In parallel, the volume of the cylinders also diminished (Figure 8), resulting in a decrease of the apparent porosity of only 5% (Figure 10). Regarding the mechanical properties, a diminution of hardness (-40%) was assessed at the surface. The core, instead, did not undergo any detectable change in terms of mechanical properties (Figure 41). This result suggested that the increase of apparent porosity was not homogeneous and affected mainly a superficial crown on the outer part of the sample. This crown seemed not to be thick enough to influence *E* measured at the surface (Figure 41).

After **8 days** of immersion, a large loss of volume, mass and density (-14%, -24% and -12% respectively, Figure 8-Figure 10) was observed, probably because of a further dissolution of DCPD. The evolution of the macroscopic aspect of the surface was evident (Figure 13) and the µ-CT scan highlighted the presence of globular precipitates close to the surface. However, these precipitates were not directly on the surface but appeared below a layer, which seemed to be denser than the rest of the sample (Figure 28). The presence of 9 wt.% OCP in the core was evidenced by XRD (Table 7), and most probably corresponded to these globular precipitates. Although XRD analyses identified the presence of apatite at the surface (Figure 21), no clear precipitates were observed by SEM at the surface (Figure 31). However, the presence of apatite at the surface might be linked to the appearance of the denser outer layer observed by µ-CT (Figure 28). The precipitation of apatitic phases is likely to induce a pH decrease. Therefore, assuming that the DCPD dissolution rate and the daily decrease in pH associated to this phenomenon remained constant, the additional diminution observed in the pH curve from day 6 (Figure 22) could be related to the beginning of the precipitation of apatite and OCP phases. However, additional experiments should be carried out to confirm if apatite really precipitated during the stay in solution, or if it crystallised from an amorphous phase during the drying stage.
The appearance of OCP did not seem to alter the mechanical properties in the inner part of the samples (Figure 41). On the contrary, the gradual dissolution of DCPD and the consequent increase of porosity at the surface caused a decrease of hardness and Young's modulus (ΔH = -55%, ΔE = - 50%, Figure 41). Slight signs of "collapse" of the porous structure, moreover, started to be visible on the load-displacement curves at the surface (Figure 42).

Between 8 and **14 days** of immersion, the samples kept on loosing volume, mass and density (-18%, -30% and -15% compared to the initial value respectively, Figure 8-Figure 10). The strong loss of mass was likely linked to the dissolution of DCPD, which was partly compensated by the precipitation of OCP (64 wt.%) and apatite (36 wt.%) at the surface and of only OCP in the core (75 wt.%) (Figure 21). When observed by SEM, the morphology of the outer part of the samples resulted to be greatly altered: DCPD was no more visible and the surface appeared covered with tightly packed platelets (Figure 31). Moreover a layer of "spongy" precipitates was spread on most of the surface. Considering the phases revealed by XRD analyses at day 14, it can be supposed that the platelets observed were composed of OCP, while the "spongy" precipitates were made of apatite. The thickness of the layer composed of globular precipitates increased compared to the one at 8d, reaching a value of 900-1100 µm (Figure 28). Due to a high dispersion of the data, no clear trend was noticed for the hardness at the surface whereas, surprisingly, it seemed that the elastic modulus recovered slightly compared to day 8 but was still lower by far than the initial properties (-40%) (Figure 41). The dispersion of data, maybe, could be justified by the fact that precipitations were not homogeneously distributed (as visible in µ-CT images, cf. Figure 28) and affected, thus, differently one area to the other of the samples. For the first time, in the inner part of the specimens, a decrease of properties (on average -8% for *H* and -30% for *E,* Figure 41) was observed. This was probably caused by the dissolution of DCPD, as confirmed by the SEM observations revealing layers inside the initial DCPD crystals (Figure 34), as was previously reported in a study by Tas and Badhuri for DCPD dissolution in simulated body fluid [4].

3.3.4 Evolution of samples immersed in PBSd

As already discussed for the other immersion media, also in PBSd a quick drop of the solution pH was observed during the first **30 minutes** of immersion (from 7.43 to 7.23, Figure 23), simultaneously with the complete dissolution of the remaining MCPM at the surface, the formation of DCPA (Figure 14 and Figure 18), a strong decrease of density (-13%, Figure 10), and a significant decrease of hardness and Young's modulus (Δ≈-60% for both, Figure 35) in the core. The discussions of these phenomena were already exposed in detail for the TRIS solution in section 3.3.2; the same considerations can apply also for the case of PBSd .

However, the pH further decreased between 30 minutes and **day 1** in PBSd, while it re-increased in TRIS solution (Figure 23), probably because of the weaker buffering capacity of PBS. Consistently with the pH drop, the amount of DCPA detected after samples drying reached its maximum at 1d both in the core (81 wt.%) and at the surface (35.5 wt.%) (Figure 15). The samples density resulted to be around 9% lower than the initial one (Figure 10). Surprisingly, although more DCPA was formed compared to the 30 minutes time point, no further losses of mass and density were measured (Figure 9, Figure 10). Here again, a possible explanation for this difference might lie in the formation of phases, which could not be detected by XRD. This could be consistent with the detection of OCP as noticed at 4 days (Figure 21). Additional FT-IR spectrophotometry measurements would be of help to clarify this point.
At the surface, no modifications of the microstructure were observed (Figure 24) and the mechanical properties were still quite scattered (Figure 35). In the core, instead, some "porous" crystals, probably corresponding to DCPA, were noticed by SEM (Figure 32). The mechanical properties were comparable to those at 30 minutes, and still very low compared to the initial ones (Δ≈-60% for both *H* and *E,* Figure 35).

The pH of the PBS solution showed an increase at **day 2**, which is also to be linked to the renewal of the solution, which took place every 24h, starting from day 1. Despite the solution refresh, the pH decreased again between 2 and **4 days** of immersion, reaching the value of 7.10 (Figure 22) and therefore causing the detection of 55% DCPA in the core of the samples (Table 5). This acidification could also be justified by the concomitant dissolution of the DCPD phase and the precipitation of

OCP, as assessed in the core by XRD analyses (Figure 21). On the surface, no new crystalline phases were detected, but this could be explained by the fact that the precipitates were located under the surface, as testified by µ-CT images (Figure 24-Figure 25). In particular, the new crystals seemed to always appear in porosities (Figure 25). However, it is not yet well understood if they developed inside porosities, which had formed before, or if OCP grew at the expense of the DCPD surrounding phase. For solving this question a further assessment, possibly *in-situ*, between day 1 and day 4 would be necessary.
Consequently to the slight diminution of the proportion of DCPA in the core, the mechanical properties increased slightly when compared to those at 1 day (Δ≈-50% for both *H* and *E,* Figure 35).

Between day 4 and **day 8**, the apparent density was almost unchanged (-8% compared to time zero, Figure 10), but both the volume and the weight of the specimens decreased (Figure 8-Figure 9), suggesting that dissolution was taking place predominantly on samples surface. During the same period, a considerable amount of OCP (92 wt.%) appeared at the surface of the specimens (Table 2). As already mentioned earlier for 4 days, it seemed that there might have been a relation between the dissolution of DCPD and the precipitation of OCP. Indeed, the core was still mainly composed of DCPD (Table 5). The pH, although still lower than the reference one (as highlighted by the blue dotted line Figure 22), increased slightly from day 5 till 7.14. Since no more DCPA was detected (Figure 21), it could be hypothesised that after five days of immersion, the residual acidity inside the specimens was completely eliminated. Given that DCPD did not convert to DCPA anymore, in the core, the mechanical properties almost recovered their initial values (Δ*H* = 0%, Δ*E* = -20%) (Figure 35).
The bright precipitates observed in µ-CT images (Figure 24) formed a 700 µm thick layer on the external surface of the specimens. Although the precipitates themselves appeared brighter and therefore denser than the bulk of the cylinder, the surrounding porosities caused a low cohesion between the outer layer and the core of the sample (Figure 11, Figure 24). Compared to the µ-CT at 4 days, it seemed that the outer layer, which covered the first precipitates, was dissolved, as highlighted by the changes in sample diameter represented in Figure 24. This permitted to expose the OCP sheet-like platelets, as observed by SEM (Figure 29).
The increase in porosity on the outer part of the sample was logically detrimental for the mechanical properties of the samples: both *H* and *E*, in fact, were diminished (respectively -60% and -50% compared to initial properties, Figure 35). This loss of mechanical properties was well visible also on the load-displacement curves obtained by micro-indentation (Figure 36): strong and rapid decrease of the applied load, in fact, showed that some “collapse” phenomena of the highly porous structure took place during the test.

At the end of the test, after **14 days** of immersion, a further loss of mass (-19%, Figure 9) and apparent density (-13%, Figure 10) were measured. From day 11 on, and despite the daily refresh, the pH always decreased back to 7.20 (Figure 22). This could be caused by the further precipitation of OCP. This latter was evidenced by the increased thickness of the precipitates layer (700 µm at 8d and 800 µm at 14d, Figure 24). The surface was mainly made of OCP (95 wt.%, Figure 21), as also confirmed by the presence of thin sheet-like platelets observed by SEM (Figure 29). The remaining crystalline phase was identified as apatite. The core, on the other hand was still composed of 92 wt.% DCPD but the crystals started to display evident signs of dissolution (Figure 32). As a consequence, the mechanical properties in the core began to significantly decrease (Δ*H* = -40% and Δ*E* = -50% compared to initial values, Figure 35). This is therefore the first time-point for which we could infer that the diminution of *H* and *E* in the core was indeed due to the evolution of the cement microstructure. Also at the surface, the mechanical properties further decreased (Δ*H* = - 68%, Δ*E* = -60% compared to initial values, Figure 35).

3.3.5 Influence of the immersion conditions

Based on the previous paragraphs, schematic representations of the main evolutions observed in the TRIS and PBS solutions are reported in Figure 46 to Figure 48. A qualitative evolution of the mechanical properties assessed by micro-indentation at the surface (in blue) and in the core (in red) is presented. These changes are correlated with the decrease (↓) and the increase (↑) of the proportion of crystalline phases and to the mass evolution versus immersion time (as qualitatively represented by the weights for scales). Finally a slice extracted from a µ-CT reconstructed volume and a SEM image of the surface depict the morphology of the material, at the macro and micro scale, after 14 days of immersion.

Comparing the different schemes, it is possible to make some hypotheses about the influence of the medium and of the immersion conditions on the evolution of the material. The changes observed after 30 minutes of immersion, however, will not be taken into account. These phenomena (pH decrease, detection of DCPA, etc.), in fact, were common to all the conditions of immersion. In addition, the presence of DCPA was likely due to an artefact induced by the drying procedure rather than a real evolution of the material consequent to the immersion tests.

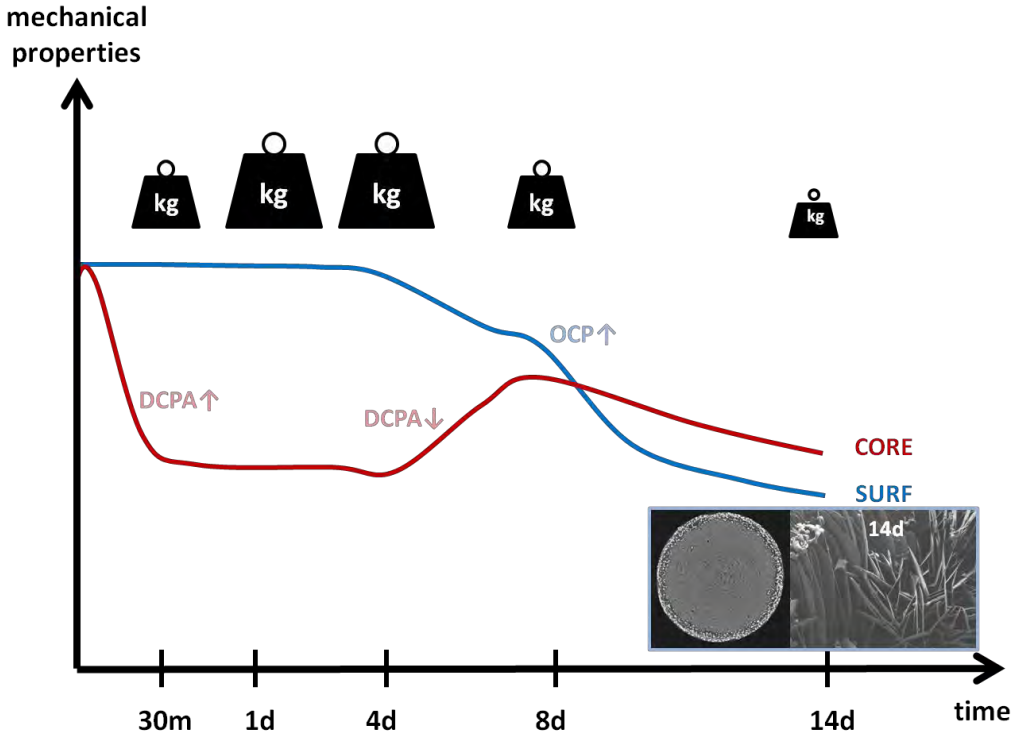

Figure 46: Schematic representation of the main changes observed during immersion of DCPD samples in PBS. The weights for scales represent the changes of the sample mass

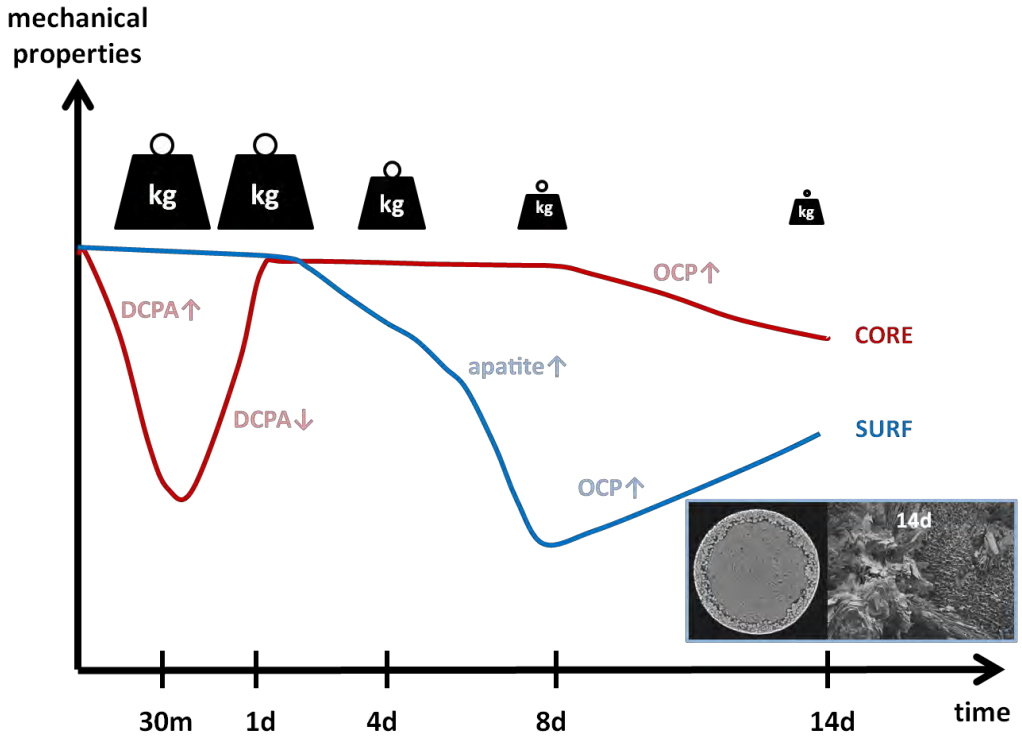

Figure 47: Schematic representation of the main changes observed during immersion of DCPD samples in TRISd. The weights for scales represent the changes of the sample mass

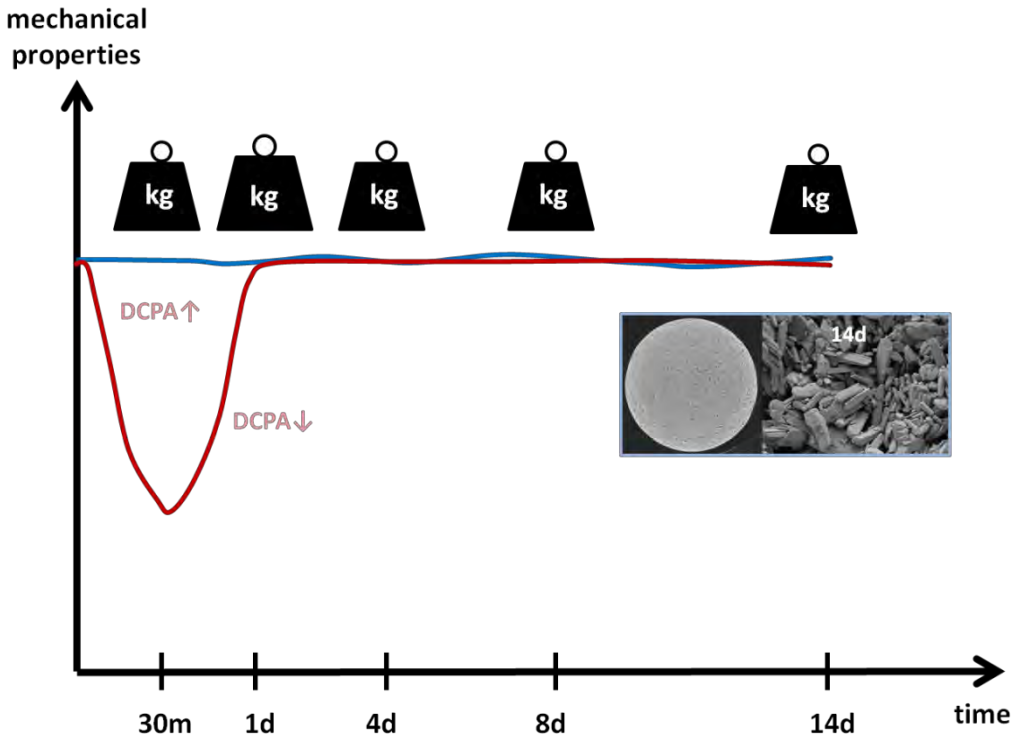

Figure 48: Schematic representation of the main changes observed during immersion of DCPD samples in TRISs. The weights for scales represent the changes of the sample mass

PBS versus TRIS

A first comparison can be done between the tests in PBSd and in TRISd (Figure 46 and Figure 47). Given that both tests were performed in dynamic conditions, the comparison between the results obtained in these two cases is likely to show the influence of the dissolution medium on the evolution of the material.

In particular, the precipitation of crystalline phases seemed to take place later in TRISd (from 8 days on) than in PBSd (from 4 days on), but, once these phenomena started, their evolution was more rapid in TRISd than in PBSd. The faster formation of precipitates in PBS is coherent with its higher content of ions: in this solution the saturation was likely reached more quickly than in TRIS, fostering, as a consequence, an earlier nucleation of new phases. On the other hand, in TRIS the dissolution process was favoured because of the absence of calcium and phosphate ions in the initial medium. Once the first precipitates were formed, the strong dissolution of the DCPD phase in this solution provided a high amount of calcium and phosphate ions necessary for sustaining the precipitation phenomena. For this reason, maybe, although they appeared later, the precipitates in TRIS tended to increase more quickly than in PBS.

The composition of the medium was also proved to have an influence on the nature of crystalline phases. In PBSd, DCPA was detected to a larger extent and for a longer time than in TRISd (above all in the core). The dissolution of the MCPM may have caused a stronger decrease of pH in PBSd than in TRISd, maybe because the first solution presents a weaker buffering capacity (Figure 22). This condition of higher residual acidity, both in the medium surrounding the specimens an in the inner part of the samples, likely enhanced the conversion of the DCPD phase into DCPA, leading to a higher final content of DCPA in the samples immersed in PBS. Moreover, for later time-points, PBSd favoured the formation of OCP, while TRISd fostered both OCP and apatite. This phenomenon was maybe due to the lower pH displayed by PBSd: OCP is indeed more stable than apatite at physiological pH (cf. Figure 10 of chapter 1). However, OCP was detected also in the inner part of samples in TRISd: in confined zones, like the porosities in the core of the specimen, in fact, the pH can be locally different and enhance, thus, the precipitation of phases that do not appear, instead, at the surface.

Also the morphology of the precipitates differed quite significantly, on a macro and micro level, between PBSd and TRISd. Small precipitates of thin platelets were observed in PBSd, while big globular agglomerates of platelets and “spongy” precipitations were noticed in TRISd (Figure 29, Figure 31). These differences are particularly highlighted when comparing the µ-CT scans for the different conditions (Figure 24, Figure 28).
All these differences definitely affected the mechanical properties, which displayed a clearly different evolution (both at the surface and in the core) in PBSd and TRISd (Figure 46, Figure 47). In particular, considering the last time-point (14d), although the weight and volume loss experienced in TRISd were higher by a factor 2 than in PBSd (Figure 8, Figure 9), the mechanical deterioration of the samples at the surface was more pronounced in PBSd (ΔH = - 68%, ΔE = - 60% compared to initial values, Figure 35) than in TRISd ($\Delta H \approx 0\%$, ΔE = - 40% compared to initial values, Figure 41). This phenomenon could be justified by the different morphology of the precipitates observed after immersion in the two solutions (Figure 24, Figure 28, Figure 29, Figure 31). The new crystalline phases noticed on the surface of specimens immersed in TRISd, in fact, appeared much more packed and cohesive than those found in PBSd and they might have presented, therefore, better mechanical properties.

Static versus dynamic

Comparing, instead, the results obtained in TRISs and TRISd, the influence of the refresh of the medium can be evaluated. Indeed, as already discussed in the section 3.3.3, the results obtained in TRISs and TRISd at day one were completely similar, proving that the use of different apparatus for the two conditions did not significantly influence the sample evolution. Differences noticed on later time-points were therefore considered as due to the static versus dynamic conditions only.
This parameter appeared to be crucial, above all on the long term (Figure 47 and Figure 48). For short time-points (up to 4 days), in fact, samples immersed in the two media followed quite similar evolutions. It should however be noticed that the daily refresh of the solution probably permitted to eliminate the residual internal acidity of brushite cements more rapidly than in static conditions. Indeed, DCPA was not detected any more after only 4 days in TRISd, whereas it remained until day 8 in TRISs. After 4 days, the evolution of the material was much more pronounced in TRISd than in TRISs. Precipitation of new phases at the surface and in the core, loss of mass and decrease of mechanical properties are all phenomena observed in dynamic conditions, but almost totally absent in static ones.

3.3.6 Experimental methods: mechanical properties

An important aspect of the present study was linked to the use of spherical micro-indentation for assessing the mechanical properties of DCPD samples and their evolution along time of immersion. Indeed, in other studies, this point is generally disregarded, and, when it is investigated, compressive strength measurements are preferred [14, 15]. Few papers also involve the use of other tests (such as 4 point bending, tension, torsion) [7]; in all cases, nevertheless, the methods employed to assess the mechanical properties involved the whole volume of the sample in the test, providing, then, a global measurement of the mechanical characteristics. Considering the differences of properties experienced between, for example, the outer and the inner parts of samples, it seems that a local measurement would be more appropriate to monitor the evolution of the samples and to correlate the mechanical properties with physico-chemical and microstructural aspects.

At time zero some differences were noticed between the surface and the core of the specimens: in particular, higher mechanical properties were measured at the surface than in the core (between 20% and 30% higher at the surface). This difference could be justified by some inhomogeneity and the preferential orientation of DCPD crystals on the surface. For all these reasons the choice of two separate references for surface and core appeared logical.
Given that the micro-indentation technique is quasi-non-destructive and requires very small surfaces for each test, it was possible to perform several indentations on the same specimen, without preventing it to be used for further tests. As a consequence, in the present work, each sample was tested at the surface before and after immersion. In this way the final results were not affected by the dispersion observed for the measurements at time zero and likely caused by the intrinsic differences between one sample and the other (Figure 4, Figure 5). This scattering of properties at time zero appears coherent with what observed in literature: Grover et al. [15], for example, obtained a standard deviation of around 30% when they measured the compressive strength of brushite cements.

Considering the results obtained at the surface and in the core after immersion it appears quite clearly that one of the crucial aspects for performing indentation tests is the surface preparation. Almost all the data obtained at the surface, in fact, were quite scattered, above all for the first time-points (Figure 35, Figure 38, Figure 41). Only when the physico-chemical and microstructural changes of the surface were enough pronounced, they could overcome the inhomogeneity of properties of the surface and be reflected into a clear trend of the values of hardness and Young's modulus. On the other hand, in the core, where the indented material was more homogeneous, the measurements

resulted much less scattered already at time zero (Figure 35, Figure 38, Figure 41). It can be stated, therefore, that the surface preparation and roughness can strongly influence both the precision and the accuracy of the measurements. This was already evidenced in previous studies [2] and was therefore taken into account from the start of this study: this is the reason why, for example, it was decided to maintain the lower flat surface of the moulds in contact with an acetate film during cement setting (cf. Chapter 2, paragraph 2.2.1).
However, it was shown that this precaution was not completely sufficient: also the presence of inhomogeneity in the specimens appeared to hinder the interpretation of the micro-indentation measurements. On the other hand, the scattering observed from one point to the other of the same specimen is a further proof of the fact that the indentation test was indeed sensible on a local scale. Therefore, it should be remembered that the sample processing procedure should always be optimised on a given material when one is willing to perform micro-indentation tests. Although evident improvements were achieved in the present work, additional enhancements are probably required, in order to further reduce the measurements scattering. For example, an increase of the sphere radius which allows to characterise a large volume (see Chapter 1, section 1.6.4) or the improvement of the sample processing.

Hardness and Young's modulus, however, always displayed a very similar trend. A clear evolution of mechanical properties, could be observed and linked to the changes of structural characteristics of the samples. In particular a strong connection between the crystalline phases present in the specimen and their mechanical properties could be highlighted. Regardless the solution of immersion, hardness and elastic modulus decreased when DCPA was present and increased again when this phase was not detected anymore. This observation appears coherent with the highly porous morphology of the DCPA crystals observed by SEM (Figure 32). Also the literature seems to corroborate this hypothesis: some studies state, in fact, that the conversion of DCPD into DCPA implies a loss of strength of each single crystal and, therefore, of the whole sample [8, 12]. Also, the dissolution of DCPD had a strong detrimental influence on the hardness and the Young's modulus of the samples, as expected (i.e., at the surface after 8 days in TRISd, Figure 41). At the surface, where this dissolution was accompanied by the precipitation of OCP and apatite, the formation of new phases did not compensate the properties loss. This was probably due to the morphology of the precipitates, which generally appeared quite porous and not cohesive (Figure 24, Figure 28).

As far as the testing conditions are concerned, the assessment of mechanical properties in humid conditions seemed to strongly influence the outcome of the tests compared to the tests on dry samples (Figure 44). When comparing the dry and the humid references, the influence of humidity on the mechanical properties seemed evident. Assuming that, DCPA was detected after 30 minutes of immersion as a consequence of the drying procedure, no DCPA should be present in the sample when still in humid conditions. Unfortunately, the composition of the humid sample was not analysed when the mechanical tests were performed. However, if the assumption about the origin of DCPA is correct, the reference in humid conditions should be composed of 100 wt.% DCPD, i.e. comparable to the composition and the microstructure of samples at t0. Therefore, the decrease of *H* and *E* compared to the dry reference should be purely linked to the presence of water.
Beside, this difference was also observed after 14 days of immersion in TRISs (Figure 44), when the composition of the specimens was for sure of pure DCPD (Table 3).
Generally, when measured in presence of moisture, the mechanical properties appeared to be strongly reduced compared to the ones measured for the very same sample in dry conditions (Figure 44). This is particularly the case for hardness (-41% decrease), more than for the Young's modulus (-16% average decrease). This phenomenon is coherent with the known influence of water-based liquids on the mechanical properties of hydrated crystals, especially on dihydrate calcium sulfate, known as gypsum. Gypsum is a material which might be compared to brushite cements in terms of microstructure (entangled platelets) and of similar formula ($CaSO_4 \cdot 2H_2O$ vs. $CaHPO_4 \cdot 2H_2O$). When gypsum is immersed in water, its fracture strength in flexion and compression are decreased by half [12, 16], whereas its Young's modulus is only decreased by 15% [17, 18]. The deleterious influence of

water on properties is explained by the influence of water on the ionic bonds between crystals, as it had directly been measured by AFM [19]. The higher sensibility noted on hardness as compared to elastic modulus can be interpreted as the combination of lower intercristalline bonds and of the apparition of irreversible crystal sliding allowing a quasi-plastic behavior in wet conditions [18]. Due to relatively close structure between gypsum and DCPD cements (entanglement of di-hydrated crystals during a setting reaction), the results obtained in indentation appears as logical. The load-penetration curves measured during indentation (Figure 45) clearly support the larger irreversible behavior of humid samples compared to the dry ones.

To conclude, micro-indentation, although affected by the surface preparation, resulted to be a suitable technique for the assessment of the evolution of the mechanical properties of degraded materials. With such a local test, in fact, it was possible to evaluate the influence of the structural and physico-chemical changes on the mechanical characteristics of the samples. In this way it was possible to measure the gradient of properties which arose between the surface and the core of the specimens after immersion. On the opposite, this could not have been possible with a classic test such as compression.

3.3.5 Comparison with Literature

Comparing the results obtained here with those present in literature, common points were found. Both Juhasz and Mandel [20, 21], for example, have demonstrated the formation of OCP on DCPD samples immersed in pseudo-physiological conditions (in SBF and DMEM respectively). Moreover, Mandel [21] stated that when the pH of the solution drops to 6.8-7.2, OCP precipitates rather than hydroxyapatite. The results of our study, although conducted in other media, seemed in agreement with these findings. In fact we observed an important formation of OCP for samples immersed in PBSd between day 4 and 8, that is to say when the pH of the medium was between 7.0 and 7.2. On the other hand in TRISd, where the pH was slightly higher (7.2-7.3), the presence of apatite was detected at the surface before that of OCP. In both cases, however, as suggested also by Kanzaki [22], DCPD in pseudo-physiological conditions did not directly convert into apatite, but rather dissolved and re-precipitated, as supported by the strong loss of mass detected both for samples in PBSd and TRISd during the time-points preceding the precipitation of new phases (-19 wt.% in PBSd at 14d and -24 wt.% in TRISd at 8d).
The precipitation of apatite (8 wt.%) was observed also by Grover et al. [15, 23] after 14 days of immersion of brushite cement in PBS in dynamic conditions (daily refresh). In our case the amount of apatite for the same time-point was lower (<5 wt.%), however, an important quantity of OCP was also detected (already since day 8). This dissimilarity can be explained by some differences in the two set-ups (Table 12). The difference of composition, the immersion liquid to mass of sample ratio (LMR) and the higher porosity of the samples could have significantly increased the dissolution of DCPD, as reflected on the mass loss, which resulted much more important in our case. This led to an earlier and more important precipitation (92 wt.% of OCP at day 8 in our case compared to 8 wt.% of apatite at day 14 in Grover's study).

Table 12: Set-up conditions and results of interest of Grover's al. study [15] compared to this thesis

Study	Sample composition	Sample porosity	PBS to Mass of sample Ratio	Mass loss after 8 days	Mass loss after 14 days
Grover and co-workers	34 wt.% DCPD + 66 wt.% β-TCP	43%	60 mL/cm^3, i.e. around 20 mL/g	7%	10%
			100 mL/g	8%	<15 wt.%
This work	100 wt.% DCPD100 wt.% in the core and 92 wt.%, plus 8 wt.% MCPM at the surface	60%	130 mL/g	15%	20%

In terms of mechanical properties another relevant study was carried out by Clement [2]. In his work, porous (60%) brushite cements were immersed in PBS in dynamic conditions (refresh as a function of pH variations) with a LMR of 60 mL/g and tested by micro-indentation. Interestingly the authors observed a decrease of properties at the surface after the first 30 minutes, followed by an increase at day 1 and a general increase in the core from day 14. The difference in the mechanical behaviour of the material compared to what observed in similar conditions (PBSd) in our study is likely linked, also in this case, to the difference in sample composition and LMR. Clement, in fact, used specimens composed mainly by DCPA (59 wt.%) and not by DCPD (22 wt.%); as a consequence the evolution of the phases, although treated in a similar way, was quite different from ours. In Clement's research the mechanical properties of the cements seemed to decrease during DCPD dissolution and in presence of DCPA, as in our case. On the other hand, Clement observed an increase of mechanical properties simultaneously with the appearance of OCP and apatite. In the present study, on the opposite, in concomitant with the precipitation of these phases, a general decrease of *H* and *E* was observed. As a conclusion, not only the crystalline phases present in the samples, but also the changes of porosity and microstructure should be taken into account. Depending on the mechanical properties of the initial material, the morphology and the localisation of the precipitates, in fact, the new phases could either strengthen or weaken the samples.

3.4 Conclusions and Perspectives

The present chapter collects the results obtained for DCPD cements immersed in PBS and TRIS (with or without refresh of the solution) for periods ranging from 30 minutes to 14 days. The evolution of the physico-chemical, micro-structural and mechanical properties of the material was followed and correlated all along the dissolution tests. Both the surface and the core of the samples were monitored, giving a new insight on the evolution of the material upon immersion.
A qualitative summary of the main results observed in the three different conditions of immersion (PBSd, TRISs and TRISd) are reported in the graphs (Figure 46 to Figure 48).

In general, a strong influence of the type of solution and of the experimental conditions was observed. In particular, the type of medium appeared to influence the composition and the morphology of the precipitates, as well as their kinetics of precipitation. An ion-rich solution, such as PBS, seemed to accelerate the first nucleation of new crystalline phases. On the other hand, the precipitating rate appeared to be slower when compared to a less ion-rich solution such as TRIS.
The refresh of the immersion solution resulted to be fundamental in the acceleration of the phenomena observed. Therefore, this testing condition not only approaches more closely the physiologic conditions, but also allows performing tests in a reasonable timeframe.

Whatever the condition of immersion, the use of micro-indentation resulted of great utility and interest for the local evaluation of the mechanical properties of degraded materials.

All the findings exposed here confirm, finally, the strong link between physico-chemical, micro-structural and mechanical changes and the importance of considering all these aspects when studying the evolution of a material.

In this perspective additional tests would be of help for further clarifications. In particular it would be interesting to:

- measure the ions release in the immersion media: this would help to better understand the dissolution and precipitation phenomena observed. It should be noted that the immersion solutions have been collected and ions concentrations measurements are on-going;
- perform *in-situ* monitoring of the evolution of the samples after immersion. In particular, *in-situ* XRD, μ-CT and micro-indentation on sample surface are suggested; this would avoid potential structural changes during drying.
- carry out Fourier-transformed Infrared spectroscopy (FT-IR) measurements: this technique would help identifying the possible presence of amorphous phases and citrate ions which could not be detected using XRD analyses;
- modify the drying protocol of the samples that have been immersed, in order to verify if this step is the cause of the formation of DCPA. In this case a different drying procedure or an improvement of the fabrication process will be required for future tests;
- perform further indentation tests in humid conditions at different time-points. Repeat the test at 30 minutes checking, at the same time, the sample composition in presence of humidity in order to verify if the conversion of DCPD into DCPA had taken place or not;
- carry out tests on period longer than 14 days in order to check if the mechanical properties keep on decreasing during immersion or augment due to the precipitation of new phases. Longer time-points, moreover, would likely allow the observation of more significant changes, also in the inner part of the samples.

References

1. Miller M, et al., *Surface roughness criteria for cement paste nanoindentation.* Cem Concr Res, 2008. 38: p. 10.
2. Clement, P., *Détermination des proprietés mécaniques de céramiques poreuses par essais de micronindentation instrumenée sphérique.* Ph.D. Thesis, 2013.
3. Baud, P., et al., *Geometric attributes of discrete compaction bands and their effect on permeability in porous sandstone.* Poro-mechanics, Destech Publications, 2009: p. 6.
4. Tas, A.C. and S.B. Bhaduri, *Chemical Processing of CaHPO4·2H2O.* Journal of the American Ceramic Society, 2004. 87(12): p. 2195-2200.
5. Bohner, M., H.P. Merkle, and J. Lemaitre, *In vitro aging of a calcium phosphate cement.* Journal of Materials Science: Materials in Medicine, 2000. 11(3): p. 155-162.
6. Martin, R.I. and P.W. Brown, *Phase Equilibria Among Acid Calcium Phosphates.* Journal of the American Ceramic Society, 1997. 80(5): p. 1263-1266.
7. Charrière, E., et al., *Mechanical characterization of brushite and hydroxyapatite cements.* Biomaterials, 2001. 22(21): p. 2937-2945.
8. Gbureck, U., et al., *Factors influencing calcium phosphate cement shelf-life.* Biomaterials, 2005. 26(17): p. 3691-3697.
9. Fulmer, M.T. and P.W. Brown, *Hydrolysis of dicalcium phosphate dihydrate to hydroxyapatite.* J Mater Sci Mater Med, 1998. 9(4): p. 197-202.
10. Giocondi, J.L., et al., *Molecular mechanisms of crystallization impacting calcium phosphate cements.* Philosophical transactions. Series A, Mathematical, physical, and engineering sciences, 2010. 368(1917): p. 1937-1961.
11. Cama, G., et al., *Tailoring brushite for in situ setting bone cements.* Materials Chemistry and Physics, 2011. 130(3): p. 1139-1145.
12. Chappuis, J., *A new model for a better understanding of the cohesion of hardened hydraulic materials.* Colloids and Surfaces A: Physicochemical and Engineering Aspects, 1999. 156(1–3): p. 223-241.
13. Hofmann, M.P., et al., *FTIR-monitoring of a fast setting brushite bone cement: effect of intermediate phases.* Journal of Materials Chemistry, 2006. 16: p. 3199–3206.
14. Huan, Z. and J. Chang, *Novel bioactive composite bone cements based on the b-tricalcium phosphate-monocalcium phosphate monohydrate composite cement system.* Acta Biomaterialia, 2009. 5(4): p. 1253-1264.
15. Grover, L.M., et al., *In vitro ageing of brushite calcium phosphate cement.* Biomaterials, 2003. 24: p. 4133–4141.
16. Andrews, H., *The effect of water contents on the strength of calcium sulfate plaster products.* J. Soc. Chem. Ind., 1946(5): p. 125-128.
17. Badens, E., et al., *Relation between Young's Modulus of set plaster and complete wetting of grain boundaries by water.* Colloids and Surfaces A: Physicochemical and Engineering Aspects, 1999. 156(1–3): p. 373-379.
18. Saâdaoui, M., et al., *Internal friction study of the influence of humidity on set plaster.* Journal of the European Ceramic Society, 2005. 25(14): p. 3281-3285.
19. Finot, E., E. Lesniewska, and J. Mutin, Journal of chemical physics. 111(14): p. 6590-6598.
20. Juhasz, J., et al., *Biological control of apatite growth in simulated body fluid and human blood serum.* Journal of Materials Science: Materials in Medicine, 2008. 19(4): p. 1823-1829.
21. Mandel, S. and A.C. Tas, *Brushite (CaHPO4·2H2O) to octacalcium phosphate (Ca8(HPO4)2(PO4)4·5H2O) transformation in DMEM solutions at 36.5 °C.* Materials Science and Engineering: C, 2010. 30(2): p. 245-254.
22. Kanzaki, N., et al., *Dissolution kinetics of dicalcium phosphate dihydrate under pseudophysiological conditions.* Journal of Crystal Growth, 2002. 235(1–4): p. 465-470.
23. Grover, L.M., et al., *Biologically mediated resorption of brushite cement in vitro.* Biomaterials, 2006. 27: p. 2178–2185.

CHAPTER 4: EVOLUTION OF POROUS B-TCP SAMPLES IN SOLUTIONS

4.1 Characterisation of β-TCP samples before immersion

Porous β-TCP samples of cylindrical shape (Ø = 9.5 mm, h = 8 mm) were received from Prof. M. Bohner (RMS Foundation, Switzerland) and resurfaced as explained in chapter 2 (paragraph 2.1.2). They were then fully characterised before immersion, referred hereafter as the reference state or time zero state.

At time zero, the material consisted only of β-TCP both at the surface and in the core, as displayed in Figure 1 (JCPDF file# 01-070-2065).

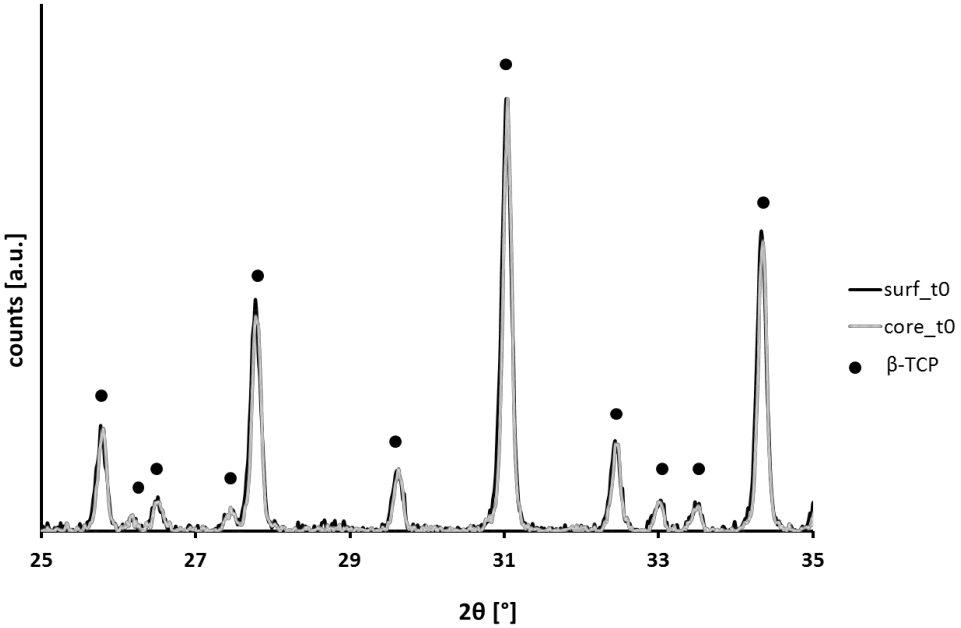

Figure 1: XRD pattern of β-TCP samples at the surface (in black) and in the core (in grey) before immersion

The microstructure of samples before immersion is shown in Figure 2: the material appeared quite homogeneous, with only small air bubbles (typically with a diameter of one hundred of microns or less) and no visible cracks. By looking at a section of sample (Figure 2-C), the surface of the specimen appeared slightly brighter than the inner part, as noted in chapter 3 for DCPD. This could be due to the sample fabrication, which processed through a cement setting reaction before thermal treatment (cf. Chapter 2). The thickness of this brighter layer, which was measured by image analysis, was equal to 50 µm (cf. "X-ray computed tomography technique" section, 2.4.2, in Chapter 2). In the present case, however, this characteristic do not affect the experimental characterisation, given that all the tests were performed on one of the two flat surfaces of the cylinders, which were resurfaced.

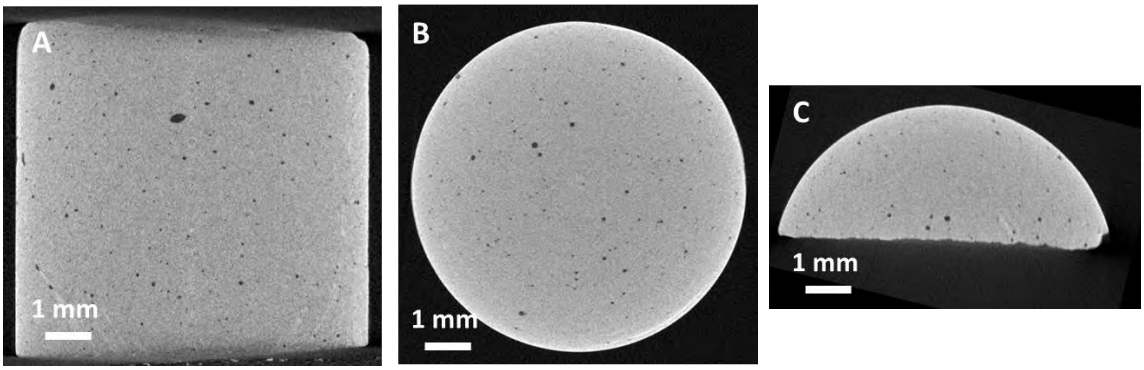

Figure 2: Frontal (A) and transverse (B) µ-CT images of an entire sample and of half a sample (C) of β-TCP at t0 (resolution of 10 µm/voxel)

The microstructure of the samples, observed by SEM before immersion, appeared composed of porous particles with a dimension generally inferior to 5 µm (Figure 3-A). Each particle, moreover, was made of smaller grains of 300-500 nm (as proved by Rietveld refinement of the XRD patterns of β-TCP presented in Figure 1) (Figure 3-B). Therefore the porosity presented two main levels: a bigger one (of some microns) due to the space between particles and a smaller one (of hundreds of nanometers) generated by the space left between the grains composing a particle.

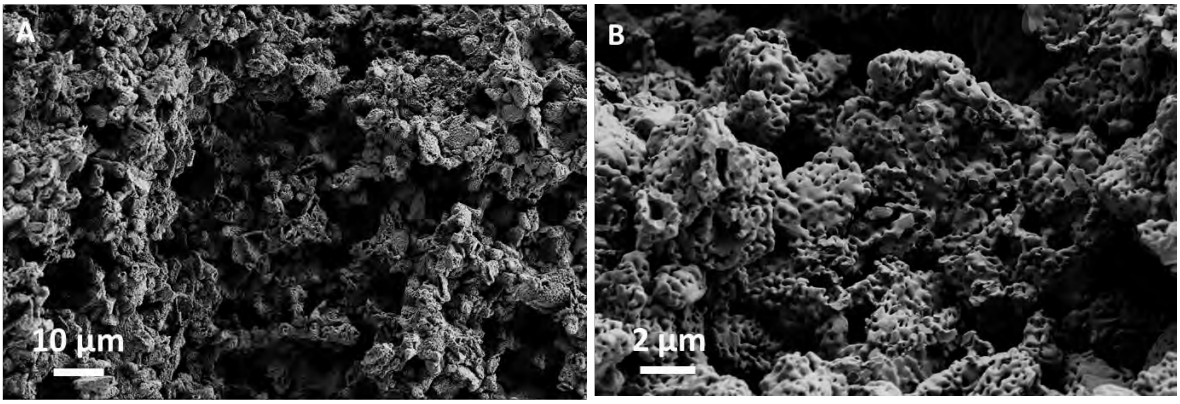

Figure 3: SEM micrographs of β-TCP samples in the core before immersion

The apparent porosity, calculated through mass and volume measurements, was equal to 79% on average. Moreover, the pore interconnection size of samples was assessed by mercury intrusion porosimetry (MIP). The results are presented as curves of incremental intrusion volume as a function of pore interconnection size.

Figure 4 displays the MIP curves obtained at the surface and in the core at time zero. Both surface and core of the same samples were tested separately, in order to obtain a value for each part of the specimen rather than a general value for its whole volume. Both appeared coherent with what observed by SEM (Figure 3): a bi-modal distribution, with a smaller peak at 170 nm and a bigger one at 3300 nm. This last resulted a bit higher in the core than at the surface, suggesting that at the surface the big porosities were slightly reduced in number.

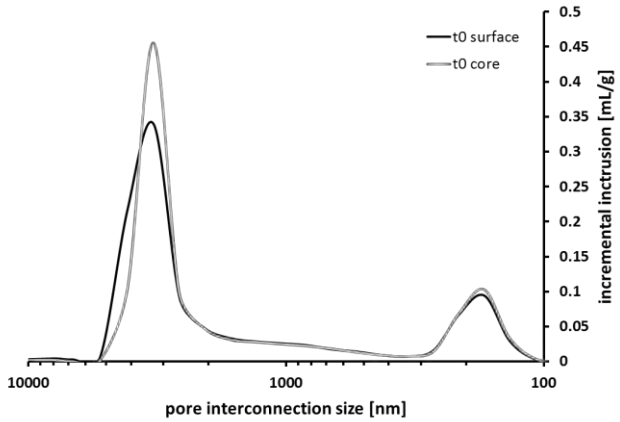

Figure 4: Incremental intrusion of Hg at the surface (in black) and in the core (in grey) of samples before immersion

The mechanical properties of β-TCP samples were assessed by means of the micro-indentation technique; experimental conditions are detailed in paragraph 2.4.3. Each specimen was indented at the surface (6 indentations) before immersion, while only four reference samples were indented in the core (9 indentations). The average values and standard deviations of *H* and *E* obtained at the surface and in the core at time zero are reported in Table 1.

It is worth to notice that on the overall the dispersion of data at time zero was quite limited. At the surface, in particular, the values of hardness showed a standard deviation of 10% (Figure 5); those of the elastic modulus, instead, were more dispersed, presenting a standard deviation of 18% (Figure 6). In the core *H* was characterised by a standard deviation of 17% (Figure 7) and *E* of 7% (Figure 8).

Finally, the roughness (RMS) of the surface and the core, measured by digital microscopy, were equal to 0.92 ± 0.33 µm and 0.94 ± 0.16 µm respectively. The maximum depth of penetration reached during micro-indentation tests at the surface and in the core was around 12 µm and resulted thus deep enough to avoid the influence of the surface roughness (which is considered significant till a depth equal to 5 times the roughness [1]).

Table 1: Average values and standard deviations of hardness and Young's modulus at t0

	avg H_{std} [MPa]	avg E_{std} [MPa]
surface	$5.0_{0.5}$	788_{139}
core	$3.8_{0.4}$	986_{44}

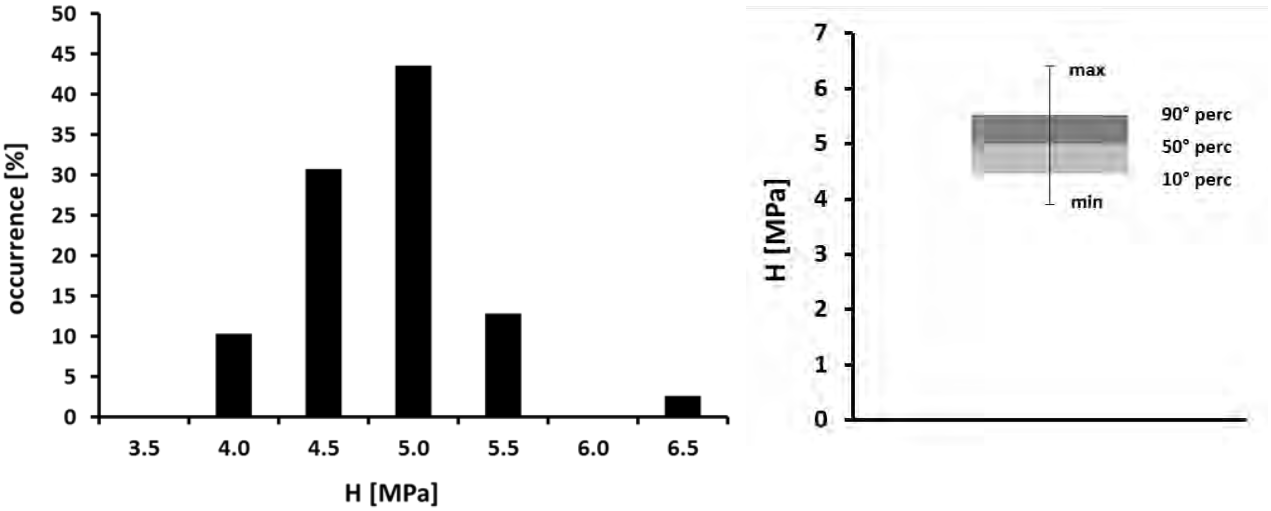

Figure 5: Distribution of hardness values obtained at the surface for all β-TCP samples at t0

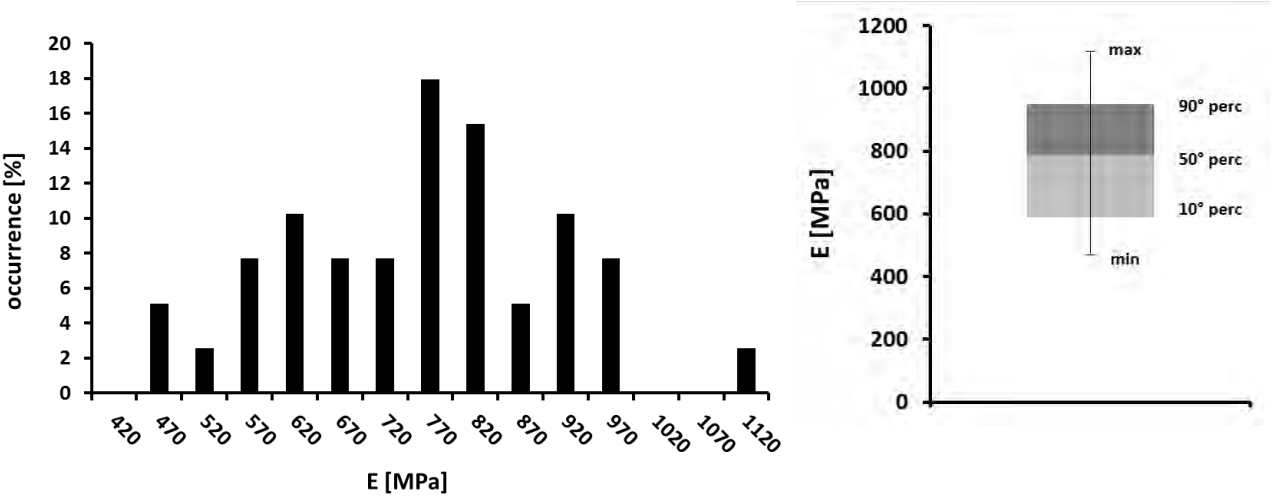

Figure 6: Distribution of values of Young's Modulus obtained at the surface for all β-TCP samples at t0

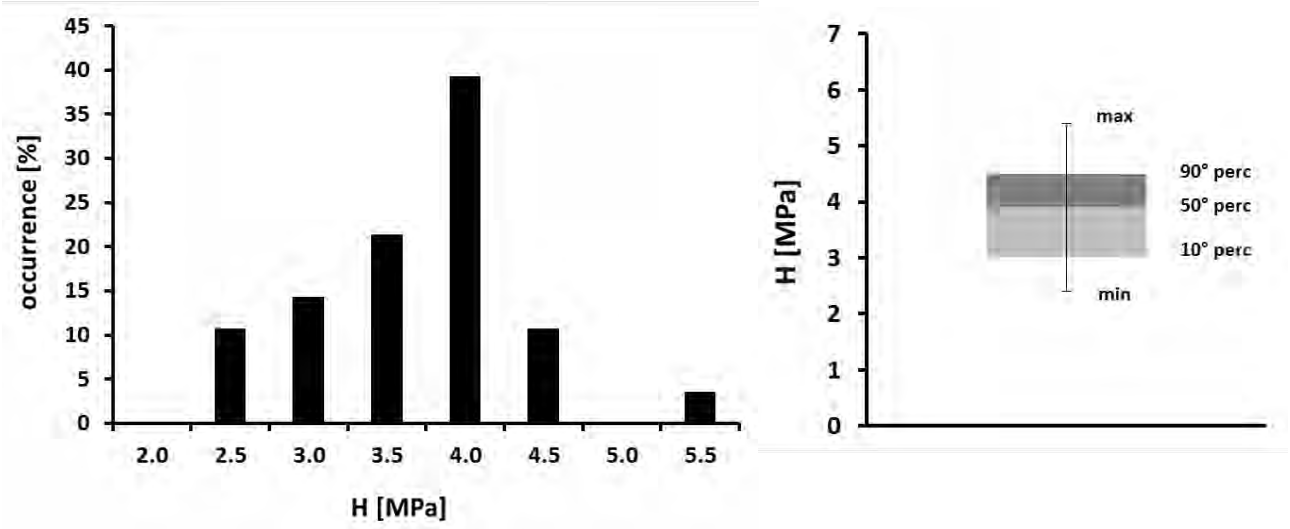

Figure 7: Distribution of hardness values obtained in the core for all β-TCP samples at t0

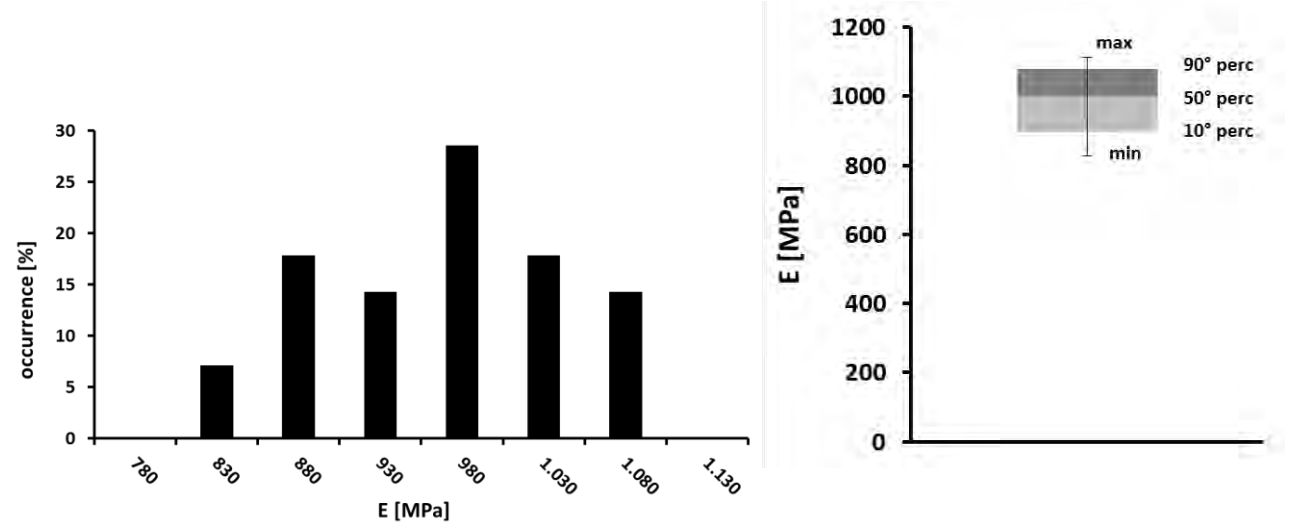

Figure 8: Distribution of values of Young's Modulus obtained in the core for all β-TCP samples at t0

4.2 Dissolution tests of β-TCP: Results

Porous β-TCP specimens underwent dissolution tests in TRIS in static and dynamic conditions (without/with refresh of the medium, denoted TRISs, respectively TRISd) and in PBS in dynamic conditions (PBSd). The time-points chosen were equal to: 1-2-4-8 weeks. The results are presented in the following sections.

4.2.1 Morphological changes

The evolutions of dimensions (measured with a ± 0.01 mm precision), mass (±0.1 mg) and apparent density of the specimens after different immersion times were calculated as percent changes compared to their initial values. The figures reported in the following graphs, thus, were obtained according to the equation:

$$\Delta X(\%) = \frac{X_{fin} - X_{in}}{X_{in}} * 100 \quad (1)$$

Where X_{in} is the value of the parameter before immersion and X_{fin} its value afterwards.

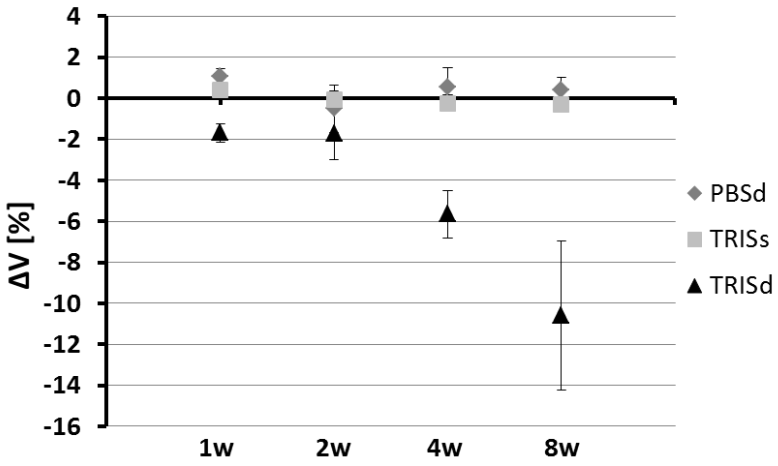

Figure 9: Percent variation of sample volume after immersion (average volume at t_0 = 0.6 cm^3), n=3 (n being the number of samples per condition)

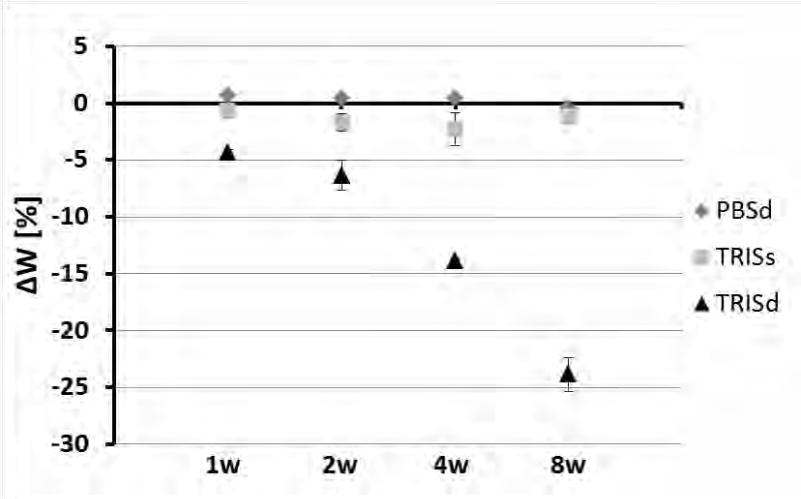

Figure 10: Percent variation of sample weight after immersion (average weight at t_0 = 0.36 g), n=3 (n being the number of samples per condition)

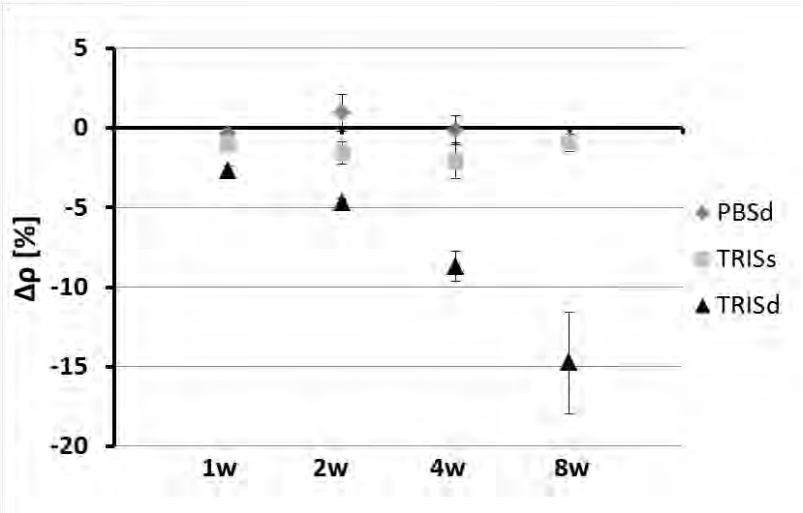

Figure 11: Percent variation of apparent density of samples after immersion (average density at t_0 = 0.7 g/cm^3), n=3 (n being the number of samples per condition)

On the overall, the data showed significant changes for samples immersed in TRISd, while only negligible variations for the specimens in the other two conditions (TRISs, PBSd).
In particular, as far as the volume is concerned (Figure 9), samples in TRISd displayed a loss that started from week 2 and constantly increased, reaching, after 8 weeks, a value of 10%. Samples immersed in TRISs and PBSd, instead, showed variations of volume close to zero all along the test.
Regarding the variation of weight, a very similar trend was observed (Figure 10). The mass loss of the specimens immersed in TRISd constantly decreased and was equal to 24% after 8 weeks. Immersion in TRISs and in PBSd did not affect significantly, instead, the mass of the specimens.
The evolution of average apparent density (Figure 11), reflected quite closely the trend observed for the mass. This appears quite reasonable, considering that the changes of weight were bigger than those of volume. As for the mass, samples in TRISd displayed the highest variations of apparent density: starting from -3% after 1 week of immersion, the density gradually decreased till the end of the test (8w, ΔW= -15%). Specimens in TRISs showed a slight loss of density after 2 and 4 weeks (around 2% in both cases), while no relevant changes were observed in PBSd.

4.2.2 Chemical changes

In parallel to the changes in volume, mass and density, the evolution of the crystalline phases present on and in the samples and the pH of the immersion solutions were monitored.

X-ray diffraction: evolution of the sample surface

After immersion, only few changes were observed on the composition of β-TCP samples. The first one was the presence of NaCl on the surface of samples dipped in PBS (Figure 12). The second phenomenon observed was the appearance of a small peak at 32.1° on the surface of samples immersed in TRISs and TRISd starting from week 2 (cf. arrow in Figure 13 and Figure 14). This peak could suggest the presence of apatite, but all the other peaks typical of this phase were not identified either because to small (such as the peak at 31.8°) or because hidden by the peaks of β-TCP. No other changes attributable to dissolution/re-precipitation phenomena were noticed in PBSd, in TRISs or in TRISd.

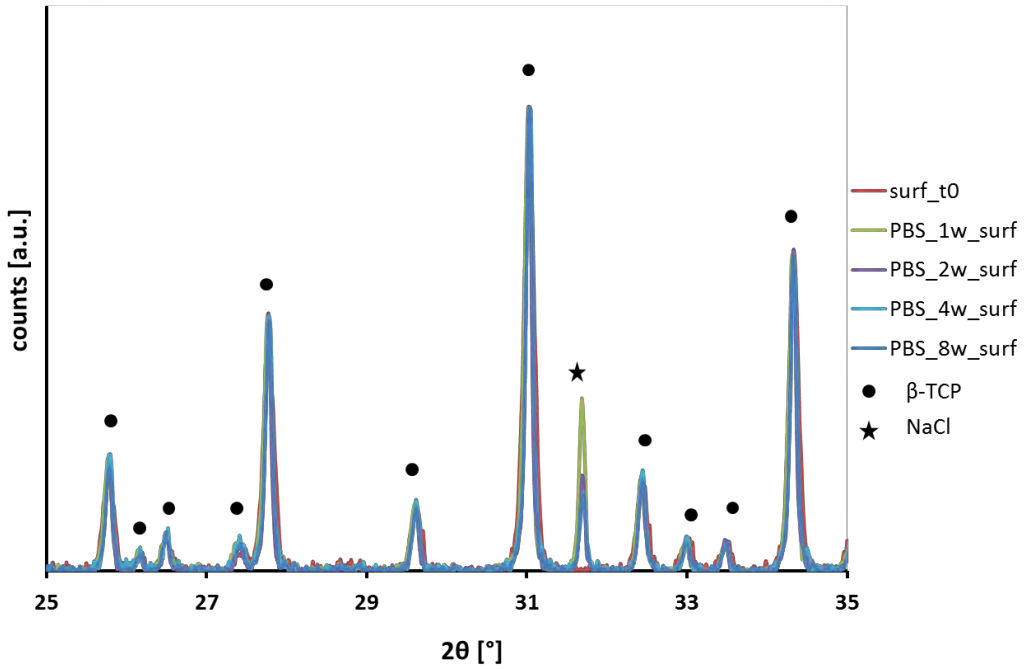

Figure 12: XRD patterns of β-TCP samples at the surface at time 0 and after 1-2-4-8 weeks in PBSd

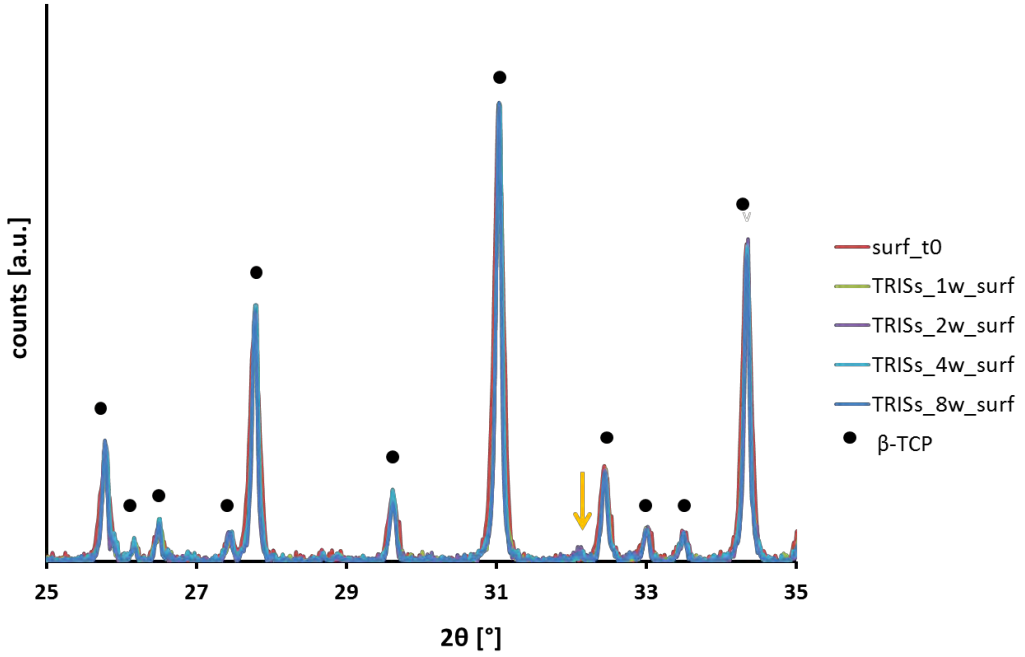

Figure 13: XRD patterns of β-TCP samples at the surface at time 0 and after 1-2-4-8 weeks in TRISs (arrow = peak at 32.1°)

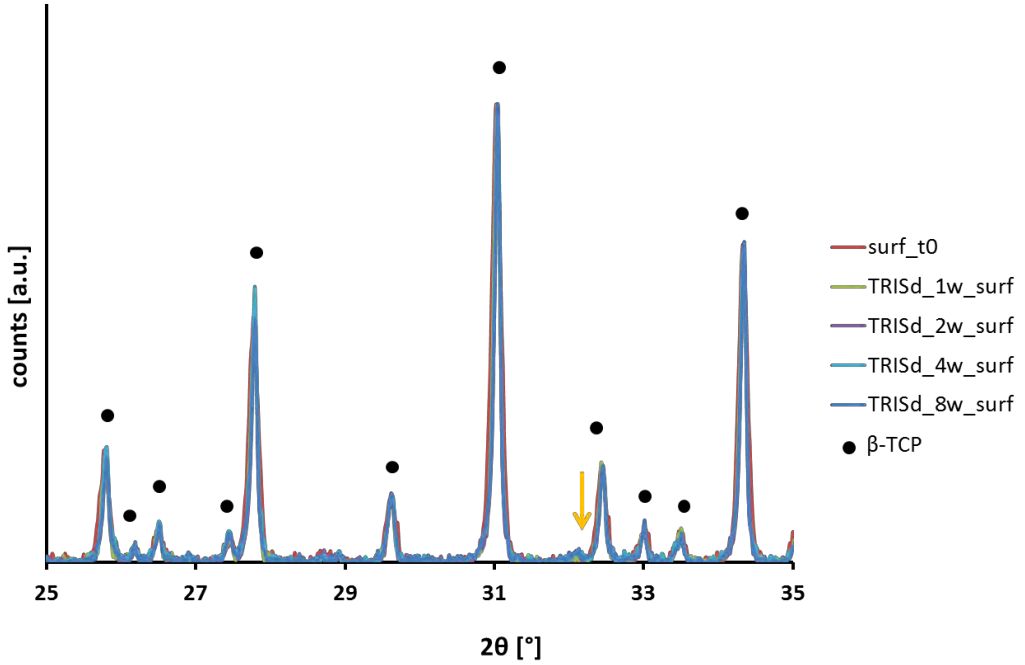

Figure 14: XRD patterns of β-TCP samples at the surface at time 0 and after 1-2-4-8 weeks in TRISd (arrow = peak at 32.1°)

X-ray diffraction: evolution of the sample core

Even less changes were observed in the core after immersion. In the inner part of the samples, in fact, only β-TCP was detected all along the tests in the three different conditions (PBSd, TRISs, TRISd, in Annex in Figure A.c.1, A.c.2, A.c.3 respectively).

pH evolution

The pH of the solutions where samples were immersed was measured all along the test. In case of dynamic conditions, the medium was daily renewed and the pH was measured just before the refresh. In parallel, the pH of reference solutions was also registered and plotted in dotted lines. For static conditions, the reference solution corresponded to the initial TRIS solution, which was kept at the same temperature in the same apparatus (orbital shaking), but without samples dipped inside. For the dynamic references, instead, the values were daily measured in the new medium used for the refresh. The results are reported in Figure 15 and Figure 16 (for clarity purposes an additional graph showing only the values of TRISd solution is presented in Annex).

Whatever the immersion conditions, no significant pH changes were recorded. The pH of PBSd, TRISs and TRISd fluctuated between 7.2 and 7.5, 7.2 and 7.3 and 7.4 and 7.5 respectively (Figure 15 and in Annex Figure A.c.4). In all cases, similar trends were observed for the references and the solutions where samples were immersed; for dynamic conditions, a temporal shift was noticed between fluctuations recorded for the references and the same fluctuations recorded for the solutions containing the samples (e.g. pH increase to 7.4 after 12 and 50 days in TRISd). The values reported for TRIS (static and dynamic) were generally lower than those reported for PBS, but this was due to the lower pH of the fresh solution.
Finally, as done for DCPD samples in Chapter 3, the pH of the first 30 minutes of immersion is reported in Figure 16. Contrary to what was observed for DCPD cements, β-TCP samples did not cause a sudden change of pH after immersion (variations < 0.05 pH unit).

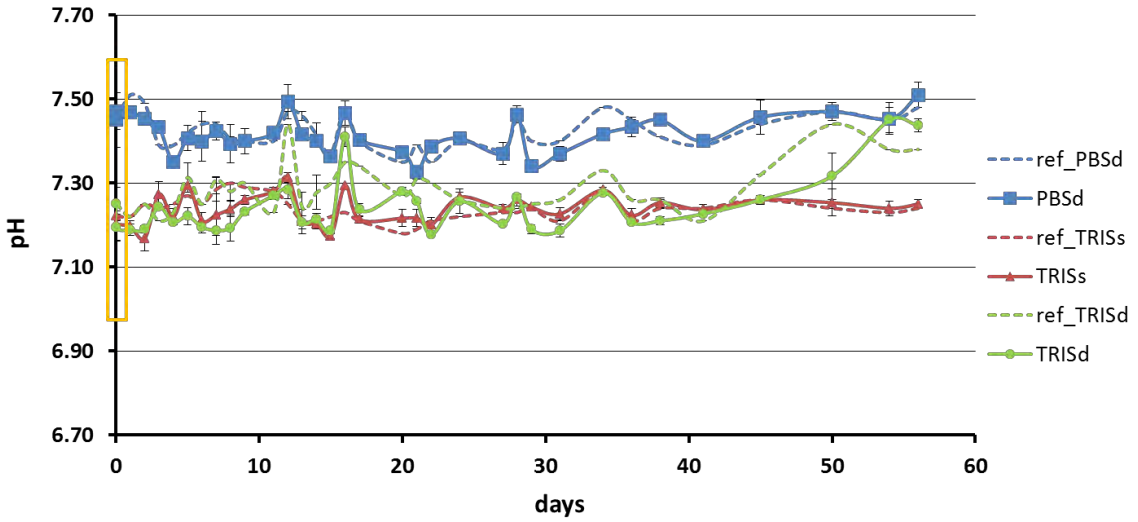

Figure 15: Evolution of pH of the solutions along the 8 weeks of test: solid lines for solutions containing samples and dotted lines for reference solutions (without samples).

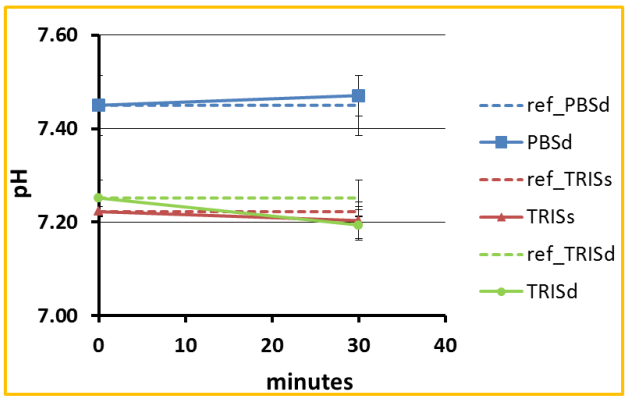

Figure 16: Evolution of pH of the solutions, first 30 minutes of immersion

4.2.3 Microstructural changes

The evolution of the samples microstructure was assessed by means of X-ray tomography. SEM analyses were also performed, but only for the longest immersion time (8 weeks). The results are collected in the present paragraph.

µ-Computed Tomography

The evolution along time of samples immersed in PBSd is reported in Figure 17. Neither the dimensions nor the microstructure of the material seemed to be altered during the tests.

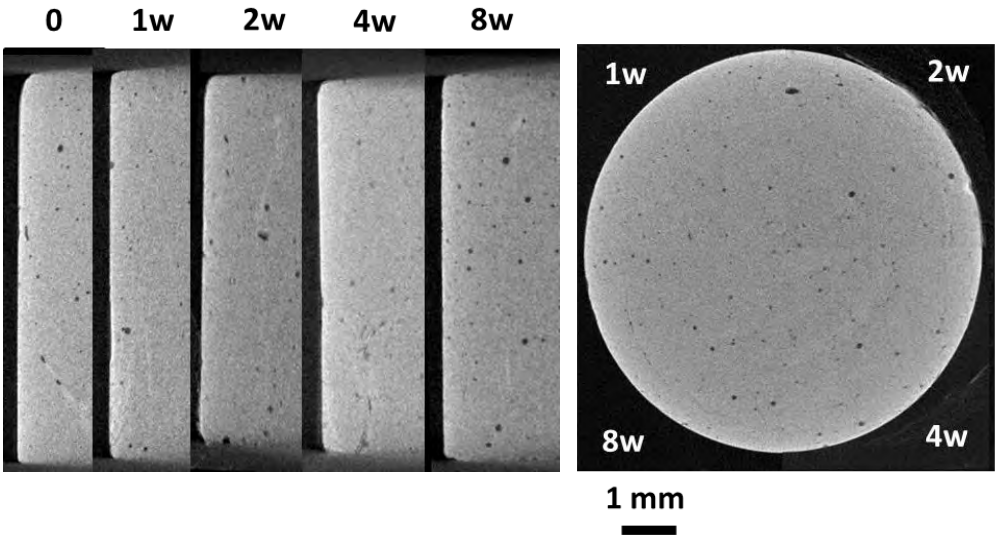

Figure 17: Frontal (left) and transverse (right) µ-CT images of β-TCP samples after different times of immersion in PBSd (resolution of 10 µm/voxel)

Also samples immersed in TRISs did not show significant changes during the first weeks of immersion neither in microstructure nor in dimensions (Figure 18). At the last time-point (8w), however, a modification was noticed close to the surface, where a ring around 350 µm thick was observed. This last seemed to be made of two layers: a first one at the surface, which appeared brighter than the rest of the sample, and a darker one underneath.

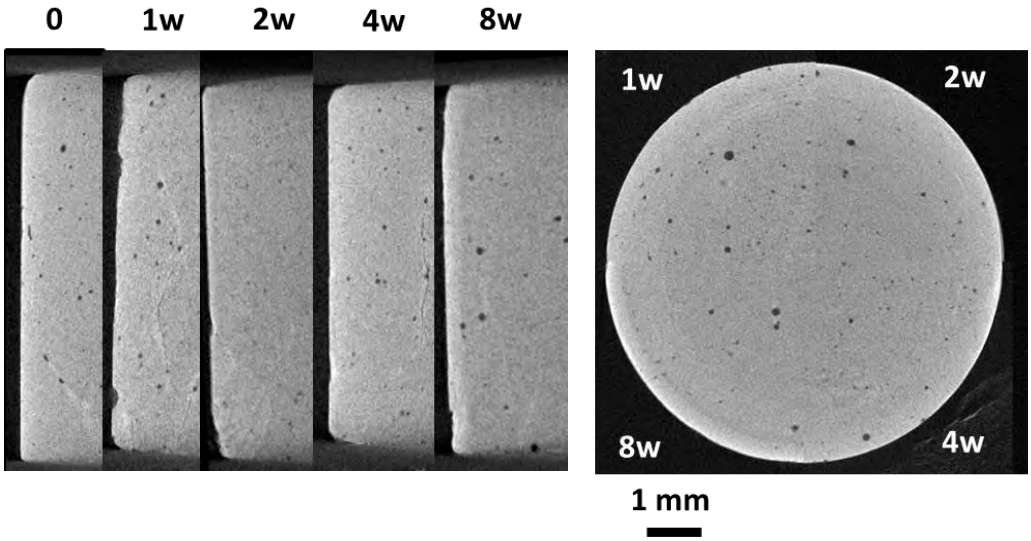

Figure 18: Frontal (left) and transverse (right) µ-CT images of β-TCP samples after different times of immersion in TRISs (resolution of 10 µm/voxel)

Samples immersed in TRISd underwent more evident changes (Figure 19). Already after one week, a slightly darker layer was noticed just below the surface. After 2 weeks, this layer appeared more evident and deeper in the sample. An observation at higher resolution (2 µm voxel size) clearly displayed the presence of this darker layer not exactly at the surface, but some hundreds of microns (200-300 µm) below it (Figure 20). After 4 weeks, the thickness of the layer reached around 600 µm. At this time-point, the layer did not shown a homogeneous grey level but appeared slightly darker in the underneath. At the end of the test, the layer increased towards the centre of the specimen. At the same time a bright, thin layer was observed at the surface. In parallel, starting from 4 weeks also the

diameter of the specimens visibly decreased, as testified by the gap present between the yellow circle in Figure 19 (representing the surface at t0) and the surface of the sample after 4w and 8w.

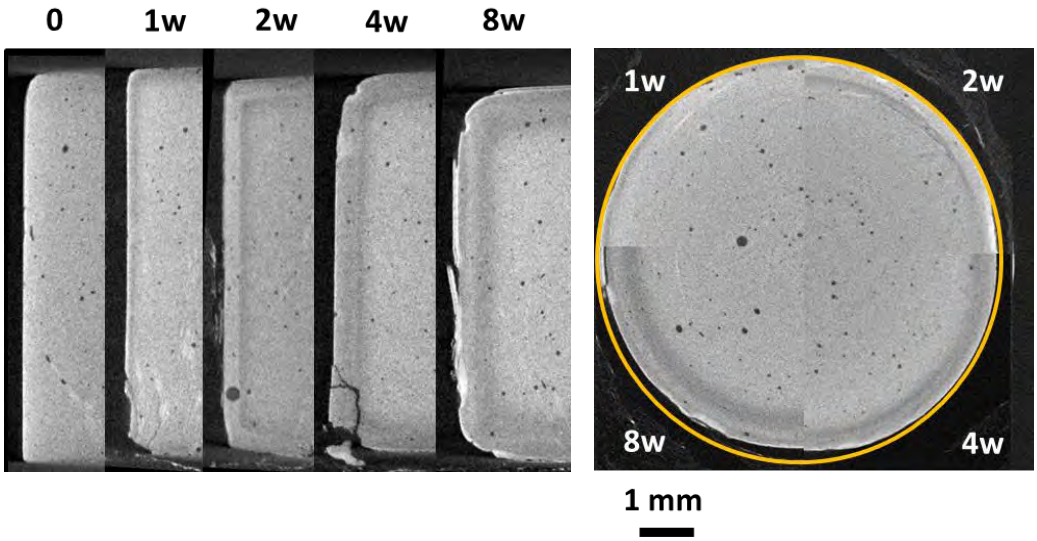

Figure 19: Frontal (left) and transverse (right) µ-CT images of β-TCP samples after different times of immersion in TRISd (resolution of 10 µm/voxel). The circle in yellow (transverse section) represents the circumference of the sample at t0

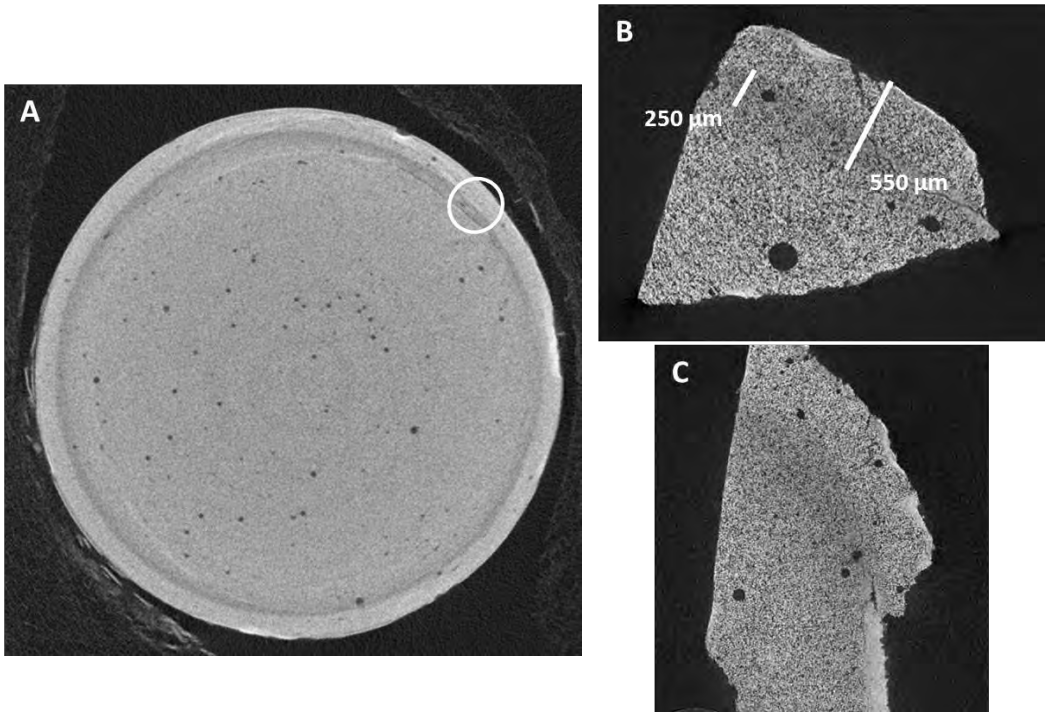

Figure 20: Transverse µ-CT image of β-TCP samples after 2 weeks in TRISd (resolution of 10 µm/voxel) (A). Higher resolution images of the circled area in A (transverse B, frontal C, 2 µm voxel size)

For a quantitative evaluation, µ-CT images were analysed by the ImageJ/Fiji shareware as detailed in Chapter 2, section 2.4.2. In particular, the thickness of the bright external layer (denoted "superficial crown") and of the dark porous one ("porous crown") were assessed at different time-points. Although the two layers were particularly visible in TRISd, the external crown, which was present already at time zero, was observed in all the specimens. Therefore, the image analyses were performed on all samples and not only for those in TRISd. The results are presented in Figure 21: each point corresponds to one

sample and the error bars represent the standard deviation of the thickness of the superficial layer around one given cylinder.

As far as samples in PBSd are concerned, the bright crown of around 50 µm already observed on µ-CT images at time zero (Figure 2) was still present at the end of the test. Indeed, its thickness gradually increased during immersion, reaching an average value of 140 µm after 8 weeks.
Also in TRISs the external crown grew, reaching an average value of 260 µm after 8 weeks. At the same time-point, the darker porous layer observed underneath the surface was 120 µm thick.
In TRISd the superficial crown gradually thickened till the average value of 150 µm at 8 weeks. The porous layer appeared already after 1 week of immersion (with a thickness of 180 µm), slightly grew after 2 weeks (230 µm), then greatly increased after 4 weeks (590 µm) and finally reached an average value of around 560 µm after 8 weeks.

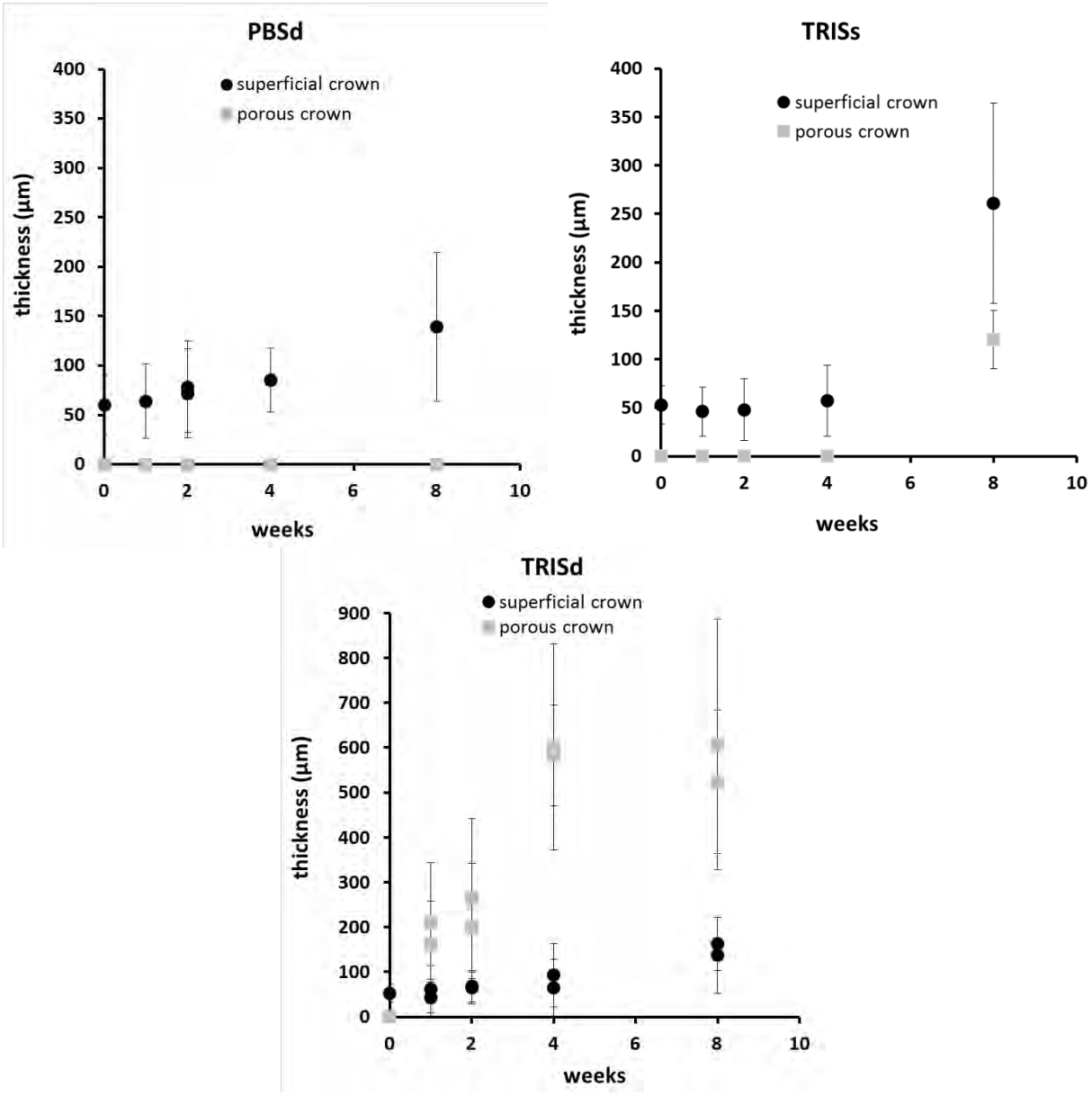

Figure 21: Thickness of layers observed by µ-CT in samples after immersion. Notice that the scale of the y-axes in TRISd graph is higher than the one of the graphs of samples immersed in PBSd and TRISs

Finally, one of the specimens immersed for 8 weeks in TRISd was embedded in an epoxy resin, cut, polished and observed by SEM. In particular, the examined zones were localised in the porous layer (green square in Figure 22) and in the transition zone between the porous layer and the bulk (orange square in Figure 22). It should be noted that the superficial crown was not anymore present. In fact, this thin layer, which had a low cohesion with the rest of the specimen (as well visible in Figure 19, 8w), detached during the embedding procedure.
The SEM images confirmed that the degraded layer (that appeared darker by µ-CT) was more porous than the bulk of the sample. In particular, this increase of porosity seemed to be caused by the loss of agglomerates of the porous particles, which formed the microstructure at t0. The dissolution of single grains constituting the porous particles could not be seen by this technique.

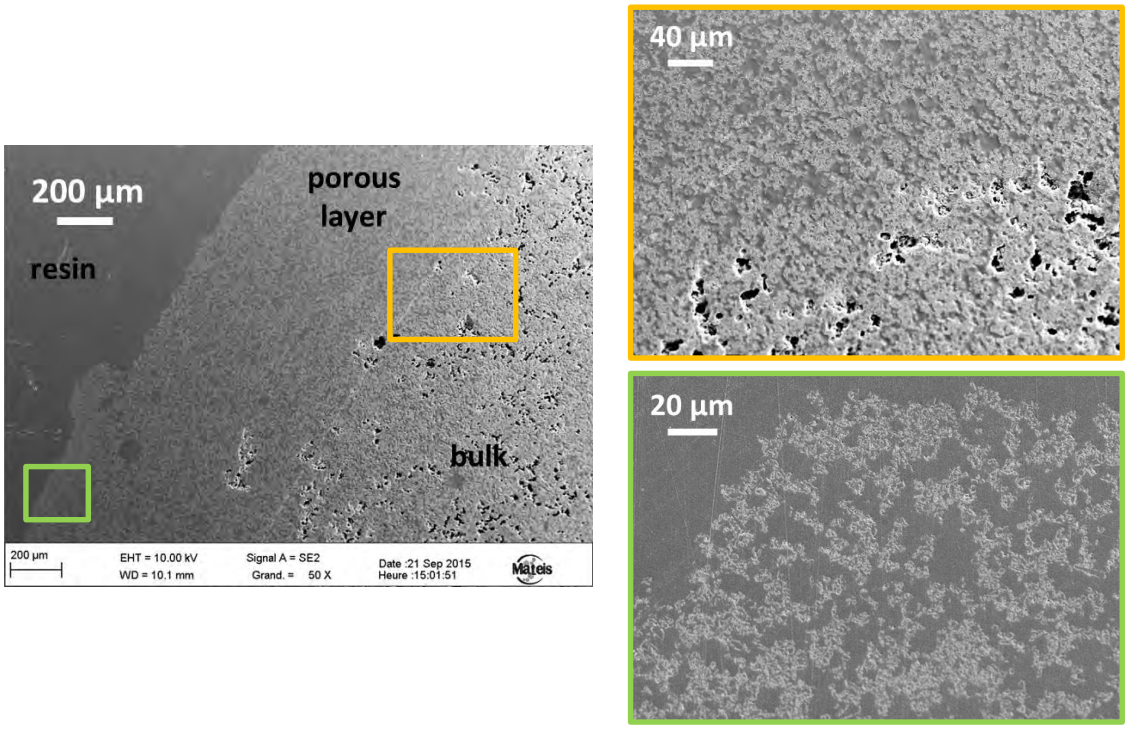

Figure 22: Micrographs of a β-TCP sample immersed for 8 weeks in TRISd and embedded in an epoxy resin before SEM observation

Scanning Electron Microscopy

After 8 weeks of immersion in PBSd, the microstructure morphology did not appear significantly changed compared to the samples before immersion (Figure 3). In the inner part of the specimens both levels of porosity present at time zero were still visible (Figure 23-A and B). Only at the surface few deposits were noticed (cf. arrow in Figure 23-C).

Also after immersion in TRISs for 8 weeks, the morphology of samples appeared almost unchanged in the core (Figure 24). No precipitations were noticed at the surface; only some small particles (probably fragments of grains stuck in the porosities) were noticed (cf. arrow in Figure 24-C).

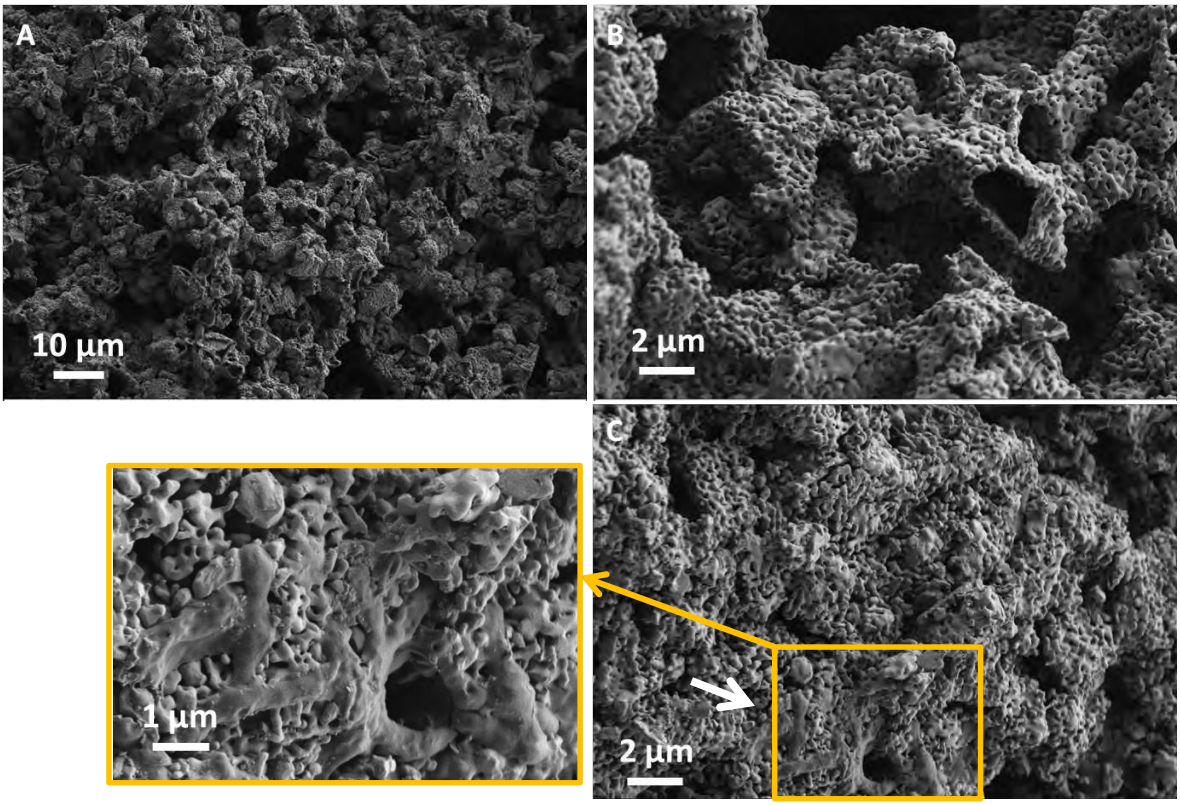

Figure 23: SEM micrographs of β-TCP samples in the core (A-B) and at the surface (C) after 8 weeks in PBSd

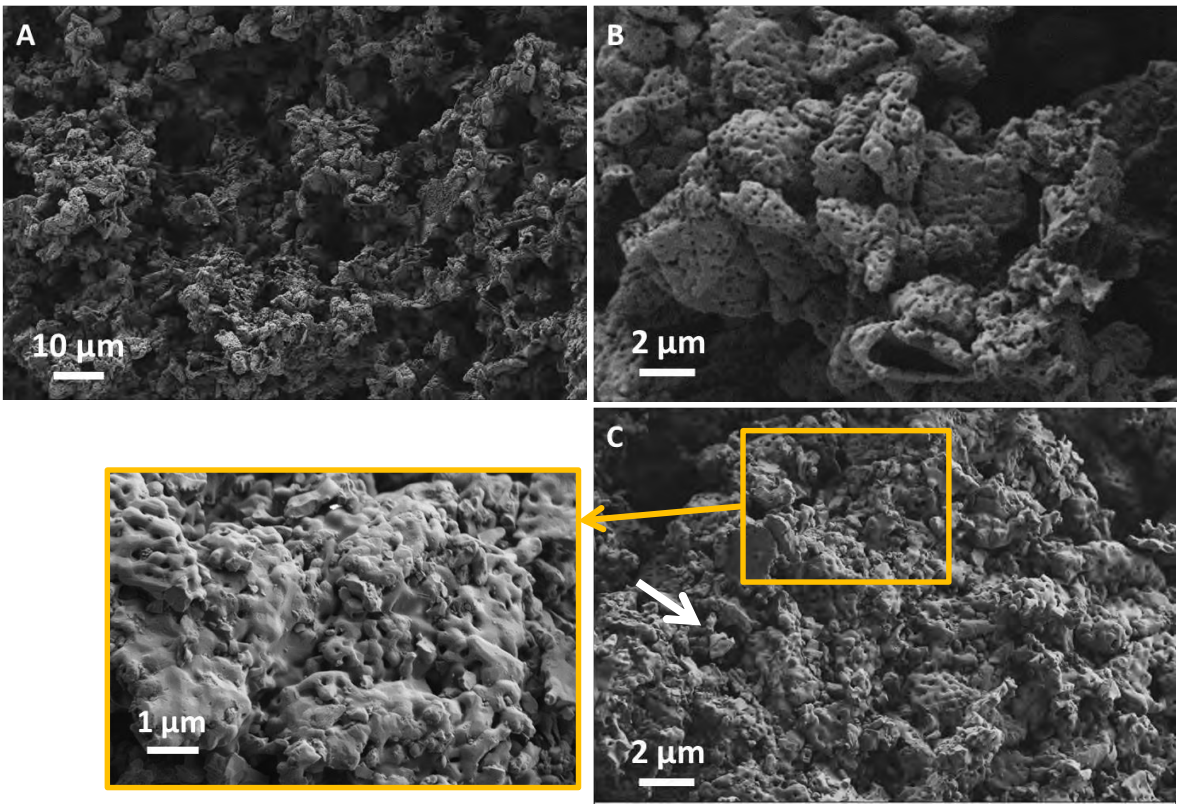

Figure 24: SEM micrographs of β-TCP in the core (A-B) and at the surface (C) after 8 weeks in TRISs

The morphology of the inner part of the samples immersed for 8 weeks in TRISd was really similar to the initial one (Figure 25-A and B). At the surface, however, some deposits were observed; moreover, small fragments of particles were spread all over the surface, partially "filling" the initial porosity (cf. arrows in Figure 25-C).

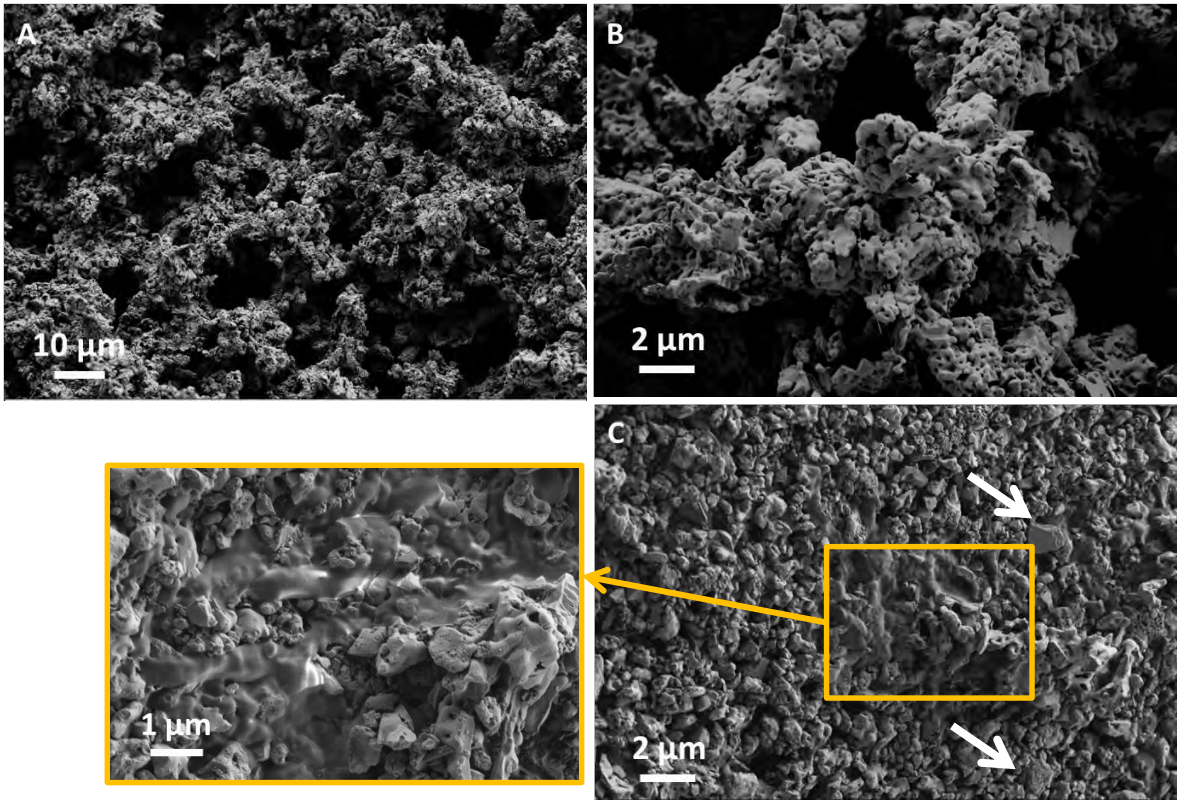

Figure 25: SEM micrographs of β-TCP samples in the core (A-B) and at the surface (C) after 8 weeks in TRISd

Mercury Intrusion Porosimetry

The evolution versus immersion time of the interconnection size distribution was monitored using mercury porosimetry measurements. For each time point, both surface and core of the same samples were tested separately. It must be underlined, however, that the measurements were performed on samples of size around 3x3x3 mm^3, which means that it was not possible to completely isolate the external part of the sample. Therefore, surface analyses involved the external layer, but also a large part underneath.

Data are divided according to the solution of immersion and presented as curves of incremental intrusion as a function of pore interconnection size. The small differences of height of the peaks between one time and another were considered less significant than their shifts on the *x*-axis.

PBSd

Even after 8 weeks of immersion, the pore interconnection size distribution and total porosity of samples immersed in PBSd did not change significantly, neither at the surface (Figure 26-left), nor in the core (Figure 26-right).

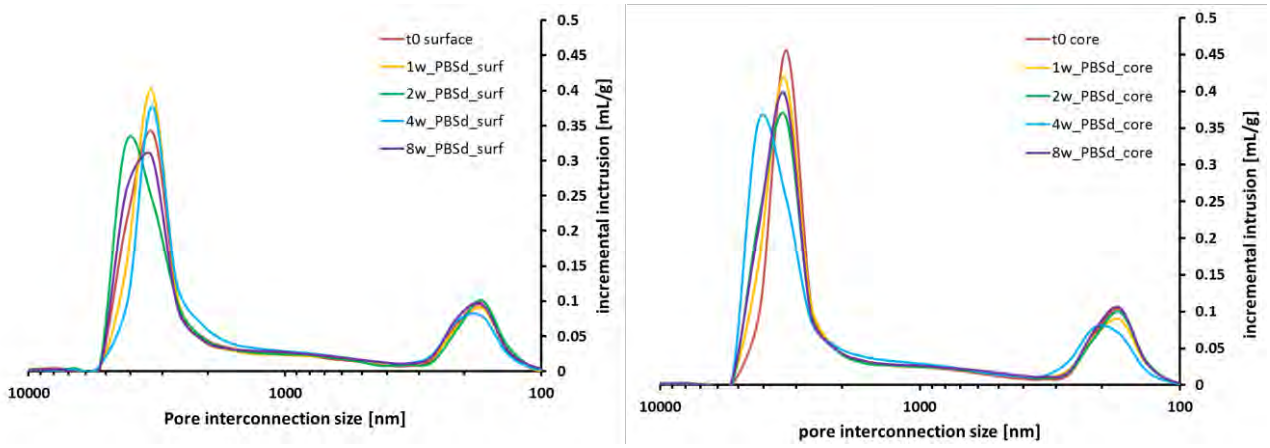

Figure 26: Incremental intrusion of Hg at the surface (left) and in the core (right) of β-TCP samples immersed for different times in PBSd

TRISs

After immersion in TRISs, samples showed slight changes at the surface after 4 and 8 weeks (Figure 27-left). After 4 and 8 weeks, the peak corresponding to the smallest interconnection size (170 nm) slightly shifted towards larger diameters (around 210 nm). Moreover, it seems that the porosity between 500 nm and 1700 nm slightly increased, showing the formation of two small bumps at 600 nm and 1300 nm (cf. arrows in Figure 27-left).
In the core, the only relevant evolution along time was the shift towards larger interconnection sizes of the highest peak (originally around 3300 nm), which after 8 weeks was located around 4000 nm (Figure 27-right).

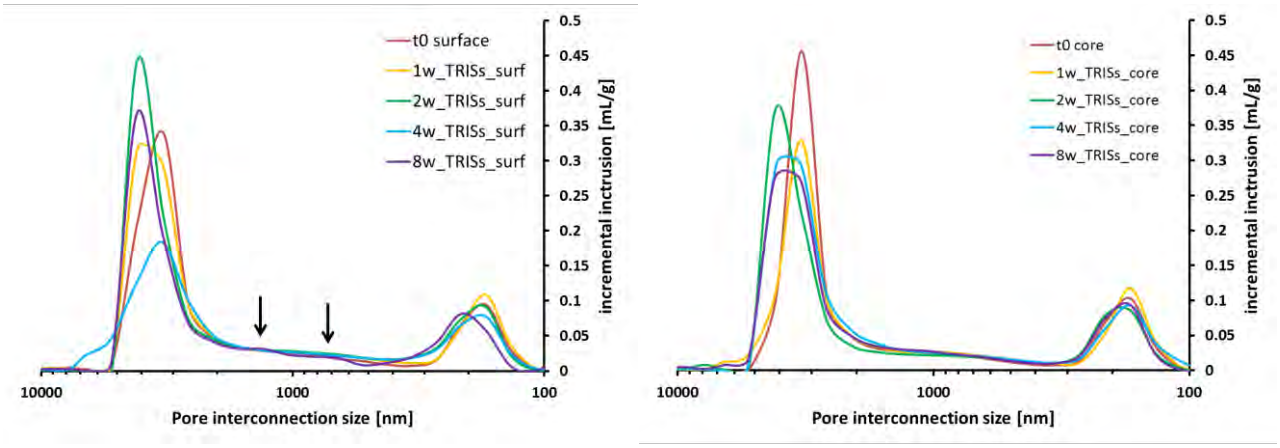

Figure 27: Incremental intrusion of Hg at the surface (left) and in the core (right) of β-TCP samples immersed for different times in TRISs

TRISd

Samples immersed in TRISd displayed evident changes at the surface (Figure 28-left): after 2 weeks, the porosity around 300-800 nm was significantly increased if compared to that at time zero. Besides, in the same interconnection size range, a third peak, centred around 660 nm, appeared after 4 weeks. Finally, at 4 and 8 weeks the highest peak (3300 nm) was slightly enlarged towards larger interconnection sizes (6000 nm).

As far as the core is concerned (Figure 28-right), the variations were less important than those observed at the surface, but nevertheless followed the same trend. After 8 weeks, in fact, the porosity comprised between 300 nm and 800 nm increased and the peaks at 3300 nm enlarged towards 6000 nm.

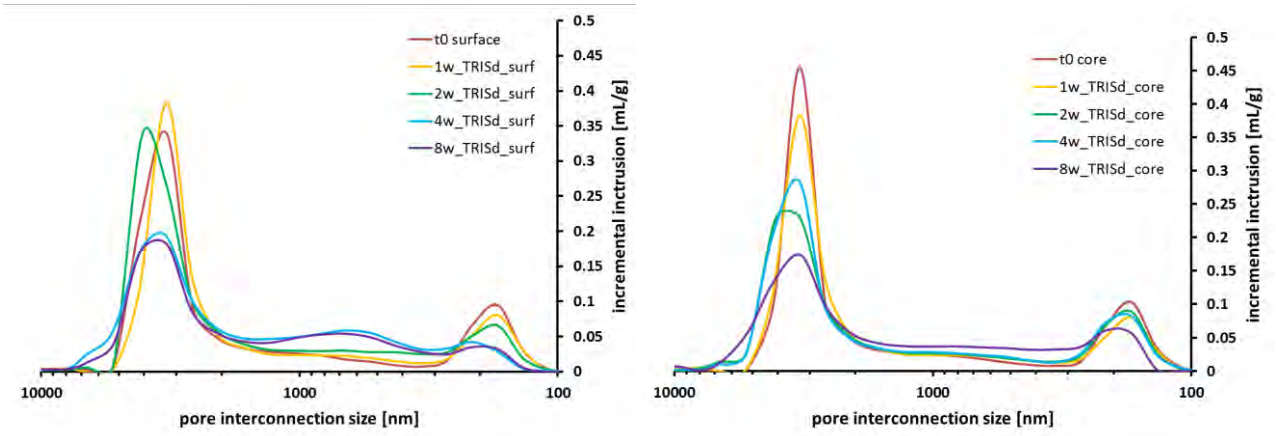

Figure 28: Incremental intrusion of Hg at the surface (left) and in the core (right) of β-TCP samples immersed for different times in TRISd

4.2.3 Mechanical changes

The mechanical properties of β-TCP samples were evaluated by means of the instrumented micro-indentation technique. In parallel, some specimens immersed for 2 weeks in TRISd underwent compression tests. The results are presented in the following pages.

4.2.3.1 Micro-indentation tests

As for DCPD (cf. chapter 3), the mechanical properties of porous β-TCP specimens were assessed at time zero and after different times of immersion in PBSd, TRISs and TRISd (for the detailed experimental conditions cf. paragraph 2.4.3, "micro-indentation" section). For each time-point, three samples were indented at the surface (6 indentations) before and after dissolution test and two were also indented in the core (9 indentations) after immersion. Therefore, the evolution of hardness *H* and Young's modulus *E* at the surface was calculated comparing the values obtained for the very same specimen before and after dissolution test. Other samples were tested in the core at time zero to serve as a reference for the core of the immersed specimens.
Graphs summarising the evolution of the average values of *H* and *E* and their standard deviations, calculated from all the collected data, are presented in the following pages. For further details, the results obtained on each sample, presented as variation in percentage compared to the initial values, are showed in Annex (Figure A.c.5-A.c.10).

PBSd

The values of hardness and Young's modulus measured at the surface and in the core after immersion in PBSd are reported in Table 2.
Analysing the variations in percentage of *H* and *E,* a quite important dispersion of data was observed at the surface after immersion in PBSd. The results in the core, on the other hand, appeared less dispersed.
At the surface, considering the standard deviation associated to each measure, the only significant change was the decrease of *H* (-26%) after 8 weeks of immersion (Figure 29-left). This variation was also visible on the representative indentation curves reported in Figure 30: for 8 weeks, the penetration depth was slightly higher when compared to the others.

Table 2: Average values and standard deviations of hardness and Young's modulus after immersion in PBSd

t	H [MPa] avg std		E [MPa] avg std	
	SURF	CORE	SURF	CORE
0	5.0 0.5	3.8 0.4	788 199	986 44
1w	4.3 0.6	4.7 0.8	763 136	1195 193
2w	3.9 0.4	4.4 0.3	621 96	1026 79
4w	4.5 0.2	3.7 0.5	753 57	906 31
8d	3.7 0.4	3.9 0.4	743 53	933 35

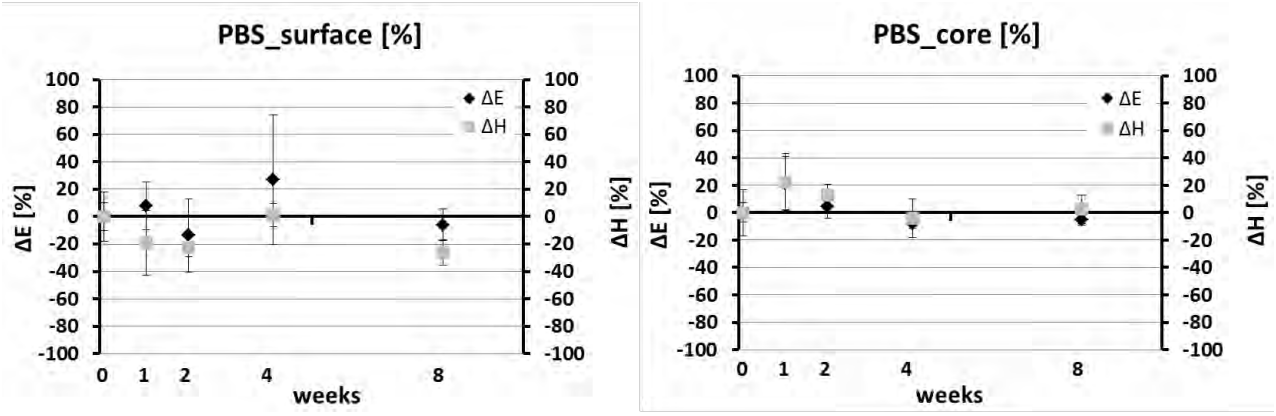

Figure 29: Variation of H and E at the surface (left) and in the core (right) of β-TCP samples after different immersion times in PBSd

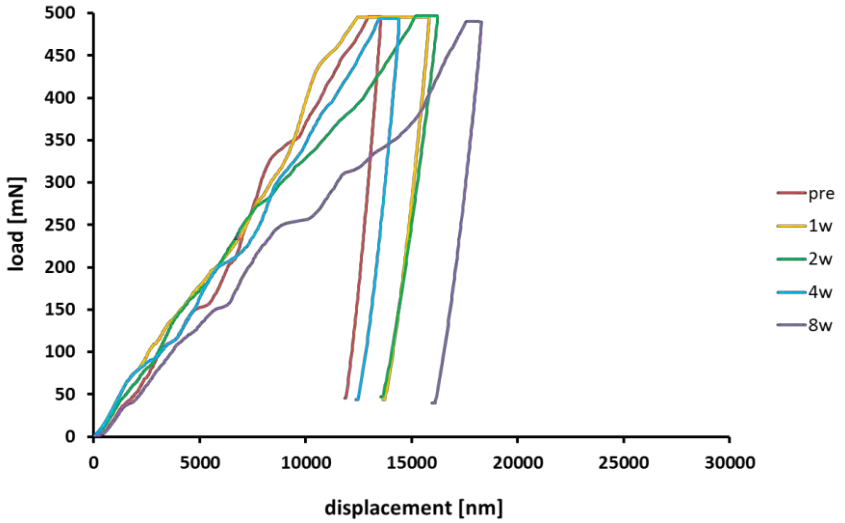

Figure 30: Representative load-displacement curves obtained at the surface of β-TCP samples after immersion in PBSd

As far as the core is concerned (Figure 29-right), the only change was the increase of *H* after one week of immersion; considering the standard deviation associated to the average value, however, this change could be considered as non-significant. In a coherent way, all the load-displacement curves appeared quite similar disregarding the time of immersion (Figure 31).

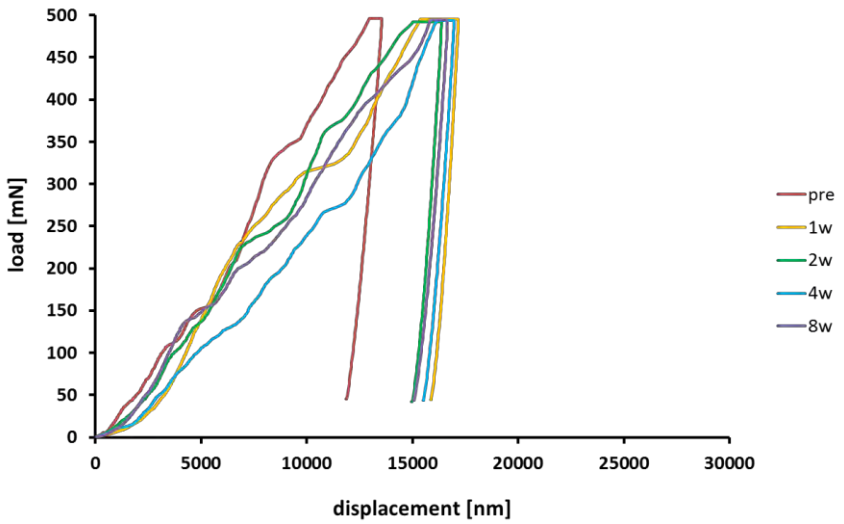

Figure 31: Representative load-displacement curves obtained in the core of β-TCP samples after immersion in PBSd

TRISs

The values of *H* and *E,* measured after immersion, are reported in Table 3. Once immersed in TRISs, the specimens displayed a general decrease of properties at the surface and no relevant variations in the core.

In particular, at the surface already after 1 week of immersion *H* and *E* underwent an average diminution of 57% and 37% respectively (Figure 32-left). At later time-points, the mechanical properties, although with some oscillations, were always significantly lower than at time zero, as also appreciated on the indentation curves reported in Figure 33 (increase of the penetration depth). In particular, the variation of hardness was comprised between -20% and -60%, while that of elastic modulus between -20% and -40%.

Table 3: Average values and standard deviations of hardness and Young's modulus after immersion in TRISs

t	H [MPa] avg std		E [MPa] avg std	
	SURF	CORE	SURF	CORE
0	$5.0_{0.5}$	$3.8_{0.4}$	788_{199}	986_{44}
1w	$2.1_{1.3}$	$3.9_{0.3}$	663_{122}	916_{16}
2w	$4.3_{0.8}$	$4.5_{0.8}$	723_{81}	1050_{133}
4w	$1.8_{0.2}$	$3.9_{0.3}$	491_{59}	919_{20}
8d	$3.5_{1.4}$	$3.7_{1.5}$	507_{199}	927_{297}

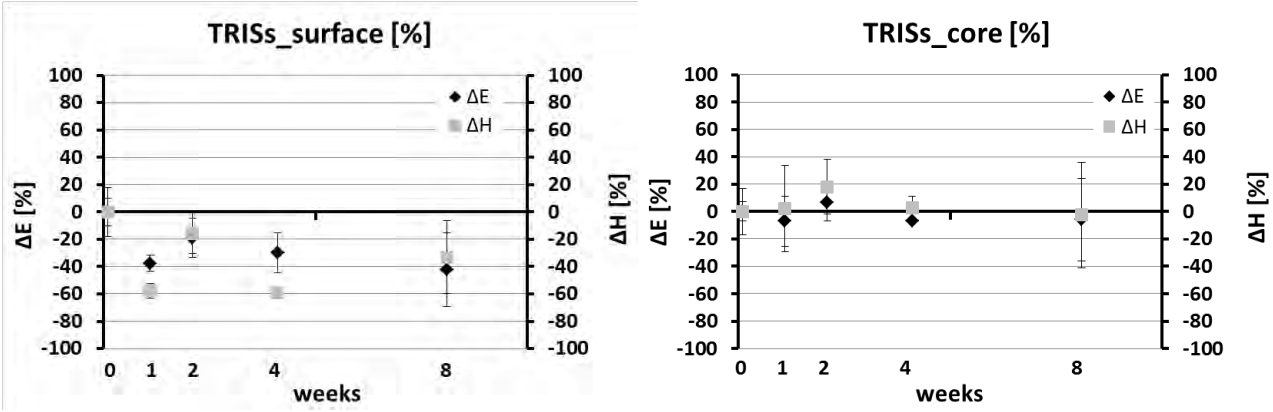

Figure 32: Variation of H and E at the surface (left) and in the core (right) of β-TCP samples after different immersion times in TRISs

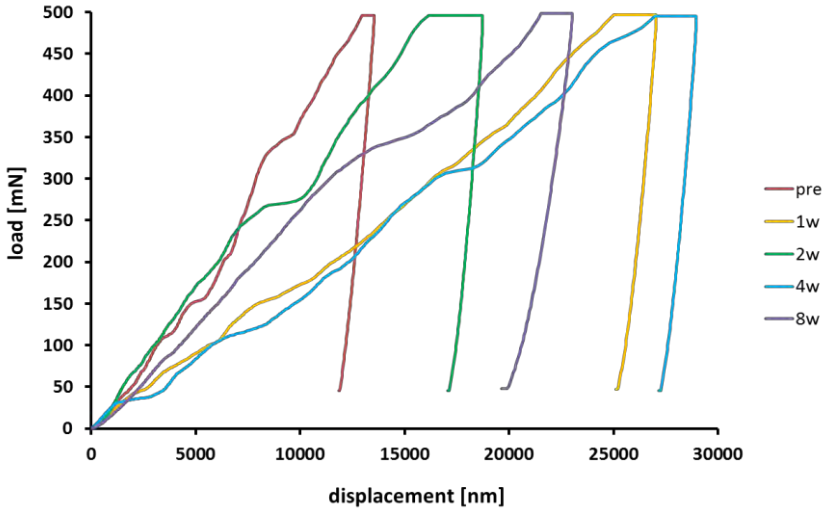

Figure 33: Representative load-displacement curves obtained at the surface of β-TCP samples after immersion in TRISs

In the core, neither the hardness nor the elastic modulus displayed significant changes (Figure 32-right), as also confirmed by the indentation curves (Figure 34), when considering the standard deviations associated to the measurements.

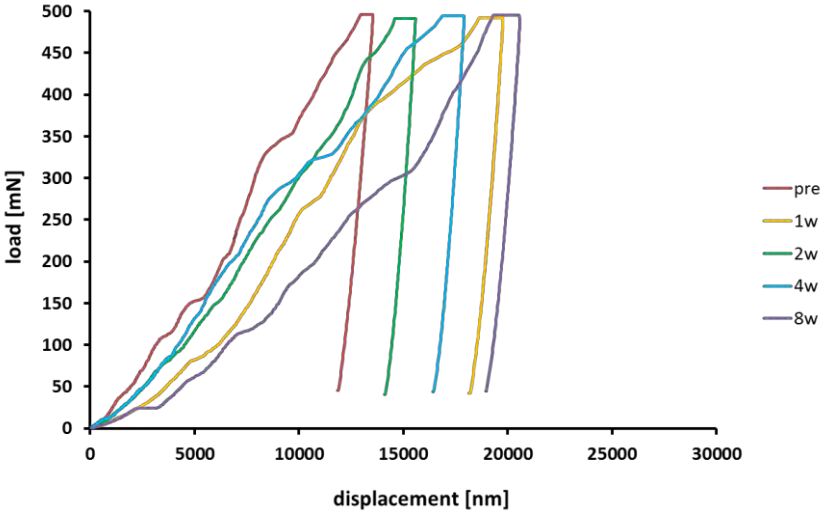

Figure 34: Representative load-displacement curves obtained in the core of β-TCP samples after immersion in TRISs

TRISd

Average values and standard deviation of *H* and *E* measured at the surface and in the core after immersion in TRISd are shown in Table 4. Already after 1 week, a decrease of almost 90% was observed for both *H* and *E* (Figure 35-left). These values were almost unchanged for all the rest of the test, with the exception of an increase of elastic modulus after 2 weeks (from -90% to -65%).

Table 4: Average values and standard deviations of hardness and Young's modulus after immersion in TRISd

t	H [MPa] avg std		E [MPa] avg std	
	SURF	CORE	SURF	CORE
0	$5.0_{0.5}$	$3.8_{0.4}$	788_{199}	986_{44}
1w	$0.5_{0.2}$	$3.8_{1.1}$	107_{31}	879_{180}
2w	$0.6_{0.3}$	$4.3_{0.1}$	233_{19}	964_{25}
4w	$0.3_{0.0}$	$4.4_{0.5}$	74_{6}	1050_{110}
8d	$0.4_{0.1}$	$4.4_{0.5}$	84_{4}	974_{95}

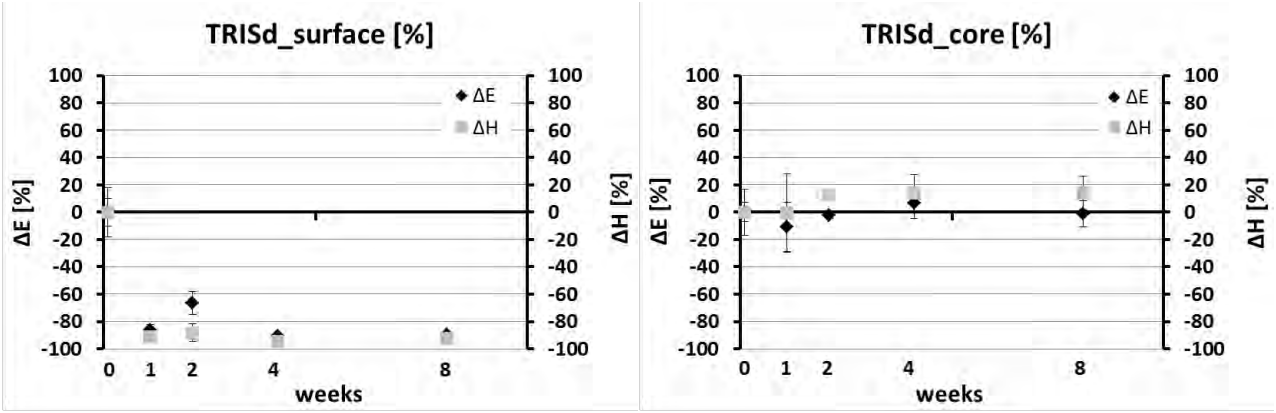

Figure 35: Variation of H and E at the surface (left) and in the core (right) of β-TCP samples after different immersion times in TRISd

After immersion the mechanical properties of the surface decreased so much that the indenter penetration reached the maximum displacement limit of the machine (25 µm). For this reason, the indentation curves present just the initial part of the loading segment and do not have any unloading part (Figure 36). However, the values of hardness and elastic modulus could be obtained without the unloading segment thanks to the use of the CSM mode, which calculates *H* and *E* during all the test and not only during the unloading segment. The so-obtained evolution of hardness and elastic modulus at the surface as a function of penetration depth is reported in Figure 37 and Figure 38. The high values observed for *E* at the beginning of the test are due to the influence of the surface roughness, as reported in literature, and, therefore, they should not be taken into account. For this reason, the obtained values were considered to be valid starting from 1-2 µm of penetration depth. Coherently with what observed on load-displacement curves, after immersion both *H* and *E* appeared much lower than at time zero. The general trend was similar for all the curves, with the exception of the hardness at 1 and 2 weeks (Figure 37). At 1 week *H* increased until 1.6 µm deep and then decreased. At 2 weeks, the hardness slightly increased for high penetration depths (Figure 37).

As far as the core is concerned, the mechanical properties did not change significantly (Figure 35-right, Figure 39). Moreover, the values of *H* and *E* measured by CSM method appeared almost constant along the penetration depth (figures not shown).

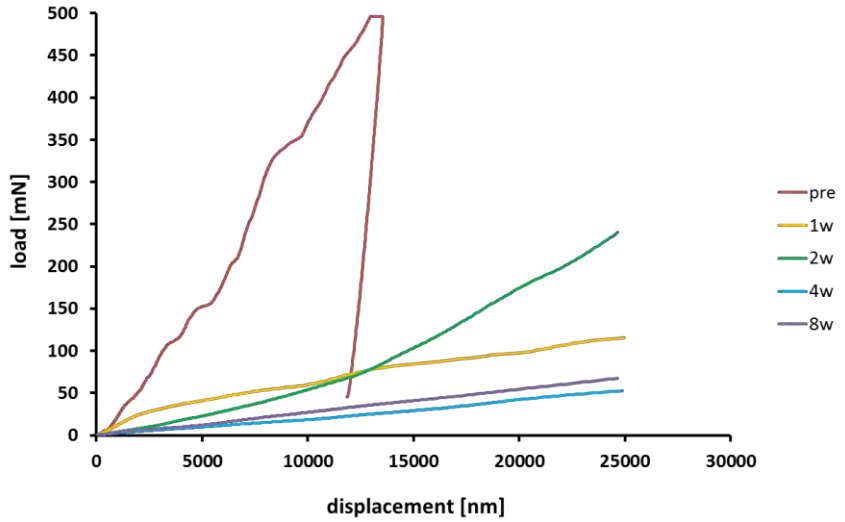

Figure 36: Representative load-displacement curves obtained at the surface of β-TCP samples after immersion in TRISd

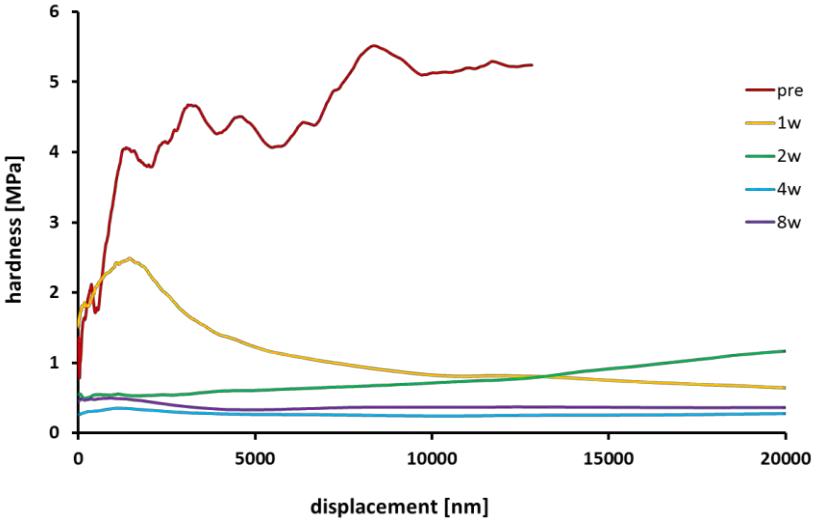

Figure 37: Representative Hardness-displacement curves obtained with the CSM method at the surface of β-TCP samples after immersion in TRISd

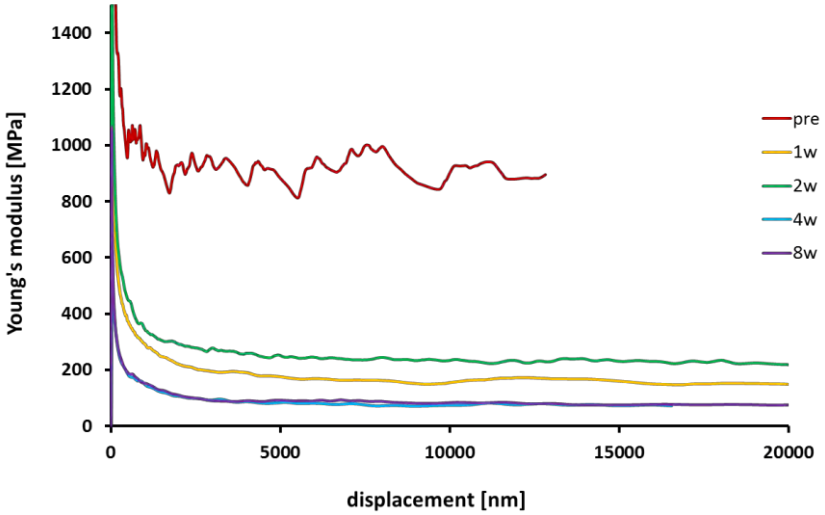

Figure 38: Representative Young's modulus-displacement curves obtained with the CSM method at the surface of β-TCP samples after immersion in TRISd

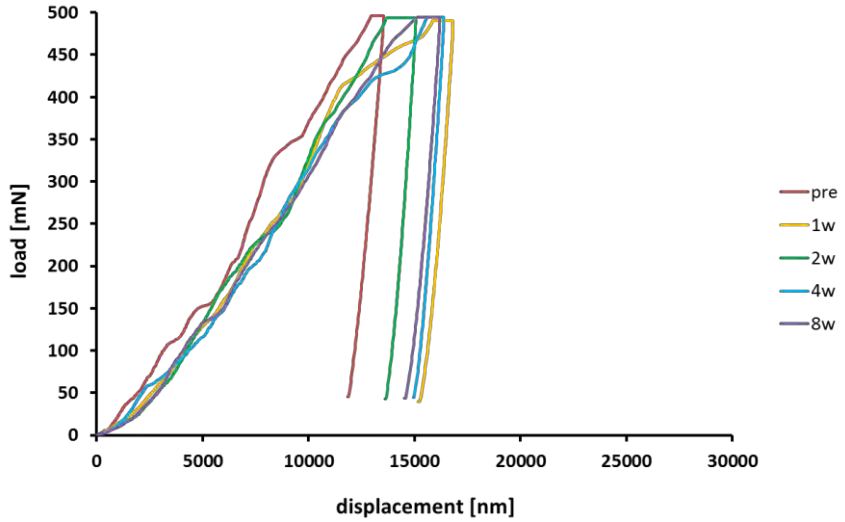

Figure 39: Representative load-displacement curves obtained in the core of β-TCP samples after immersion in TRISd

Mechanical tests performed in humid conditions

As for DCPD samples (section 3.2.4 of Chapter 3), some mechanical tests in humid conditions were performed in order to approach an *in-situ* analysis and to evaluate the influence of the presence of the liquid phase in the pores (and complementary of the drying process) on the properties of the material. For this purpose, two samples were indented at time zero in dry conditions, immersed for 30 minutes in TRISd and indented again to obtain the reference in humid state ("pre_humid"). Afterwards, the specimens were immersed for 2 weeks in TRISd and, once withdrawn, tested at the surface when still humid ("post_humid") and then after drying ("post_dry").

Graphs in Figure 40 report the values of hardness and Young's modulus obtained in the different conditions; the standard deviation derives from different indentations performed on the same sample. Both in dry and humid conditions, *H* and *E* appeared dramatically diminished after 2 weeks immersion. In addition, the presence of humidity strongly decreased the values of hardness both before and after immersion, as can be noticed also on the indentation curves reported in Figure 41. On the other hand, the elastic modulus was not significantly affected by the presence of liquid.

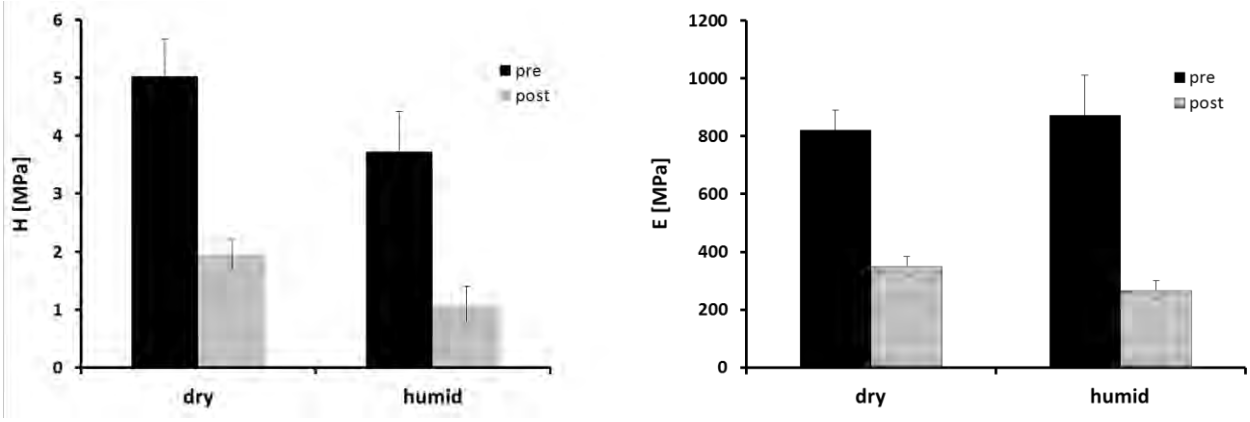

Figure 40: Values of hardness and elastic modulus at the surface in dry and humid conditions before and after immersion (2w, TRISd)

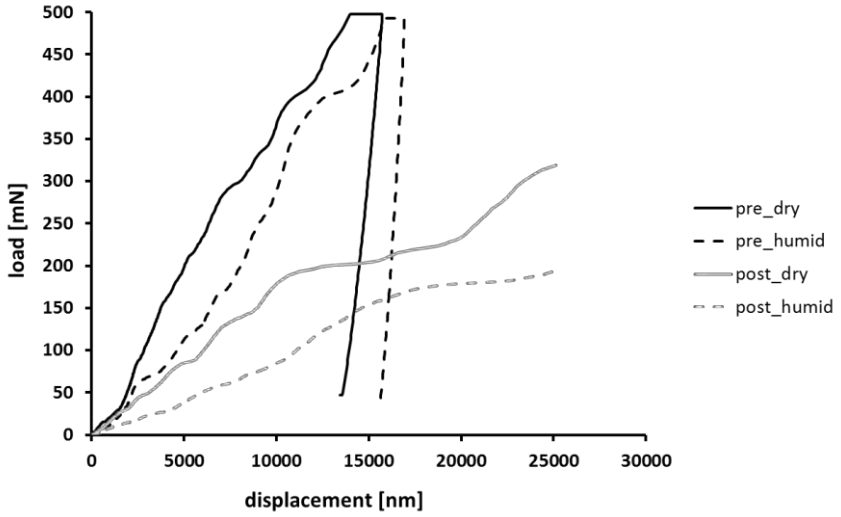

Figure 41: Indentation curves obtained in dry and humid conditions before and after immersion of porous β-TCP samples (2w, TRISd)

Gradient of mechanical properties: further micro-indentation tests

In order to further explore the potentialities of the micro-indentation test, two samples retrieved after 1 and 2 weeks from TRISd were cut and then indented all along their diameter (Figure 42). The results are showed in Figure 43; 9 points were tested on the sample immersed for 1 week and 4 points on the specimen that stayed 2 weeks in TRISd. The distance between one indentation and the next one was of 1 mm minimum, while the distance between indentations and the edge of the sample was of about 200-300 µm. Considering that the penetration depth was generally below 15 µm, the indentation radius was on average around 150 µm: therefore, the chosen distance between each test was enough to avoid any interaction between one indentation and the adjacent one (as a rule of thumb, minimum distance equal to 4 times the indentation radius).

Some exceptions are present, such as the hardness at the very centre (point *e*) of the sample at 1 week, but on the overall the mechanical properties appeared lower on the part of the section close to the surface (where the porous layer was observed) and increased moving towards the centre of the specimen. In a coherent way, the load-displacement curves (Figure A.c.11 in Annex) displayed a higher depth of penetration (which implies a lower *H*) for the points closer to the surface. These tests proved how sensitive the micro-indentation can be and opened new perspective for future experiments.

Additional work, and in particular numerical simulations, is needed to estimate the volume of material (depth and width) tested during indentation, to better comprehend the obtained results.

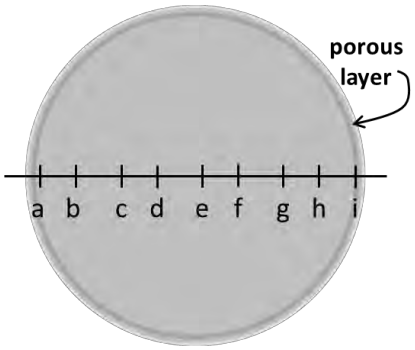

Figure 42: Scheme of the section of a degraded sample, after 1 weeks of immersion TRISd. The letters correspond to the points were indentations were performed. The darker ring close to the surface represents the porous layer observed by µ-CT

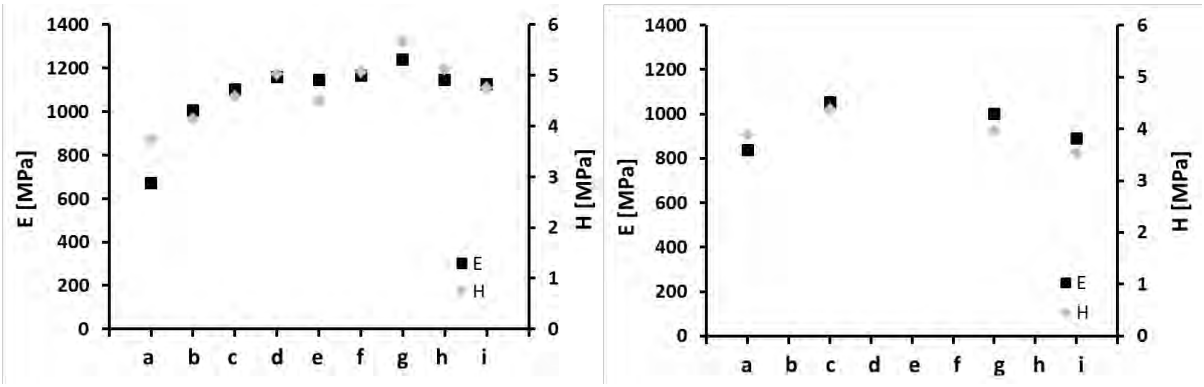

Figure 43: Values of hardness and Young's modulus obtained along the section of samples (cf. fig.42) immersed for 1w (left) and 2w (right) in TRISd

4.2.3.2 Compression tests

The conditions of compression tests are detailed in chapter 2 (paragraph 2.4.3, "compression" section); six samples were compressed at time zero and six after immersion in TRISd for 2 weeks. For some samples several loading/unloading cycles were applied, in order to obtain the Young's modulus (and its evolution along compression test), which was calculated according to the equation (2):

$$E = \frac{\sigma}{\varepsilon} = \frac{F}{S} * \frac{h}{\Delta h} = \frac{F}{\Delta h} * \frac{h}{S} \qquad (2)$$

where *F* was the applied load, *S* the section of the sample, *h* the height of the sample and *Δh* the displacement measured during the test.
For the calculation of *E* and of the compressive strength, two different approaches were followed. For the first approach, denoted as "direct", total *h* and *S* were measured on the samples after immersion, while for the second one, referred as "corrected" measurement, the height and the surface were corrected by subtracting the thickness of the porous layer observed by µ-CT (Figure 21).
Supposing that the load is sustained by the inner part of the sample more than by the porous layer, it can be hypothesised that the values of *E* obtained with the second approach and calculated on the load dwell would correspond to those of the core of the samples.

Figure 44 reports two representative load-displacement curves obtained before and after immersion tests. After 2 weeks, the slope of the loading segment decreased significantly; also the maximum load appeared much lower after immersion, suggesting a decrease of compressive strength. Compressive strengths calculated for two representative samples are reported in Figure 45: after immersion the average strength appeared diminished of around 30%, from 2.9 MPa to 2.0 MPa. The corrected value, considering a smaller section for the calculation, led to an average strength of 2.2 MPa: this value was 10% higher than the "not-corrected" one, but still much smaller than the one obtained before immersion.

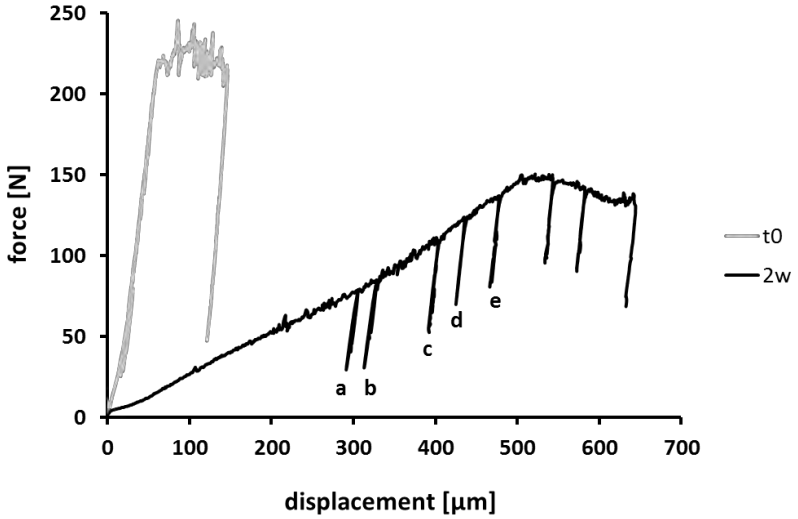

Figure 44: Representative compressive force-displacement curves before (in grey) and after two weeks (in black) immersion in TRISd. Loading/unloading cycles (a, b, c, d, e…) can be noted on the curve after immersion.

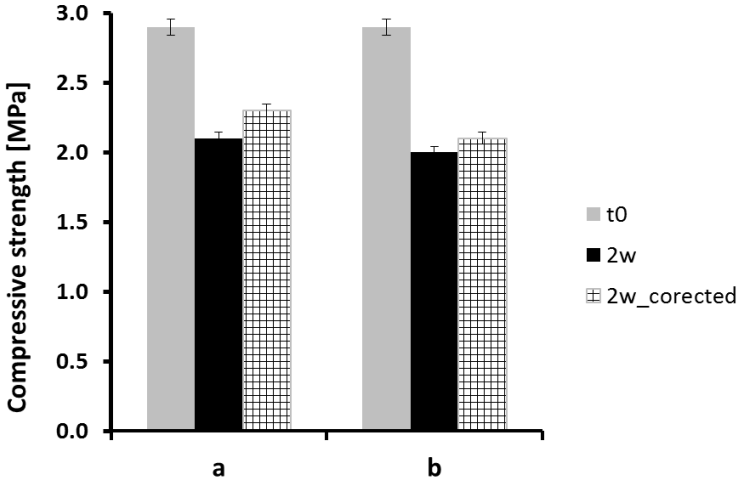

Figure 45: Compressive strength before (in grey) and after (in black and squared) immersion (2w in TRISd), with and without correction

Compressive Young's modulus was calculated from the slope of the loading/unloading cycles. As an example, Table 6 shows the values of *E* calculated on the cycles represented in Figure 44; also in this case both the "direct" and the "corrected" moduli are reported. Whatever the approach for its calculation, the Young's modulus increased along the loading curve.

Pictures taken during the compression tests are reported in Figure 46 and illustrate how during the loading segment the external porous layer cracked concomitantly with jagged parts of the curve. After the load peak, the calculation of the Young's modulus from the load-unload cycles showed a decrease

of the sample's stiffness. This was linked to a localisation of the deformation by crack propagation; these values were therefore considered as not representative of an average behaviour of the samples and were not taken into account.

Table 5: Values of Young's modulus after immersion (2w in TRISd) calculated on the slope of the compression curve (cf. Figure 44)

cycle	E_{direct} [MPa]	$E_{corrected}$ [MPa]
a	339	352
b	380	394
c	512	532
d	653	677
e	875	908

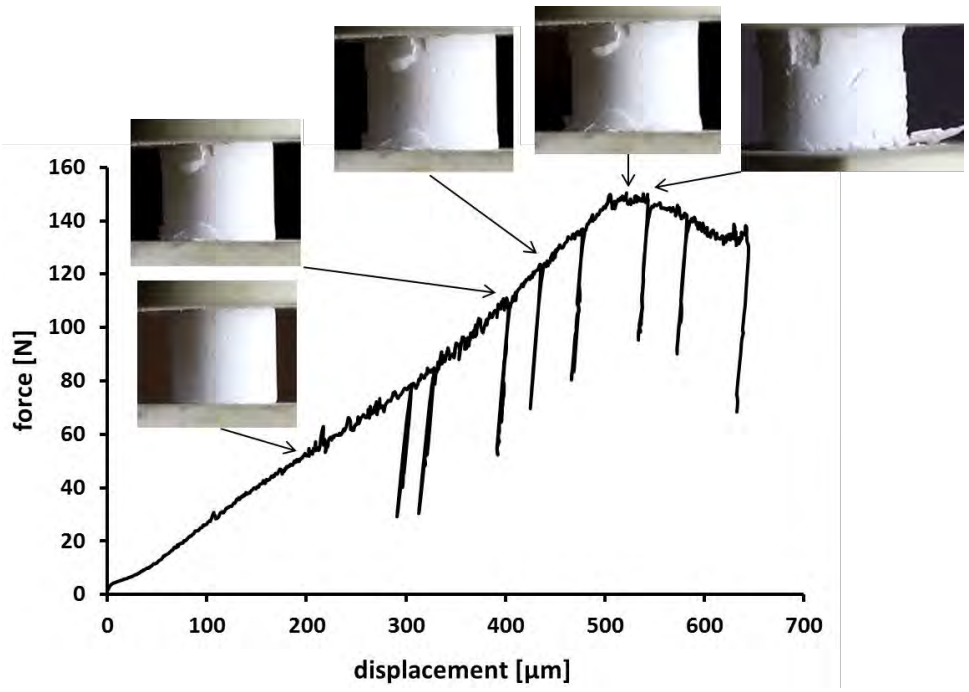

Figure 46: Compressive force-displacement curve after 2 weeks immersion in TRISd and corresponding pictures. The two compressive plates were not parallel because they were in contact with a spherical joint; in this way, the load was homogeneously distributed on the whole surface of the sample.

Finally the values of elastic modulus obtained by compression were compared to those calculated by micro-indentation. Table 6 summarises the averages values and standard deviations of Young's moduli calculated before and after immersion with compression and indentation techniques. For compression tests, the values of elastic modulus calculated during the loading/unloading cycles on the slope are likely influenced by the presence of the porous top and bottom layers, while those calculated on the stress plateau (after the maximum compressive strength) are probably affected by the formation of cracks in the core of the sample. As a consequence, the values reported for the compression tests are those calculated during the last loading/unloading cycle of the slope (cycle "e", Table 5 and Figure 46). At this point, in fact, the influence of the porous layer should be minimal on the values of elastic modulus and, at the same time, cracks should not have appeared yet in the inner part of the sample.

Table 6: Average values and standard deviations of Young's modulus before and after immersion (2w in TRISd) calculated by indentation and compression tests

t	Method and localisation	average E_{std} [MPa]	average $E_{corrected\ std}$ [MPa]
0	**indentation at the surface**	788 $_{139}$	-
0	**compression**	747 $_{272}$	-
2 weeks	**indentation at the surface**	233 $_{19}$	-
2 weeks	**indentation in the core**	964 $_{25}$	-
2 weeks	**compression**	664 $_{298}$	690 $_{309}$

Considering the standard deviation of the data, the values of Young's modulus calculated at time zero by compression were coherent with those obtained by micro-indentation.
After immersion, the Young's modulus calculated by the compression tests on the last loading/unloading cycle was quite different from both values obtained by micro-indentation, but closer, to some extent, to those calculated in the core.

4.3 Discussion

Results collected during dissolution tests of porous β-TCP samples will be discussed according to the different immersion conditions. The attention, in general, will mainly be focused on samples immersed in TRISd, where the majority of changes were observed; for samples immersed in this solution, therefore, the evolution of the material will be detailed for each time-point.

4.3.1 Initial β-TCP samples

The microstructure of the porous β-TCP samples was characterised by porous particles with a dimension generally inferior to 5 µm. Each particle was made of smaller grains of 300-500 nm (Figure 3). This microstructure, which could seem unusual for β-TCP, was likely due to the processing of the samples (cf. Chapter 2.1.2). When the initial powder and liquid phase were mixed and emulsified in order to obtain porous samples, agglomerates of CDHA crystals probably formed. During the thermal treatment, when CDHA was converted into β-TCP, the morphology of the agglomerates of CDHA was presumably maintained. At this stage, it is assumed that oil bubbles burnt out, leaving the micro-sized porosity, while the CDHA crystals converted into β-TCP grains, which were not fully sintered, leading to the appearance of the nanometric porosities observed in the final material.

As described at the beginning of the chapter (section 4.1) some differences were noticed between the surface and the core of the specimens already at time zero.

In particular, by looking at a section of sample, obtained by µ-CT (Figure 2-C), the surface of the specimen appeared slightly brighter than the inner part, as noted in chapter 3 for DCPD. This could be due to the sample fabrication, which processed through a cement setting reaction before thermal treatment (cf. Chapter 2). Once moulded, the crystals in the paste are likely to organise differently in proximity of the walls of the mould, creating zones with a slight denser microstructure. This gradient was then maintained, if not strengthen, during the sintering stage. It should be noted that roughly half of the specimens were characterised by the presence of brighter concentric rings (Figure in Annex A.c.12), also probably caused by the cement cast.
The higher density of the lateral surface of the cylinder, which was in direct contact with the immersion solutions, could have had an influence on the dissolution behaviour of the sample. In the present case,

however, it should not have affected the specimen characterisations, given that all the tests were performed on the flat surfaces of the cylinders, which were resurfaced.
Another difference regarded the mechanical properties which presented different values at the surface and in the core (*H* higher at the surface and *E* higher in the core). This disparity could have been induced by the different preparation of the two parts of the samples. In particular, the surface underwent a polishing treatment that, although really gentle, could have slightly altered its properties compared to the ones of the core (for instance because of powder and little debris left in the porosities).

4.3.2 Evolution of samples in PBSd

None of the properties of samples immersed in PBSd displayed significant changes (Figure 9-Figure 11, Figure 26, Figure 29). In the same way, the XRD diffraction did not detect the appearance of new phases with the exception of NaCl at the surface (Figure 12); this salt, in fact, is contained in relatively high concentration (around 155 mM) in PBS medium and it is likely to precipitate at the surface of the specimens immersed in this solution (despite the rinsing step). It appears logical, then, that the pH of the PBSd containing samples did not differ from the reference solution by more than 0.08 (Figure 15). Also the microstructure of the material, checked by µ-CT, did not evolve along time (Figure 17). The only change observed was the slight increase of thickness of the external denser layer; this phenomenon could be partly justified by the appearance of NaCl as detected by X-ray diffraction. On the other hand, this last technique did not identify the presence of other phases, so it is likely that the precipitates observed by SEM at the surface of samples after 8w in PBSd were not crystalline (Figure 23). It is possible, in fact, that the set up conditions (humidity, temperature) caused the formation of organic precipitates, likely microbial or fungal.

4.3.3 Evolution of samples in TRISs

Samples immersed in TRISs underwent only negligible changes of volume, weight and density (Figure 9-Figure 11): the maximum loss, in fact, was observed after 4 weeks and it accounted for around -2% of weight and density, while the volume was almost unchanged.
In terms of formation of new phases, a small peak at 2θ= 32.1° was observed at the surface from 2 weeks (Figure 13). This could correspond to one of the main peaks of apatite; all the other peaks typical of this material are either in correspondence with β-TCP peaks or much smaller than the one at 32.1°, as a consequence, the identification of this phase appeared quite difficult. In any case, even if a small amount of apatite precipitated, no significant changes of pH were observed all along the duration of the tests (Figure 15)(pH difference with the reference solution ≤ 0.07).
The µ-CT analyses pointed out the appearance of a porous layer close to the surface starting from 8 weeks (Figure 18). This layer was evaluated as around 120 µm thick and appeared in contact with a denser (thus brighter) layer at the external surface, the so-called “superficial crown” (Figure 21), of about 250 µm. This denser layer could be linked, maybe, to the debris observed at 8 weeks by SEM analyses, which appeared to “fill” the superficial porosities (Figure 24). This phenomenon, however, was not reflected on the curved obtained by mercury porosimetry (Figure 27). The fragment of sample used for this analysis, in fact, was some millimetres thick and included, therefore, the superficial crown, the porous crown and a small portion of core. As a consequence, the curves reported all the changes that took places on these three portions of the specimens. Among these modifications the most evident one was certainly the appearance of the porous layer, so it is likely that the changes observed on the pore interconnection size distribution at 8 weeks were linked to this phenomenon and they somehow concealed the possible decrease of porosity at the surface. The only clear change was the shift of the small interconnections peak from 170 nm to 210 nm. It also seemed that an intermediate interconnection size appeared around 600 nm and 1300 nm. While this small evolution should be analysed with care, it seems consistent with what is significantly observed in TRISd. All these data induce to think that the formation of the porous layer was due to the enlargement of part of the small

interconnection diameter (shift from 170 nm to 210 nm) and to the detachment of some grains which originated the intermediate size distribution (peaks to 600 nm and 1300 nm).
In terms of mechanical properties, a decrease of hardness and Young's modulus was noticed already after 1 week (ΔH = -57%, ΔH = -38%, Figure 32), suggesting that the dissolution process, although clearly visible by µ-CT analyses only after 8 weeks, started to weaken the β-TCP structure already at earlier time-points.
In the core, on the other hand, no changes of microstructure and composition were observed (Figure 18, Annex A.c.1). Coherently, also the mechanical properties did not evolve during immersion (Figure 32).

4.3.4 Evolution of samples in TRISd

The major changes observed during the dissolution tests of β-TCP took place in TRISd. Already after **1 week**, the samples displayed significant losses of volume, mass and density (-2%, -5% and -3% respectively, Figure 9-Figure 11). The formation of a porous layer (180 µm thick) close to the surface was observed by µ-CT (Figure 19). Mercury-intrusion porosimetry, however, did not show relevant changes at the surface (Figure 28), probably because the volume of the porous layer was too small when compared to the total volume, which was tested, to significantly affect the pore interconnection size distribution. Also in the core the porosity was unaltered. The mechanical properties dramatically decreased at the surface (ΔH = -90%, ΔE = -85%), while they were on the overall unaffected in the core (Figure 35). It was quite evident, therefore, that the appearance of the superficial porous layer had a detrimental effect on the mechanical properties of β-TCP. This influence seemed to be reflected at the surface above all on the hardness-displacement curve, which presented two different behaviours along indentation depth (Figure 37). In the first part of the test, the hardness was likely influenced by the relatively dense superficial crown (50 µm thick) and displayed, therefore, values of up to 2.5 MPa. In the second part (starting from about 1.6 µm of penetration), instead, when a deeper volume of sample was involved in the test, *H* strongly decreased, reaching values below 1 MPa, maybe because of the influence of the porous layer. On the other hand, the values of *E* observed on the Young's modulus-displacement curve, being affected by a deeper volume, reflected mainly the properties of the porous layer and did not show two separate behaviours (Figure 38).

After **2 weeks**, samples lost slightly more mass and density (ΔW = -6% and Δρ = -5% compared to value at t0, Figure 9-Figure 11), and a small amount of crystalline phase was detected at the surface (maybe apatite, peak at 32.1°, Figure 14). At the same time-point, the porous layer close to the surface thickened, reaching 230 µm, while the superficial crow did not show further changes (thickness = 60 µm, Figure 21). For sake of completeness also a µ-CT image of a sample used for compression tests is reported here (Figure 47). Although the specimens for compression were immersed for 2 weeks in TRISd in the very same conditions as used for samples that underwent indentation, in some cases the morphology of the porous layer was slightly different. A second porous layer, thinner and more internal, was visible, suggesting that the division adopted in this work between one superficial crown and one porous layer could be, for some cases, a bit too schematic.
The formation of porous concentric layers below the sample surface, as observed after immersion in TRIS, could derive from the microstructure of the initial samples. It is actually possible that during the cement cast, some particles gathered in specific zones. The difference of density of these zones would have been maintained, if not increased, by the sintering process. Indeed, µ-CT images at time zero showed that β-TCP cylinders were characterised by the presence of a brighter surface layer (Figure 2) or, in some cases, by brighter concentric rings in the bulk of the specimen (Figure 112), probably corresponding to denser layers in the sample.
During the immersion tests, the denser parts of the sample could have dissolved less quickly than the more porous ones. This could have led to the formation of an external brighter crown, which would have not been significantly altered by the stay in solution. Below this superficial crown, one (Figure 19) or several (Figure 47) porous layer(s) could have resulted from the early dissolution of the zones, which

were already more porous at t0. This would explain why, although the degradation phenomenon progressed in a centripetal manner, it did not start from the surface but below the surface, and in few cases at different depths in the samples.
In order to confim this hypothesis, it would be useful to check by µ-CT the green body used for the production of the specimens. In this way, it would be possible to verify if the brighter rings were already present, and they were caused, thus, by the casting process, or if they appeared only later, as a consequence of the sintering step. Moreover, it could be helpful to perform dissolution tests with samples completely resurfaced, in order to eliminate the initial external crown, and check how this would affect the formation and the location of porous layers.

After 2 weeks of immersion, the pore interconnection size distribution at the surface displayed an increase of porosity interconnections in the range of 300-800 nm (Figure 28) and the mechanical properties kept on being much lower than the original ones (ΔH = -90%, ΔE = -70%, Figure 35). A possible hypothesis, therefore, is that between 1 week and 2 weeks the porous layer increased, affecting porosity and mass, but without further influencing the mechanical properties. The values of *H* and *E*, moreover, appeared almost constant along the indentation depth (Figure 37-Figure 38); this suggests that the mechanical properties of the surface were mainly dictated by the porous layer, while the influence of the denser external layer observed after 1 week was no more visible.
Finally, as far as the inner part of the samples is concerned, no evolution was observed in terms of microstructure, chemistry and mechanics.

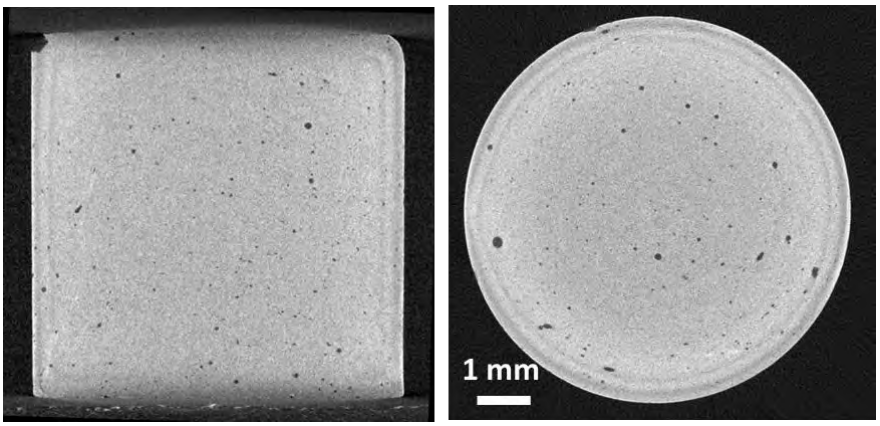

Figure 47: Frontal (left) and transverse (right) µ-CT images of a β-TCP sample prepared for compression tests (e.i. immersion of 2w in TRISd) (resolution of 10 µm/voxel)

After **4 weeks** of immersion, a further important loss of volume, mass and density was observed on β-TCP samples (ΔV = -6%, ΔW = -14% and Δρ = -9% compared to value at t0, Figure 9-Figure 11). At the same time the thickness of the porous layer observed by µ-CT increased, reaching an average value of 590 µm (while the external crown was almost unchanged) (Figure 19 and Figure 21). Moreover, mercury intrusion detected the clear presence of an intermediate porosity interconnection size centred on 660 nm and a slight enlargement of the major peak towards 6000 nm (Figure 28). These results suggested that the increase of porosity was linked to an augmentation of pore interconnection both at the nano- (660 nm) and micron- (6000 nm) level. As already hypothesised for the augmentation of porosity observed after 8 weeks in TRISs, in the case of TRISd also, the increase of porosity could be due on one side to the enlargement of the small inter-granular porosities and on the other to the detachment of bigger grains.
In terms of chemical composition, the possible presence at the surface of apatite observed after 2 weeks was confirmed by the continuous presence of the peak detected by XRD at 32.1° (Figure 14).
Connecting the evolution of volume, mass, porosity and the µ-CT observations, it can be hypothesised that part of the porous layer observed at 2 weeks detached, causing the loss of volume detected after 4 weeks. This loss could have been either caused by the eased propagation of cracks in the porous

layer (see 4 weeks sample in Figure 19) or by the weak cohesion between the superficial crown and the porous layer (see 8 weeks sample in Figure 19). According to the dimensions of samples at 4 weeks, the diameter of the specimens lost around 240 µm between 2 and 4 weeks, suggesting that the detached layer was about 120 µm thick. This value is perfectly coherent with the thickness of external crown (60 µm) and porous layer (230 µm) measured at 2 weeks (Figure 21). If the detached layer was 120 µm thick, the detachment should have started in the porous layer, as one could expect. According to µ-CT observations, moreover, the porous layer further increase in depth (Figure 19).
The mechanical properties, finally, were greatly decreased compared to values at time zero (ΔH = -95%, ΔE = -90%, Figure 35), but did not result significantly altered compared to hardness and Young's modulus measured after 1 and 2 weeks of immersion. Moreover, the values of *H* and *E* as a function of indentation depth appeared constant all along the test (Figure 37-Figure 38). Comparing this trends with the ones observed at 1 and 2 weeks, it can be hypothesised that the degradation continued along immersion time (*H* and *E* were still much lower than at t0), but that the measurements of mechanical properties were affected mainly by the first signs of degradation. In fact, despite the increase of thickness of the porous layer observed between 2 and 4 weeks, the values of hardness and Young's modulus measured at the surface did not further decrease.
On the other hand, once again no relevant changes were observed in the inner part of the samples.

The **8 weeks** immersion caused a further loss of volume, mass and density (ΔV = -11%, ΔW = -24% and Δρ = -15% compared to value at t0, Figure 9-Figure 11). The porous layer observed by µ-CT was 560 µm thick in average (Figure 19 and Figure 21) and its porosity was well visible also on pore interconnection size distribution curves (peak around 660 nm and enlargement of the major peak towards 6000 nm, Figure 28).
XRD pattern still displayed the peak at 32.1° observed for the previous time-points (Figure 14). SEM images (Figure 25) pointed out the presence at the surface of small precipitates comparable to those (maybe of organic nature) observed in PBSd (Figure 23). Moreover, the porosity at the surface appeared "filled" by small fragments of β-TCP.
The values of hardness and Young's modulus measured at this time-point (ΔH = -92%, ΔE = -90%) were really close to those at 4 weeks (Figure 35). Once again, a possible hypothesis is that the porous layer thickened between 4 and 8 weeks and part of it detached, causing a decrease in diameter of the sample of around 450 µm.
At this time-point, finally, also the core of the samples displayed a slight evolution. The porosity between 300 nm and 800 nm, in fact, increased and a bump appeared at 6000 nm (Figure 28). Despite these changes, the mechanical properties were unaltered.

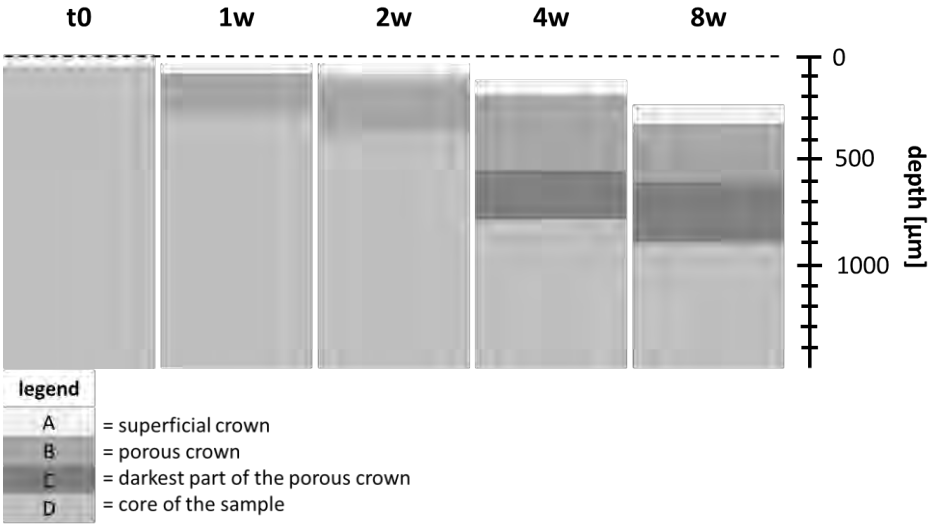

Figure 48: Schematic evolution with time of the different layers observed by µ-CT in samples immersed in TRISd

On the overall, the evolution of β-TCP samples in TRISd seemed to result only from a dissolution process; this caused an increase of porosity (mainly around 660 nm interconnection size) in a zone close to the surface of the sample, originating a strong decrease of mechanical properties of the outer part of the specimen. The porous layer, moreover, appeared to thicken in a centripetal manner causing, from time to time, the detachment of its most external layer. In addition, the properties of this porous layer (in particular its density) probably changed along immersion, as explained in the following lines and schematically represented in Figure 48.
Comparing the relative losses in volume and in mass for a same time-point, the change in dimension does not seem to be strong enough to justify the observed loss of weight with the assumption that dissolution occurs only at the external surface. This difference suggests that the additional loss of mass was due to an increase of porosity, likely localised in the porous layer close to the surface. Knowing the thickness of the porous layer detected by µ-CT, it is possible to calculate its total volume and its percentage compared to the volume of the whole sample. Finally, hypothesising that the core was unaltered (as suggested by the results of micro-indentation tests), it is possible to deduce how much the density of the porous layer was decreased compared to the one of the core. For this purpose it is enough to divide the additional percent loss of mass by the volume of the porous layer. Table 7, summarising the percentages just described, shows how the apparent density and porosity of the porous layer changed during time. After a first stable decrease for the first two weeks, the density reached almost half of its original value (-49%), leading to a porosity of 89% (compared to 79% of t0). However, after 4 weeks the density of the porous layer appeared increased (-34%, i.e. porosity of 86%) compared to the value of the previous time-point. This difference can be explained by the fact that part of the highly porous layer which was visible at 2w detached between 2 and 4 weeks, so that the porous layer observed at 4w was, on the overall, slightly denser. At 8 weeks, finally, part of the porous layer seemed to detach, while the remaining one underwent a further decrease of density (becoming 53% less dense than at t0, which corresponds to a porosity of 90%).

Table 7: Difference between loss of mass (ΔW) and volume (ΔV), percentage of volume made of porous layer (V por), theoretical decrease of density of the porous layer compared to the core and final porosity of the porous layer

t	|ΔW-ΔV| [%]	V por [%]	theoretical decrease ρ [%]	porosity of the porous layer [%]
1w TRISd	3	8	-34	86
2w TRISd	5	10	-49	89
4w TRISd	8	24	-34	86
8w TRISd	13	25	-53	90

4.3.5 Influence of the immersion conditions

As observed for DCPD samples, the comparison between the results obtained in TRISs and TRISd can give information about the influence of the solution refresh, while the comparison between PBSd and TRISd allows to evaluate the importance of the medium choice.

Static versus dynamic

Only after 8 weeks of immersion, samples in TRISs started to show phenomena similar to those observed in TRISd already after one week (Figure 18, Figure 32 and Figure 19, Figure 35 respectively). Moreover, despite the longer time of immersion, the changes noticed in static conditions were less pronounced than those in the dynamic set-up. The loss of weight, the increase in porosity and the decrease of mechanical properties assessed after 8 weeks in TRISs were, in fact, less strong than those measured after one week in TRISd. This observation confirm the strong influence of the refresh on the degradation process of the material.

PBS versus TRIS

Samples immersed in TRISd underwent important changes in their microstructure and mechanical properties, already after one week of immersion (Figure 19, Figure 35). On the other hand the specimens immersed in PBS did not display significant changes even after 8 weeks (Figure 17, Figure 29). This difference of behaviour suggests that the solution composition (i.e. the ion content) has even more influence on the evolution of the material than the periodic refresh of the medium. Indeed this is coherent with the fact that in TRIS solution the properties of the samples changed even in static conditions.
The stronger phenomena observed in TRIS in comparison to PBS can be explained by the different compositions of the media. TRIS does not contain calcium and phosphates ions and it favours, thus, the dissolution of β-TCP. On the contrary, PBS, containing phosphates, hinders the dissolution of the material.

4.3.6 Experimental methods: mechanical properties

As explained in paragraph 4.2.3, some micro-indentation tests were performed in humid conditions in order to approach an *in-situ* measurement.
The evolution of properties along immersion time appeared similar in dry and humid conditions (Figure 40). However, the humidity strongly decreased the values of hardness both before and after immersion, as could be noticed also on the indentation curves, where a much higher penetration depth was reached (Figure 41). On the other hand, the elastic modulus was not significantly affected by the presence of liquid.
On the overall, therefore, humid condition did not seem to alter Young's modulus and therefore the elastic behaviour of the material, but the presence of water appeared to ease its irreversible deformation (likely because of a reduction of friction).

As far as compression tests are concerned, it clearly appears in literature [2-4] that for the assessment of the mechanical properties of bone substitutes this technique is the most diffused. However, compression might not be the optimal test for following the evolution of the mechanical properties of degradable materials. This kind of measurements, in fact, involves the whole volume of the sample and cannot detect, therefore, small changes that take place on localised areas of the specimen (such as the surface or the core). Moreover, compression measurements are strongly influenced by the test conditions (for example by the friction between the sample and the plates between which it is positioned).
One of the peculiar aspects of this study was the use of the instrumented micro-indentation method and the comparison between the results obtained by this technique and by compression tests.

The micro-indentation technique appeared particularly sensitive to the early signs of degradation. For example, in TRISs, although no changes were detected by usual characterizations techniques before 8 weeks, the mechanical properties of the surface were already decreased by -50% after one week (Figure 32-left). In TRISd, for the first time-points, only small changes were detected by analyses such as porosimetry and μ-CT (10 μm/voxel), whereas the mechanical properties measured by micro-indentation at the surface of the samples resulted to be already strongly decreased compared to the initial values (Figure 35-left). In the core, on the other hand, almost no changes were detected (Figure 32-right, Figure 35-right).

Additional compression tests were performed on 2 weeks samples, in order to compare the information offered by this technique to those gathered by micro-indentation. As clearly visible in Figure 44, after immersion not only the compressive strength, but also the slope of the loading segment decreased significantly, probably because of early damage of the external porous layers. Moreover, the Young's modulus increased along the loading curve: the closest to the compressive strength the loading/unloading cycle was, the highest the value of *E*. This behaviour can be probably

explained by the fact that during the loading the porous layer was gradually compressed and compacted, as visible on the pictures of Figure 46. As a consequence, the influence of its springback on *E* decreased during the compression test. Therefore, loading/unloading cycles performed before reaching the load plateau provided values of Young's modulus which reflected the properties of both the external porous layer and the bulk.
Taking into account the standard deviation of data, the values of Young's modulus calculated at time zero by compression were coherent with those obtained by micro-indentation (Table 6).
After immersion, on the other hand, Young's modulus assessed by compression was in-between the values obtained at the surface and in the core by indentation. In particular, its value was closer to the one of the core, as appears logical, given that the bulk is supposed to sustain the majority of the load. Although the influence of the porous layer on the value of *E* appeared to decrease along the loading curve, it was impossible to dissociate the influence of each part of the specimen (i.e. surface and core) on the final result. Given that after immersion the material is not any more homogeneous, it is necessary to make some hypotheses in order to be able to compare the results of compression tests with those of indentation. This is why the interpretation and choice of the values obtained with the first technique appears much more complicated than in the case of micro-indentation, where the different parts of the specimen can be tested separately.
In addition, when using compression tests, one should provide not only the value of compressive strength (as it often happens in literature), but also the test conditions and the load-displacement curves. In fact, these data are of great help in the interpretation of the results and can give additional information on the mechanical properties of the material.

On the overall, it can be concluded that, although several information can be obtained by an accurate interpretation of compression curves, this is a structural test rather than a material one. Indeed, compression measurements are strongly affected by the geometry of the specimen and by the conditions of contact between the sample and the platens. Therefore, when a more local analysis of a specific part of a sample is required, as it is the case for resorbable materials showing partial degradation, compression is not the best option. For example, considering that *E* measured by compression is mainly affected by the bulk of the sample, it would have been impossible to detect early degradation signs localised at the surface, as done in this work for TRISs with the micro-indentation technique. On the opposite, as displayed in the present work, micro-indentation appears to accomplish quite well this task, providing information localised enough to assess the mechanical properties of a degraded material. It is even possible to assess a gradient of properties along the sample diameter (Figure 43). Nevertheless, it is worth to notice that a certain dispersion of micro-indentation data was observed at the surface (above all t0) and in the core. This scattering was likely linked to the surface preparation and to the intrinsic differences between one sample and the others: as known, in fact, the micro-indentation technique is highly influenced by the surface state and demands, therefore, an accurate sample preparation. It should be highlighted, moreover, that if the constitutive law of the material is sought, specific additional work is needed for the analysis. In the indentation tests, contrary to compression ones, stress and strain are not homogeneous: as a consequence, as shown in previous works [5, 6], a numerical analysis of the test using finite element models is needed in order to obtain the constitutive law of the material.

4.3.7 Comparison with Literature

Trying to compare the results here obtained with those found in literature appears to be a quite difficult task. Few studies, in fact, have been dedicated to pure β-TCP and among these the experimental conditions adopted are often far from those used in the present work.
Ducheyne, Tang, Bohner and Lemaître [7-9], for example, have investigated in detail the dissolution kinetics of β-TCP. All these works provide deep analyses of the dissolution rate and the concentration of ions released in the medium. However, the evolution of the microstructure of the samples and its influence on the mechanical properties of the material are not investigated. Moreover, these experiments last at maximum few hours and analyse, therefore, only short-term phenomena.

Other works, instead, focus more on the mechanical properties of degraded materials, but often involve the use samples composed not only of β-TCP. For example, Hsu et al. [3] immersed porous biphasic samples (HAp/β-TCP – 3/97wt.%) in acidic water (pH = 4) and Ringer's solution in static conditions for up to 26 weeks. The changes of mechanical properties were then assessed by means of compression and 4-point bending tests. Considering the compositions of the media, one could establish a parallel between water used by Hsu and TRIS used in the present work on one hand, and between Ringer's solution and PBS on the other. Water and TRIS, in fact, containing neither calcium nor phosphate, are expected to favour dissolution of β-TCP, while Ringer's solution and PBS, containing calcium and phosphate respectively, should foster the precipitation of new phases. Coherently with these hypotheses, Hsu observed a slight decrease of properties for samples in water, while no changes for those in Ringer's solution. In a similar way in our study the major changes were observed in TRIS. However establishing a real comparison between the two studies results difficult: some conditions of Hsu's test differed from those adopted in the present work (i.e. static vs refresh of medium) and others were not reported (e.g. the porosity of the samples) One interesting point, anyway, is that the changes observed by 4-point bending were not visible, instead, on uniaxial compression tests: this seems to confirm that this technique is often limited by its low sensibility to microstructural changes.
Another study dealing with β-TCP-based materials is the one by Sànchez-Salcedo [10]: comparing the changes of HAp/β-TCP (27/73wt.%) porous (80% porosity) scaffolds in SBF in static conditions and orbital stirring (dynamic conditions), the researchers observed an accelerated evolution in dynamic conditions. Our tests, comparing orbital stirring and refresh, examined "one step further" and gave a confirmation of the strong influence of set-up conditions on the outcome of the experiments. Also in our study, in fact, the major changes were observed in dynamic conditions where the evolution of the sample was faster and more evident compared to the static one.
An additional study which presents some common points with ours was performed by Dong-Hyun [4]. In this experiment HAp/β-TCP (60/40wt.%) porous scaffolds with different porosities (43% and 46%) were immersed in Hank's solution (containing calcium and phosphate) for up to 8 weeks with a refresh of the medium every 2 days. The assessment of the mechanical properties of the specimens, performed by uniaxial compression, displayed a loss of compressive strength of 30% for the most porous samples and of 40% for the less porous ones (which contained not only β-TCP, but also α-TCP). The precipitation of nano-crystals of apatite was noticed on both types of scaffolds, but this could not be translated into a clear influence on the compression curves and, as a consequence, on the mechanical properties. The observed decrease of strength is coherent with the changes that we assessed in TRIS (static and dynamic) but cannot be correlated with those in PBSd. However, the decreases of mechanical properties measured in our case were on the overall stronger than those observed by Dong-Hyun. This difference can probably be explained by the pure β-TCP composition, grain size, higher porosity, more frequent refresh and higher liquid-to-mass of sample ratio we adopted in comparison to Dong-Hyun's study.

4.4 Conclusions and Perspectives

The present work proved how the evolution of β-TCP was linked to microstructural changes (in particular the degree of porosity) rather than chemical ones, since very little precipitations of crystalline phases were observed in all the tested conditions.
Moreover, the strong influence of both the immersion solution and the set-up was confirmed, showing that the major changes took place in the solution with the lowest saturation (namely TRIS, which does contain neither calcium nor phosphate) and in dynamic conditions.
As for DCPD, also β-TCP samples displayed a degradation process which started from the surface and moved towards the centre of the specimen. A porous and fragile layer appeared underneath the surface of the samples. Although its mechanisms of formation still need to be clarified, its observation

was eased by the use of micro-computed tomography. This technique provided information on parts of the specimens otherwise inaccessible and was, therefore, of great interest.
The formation of a porous layer created a gradient of properties that was assessed thanks to the use of the instrumented micro-indention technique. When compared to compression, micro-indentation resulted to be more suitable for the assessment of mechanical properties of a degraded material. The results of this kind of tests, in fact, provide information on a local scale and are also easier to interpret. Moreover, instrumented micro-indentation resulted quite sensitive and allowed the identification of the first degradation signs even before any other modification of the sample was detected by the other characterisation techniques.
A final remark worthy to be underlined is that although β-TCP is often considered as not "biosoluble", given that its solubility in physiologic conditions is lower than those of OCP [11], we showed that in specific conditions β-TCP degrades through dissolution phenomena. A possible hypothesis, in fact, would be that tuning some specific properties of the material, such as its porosity, β-TCP could behave as a "biosoluble" ceramic.
An interesting perspective from this point of view would be the evaluation of the influence of porosity on the degradation of β-TCP. A previous work by Ito and others [12] has shown that the relative dissolution rate of TCP samples was increased more by an augmentation of microporosity than of macroporosity. This appears coherent with the fact that the dissolution of this type of material usually starts at the grain boundaries [13, 14]. For this purpose, samples such as those used in this study could be thermally treated, in order to selectively eliminate the nano-porosities present in the original specimens, then immersed in the same conditions used for the present work and finally tested. Comparing the results with those of the present study, therefore, it would be possible to uncouple and evaluate the influence of nano and micro porosities respectively.
In this objective, some preliminary tests of thermal treatment have been already performed; some samples underwent a treatment of 30 minutes at 850, 900, 950 or 1000°C. With increasing temperature, a shift toward larger interconnection sizes was observed for the smallest porosities (cf. Figure A.c.13 in Annex). This seems to show that the thermal treatment induced a coalescence of the smallest porosities, while the largest pores did not seem to be as affected. Further adjustments would be needed to completely eliminate the smallest porosity without significantly alter other important parameters such as the grain size; however these preliminary results already give some interesting inputs for future investigations. In parallel, it might also be interesting to perform further tests with samples presenting zones of different controlled porosities, to confirm or reject the hypothesis concerning the formation of porous layer(s) underneath the surface.

Finally, as a future perspective, it would be interesting to perform some additional tests to further clarify the observed phenomena. In particular it would be useful to:

- measure the concentration of ions released in the immersion solution: this would help in the comprehension of the dissolution and precipitation phenomena observed. Moreover, these results could be compared with the data present in literature. It should be noted that the immersion solutions have been collected and ions concentrations measurements are on-going;
- carry out Fourier-transformed Infrared spectroscopy (FT-IR) measurements, in order to detect the possible presence of amorphous phases which could not be observed using XRD analyses.

References

1. Miller M, et al., *Surface roughness criteria for cement paste nanoindentation.* Cem Concr Res, 2008. 38: p. 10.
2. Santos, C.F.L., et al., *Design and production of sintered β-tricalcium phosphate 3D scaffolds for bone tissue regeneration.* Materials Science and Engineering: C, 2012. 32(5): p. 1293-1298.
3. Hsu, Y.H., I.G. Turner, and A.W. Miles, *Mechanical properties of three different compositions of calcium phosphate bioceramic following immersion in Ringer's solution and distilled water.* Journal of Materials Science: Materials in Medicine, 2009. 20(12): p. 2367-2374.
4. Kim, D.-H., et al., *In vitro biodegradable and mechanical performance of biphasic calcium phosphate porous scaffolds with unidirectional macro-pore structure.* Ceramics International, 2014(0).
5. Clement, P., *Détermination des proprietés mécaniques de céramiques poreuses par essais de micronindentation instrumenée sphérique.* Ph.D. Thesis, 2013.
6. Staub, D., *Propriétés mécaniques des céramiques en alumine de forte porosité pour les supports de catalyseurs.* Thèse INSA LYON, 2014.
7. Ducheyne, P., S. Radin, and L. King, *The effect of calcium phosphate ceramic composition and structure on in vitro behavior. I. Dissolution.* J Biomed Mater Res, 1993. 27(1): p. 25-34.
8. Tang, R.K., et al., *Kinetics of dissolution of beta-tricalcium phosphate.* Langmuir, 2001. 17(11): p. 3480-3485.
9. Bohner, M., J. Lemaître, and T.A. Ring, *Kinetics of Dissolution of β-Tricalcium Phosphate.* Journal of Colloid and Interface Science, 1997. 190(1): p. 37-48.
10. Sanchez-Salcedo, S., et al., *In vitro structural changes in porous HA/β-TCP scaffolds in simulated body fluid.* Acta Biomaterialia, 2009. 5(7): p. 2738-2751.
11. Bohner, M., *Bioresorbable ceramics*. Degradation rate of bioresorbable materials - Prediction and evaluation, ed. F. Buchanan2008, Boston: Woodhead publishing in Materials.
12. Ito, A., et al., *Interlaboratory studies on in vitro test methods for estimating in vivo resorption of calcium phosphate ceramics.* Acta Biomater, 2015. 25: p. 347-55.
13. H. K. Koerten, J.v.d.M., *Degradation of calcium phosphate ceramics.* J Biomed Mater Res., 1999. 44(78-86).
14. Schaefer, S., et al., *How degradation of calcium phosphate bone substitute materials is influenced by phase composition and porosity.* Advanced Engineering Materials, 2011. 13(4): p. 342-350.

CHAPTER 5: EVOLUTION OF DENSE β-TCP SAMPLES IN PRESENCE OF OSTEOCLAST-LIKE CELLS

The present chapter is focused on cellular tests performed under the supervision of Prof. Aldo Boccaccini and Dr. Rainer Detsch during two three-months stays at the Institute of Biomaterials of the Friedrich-Alexander Universität of Erlangen-Nürnberg (Germany). The aim of these tests was to evaluate the evolution of the properties and characteristics of a bone substitute model material for bone substitutes application when in contact with cells in charge of bone resorption. The approach and techniques used, thus, were similar to those reported in the previous chapters about acellular tests, but were focused on cellular resorption phenomena more than on acellular, physico-chemical, dissolution/precipitation events. In particular, the main purpose was to investigate which phenomena took place on the material during the resorption processes and how the properties of the material affected both these events and the cellular behavior. For this purpose, two different kinds of samples were used: pure dense β-TCP (named hereafter TCP_NoMg) and dense β-TCP doped with 5 mol.% of magnesium (named TCP_Mg). The addition of Mg was likely to affect some properties of β-TCP such as the solubility of its grains and grain boundaries, which might influence thus the kinetics and mechanisms of cellular resorption.

5.1 Materials

Pure and doped TCP dense samples were obtained as described in chapter 2 (paragraph 2.1.3) by pressing and sintering the initial powders, which were provided by Prof. Marc Bohner (RMS Foundation, Bettlach, Switzerland). The resulting specimens, small discs of around 8.5 mm in diameter and 4 mm in height, were characterised at time zero by means of XRD, SEM and TEM analyses. Moreover apparent density of each sample was computed, resulting in an average porosity of 7.8 ± 0.8 % for TCP_NoMg and 8.1 ± 0.9 % for TCP_Mg. The outcomes of these analyses at time zero are reported in the present paragraph.

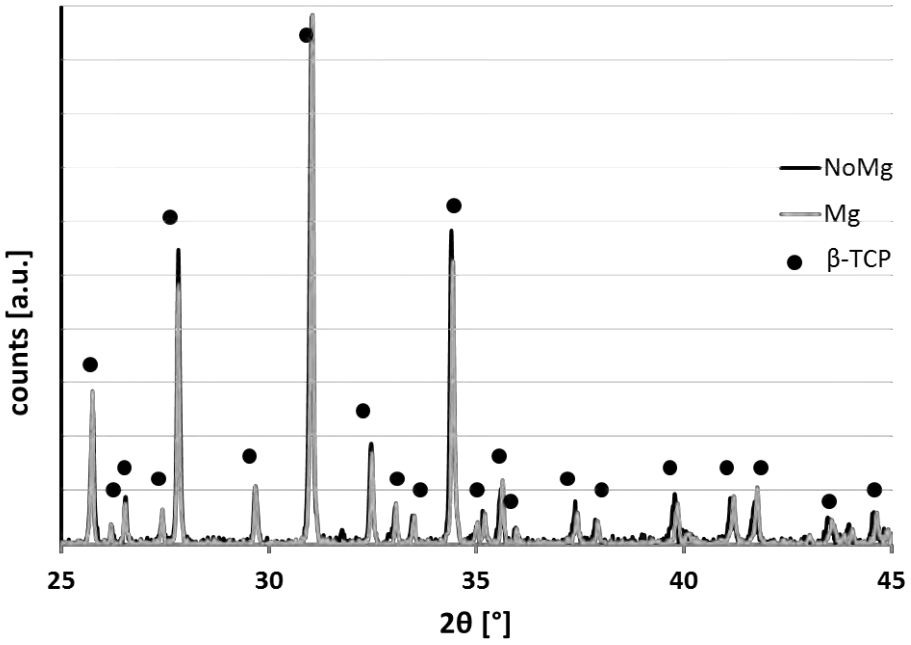

Figure 1: XRD pattern of TCP_NoMg (in black) and TCP_Mg samples (in grey) before cell culture

X-ray patterns did not display significant differences between doped and un-doped TCP (Figure 1): in both cases all peaks corresponded to the beta-tricalcium phase. Since no phase due to the presence of magnesium was detected, further investigations were conducted to detect its location.

Thin slices of pure TCP were analysed by means of TEM coupled with EDX (Energy Dispersive X-ray Spectrometry). As illustrated in Figure 2 the composition of different zones was assessed, in order to identify possible inhomogeneities. In particular, zone 1 refers to the first grain, zones 3 and 5 to the second one and 2 and 4 to the grain boundary. Values reported in Table 1 concern the percentage in weight of P and Ca and the molar ratio Ca/P. Boxes are coloured in green if they display a value almost equal (±1%) to the expected one, in red for lower values and blue for higher ones.
The results showed some differences between one grain and the other (cf. zones 1 and 3), but a certain uniformity inside the same grain (cf. zones 3 and 5). Also the grain boundary (zones 2 and 4) displayed a quite homogeneous composition, close to the one of grains. On the overall the molar ratio between calcium and phosphorus, expected to be equal to 1.5, was lower because of an apparent higher concentration of P.

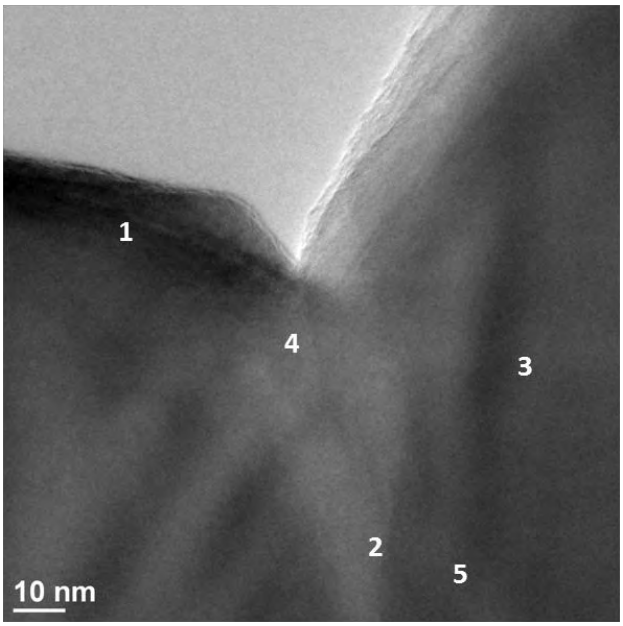

Figure 2: TEM image of TCP_NoMg sample (Image: L. Joly-Pottuz). Numbers correspond to areas where EDX analyses were performed

Table 1: Chemical composition of TCP_NoMg: evaluation of the weight percentage of calcium and phosphorus atoms and of the molar Ca/P ratio. Numeration of zones refers to points highlighted in Figure 2. Boxes in green display a value almost equal (±1%) to the expected one, red boxes lower values and blue boxes higher ones

	P [%wt]	Ca [%wt]	Ca/P [mol/mol]
expected value	20	39	1.5
zone	measured		
1	28.7	48.7	1.3
2	33.2	42.8	1.0
3	38.5	39.8	0.8
4	31.8	38.3	0.9
5	38.4	38.3	0.8

TCP_Mg resulted to be composed of only crystalline phases; no halos due to amorphous phases were observed in the acquired diffraction patterns (Figure 3). As in the case of pure TCP, small differences were observed between the composition of one grain and the other. The analyses of grain boundaries confirmed a presence of magnesium comparable to that of grains if not slightly higher (zone 2 in Table 2). To conclude, it should be added that some areas presented a percentage of Mg higher, and some other lower, than the expected one (1.2 wt.%, corresponding to 5 mol.%), but on the average the measured values were close to the theoretic ones.

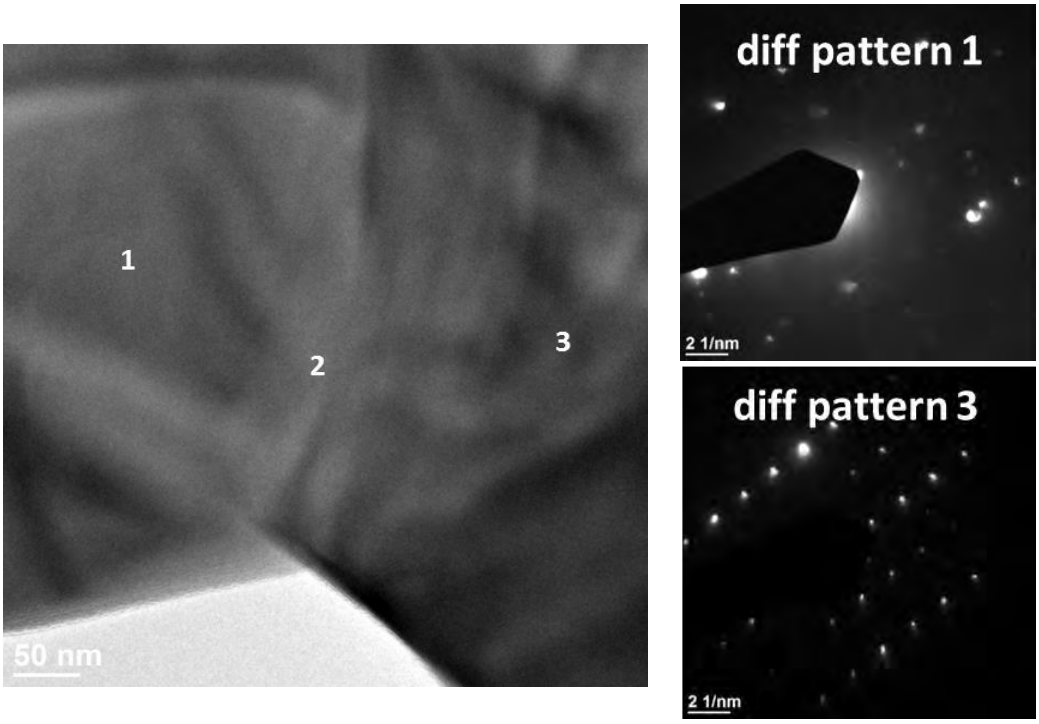

Figure 3: TEM image of TCP_Mg (left) and diffraction patterns corresponding to zone 1 and 3 (right) (Images: L. Joly-Pottuz). Numbers correspond to areas where EDX analyses were performed

Table 2: Chemical composition of TCP_Mg: evaluation of the weight percentage of phosphorus, calcium and magnesium atoms and of the molar Ca/P ratio. Numeration of zones refers to points highlighted in Figure 3. Boxes in green display a value almost equal (±1%) to the expected one, red boxes lower values and blue boxes higher ones.

	P [%wt]	Ca [%wt]	Mg [%wt]	(Ca+Mg)/P [mol/mol]
expected value	20	37	1.2	1.5
zone	measured			
1	21.9	30.6	1.1	1.4
2	20.9	30.9	1.6	1.6
3	21.4	32.3	1.5	1.6

At time zero, the doped and un-doped materials displayed a quite similar microstructure (Figure 4), with comparable mean grain size (TCP_NoMg = 1.5 µm, TCP_Mg = 2.4 µm) and porosity (TCP_NoMg = 7.8%, TCP_Mg = 8.1%). Also the average roughness did not vary significantly from one material to the other (R_{RMS} TCP_NoMg = 2.0 µm, R_{RMS} TCP_Mg = 2.4 µm, R_a TCP_NoMg = 1.5 µm, R_a TCP_Mg =

1.7 µm). The only difference worthy to be noticed was the presence in some parts of TCP_NoMg of a kind of "layer" on top of some grains (as can be seen in the low left corner of image B in Figure 4) that could not be found, on the contrary, on TCP_Mg.

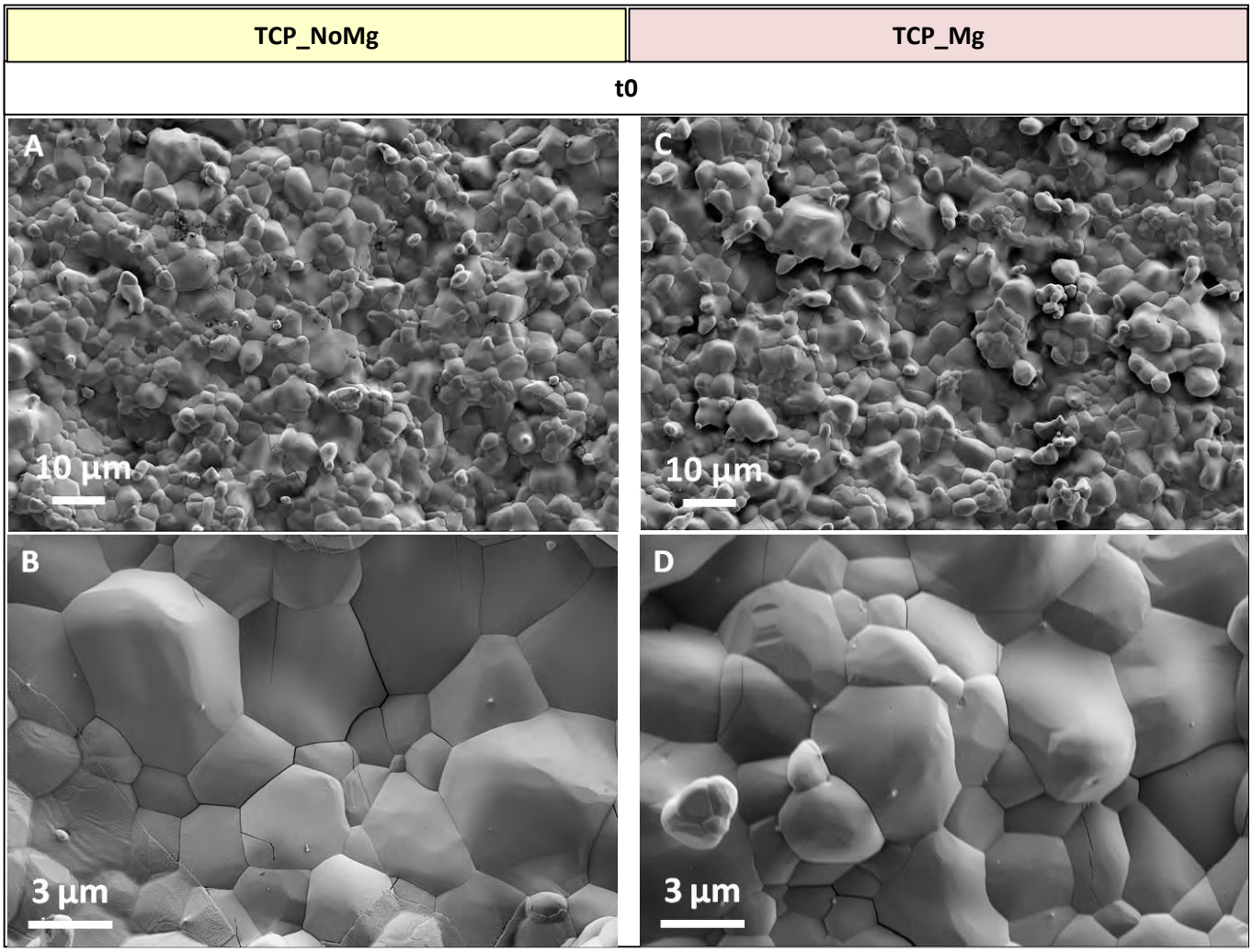

Figure 4: SEM micrographs of TCP_NoMg and TCP_Mg samples before immersion

5.2 Investigation of the cells behaviour

As explained in paragraph 1.2, in physiologic conditions the cells in charge of resorbing bone matrix are the osteoclasts. However, this kind of cell is quite difficult to collect because of its scarcity in non-pathological conditions and because of the difficulties in handling calcified tissue [1]. For these reasons, it is often preferred to use osteoclast-like cells, which are obtained in differentiating osteoclasts precursors with growth factors and which "mimick" osteoclasts' activity.

Some preliminary tests were performed culturing directly monocytes (osteoclasts precursors) on the surface of the materials and trying to differentiate them once on the β-TCP samples. Detailed results of these preliminary tests are provided in Annex (A.d). Briefly, osteoclasts activity was not supported by β-TCP samples. However, it could not be concluded if this was due to a low differentiation of precursor cells, or if it was due to a low activity of differentiated cells. In order to avoid this problem,

and to favour the differentiation of monocytes into osteoclasts, a second approach was followed for growing the cells for all tests described in the following pages.

In the present case, murine monocytes RAW 264.7 were chosen as precursors; the cells were grown with stimulating factors RANKL and MCSF following the protocol detailed in paragraph 2.3. It is worth to underline that, at this stage, different types of cells can be found in the culture medium since some might have differentiated, others might not have. In particular, monocytes (mononucleated cells of around 10 µm in diameter) might have coexisted with osteoclast-like cells (multinucleated cells of tens of microns in diameter). After the differentiation process, the cells were seeded on β-TCP samples and on glass discs used as reference substrates. The cells were then incubated for 2, 4 and 7 days respectively and later analysed according to the techniques listed in paragraph 2.5.

5.2.1 Cell viability and density

Cell viability and proliferation were assessed by WST assay (Water Soluble Tetrazolium); results are plotted in Figure 5. The results were coupled with the values of cell density measured on each sample type (Figure 6) by analysing fluorescence images.

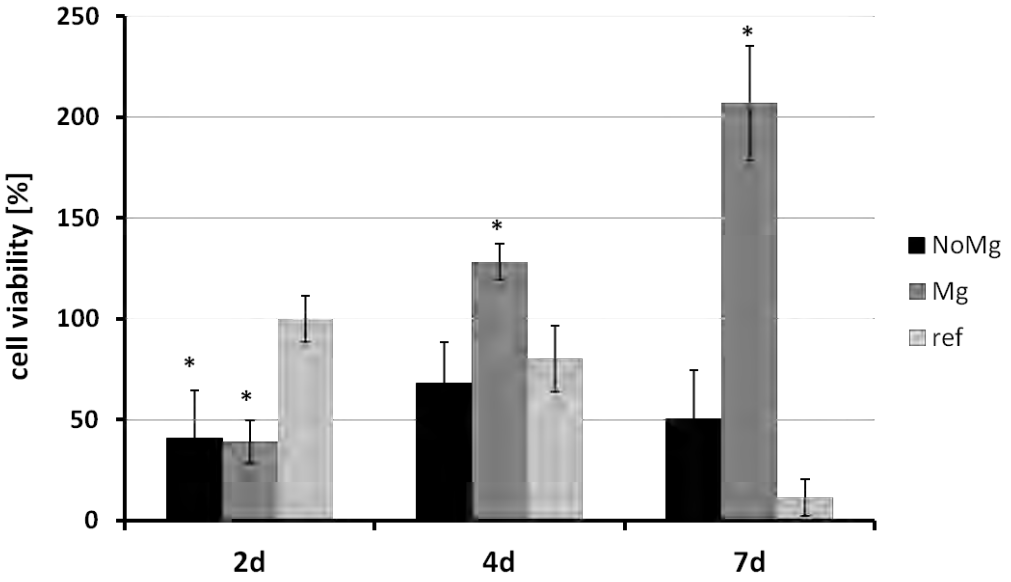

Figure 5: Cell viability. Asterisks point out statistically significant differences in comparison to values obtained for the reference materials (glass discs, denoted as "ref")

As illustrated in Figure 5, after an initial lower value for cell viability on TCP compared to those on the reference material, the viability of cells increased on TCP_Mg and remained almost stable on TCP_NoMg; on the reference discs, cell viability decreased along time. Significant differences could be measured between both TCPs and the reference material at day 2, when the cells on the reference discs displayed a higher viability. For later time-points, only TCP_Mg differed significantly from the reference material.

As far as cell density is concerned (Figure 6), the general trend showed an increase between day 2 and day 4, followed by a decrease between day 4 and day 7. A peak of maximum cell density was reached, therefore, after 4 days of culture for every material. This trend was common to all samples (TCP_NoMg, TCP_Mg, reference); none of them, in fact, differed significantly from the others, except for TCP_Mg, which displayed a higher density than the reference at day 7.

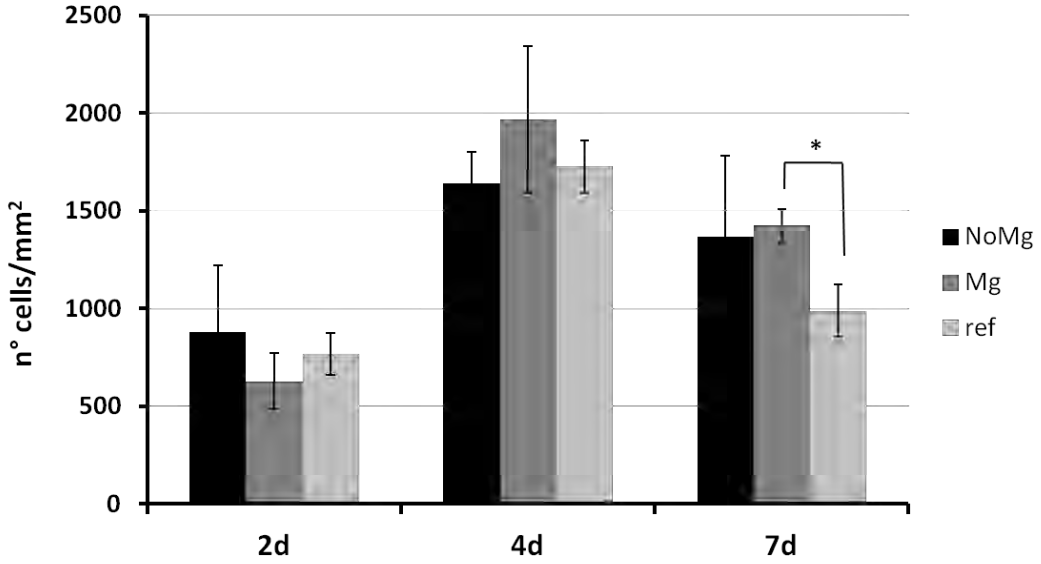

Figure 6: Cell density for TCP_NoMg, TCP_Mg and reference (glass discs, denoted as "ref") at different time-points. Asterisks point out statistically significant differences

Comparing the first two graphs (Figure 5 and Figure 6), it can be noticed that the number of cells and the viability were not directly proportional for all cases. In particular for TCP_NoMg samples cell density and viability seemed to follow the same trend, while this did not happen for TCP_Mg and reference samples. In fact, for doped-samples the viability of cells increased constantly along time although the cell number did not. On the opposite, cells on the reference discs displayed a decrease of viability all along the test, with a particularly evident drop at day 7. For a direct comparison of cell density and viability on each material Figure A.d.9-A.d.10 in Annex can be consulted.

Since previous tests did not permit to differentiate the different cells types, additional analyses were performed with another batch of cells grown for 2 days in the same conditions. In this case, not only the viability was evaluated, but also LDH (lactase dehydrogenase), SAP (acid phosphatase) and TRAP (tartrate resistant acid phosphatase) activities. LDH was used as a marker of cell proliferation; for this purpose only the LDH contained inside the cells was counted, while the one present in the medium (resulting of cell membrane damaging) was not considered. SAP was used for evaluating monocytes activity, while TRAP was a marker for osteoclasts activity. All the measurements were carried out through colorimetric assays.

As can be observed from the first graph (Figure 7), the cell proliferation (LDH activity) was slightly higher on both TCPs compared to the reference; moreover, cell viability was extremely high on both TCP_NoMg and TCP_Mg. No statistical differences were noticed between the doped and the undoped β-TCP. Monocytes activity (SAP) followed a similar trend, with on average higher values for TCP_NoMg and TCP_Mg than for the reference (Figure 8). On the opposite, osteoclasts (TRAP) activity was significantly lower on TCP than on the reference glass discs (Figure 8).

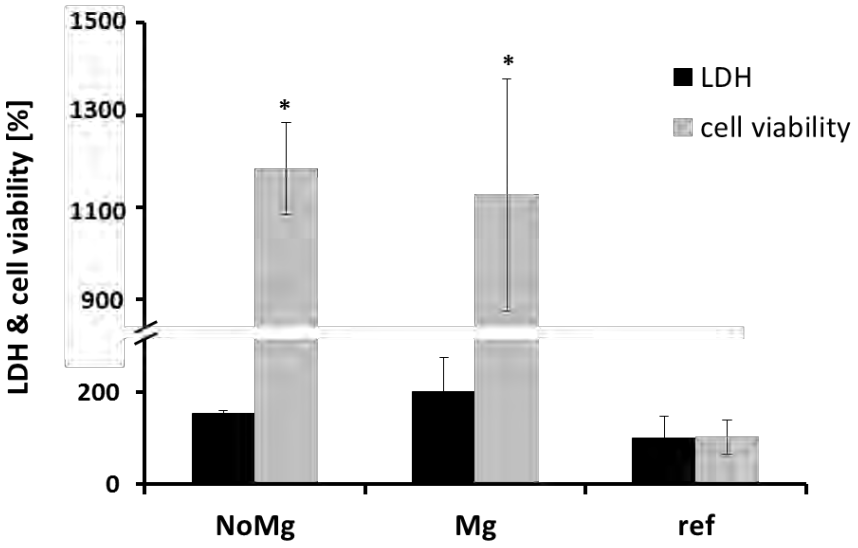

Figure 7: LDH (marker for cell proliferation, in black) and cell viability (measured by WST assay, in grey) after 2 days of culture. Asterisks point out statistically significant differences

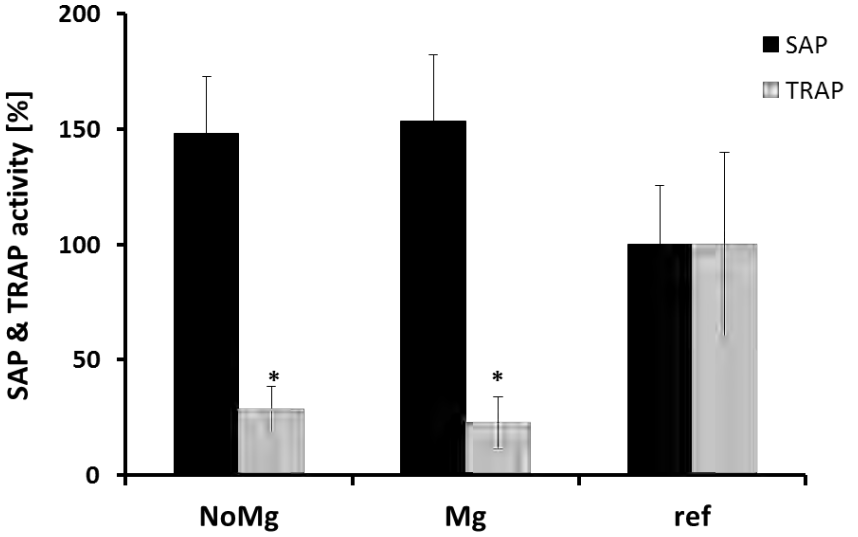

Figure 8: SAP (marker for activity of monocytes, in black) and TRAP (marker for activity of osteoclasts, in grey) activities after 2 days of culture. Asterisks point out statistically significant differences

5.2.2 Cell morphology

Cell morphology was evaluated by means of fluorescence staining; actin filaments of the cytoskeleton, stained with phalloidin, appeared in red, while nuclei (stained with sytox) were in bright green. Figure 9 reports images of cells cultured on the reference glass discs and on β-TCP (pure and Mg-doped) for 2, 4 and 7 days. An image taken at t0 shows how the cells looked like before being scratched, centrifuged and seeded on the surface of the samples.

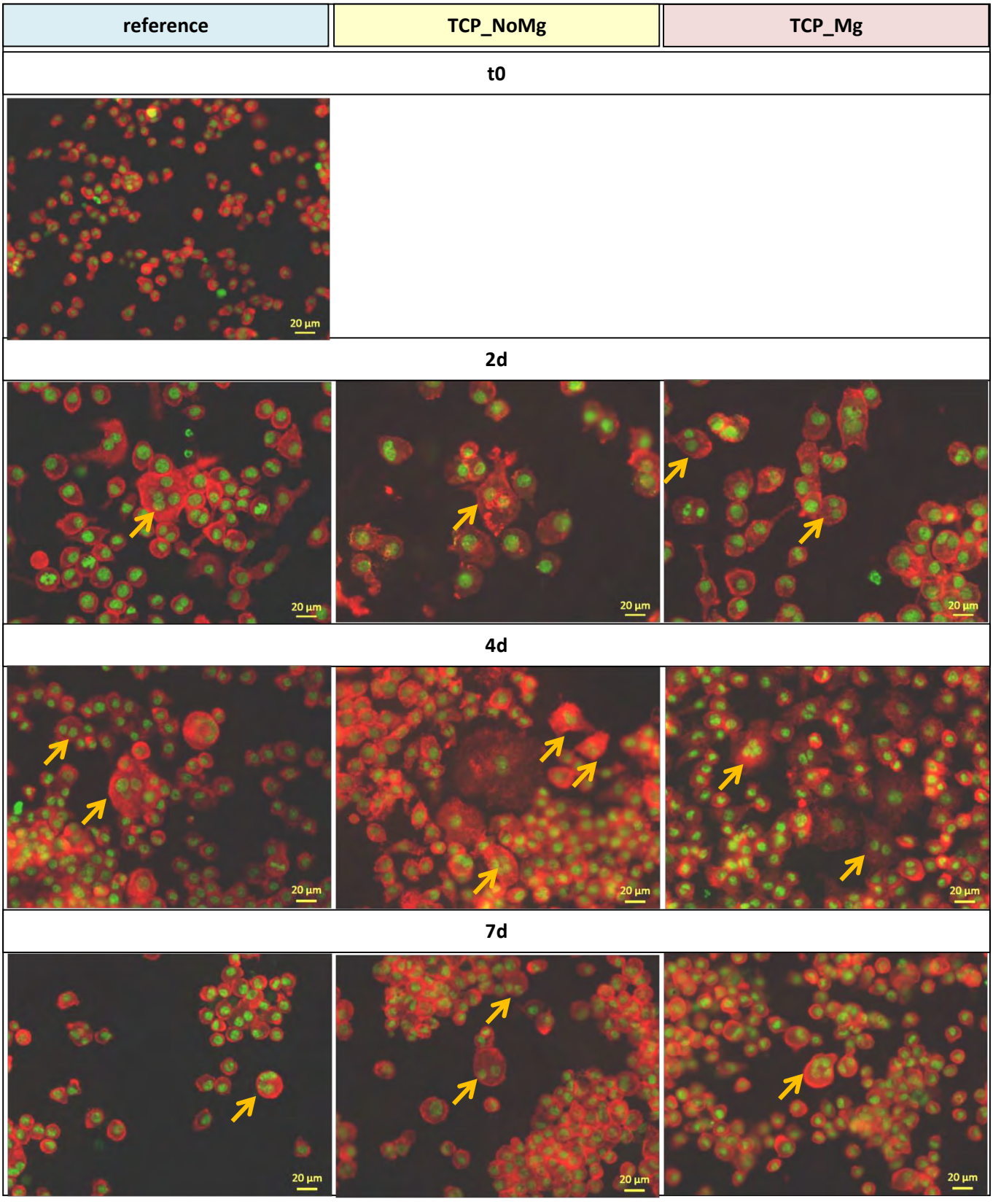

Figure 9: Fluorescence images of cells cultured on reference and β-TCP samples for different times. Actin filaments of the cytoskeleton appear in red, cell nuclei in bright green and arrows point out multinucleated cells.

Comparing the cells at t0 with those at further time-points it is possible to notice a difference in size: on the overall, cells at t0 presented a smaller diameter. This dissimilarity could be explained by the fact that the cells seeded on the samples underwent a centrifugation stage: as a consequence, the

smaller cells present at t0 were discarded during this operation and only the bigger ones were moved onto the samples.
After 2 days of culture, cells appeared to well adhere at the surface of all the materials in a comparable way. A closer look to the actin filaments, often very stretched, disclosed that the cells were still spreading and moving on the surface. Moreover some multinucleated cells were visible, as highlighted by arrows in Figure 9.
After 4 days, large multinucleated cells could be identified on all the samples and the morphology of the cytoskeleton was rounder compare to that at day 2, suggesting that the cells had adhered on the substrate and were not moving anymore.
At day 7, finally, a significative decrease in cell number was observed for all the samples: very few large multinucleated cells could be found on β-TCP specimens (both pure and doped) and almost none was observed on the reference glass discs.

For a closer look to their morphology, cells were also fixed and observed by means of SEM (protocol described in Chapter 2, paragraph 2.5.2). The following figures report the images taken for samples with and without magnesium after an incubation time of 4 and 7 days (Figure 10 and Figure 11).

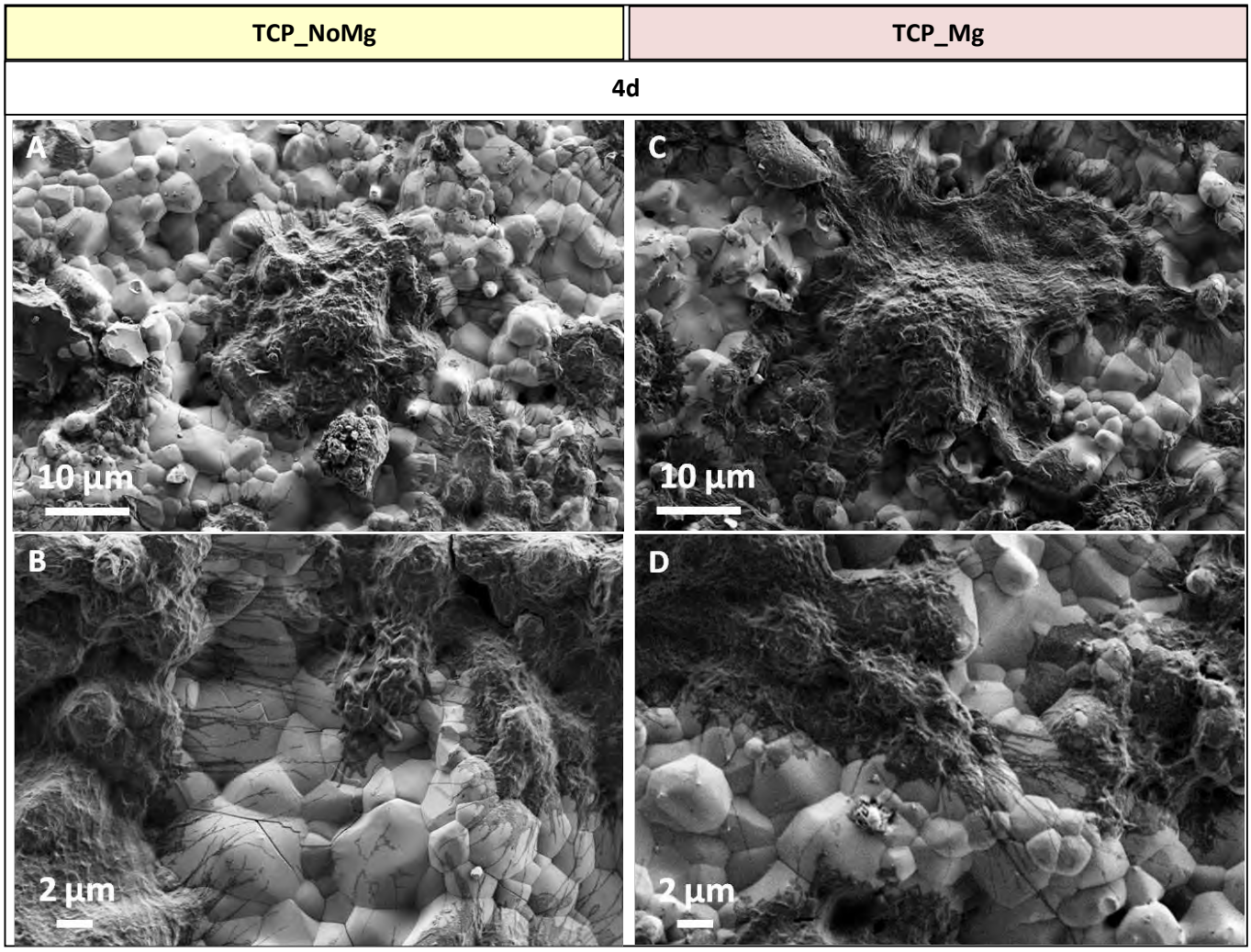

Figure 10: SEM micrographs of cells on β-TCP samples with (C, D) and without (A, B) magnesium after 4 days of culture

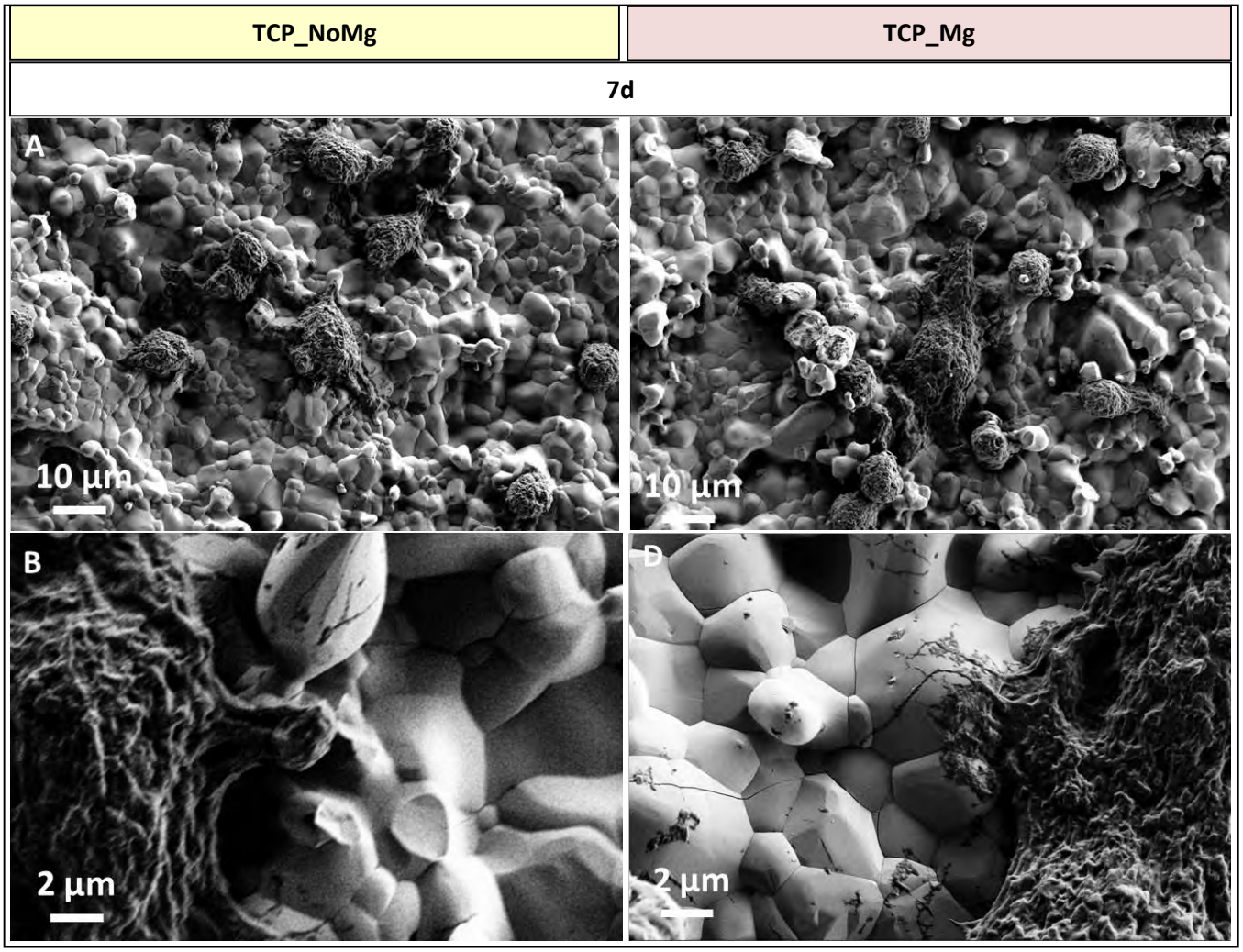

Figure 11: SEM micrographs of cells on β-TCP samples with (A, B) and without (C, D) magnesium after 7 days of culture

SEM micrographs confirmed what had been observed thanks to the fluorescence images: after 4 days of culture, the cells appeared well spread (Figure 10, images A, C), with filopodia strongly adherent on the surface of the samples (Figure 10, images B, D). No differences could be noticed comparing pure and Mg-doped β-TCP. After 7 days, the cell morphology appeared to be changed (Figure 11, images A-D): a much rounded shape was predominant and the adhesion of cells seemed to be decreased if compared to that at 4 days. Also in this case no significant differences were noticeable between TCP_NoMg and TCP_Mg.

For assessing the presence of osteoclast-like cells, TRAP staining test was performed both on samples and on reference glass discs. The results are reported in Figure 12.

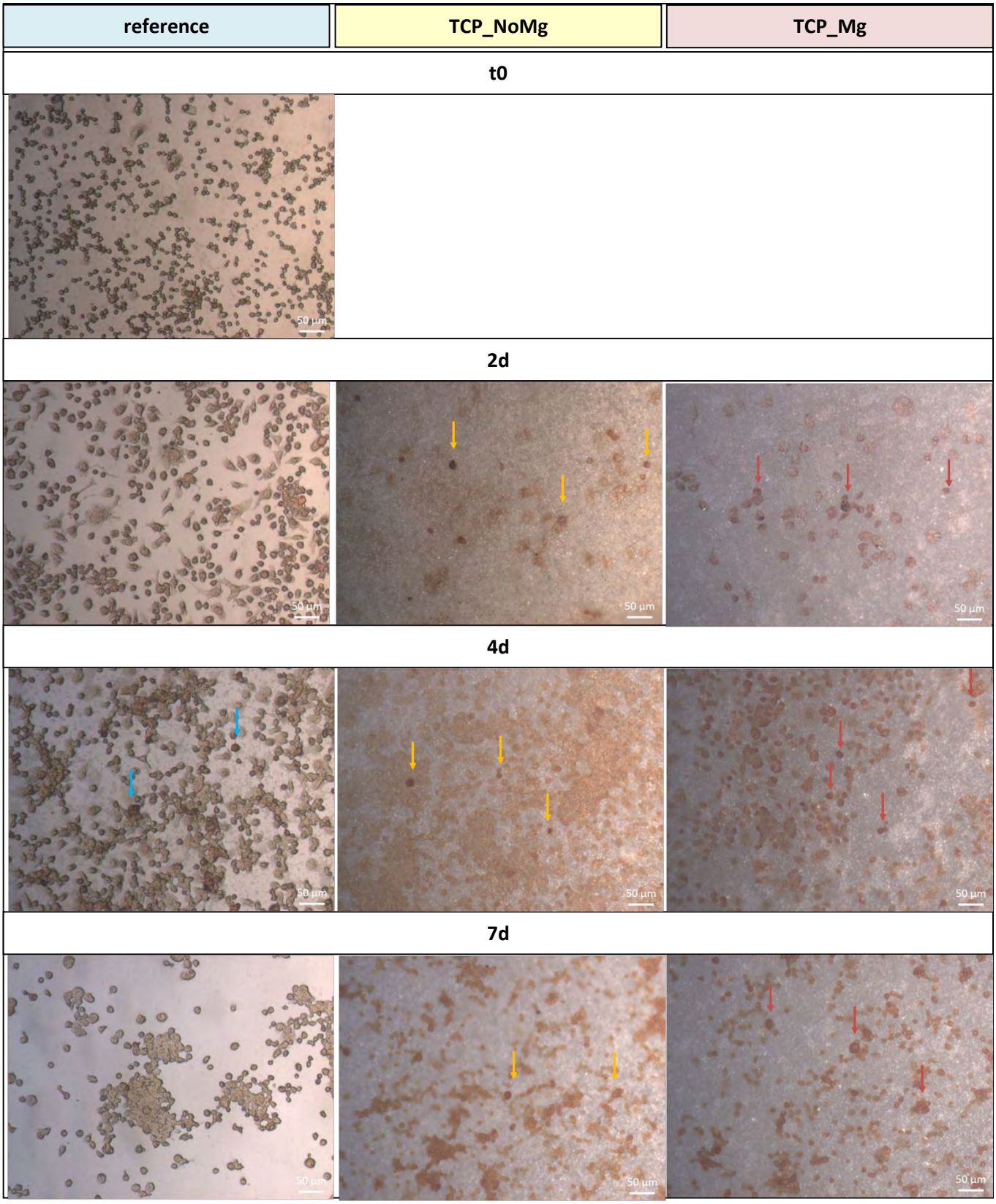

Figure 12: Images of TRAP-stained cells on all materials after different times of culture (scale bar = 50 µm). Arrows point out TRAP-negative cells.

After the staining, the majority of cells displayed a yellowish color, indicating a positive result to the test. Some cells could be clearly identified as TRAP-negative thanks to their dark color and are pointed out by arrows in the images of Figure 12. Comparing the results obtained at different time-points for the two materials (TCP_NoMg, TCP_Mg) slightly less TRAP-positive cells were observed on TCP_Mg than on TCP_NoMg. In all cases, the observation of stained cells was quite difficult on the reference discs, because of the limited contrast between the cells and the substrate. Observing the evolution during time of a single material, the same considerations expressed for SEM and fluorescence images can be drawn again. The cell density grew considerably between day 2 and 4 and clearly decreased before reaching day 7. This trend, finally, was common to all the substrates (TCP_NoMg, TCP_Mg, reference).

On the basis of the results of cell viability (WST, Figure 5), cell density (Figure 6), fluorescence (Figure 9) and SEM (Figure 10 and Figure 11) analyses, samples at 4 days were considered as being more valuable compared to those at other time-points. After 4 days of culture, in fact, cell morphology, viability and density displayed the most favourable values in terms of possibility of formation of osteoclast-like cells and of resorption pits. For this reason, further analyses were performed on the fluorescence images of samples at day 4, in order to assess the dimension of cells, the amount of multinucleated ones and the number of nuclei. The results are reported in Figure 13, Figure 14 and Figure 15.

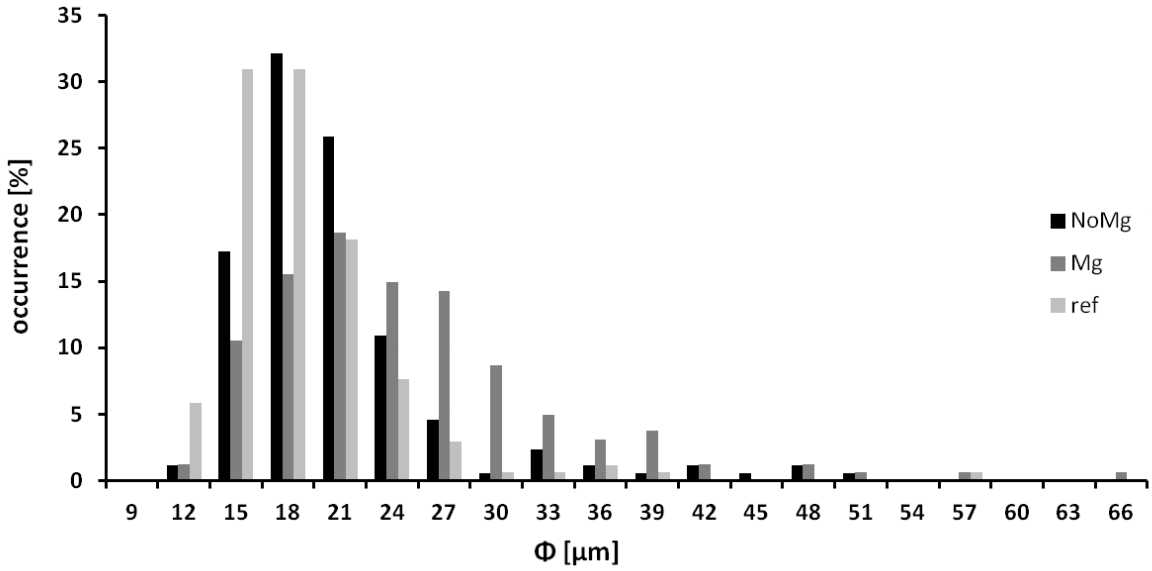

Figure 13: Distribution of cells diameter for the different samples at day 4 (glass discs in light-grey, Mg-doped β-TCP in grey and pure β-TCP samples in black).

Table 3: Median, 10° percentile and 90° percentile of cell diameter at day 4 (values assessed from the histogram presented in Figure 13)

Substrate composition	median [µm]	10° percentile [µm]	90° percentile [µm]
TCP_NoMg	21	16	27
TCP_Mg	24	17	36
Reference glass discs	19	15	24

As far as the cell diameter is concerned (Figure 13), the values obtained for TCP_NoMg and reference seemed to be pretty similar both in terms of average (NoMg = 21 µm, reference = 19 µm) and distribution (10° and 90° percentile in Table 3). Slightly higher values were observed, instead, for TCP_Mg, which displayed an average diameter of 24 µm and a broader size distribution (mainly shifted towards higher diameters).

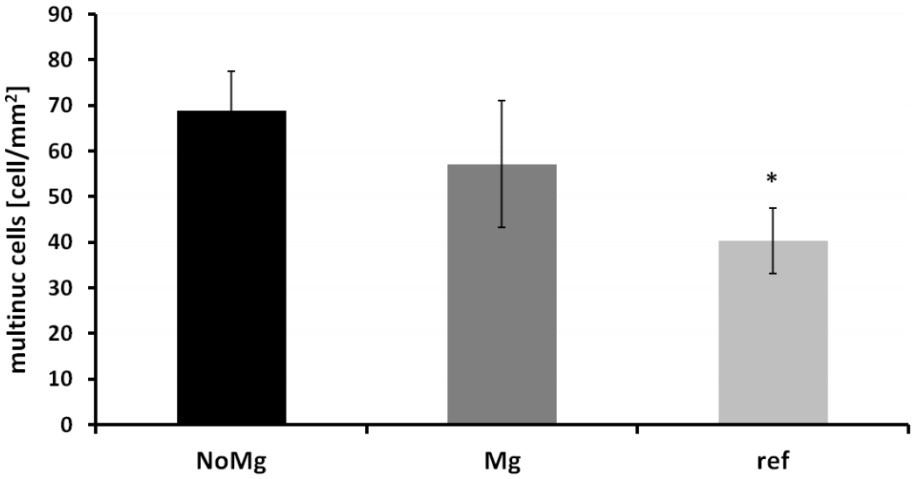

Figure 14: Density of multinucleated cells on all substrates at day 4 (pure β-TCP samples in black, Mg-doped β-TCP in grey and glass discs in light-grey)

Table 4: Density of non-multinucleated and multinucleated cells on all substrates at day 4

Substrate composition	average cell density ± std [cell/mm²]	average density of multinucleated cells ± std [cell/mm²]	Density ratio multinucleated cells/all cells [%]
TCP_NoMg	1640 ± 160	69 ± 9	4
TCP_Mg	1970 ± 370	57 ± 14	3
Reference glass discs	1730 ± 130	40 ± 7	2

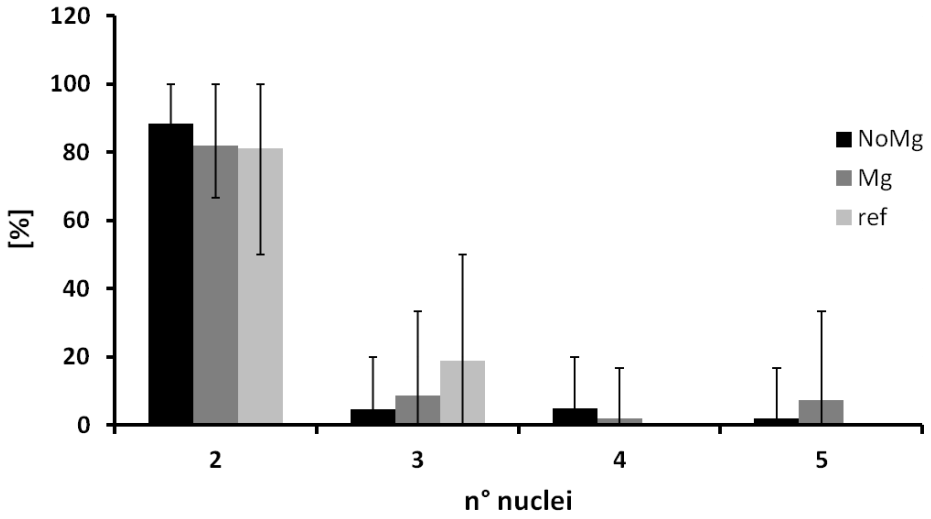

Figure 15: Number of nuclei in multi-nucleated cells on all substrate types at day 4 (pure β-TCP samples in black, Mg-doped β-TCP in grey and glass discs in light-grey)

Analysing the surface density of multinucleated cells, a lower density could be observed on the reference samples, while no significant difference was assessed between TCP_NoMg and TCP_Mg (Figure 14). However, once these values were normalised to the total cell density of each material, it appeared that the occurrence of multinucleated cells was not the same for all the samples. In fact, as shown in the last column of Table 4, although the difference was not very pronounced, the percentage of multinucleated cells appeared to be slightly higher on TCP_NoMg samples (4%) compared to TCP_Mg (3%) and reference substrates (2%). For all materials, moreover, multinucleated cells generally had only 2 nuclei, 3 nuclei to a minor extent and, in a few cases, more than 3 (Figure 15). The distribution of multinucleated cells, finally, did not appear very homogeneous from one zone to the other, causing, thus, the high dispersion of values reported in Figure 15.

5.3 Investigation of materials evolution

One of the main purposes of the present study was a better understanding of the resorption processes induced by cells from the material point of view. That is to say, analyses were not only focused on cells (their number, viability, morphology…), but also on the phenomena that would take place on the material when it underwent cellular degradation. For this purpose, at the end of the tests, cells were removed from the surfaces and the samples were further analysed. Moreover, dissolution tests in RPMI and 0.9% NaCl solution were run in parallel (as explained in paragraph 2.4), in order to be able to distinguish the phenomena induced on the materials by dissolution from those induced by cellular activity. NaCl solution was adopted since it is often considered a physiological saline reference solution.

5.3.1 Cellular tests

Once the cells had been observed (SEM, TRAP and fluorescence staining), they were removed from the samples by means of SDS (sodium dodecyl sulphate) and the surfaces of the specimens were observed with a SEM. The images obtained are reported in Figure 16, Figure 17 and Figure 18.

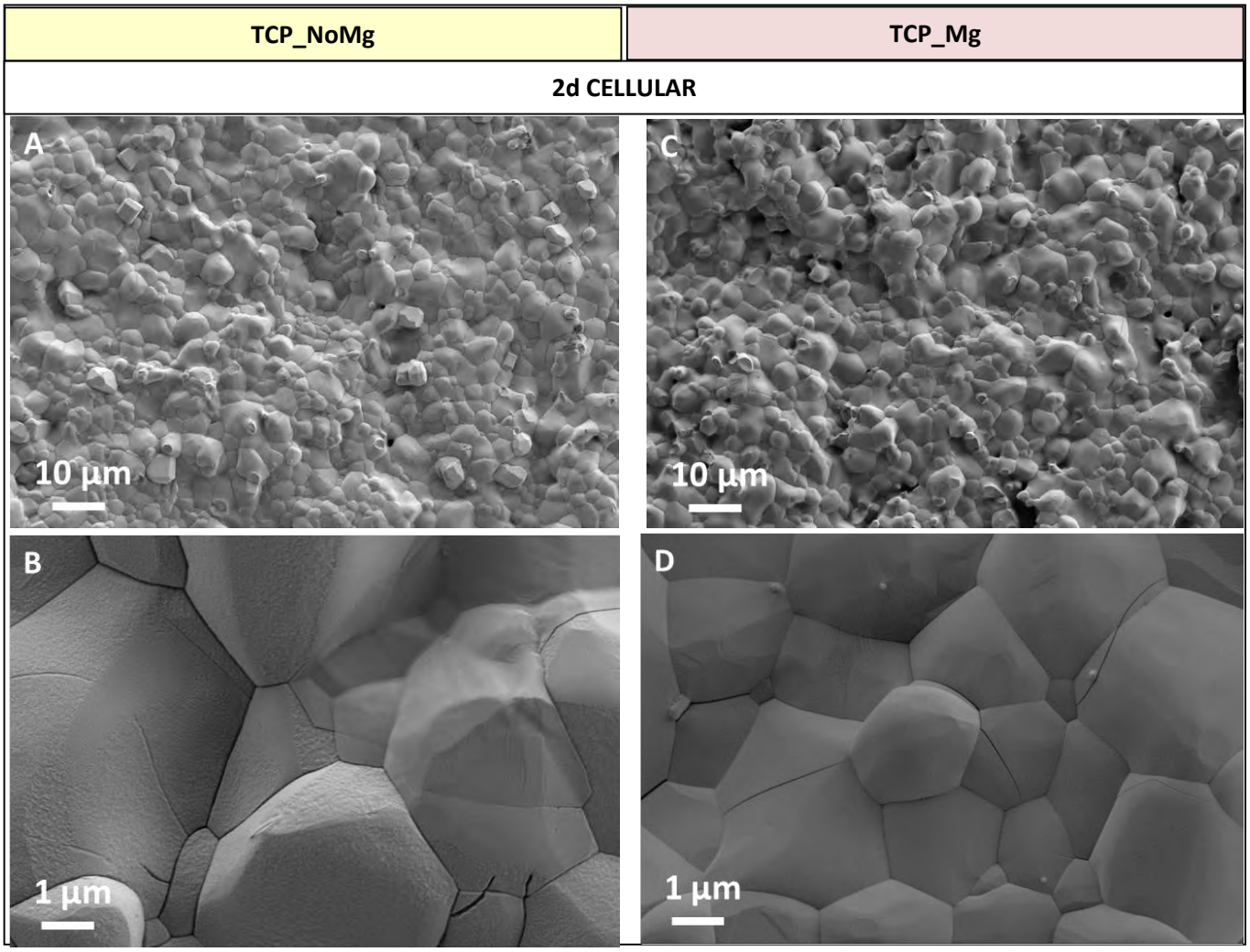

Figure 16: SEM micrographs of samples once the cells were removed (after 2 days of culture). β-TCP with (C, D) and without (A, B) magnesium

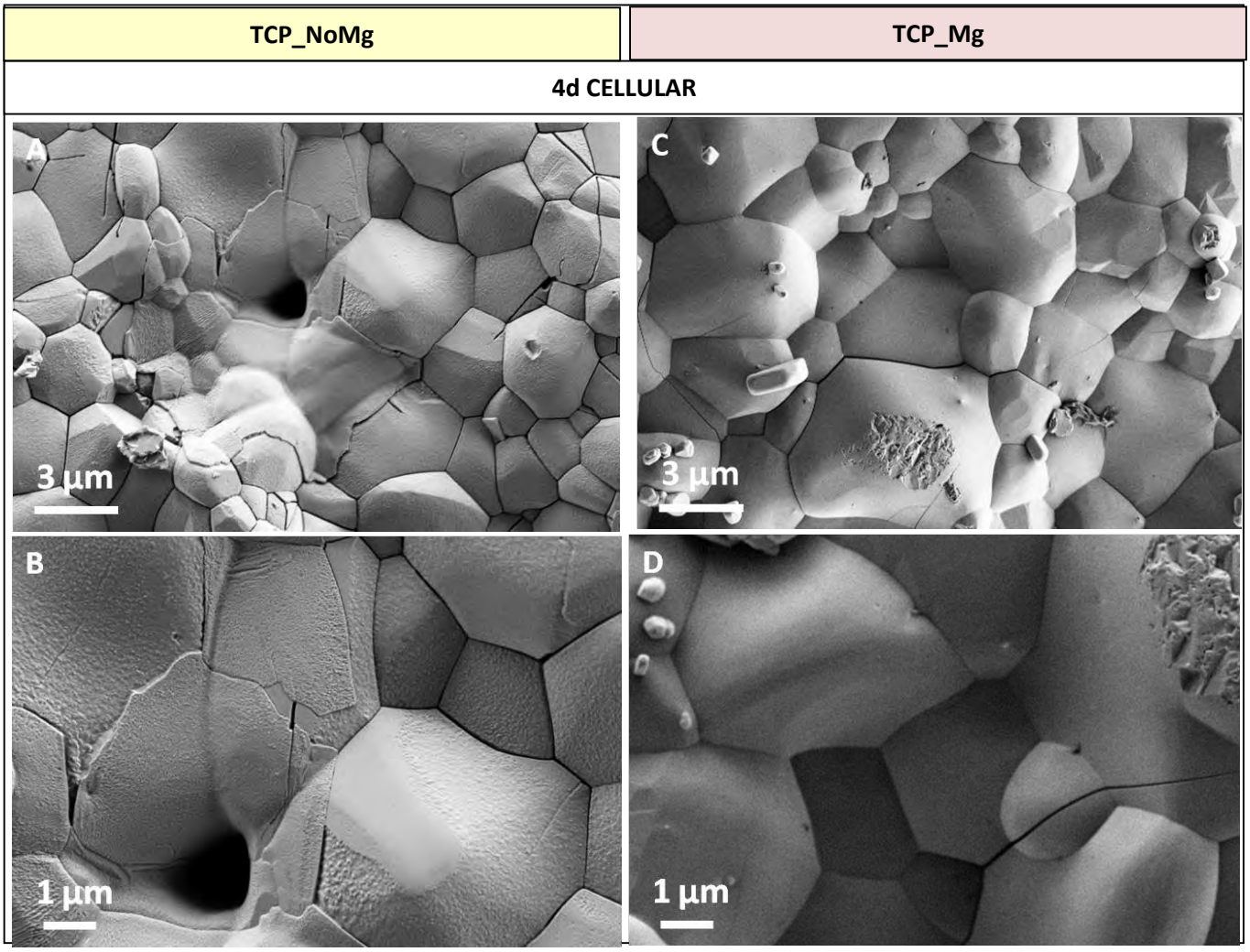

Figure 17: SEM micrographs of samples once the cells were removed (after 4 days of culture). β-TCP with (C, D) and without (A, B) magnesium

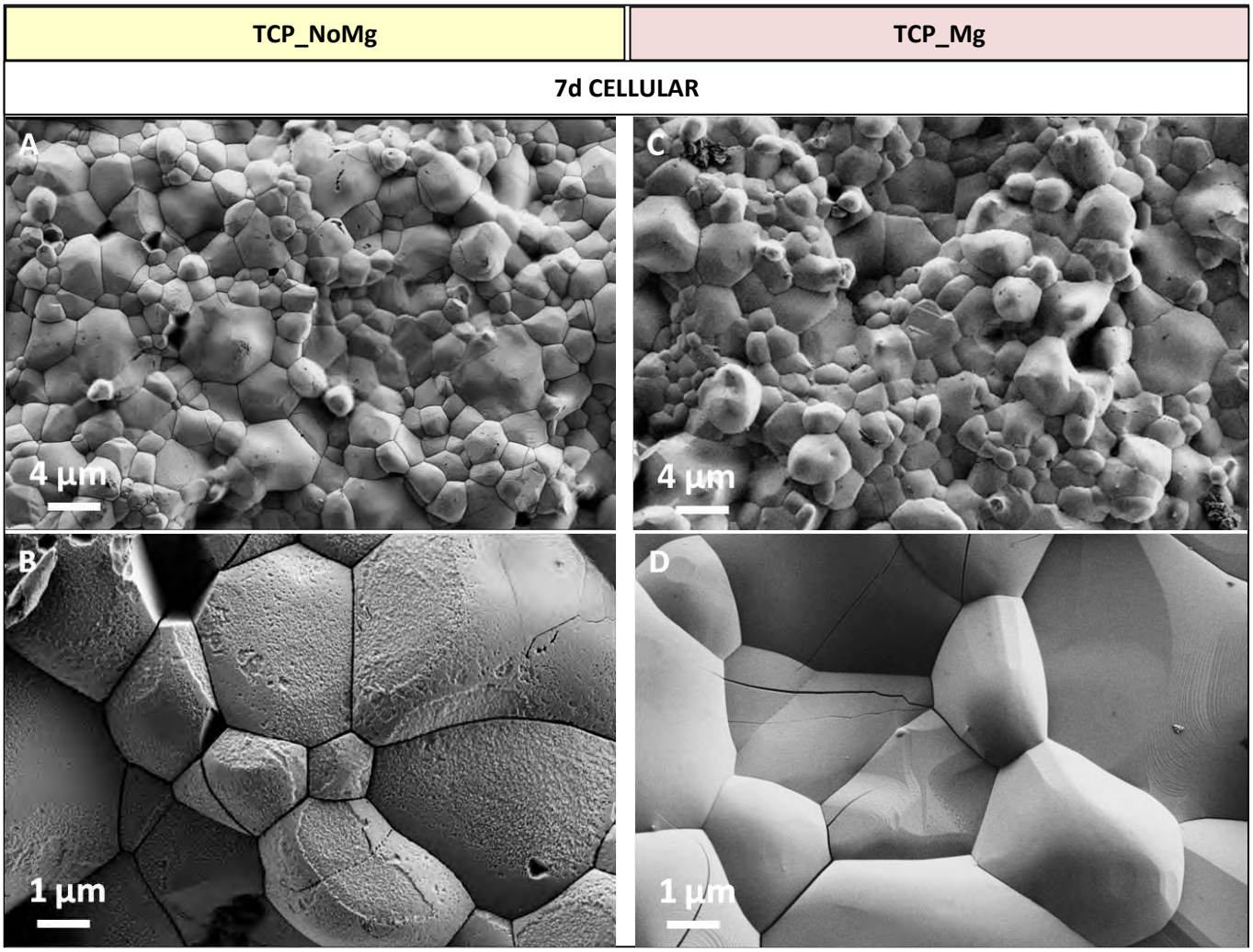

Figure 18: SEM micrographs of samples once the cells were removed (after 7 days of culture). β-TCP with (C, D) and without (A, B) magnesium

After cell removal, TCP_NoMg samples showed signs of a slight dissolution: grain boundaries appeared more marked and grains displayed etching phenomena on their surface. These signs, just outlined after 2 days of immersion (Figure 16), were already well visible at day 4 (Figure 17) and seemed to be a bit more pronounced after 7 days (Figure 18). On the opposite, no significant changes were noticed for TCP_Mg specimens.

5.3.2 Acellular tests

Samples for dissolution tests were weighted and measured before and after immersion. The graphs in Figure 19 report the change of weight in percentage for TCP_NoMg and TCP_Mg after immersion in RPMI (pH at t0 = 7.4) and 0.9% NaCl (pH at t0 = 6.3) solutions, compared to the initial value.

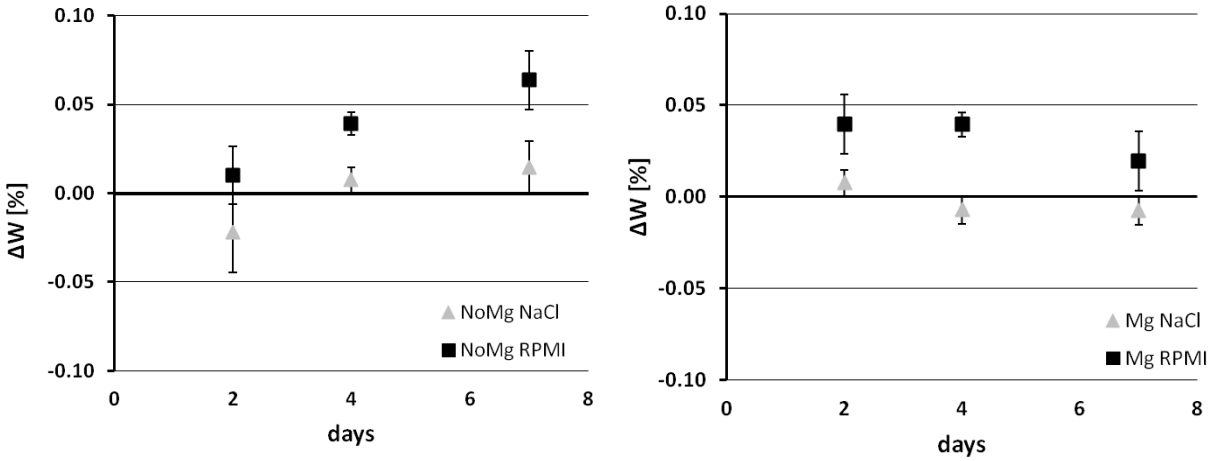

Figure 19: Variations of weight in percentage of pure (left) and Mg-doped (right) samples after acellular dissolution tests. Error bars represent the standard deviation of the measurements. Average weight at time zero: TCP_NoMg = 0.67 g, TCP_Mg=0.66 g

After immersion, both TCP_NoMg and TCP_Mg showed very small changes in weight. For all time-points, both materials seemed to display a slight increase of weight (≈0.05%) after immersion in RPMI and no changes for immersion in NaCl. However, considering that the initial weight of samples was on average 0.6 g, a change of 0.05% can be converted into 0.3 mg in total, which can be considered negligible if compared to the precision of the scale used.

The possible evolution of crystalline phases was monitored by XRD analyses as reported in Figure 20 and Figure A.d.11 in Annex.

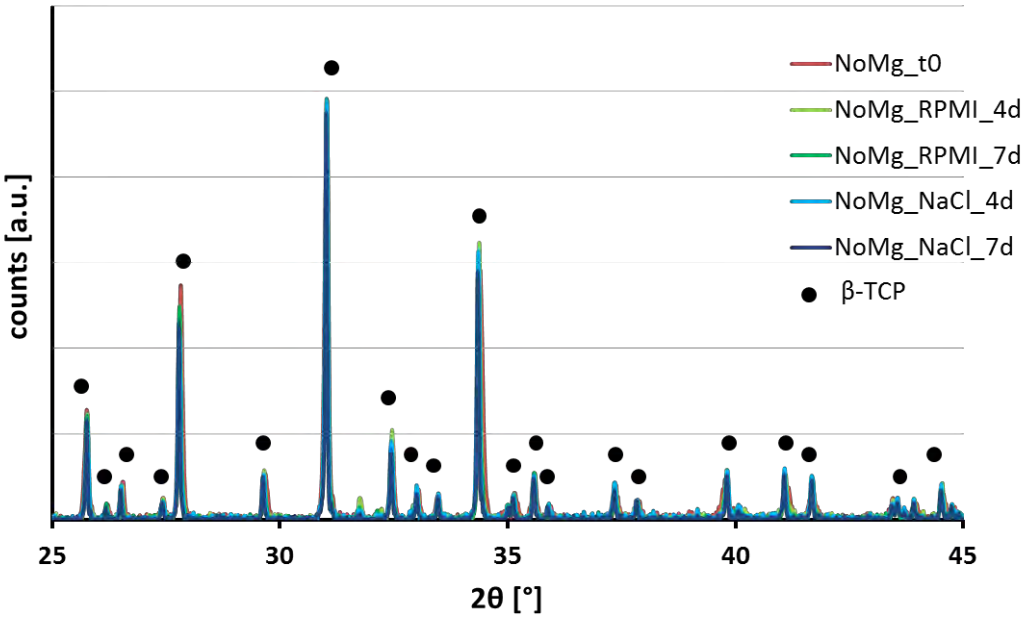

Figure 20: XRD pattern of TCP_NoMg samples after 4 and 7 days of immersion in RPMI (without cells) and NaCl

TCP_NoMg and TCP_Mg diffractograms at time zero did not display visible differences (Figure 1). When comparing diffractograms acquired for the two materials after immersion in RPMI and NaCl for 4 and 7 days, no significant modifications could be noticed (Figure 20 and Figure A.d.11 in Annex),

supporting, thus, the idea that possible increases of weight due to crystalline precipitations could be considered as negligible.
The evolution of the microstructure of the materials was also monitored by SEM analyses. In particular, TCP_NoMg and TCP_Mg samples were observed before and after immersion in RPMI and 0.9% NaCl solution for 4 and 7 days.

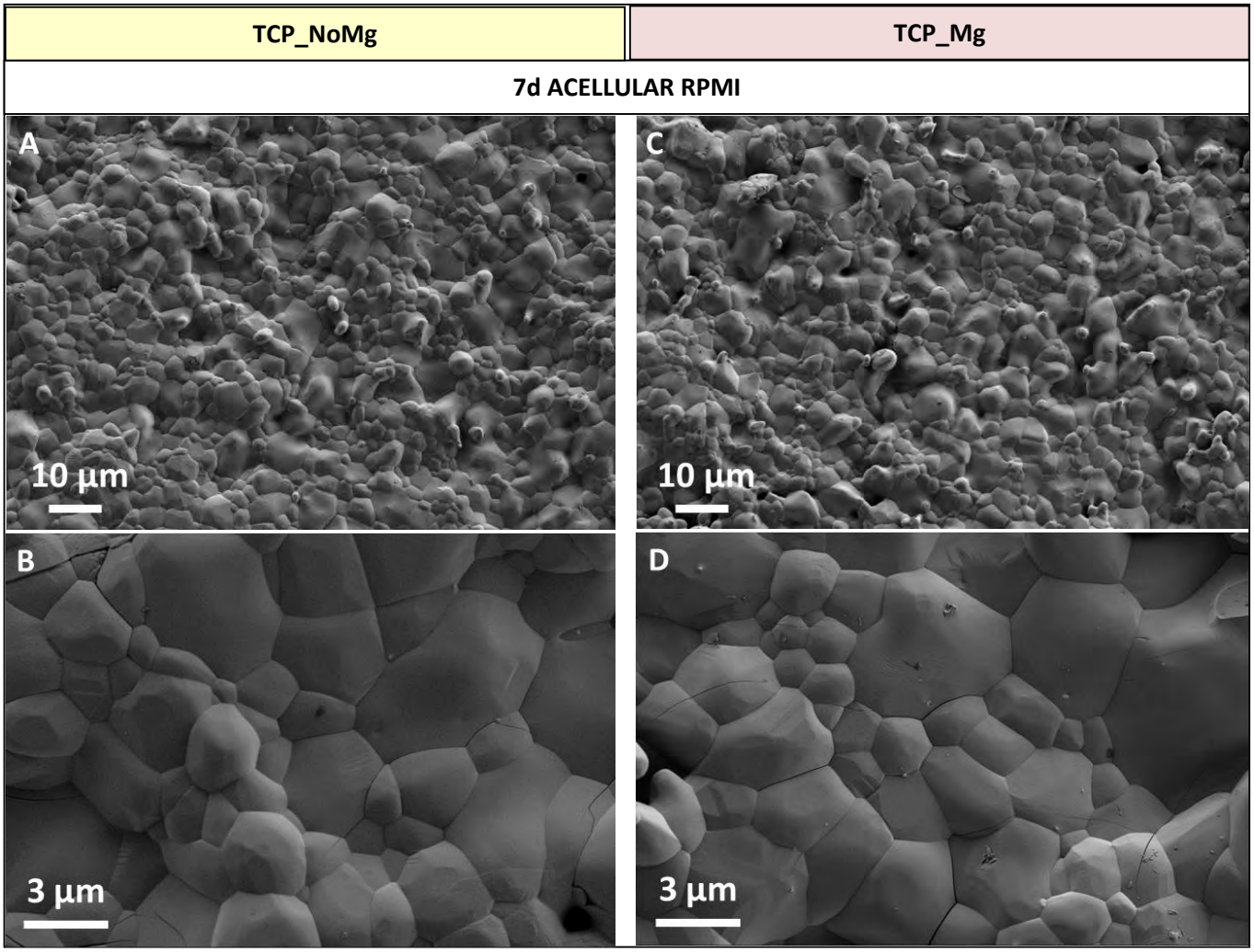

Figure 21: SEM micrographs of β-TCP samples with (C, D) and without (A, B) magnesium after 7 days of immersion in RPMI without cells

After immersion in RPMI for 4 and 7 days the microstructure of both materials did not seem to be altered (Figure A.d.12 in Annex and Figure 21) compared to those at t0 (Figure 4). Neither precipitation nor dissolution traces could be observed and the "layer" seen on TCP_NoMg specimens at t0 was still visible (e.g. image B in Figure A.d.12 in Annex).

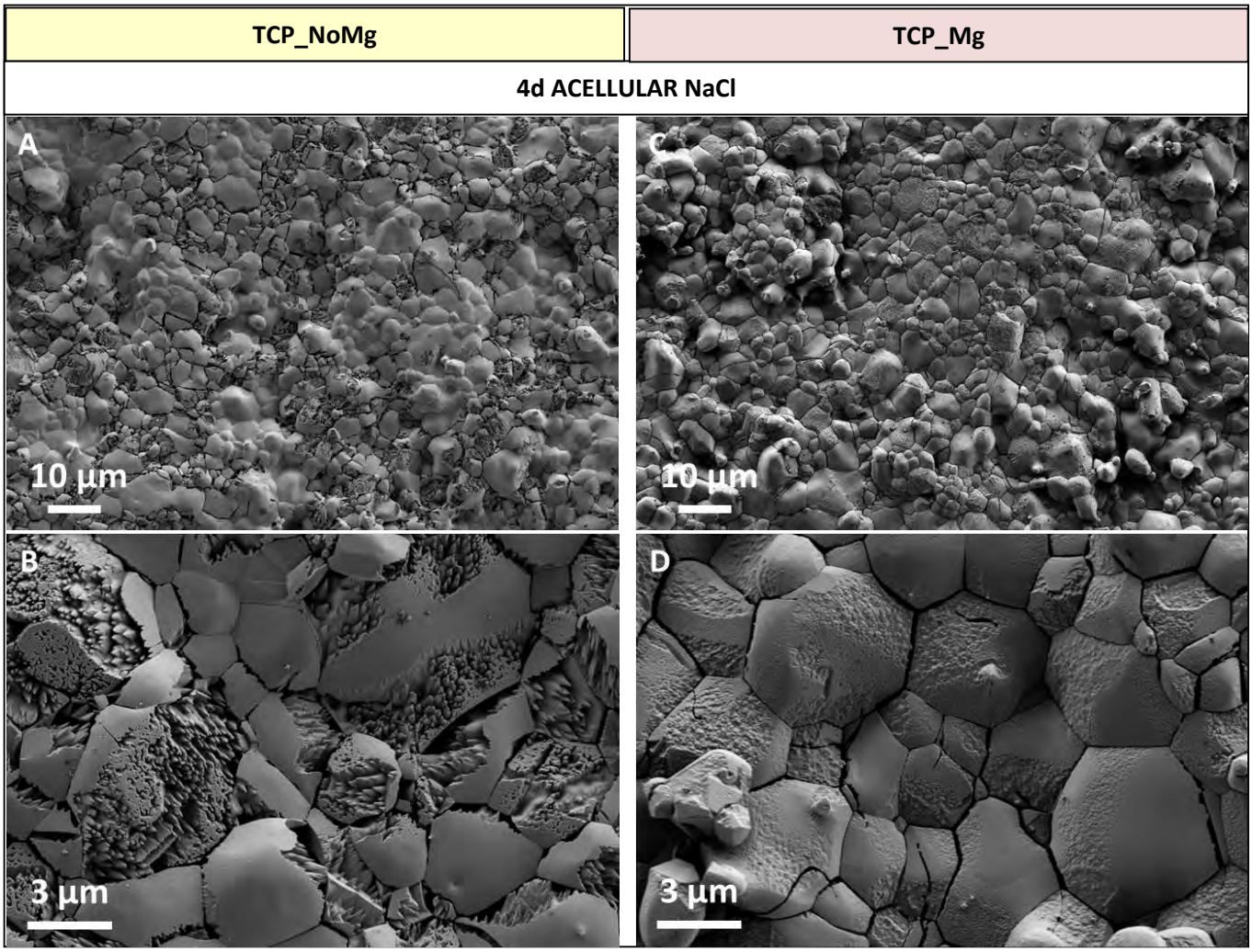

Figure 22: SEM micrographs of β-TCP samples with (C, D) and without (A, B) magnesium after 4 days of immersion in 0.9% NaCl solution without cells

On the contrary to what was observed for RPMI, samples immersed in NaCl solution displayed a clear evolution (Figure 22 and Figure 23). For both materials after immersion the grains boundaries seemed to be etched and some grains also displayed signs of erosion. Comparing doped and pure TCP, it could be noticed that the dissolution phenomena were evenly distributed on the former one, while concentrated in some zones on the latter. For TCP_NoMg samples, dissolution did not seem to affect the area covered by the "layer" already observed at time zero (Figure 4). However, where dissolved, pure TCP presented a deeper etching than that observed on doped TCP. Finally, when comparing the same material at different times of immersion, no clear evolution was noticed: between 4 and 7 days of immersion the dissolution phenomena did not seem to increase significantly.

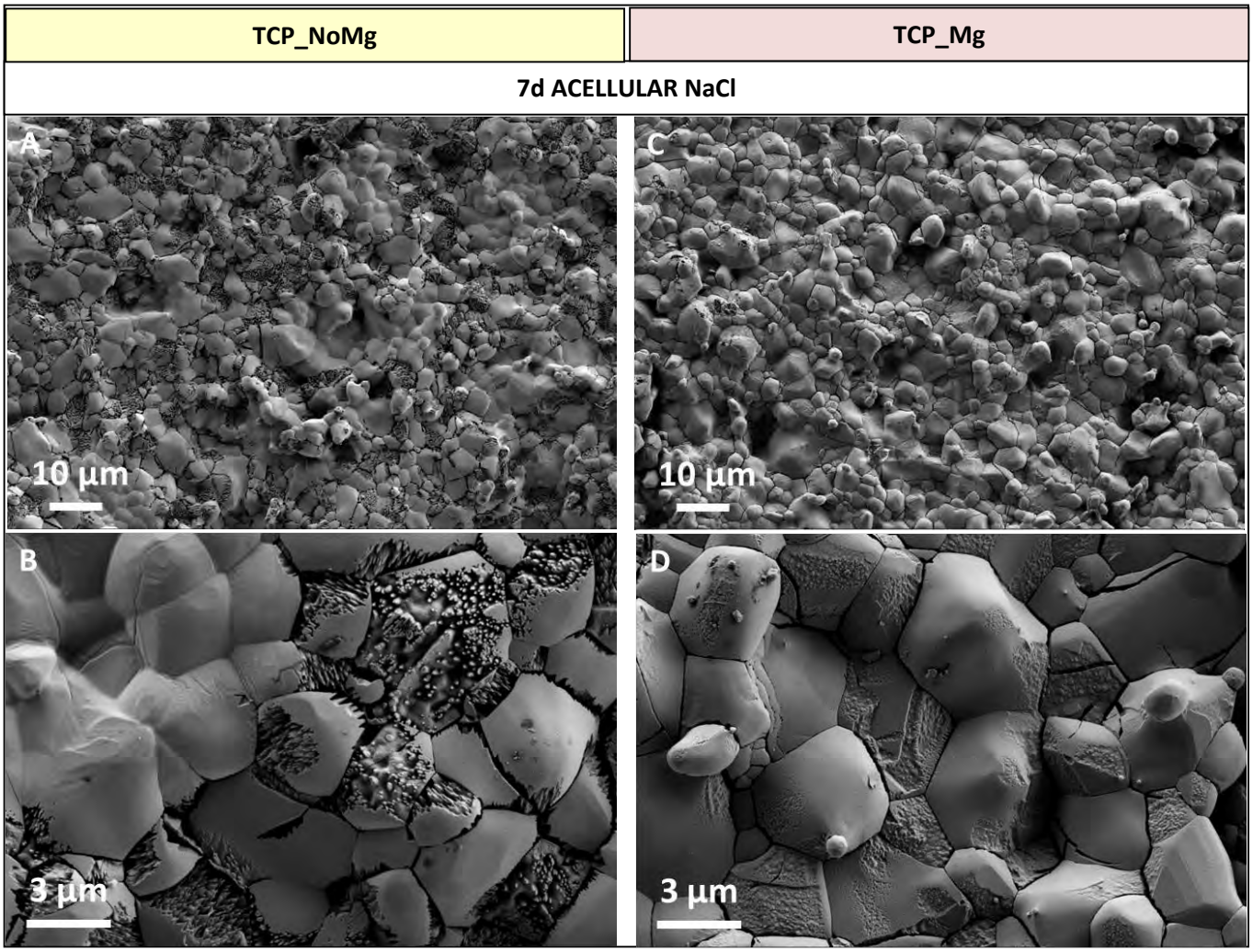

Figure 23: SEM micrographs of β-TCP samples with (C, D) and without (A, B) magnesium after 7 days of immersion in 0.9% NaCl solution without cells

5.4 Analysis of immersion solutions

For sake of completeness, the media of cellular and acellular tests were retrieved at each time-point and analysed. In particular, pH value and concentration of calcium were measured, in order to better understand the possible release and consumption of ions due to dissolution/resorption and precipitation phenomena respectively.

5.4.1 Acellular tests

As far as dissolution tests are concerned, two different evolutions were observed for RPMI and NaCl solutions.

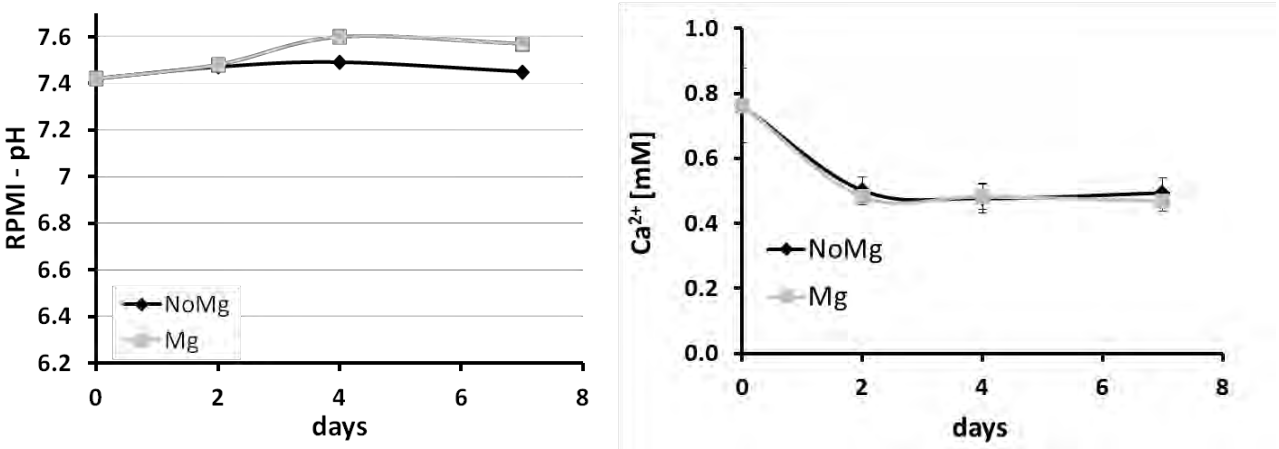

Figure 24: pH (left) and calcium concentration (right) of RPMI solution after different times of immersion of TCP_NoMg and TCP_Mg samples, without cells

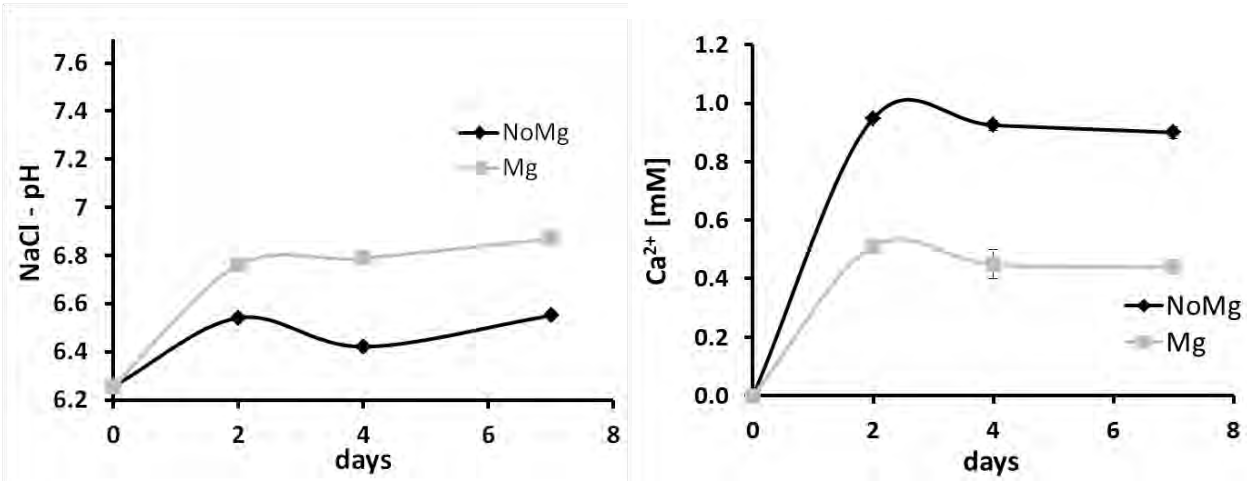

Figure 25: pH (left) and calcium concentration (right) of 0.9% NaCl after different times of immersion of TCP_NoMg and TCP_Mg samples, without cells

In the first medium (RPMI), a slight increase of pH was noticed (mainly between day 2 and 4) for both TCP_NoMg and TCP_Mg samples (Figure 24, left). At the same time, the calcium concentration showed a quite pronounced decrease for both materials: it dropped from around 0.8 mM (value of pure RPMI medium) to around 0.5 mg/L and then reached a plateau (Figure 24, right).
In the NaCl solution, instead, the pH value displayed an increase in the first 48 hours, followed by a stabilisation and a slight further increase between 4 and 7 days (Figure 25, left). The same trend was observed for both kinds of TCP, but the values recorded for the doped material were on the overall higher than those of pure TCP. The concentration of calcium ions increased from zero to around 0.5 mM for TCP_Mg and to 1 mM for TCP_NoMg in the first two days. Then, it stayed almost unchanged till the end of the tests (Figure 25, right).

5.4.2 Cellular tests

On the contrary to what observed for acellular tests in RPMI, an acidification occurred, mainly between 2 and 4 days, in the cell culture medium (RPMI) when cells were put in contact with samples (Figure 26, left). This phenomenon was observed to a quite similar extent for pure TCP and the reference glass discs and slightly less for Mg-doped TCP. Calcium ions concentration showed a decrease in the first 48 hours, reaching values of around 0.5 mM for both TCP samples and 0.6 mg/L for the reference substrate (Figure 26, right).

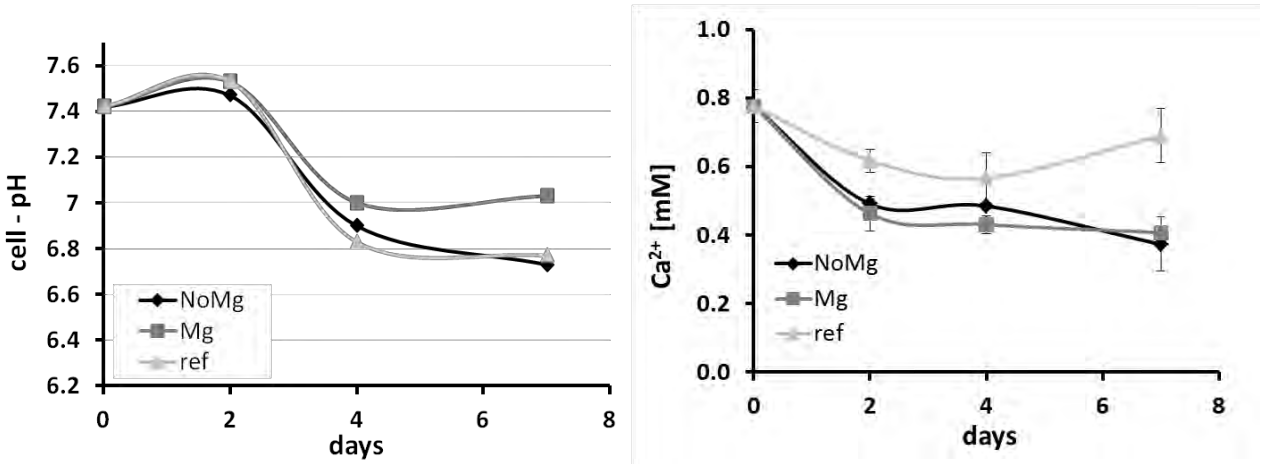

Figure 26: pH (left) and calcium concentration (right) of the RPMI solution after different times of cell culture on TCP_NoMg and TCP_Mg samples

5.5 Discussion

5.5.1 Initial β-TCP samples

As detailed in Chapter 2 (section 2.1.3), dense β-TCP samples were prepared by sintering of pressed powders. As it can be noticed in Figure 27, samples at t0 were not completely white; in particular TCP_Mg samples were characterised by a brownish colour. This colouring appeared homogenous in the whole volume of the specimen, with no significant gradient between one part and the others.
Considering that a thermal treatment at high temperature was applied for sintering the samples, it was unlikely that the colour was due to residual traces of fumaric acid, which was used during the production of the initial powders. Beside, the powders, which were below the pressed samples had turned white again with the removal of the fumaric acid (Figure 27). It was possible, instead, that during the thermal treatment, oxygen vacancies formed within the crystal lattice, causing the altered colour of the final samples. For clarifying the origin of the colouration, additional tests (such as performing the sintering process in a controlled atmosphere) would be necessary. Another possible cause of this brownish colour would be the presence of other phases in the Mg-doped samples.

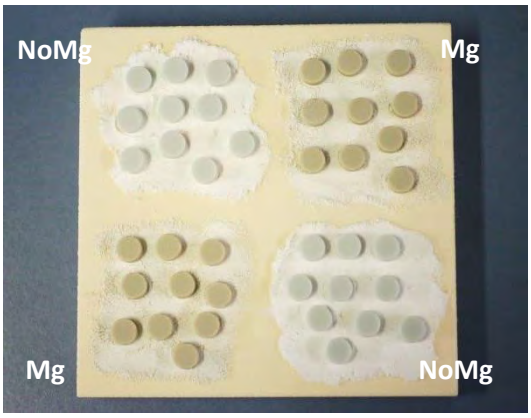

Figure 27: dense β-TCP samples obtained after sintering (cf. Chapter 2, section 2.1.3).

Therefore, the composition of β-TCP samples, both pure and Mg-doped, was carefully checked. XRD patterns of TCP_NoMg and TCP_Mg samples at time zero showed only peaks corresponding to the β-TCP phase (Figure 1). This suggested that the Mg-doping did not form any detectable crystalline phase, either because in too low amount (5 mol.%) to be detected by this technique, or because an amorphous phase formed or because magnesium was incorporated in the β-TCP lattice replacing Ca^{2+} ions as hypothesised also by other authors [2].

TEM analyses confirmed the overall homogeneous composition of grains and grain boundaries of the un-doped and doped samples (Figure 2 and Figure 3). No amorphous phase was found and no segregation of particular phases at grain boundaries was noticed in the analysed areas. However, it should be noted that, when performing the measurements, the electron beam tended to damage and pierce the thin slices. Therefore, a limited number of analyses could be performed successfully (around 10 analyses for both TCP_NoMg and TCP_Mg). The difference between the expected and the measured calcium to phosphorus ratio, which was noticed in some cases (above all for TCP_NoMg), might be due to these experimental difficulties.

5.5.2 Evolution of dense β-TCP samples when immersed in cell culture medium, with or without osteoclast-like cells

From viability measurements, SEM and fluorescence images (from Figure 5 to Figure 11), cells seeded on both pure and doped β-TCP displayed a higher viability and a morphology closer to the one of osteoclast-like cells compared to that of cells grown on the reference substrates. Cells on β-TCP, in fact, were characterised by a well spread structure, with a diameter and a number of multinucleated cells slightly higher than that of the reference glass discs (Figure 13 to Figure 15). This was coherent with what is reported in literature [3-5]. On the overall, thus, it was possible to state that both pure and doped β-TCP were cytocompatible*. Also, it validated the approach adopted in this work (cells transfer on the samples once grown and differentiated) and showed that the seeding protocol was correctly carried out.
Moreover, the additional measurements performed at 2 days confirmed that cell viability (WST) and proliferation (LDH) were high on both β-TCP types (Figure 7), with a strong monocytes activity (SAP). However, the osteoclasts activity (TRAP) did not seem to be favoured neither by TCP_NoMg nor by TCP_Mg samples (Figure 8).
Comparing in detail TCP_NoMg and TCP_Mg samples at day 4, it was noticed that the latter was characterised by the highest cell density and proliferation (Figure 5 and Figure 6). Moreover, the cell diameter was slightly larger than that measured on pure β-TCP and on the reference material (Figure 13). At the same time, however, the percentage of multinucleated cells on doped β-TCP was lower than on pure β-TCP (but still higher than on the reference discs) and the number of TRAP-negative

cells was higher (Figure 12 and Figure 14). All these results together induced to believe that Mg-doping supported monocytes proliferation, did not completely hinder the differentiation of osteoclasts, but clearly inhibited their activation. This hypothesis seems to be supported also by the work of other groups which, in similar conditions and in presence of magnesium, found a high monocytes proliferation, but a limited formation of osteoclast-like cells and very few resorption signs [6, 7]. Moreover, other researchers observed that Mg-deficiency (cell cultured medium deprived to magnesium) leaded to a higher number of osteoclasts; at the same time, however, those cells were less active [8]. On the other hand, another study by Wu et al. [9] showed that below a certain concentration (6 mM), magnesium extracts increased resorption activity on dentine. A similar result was obtained *in-vivo* by Ito et al. [10]: more osteoclasts were observed around magnesium-doped β-TCP than pure β-TCP implants in rabbits (magnesium between 1.0 and 3.4 mol.%). In the experiments reported in this chapter, the release of calcium in the cell culture medium was around 0.4 mM (Figure 26). If we suppose that for 95 moles of calcium released, there was 5 moles of released magnesium (according to the 5 mol.% of Mg content in the doped β-TCP samples), the total release of Mg would corresponds to 20 µM. Therefore, the conditions should have been favourable to resorption according to Wu's and Ito's studies.
The debate about the effect of magnesium on osteoclastic cells, thus, is still open, but the present work seems to support the idea that magnesium may inhibit the resorption process.

No relevant signs of **resorption** and no lacunae could be noticed neither on pure nor on doped β-TCP. This could be due either to the test conditions or to the material itself.
Some studies, in fact, showed that osteoclast activity is greatly increased at pH around 6.5 [11]. In the present case, the values recorded for the pH of the medium were at least equal to 6.8 (Figure 26); this could have prevented to some extent the osteoclast resorption.
Another possible reason for the lack of resorption of β-TCP samples was given by Detsch et al. [12]: according to their study, the calcium released in the medium through the dissolution of β-TCP would inhibit the osteoclast activity. These cells, in fact, sensing a concentration of calcium high enough, would not "feel" the need of resorbing material to release further calcium ions. It could be argued that in the present study the concentration of calcium observed in the medium in presence of cells actually diminished during the test and should have fostered, thus, osteoclast activity (Figure 26). However both the ion concentration of the medium around the cell and that below its sealing zone could play a role and, at present, it is not clear which one of the two is more crucial for the osteoclast behaviour. Moreover, it is possible that the pH in the area below the sealing zone, which was completely confined, differed from the extracellular one. In the same way, it is likely that also the ion concentration in that zone diverged from the one measured in the medium. As a consequence, the values of pH and calcium ions recorded in the extracellular medium (as done in the present work Figure 26) could reflect the material dissolution and cell metabolism; but these data should be interpreted with caution when used as a marker of the "real" pH and ions sensed by osteoclast-like cells.
On a similar line, a further explanation was provided in another work of Schaefer and Detsch [3] in which RAW 264.7 cells were cultured on dense and porous HAp, β-TCP and biphasic calcium phosphate (BCP) samples for up to 21 days. Although cell proliferation and osteoclast formation was comparable on all materials, almost no lacunae were observed on β-TCP. The authors speculated that the rapid dissolution of β-TCP could inhibit the resorption activity, suggesting that phase composition and porosity of the samples can have a strong influence on this process.
Finally, another possible explanation for the lack of resorption signs was given by Davison et al. [13]. In their work, Davison and his colleagues compared the resorption of submicron- and micron-scale featured β-TCP. $CD14^+$ monocytes were cultured on the samples for 25 days with the addition of MCSF or MCSF and RANKL in order to induce the formation of foreign body giant cells (FBGC) or osteoclasts (OCl) respectively. This time elapsed, both cells and samples were analysed. The results showed that, while on the short term cell attachment on the two materials was equivalent, on the

long term the cell viability was higher on the submicron β-TCP (TCPs) than on the micron one (TCPb). Even more interestingly, OCI and FBGC activation was favoured by TCPs, while on TCPb osteoclasts were smaller and no lacunae were identified (Figure 28). The authors concluded that osteoclast resorption can be highly influenced by the surface architecture and that, in particular, "*sub-micron scale surface structure promotes osteoclast activation and resorption, but on the other hand, larger micron-scale surface structure may block osteoclast activation and resorption, rendering TCP appreciably non-resorbable in these experimental conditions*" [13]. Comparing the main parameters (namely grain size and roughness) of TCPs and TCPb with those of the samples used in our study, it can be noticed how the characteristics of TCP_NoMg and TCP_Mg are closer to those of TCPb rather than of TCPs (Table 5). Therefore, it may be hypothesised that also in our case the lack of lacunae was due to the surface architecture of the samples which, being in the micron-scale range, might have blocked osteoclast activation and resorption. In addition, coherently with Davison's conclusions, also Detsch observed that increasing the sintering temperature of β-TCP (and, as a consequence, its grain size) the total resorption decreases [14].

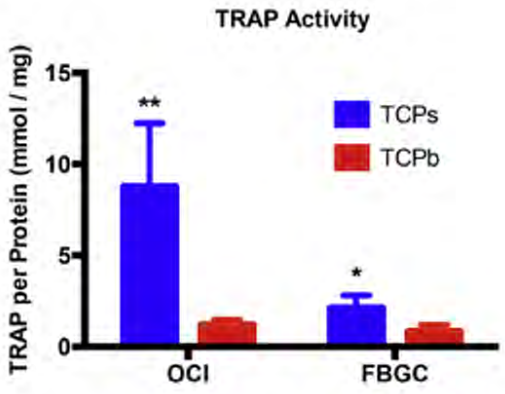

Figure 28: TRAP activity of osteoclasts (OCI) and foreign body giant cells (FBGC) cultured on submicron- (TCPs) and micron-scale (TCPb) featured β-TCP [13]

Table 5: Grain size and roughness of samples of Davison and co-workers' work [13] and of the present thesis

sample	TCPs [13]	TCPb [13]	TCP_NoMg (this work)	TCP_Mg (this work)
Grain diameter [µm]	1.0	3.7	1.5	2.4
R_a [µm]	0.1	1.3	1.5	1.7
R_{RMS} [µm]	0.2	1.6	2.0	2.4

Although in our study no resorption was observed, some signs of **dissolution** were identified both in case of cellular and acellular tests.

On TCP_NoMg samples where cells were removed, in particular, grain boundaries were more pronounced and some grains appeared slightly etched (Figure 17 and Figure 18). These phenomena were observed after 4 days and seemed to be slightly increased after 7 days. One possible explanation is that the observed dissolution might be induced by the decrease of pH measured in the medium between 2 and 4 days (Figure 26).This pH drop was likely caused by the cellular metabolic activity. Then, only small changes were observed on the samples between 4 and 7 days coherently with the pH, which was almost constant between day 4 and 7. Moreover, when comparing samples surfaces at 2 and 4 days after cell removal (Figure 16 and Figure 17), the etching was much more visible at day 4, i.e. exactly after the pH dropped.

Another hypothesis is that the treatment used for removing the cells affected the surface of the samples, causing an etching effect. Preliminary tests showed that trypsin, normally used for detaching cells, caused etching of TCP_NoMg (mainly at grain boundaries). For this reason, in the present work a simple immersion in sodium dodecyl sulphate (SDS) in ultrasounds was preferred to trypsin to remove the cells from the samples. However, SDS is a quite strong anion and could chelate calcium ions, causing the etching of TCP_NoMg observed after cell removal. This would be in agreement with the fact that no dissolution was observed on pure β-TCP samples immersed in RPMI in the very same conditions but without cells (Figure 21 and Figure A.d.12). On the other hand, during acellular tests in RMPI, the pH never reached values lower than 7.4, so the samples did not undergo acidic conditions. Finally, if the etching signs were caused by SDS, the same degree of dissolution should be observed on all TCP_NoMg samples from which cells were removed, irrespective of the immersion time. However, as shown in Figure 16-Figure 18, this was not the case, given that after 2 days the dissolution degree appeared much less extended than after 4 and 7 days, although all the samples were treated with SDS in the same manner. In conclusion, thus, the phenomena of etching observed on pure β-TCP were more likely due to pH changes than to the use of SDS.

Regarding TCP_Mg, no signs of dissolution were found neither after cell removal nor after acellular tests in RPMI. Therefore, whatever the cause of TCP_NoMg dissolution was (acidic pH, SDS), it is sure that it affected differently pure and doped material. This last one, in fact, seemed to be less soluble both at grain boundary and surface (Figure 16-Figure 18 and Figure 21-Figure 23). This behaviour could be linked to the fact that magnesium ions are slightly smaller than calcium ones. As a consequence, when magnesium substitutes calcium in the β-TCP lattice, the covalent bond with oxygen becomes shorter and stronger [2]. The result is a stabilization of the lattice, which could imply a higher resistance to dissolution.
A further proof of this behaviour was given by dissolution tests in 0.9% NaCl solution. This solution, did not contain any calcium and phosphate ions, and was characterised by an acidic pH and a high ionic gradient with regard to β-TCP samples. As a consequence, NaCl solution was likely to induce dissolution processes in the samples. Indeed, these phenomena were observed for TCP_NoMg: grain boundaries and surfaces appeared greatly etched after 4 and 7 days (Figure 22 and Figure 23). On the opposite, doped β-TCP immersed in NaCl solution displayed only slight signs of dissolution, confirming the lower solubility of this material. Moreover, this hypothesis was corroborated by the concentration of calcium measured in the media (Figure 25): NaCl solution where TCP_NoMg was immersed contained a higher concentration of Ca^{2+} when compared to TCP_Mg. As a confirmation, really close values of calcium release were observed by Schaefer and Detsch [3] after immersing β-TCP dense samples in TRIS-buffered solution (without calcium and phosphate) for 7 days, as shown in Figure 29.

On the overall, during acellular tests in RPMI and NaCl no precipitation of new crystalline phases was detected and the changes in weight were almost negligible (Figure 19, Figure 20 and Figure A.d.11 in Annex). However, both for TCP_NoMg and TCP_Mg, a decrease of calcium concentration in RPMI was noticed after immersion (Figure 26). This induces to think that some precipitations took place probably because the medium reached its saturation towards calcium ions. In any case, if present, the amount of precipitations seemed to be very low, almost inconsequential on the weight of the samples and not detectable by XRD and SEM.

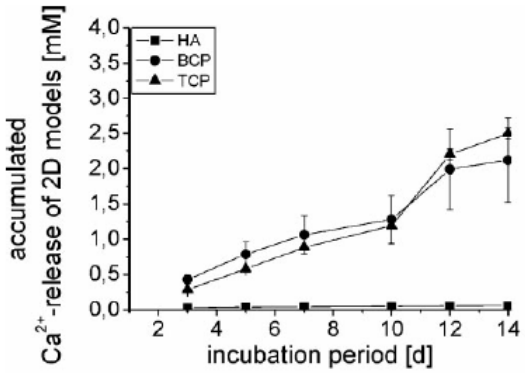

Figure 29: Release of calcium ions in TRIS-buffered solution (pH = 7.4) from dense β-TCP samples (triangles) compared to dense HA and biphasic (BCP) samples [3]

5.6 Conclusions and Perspectives

Taking into account all the data collected during the tests presented in this Chapter, the following main conclusions can be drawn:

- as-produced Mg-doped β-TCP samples had a brownish colour. However, none of the performed characterisations permitted to accurate the reason of this colour;
- no phase segregation and no amorphous phases were found at the grain boundaries of pure and Mg-doped β-TCP samples;
- neither pure nor Mg-doped β-TCP affected negatively cell growth (monocytes and osteoclast-like cells); both materials resulted to be cytocompatible*;
- Mg-doped β-TCP inhibited osteoclasts' activation. Signs of resorption, however, were limited on pure β-TCP too. Possible causes of inhibition are the chemistry of the material, the release of calcium ions and/or the topography of the surface;
- 5 mol.% of Mg-doping affected significantly the properties of the material, in particular reducing its solubility. Its grain boundaries were shown to be significantly more resistant to dissolution processes than those of pure β-TCP.

These considerations could be used as a starting point for further studies regarding from one side the influence of doping on osteoclasts and on the other side the modification induced by Mg on the β-TCP lattice and properties. Questions such as "how does TCP_Mg inhibit osteoclasts' activation?" or "to which extent does Mg-doping affect β-TCP properties?" could be further deepened and, hopefully, solved.
In this perspective, it would be interesting to perform new experiments following the same cell culture protocol, but varying two important parameters of the material:

- topography: samples with sub-micron grain size and roughness would allow the evaluation of the influence of topography on osteoclasts' activation
- doping: an increase in magnesium content would enhance the difference between TCP_NoMg and TCP_Mg, easing the identification of the consequences of the doping.

As far as the cell culture is concerned, the protocol used during this study seems promising. The initial stimulation with only MCSF, to foster cell fusion, followed by the addiction of RANKL, to induce differentiation and activation, is in agreement with the differentiation path of osteoclasts. Growing the cells on a substrate and then moving them, instead of growing them directly on the samples, appeared to be a good way to avoid problems of differentiation induced by ions released by the material. Moreover, it helped to distinguish the phenomena induced by cells from those due to dissolution: with this protocol, the samples were immersed for a maximum of 7 days, while in case of direct culture the specimens were immersed also for all the time necessary to cell differentiation

(>14 days, Annex A.d) and they resulted, thus, more exposed to dissolution processes. An amelioration of the protocol, finally, could be the use of a more significant material as reference, such as dentine. In this way, in fact, the experimental conditions would be closer to the physiologic ones and it would be possible to evaluate the signs of resorption induced by cells also on the reference substrates.

References

1. Schilling, A.F., et al., *Resorbability of bone substitute biomaterials by human osteoclasts.* Biomaterials, 2004. **25**: p. 3963–3972.
2. Singh, S.S., et al., *MC3T3-E1 Proliferation and Differentiation on Biphasic Mixtures of Mg Substituted β-Tricalcium Phosphate and Amorphous Calcium Phosphate.* Materials Science and Engineering: C.
3. Schaefer, S., et al., *How degradation of calcium phosphate bone substitute materials is influenced by phase composition and porosity.* Advanced Engineering Materials, 2011. **13**(4): p. 342-350.
4. Detsch, R., et al., *In vitro-Osteoclastic Activity Studies on Surfaces of 3D Printed Calcium Phosphate Scaffolds.* JOURNAL OF BIOMATERIALS APPLICATIONS, 2010.
5. Okazaki, Y., et al., *Osteoclast Response to Bioactive Surface Modification of Hydroxyapatite.* Open Journal of Stomatology, 2014. **4**: p. 5.
6. Bose, M.R.S., *Osteoclastogenesis and osteoclastic resorption of tricalcium phosphate: Effect of strontium and magnesium doping.* J Biomed Mater Res, 2012. **100A**: p. 2450–2461.
7. Qu, Z.Z.X., *The effect of metallic magnesium degradation products on osteoclastinduced osteolysis and attenuation of NF-kB and NFATc1 signaling.* Biomaterials, 2014. **35**: p. 6299-6310.
8. Belluci, M.M., et al., *Magnesium deficiency results in an increased formation of osteoclasts.* The Journal of Nutritional Biochemistry, 2013. **24**(8): p. 1488-1498.
9. Wu, L., et al., *Effects of extracellular magnesium on the differentiation and function of human osteoclasts.* Acta Biomaterialia, 2014. **10**(6): p. 2843-2854.
10. Ito, A., et al., *Interlaboratory studies on in vitro test methods for estimating in vivo resorption of calcium phosphate ceramics.* Acta Biomater, 2015. **25**: p. 347-55.
11. Mandel, S. and A.C. Tas, *Brushite (CaHPO4·2H2O) to octacalcium phosphate (Ca8(HPO4)2(PO4)4·5H2O) transformation in DMEM solutions at 36.5 °C.* Materials Science and Engineering: C, 2010. **30**(2): p. 245-254.
12. Detsch, R., et al., *The resorption of nanocrystalline calcium phosphates by osteoclast-like cells.* Acta Biomaterialia, 2010. **6**: p. 3223–3233.
13. Davison, N.L., et al., *Osteoclast resorption of beta-tricalcium phosphate controlled by surface architecture.* Biomaterials, 2014. **35**(26): p. 7441-7451.
14. Detsch, R., *In vitro-Untersuchungen zur Osteoklastogenese und Osteogenese auf Calciumphosphat-basierten Knochenersatzmaterialien: Einfluss von verschiedenen Materialparametern.* mensch und buch verlag edition, 2009.

General conclusions

The present Ph.D. thesis work was aimed to establish and assess an experimental methodology to monitor the evolution of resorbable bone substitutes, **coupling the mechanical, microstructural and physico-chemical aspects**. In fact, although these materials are currently used in surgical practice as bone grafts, their degradation process is not fully documented. However, the knowledge of these phenomena is fundamental to improve the performances of this kind of bone substitutes: the resorption rate needs to be optimised and balanced with bone tissue regeneration. In fact, if all parameters, which affect their degradation, were perfectly understood, it would be possible to eventually control them in order to tailor the degradation of the bone graft according to the patient's need.

The general idea of this work was to assess this experimental methodology by performing **dissolution tests *in-vitro*** with and without cells on two different calcium phosphate bone substitutes. The chosen materials were dicalcium phosphate dihydrate (**DCPD**, $CaHPO_4 \cdot 2H_2O$) and beta-tricalcium phosphate (**β-TCP**, β-$Ca_3(PO_4)_2$). Although being both calcium phosphates, these ceramics present quite different properties and can be used, thus, as model for two main classes of bone substitutes. DCPD, in fact, is an example of material obtained by setting reaction at low temperature, whereas β-TCP is representative for the class of ceramics obtained at high temperature by sintering process. DCPD has a high solubility in physiological conditions and is likely to dissolve after implantation. It can therefore be classified as being "biosoluble". On the other hand, β-TCP, being less soluble, is more likely resorbed trough cellular activity and can be identified, as a consequence, as "bioresorbable".
Therefore, another part of this work was devoted to the study of the degradation phenomena induced by cells (**osteoclast-like cells** in particular). For this purpose cell culture tests, performed during a stay at the department of Materials Science and Engineering of Prof. Aldo Boccaccini (FAU Erlangen-Nürnberg, Germany), were carried out on β-TCP samples. The material was tested in form of dense specimens made of pure or doped (5 mol.% of magnesium) β-TCP. The interest of adding magnesium was double: the doping was expected to both modify the properties of the material (e.g., its dissolution) and to affect the cell behaviour.

For the dissolution tests, porous DCPD samples (60% porosity) were produced through setting reaction at room temperature. Porous β-TCP specimens (79% porosity), kindly provided by Prof. Marc Bohner (RMS Foundation, Bettlach, Switzerland), were obtained by sintering an emulsified apatite cement. The samples underwent dissolution tests *in vitro* in TRIS-buffered and PBS (Phosphate Buffered Saline) solutions for up to 14 days in the case of DCPD and 8 weeks for β-TCP. Both static (with stirring only) and dynamic (with daily refresh) conditions were performed with TRIS solution (TRISs and TRISd respectively), while PBS was used only for dynamic tests (PBSd). In order to evaluate the evolution of these materials, the samples were fully analysed before and after dissolution tests. The physico-chemical properties were assessed by means of XRD (X-Ray Diffraction) and pH measurements, while the micro-structure was observed by SEM (Scanning Electron Microscopy) and µ-CT (X-ray Computed Tomography). The mechanical properties, finally, were assessed by spherical instrumented micro-indentation; this technique was chosen because it offers the possibility to evaluate properties such as Young's Modulus and hardness, on a local scale, at different locations of interest and in a quasi-non-destructive way.

The results obtained from **dissolution tests of DCPD samples** highlighted the strong influence of the immersion medium and the set-up conditions on the evolution of the material.
The precipitation, mainly at the sample surface, of new crystalline phases seemed to be accelerated in PBSd compared to TRISd. However, once the first precipitates were detected, their increase was

faster in TRISd than in PBSd. The medium resulted to influence the precipitates also in terms of chemical composition and morphology. Small agglomerates of OCP thin platelets (octacalcium phosphate, $Ca_8(HPO_4)_2(PO_4)_4 \cdot 5H_2O$) were found in PBS, while OCP and apatite in form of more compact groups of platelets and "spongy" precipitates were observed in TRIS. The µ-CT acquisitions permitted to highlight how the microstructure of the immersed samples, and especially of their outer parts, was significantly different depending on the immersion solution.
The medium refresh appeared to be another crucial parameter: comparing TRISd and TRISs, in fact, the evolution of the material resulted much more pronounced in dynamic conditions.
In general, the changes, which took place in the samples started from the surface, or more precisely just below the surface, and moved later towards the inner part of the cylinders. This phenomenon resulted in a gradient of properties between the surface and the core of the specimens which was reflected on the mechanical properties assessed by micro-indentation. On the overall, a stronger decrease of hardness and elastic modulus was measured on surface of the samples, while changes detected at core were smaller and delayed. Correlating all the observed modifications along time, it appeared quite clearly how the changes of porosity, microstructure and crystalline phases all affected the mechanics of the samples. This observation proved how strongly interconnected the evolutions of the chemical, structural and mechanical properties are and further confirmed the need to consider all these aspects when analysing the evolution of a material.

As far as **dissolution tests of porous β-TCP samples** are concerned, the influence of medium type and set-up conditions was also confirmed. In fact, the majority of changes took place in TRIS-buffered solution, under dynamic conditions. Differently from what observed for DCPD specimens, however, the evolution of β-TCP samples did not imply the precipitation of crystalline phases, but seemed to be driven mainly by dissolution, leading to micro-structural changes. The decrease of mechanical properties, mostly observed at the surface of samples immersed in TRISd, could be correlated to the increase of porosity detected just below the surface after immersion. This observation gives a new interesting insight on the degradation of β-TCP: this material, in fact, is commonly considered "bioresorbable" (by cells), but not "biosoluble" (by physico-chemical processes). In the present study, however, we demonstrated how in specific conditions (namely high degree of porosity of the samples, immersion in solutions poor of ions and with refresh) this ceramic displays characteristic typical of "biosoluble" materials.

Concerning the method adopted in this work to monitor the evolution of the mechanical properties of resorbable samples, the validity and utility of **instrumented micro-indentation** were fully confirmed.
A bibliographic research pointed out how the majority of studies on the evolution of degradable bone substitutes either does not encompass the evaluation of the mechanical properties of the material or involves the use of standard tests, which provide information on the total volume of the specimen (namely compression and, 4-point bending in some cases). However, this work showed that during the degradation processes, samples did not evolve homogeneously and that a gradient of properties appeared between different parts of the same specimen. Techniques such as compression, as said, are not local enough to detect these gradients, while the output of this work is that instrumented micro-indentation perfectly suits these local examinations.
Indeed, a comparison between the results obtained by compression and instrumented micro-indentation tests on porous β-TCP specimens confirmed this hypothesis. Thanks to the use of micro-indentation, in fact, it was possible to distinguish the properties of different parts of the same sample. This enabled the evaluation of the influence of the porous external layer on the properties of the degraded material.
In addition tests could be performed on the very same sample before and after immersion thanks to the micro-indentation technique, which is quasi non-destructive. In this way, the evolution of a specific specimen could be monitored along time. Indeed, results presented in this thesis showed

that the indentations performed prior to immersion tests did not altered the evolution of samples in a significant manner.
This technique resulted also to be quite sensitive: in the case of relatively slow phenomena of degradation, such as those that took place in porous β-TCP samples in TRISs, micro-indentation revealed a decrease of mechanical properties when all the other characterisation techniques had not yet shown any significant change.
A further added value of instrumented micro-indentation is linked to the low restrictions in terms of sample geometry. Although the specimen surface needs to be carefully prepared, the sample itself can have whichever shape, needing only two parallel and flat surfaces. As a consequence, this technique could be applied in the future on samples with a disc-shape, such as those used in this study for cell culture, as well as on much more irregular geometries, such as those of explants.

To conclude, although some precautions need to be taken (above all regarding the surface preparation of the sample), the instrumented micro-indentation technique resulted to be of fundamental help for monitoring the mechanical properties of degraded materials.

For **cellular tests** (performed in collaboration with Prof. Aldo Boccaccini and Dr. Rainer Detsch, FAU University, Erlangen, Germany), pure and Mg-doped β-TCP powders were pressed (uniaxially and isostatically) and sintered in order to obtain dense samples (porosity < 9%). RAW 264.7 cells were cultured with growth factors (MCSF and RANKL) in order to induce their differentiation in osteoclast-like cells and were then seeded on samples. After 2, 4 and 7 days respectively, cells and specimens underwent several analyses. Fluorescence and TRAP staining, SEM observations, viability measurements were performed on cells, while samples were analysed by SEM after cell removal. In addition, dissolution tests in cell culture medium (RPMI) and in a reference saline solution (0.9% NaCl) were run in parallel, in order to evaluate the modifications of the samples induced by pure dissolution and not by cellular activity.
Cellular tests on pure and doped β-TCP samples confirmed the good cytocompatibility of both materials. However, osteoclastic activation did not seem to be favoured by β-TCP. Among the possible causes, the influence of the topography of the samples (micron-scale roughness and grain size) on osteoclasts' activation offers an interesting track that would be worthy to be further investigated. Another explanation, already suggested by previous works, would be the too high calcium release of β-TCP in the cell culture medium, which would tend to hinder the osteoclast activity. Finally, the addition of magnesium appeared to affect mainly the properties of the material, decreasing its dissolution rate.

To conclude, this study has given a deeper insight on the evolution after immersion of two calcium phosphates commonly used as bone substitutes, showing how crucial the choice of the experimental conditions is. Moreover, instrumented micro-indentation has been proved to be a suitable technique for assessing the mechanical properties of bone substitutes and, even more interestingly, for monitoring their evolution after immersion. We have proved, in fact, how physico-chemical, micro-structural and mechanical changes are strongly correlated one with the other and should all be taken into account when the evolution of a material is studied.

For the future, it would be interesting to complete and deepen the work here presented and in particular:

- measure the ion concentration (calcium, orthophosphates, magnesium) in media collected during cell culture and dissolution tests;
- understand the influence of possible amorphous phases and of citrate ions in DCPD cements thanks to Fourier-Transformed Infra Red spectroscopy;

- perform dissolution tests in other media with a composition closer to the physiologic one in terms of ions concentration. Moreover, fluids containing proteins could be used;
- make additional indentation tests in humid conditions at different time-points in order to evaluate the influence of the drying protocol, of the presence of humidity and understand if it is a relevant parameter to take into account when testing bone graft materials;
- apply the inverse identification method on the collected indentation data; in this way, following the approach described in Clement's work [1], it would be possible to gather even more information from the mechanical tests (description of the constitutive law of the neat and the degraded materials);
- evaluate the influence of the porosity on the degradation process of β-TCP; for this purpose preliminary sintering tests have already been done for tailoring the pore size distribution of the samples;
- carry out *in-situ* tests, such as:
    - XRD during the first days of immersion of DCPD samples, in order to monitor step by step the early changes that take place in the material,
    - micro-indentation of the sample surface directly performed in the immersion solution,
    - micro-CT monitored indentation, in order to observe in real-time the damaging process of degraded DCPD and β-TCP specimens;
- perform dissolution tests on other bone substitutes, such as biphasic calcium phosphates;
- repeat the cellular assays on samples with sub-micrometric roughness and grain size, in order to understand the influence of topography on osteoclasts' activation. Further tests with TCP doped with a higher content of magnesium, moreover, would be useful to clearly identify the influence of the doping on the properties of the material.

1. Clement, P., *Détermination des proprietés mécaniques de céramiques poreuses par essais de micronindentation instrumenée sphérique.* Ph.D. Thesis, 2013.

Résumé

Ce travail de thèse avait pour objectif la mise au point et la validation d'une méthodologie expérimentale pour le suivi de l'évolution de substituts osseux en **couplant les aspects mécaniques, microstructuraux et physico-chimiques**. En fait, même si ce type de matériaux est couramment utilisé dans la pratique chirurgicale, leur processus de dégradation reste peu documenté. Cependant, la connaissance des phénomènes mis en jeu est fondamentale pour améliorer le comportement de ce type de substituts osseux : la vitesse de résorption doit être optimisée et équilibrée avec la repousse osseuse. Ainsi, en connaissant quels sont les paramètres qui affectent l'évolution des substituts après implantation, il serait potentiellement possible de les modifier pour adapter les matériaux aux besoins du patient.

L'idée générale de ce travail était de réaliser des tests de **dissolution *in-vitro*** avec et sans cellules sur deux types de substituts osseux à base de phosphates de calcium (CaP) et de suivre leurs propriétés physico-chimiques, microstructurales et mécaniques au cours du temps. Deux matériaux ont été choisis: le *phosphate dicalcique dihydraté* (**DCPD**, $CaHPO_4 \cdot 2H_2O$) et le *phosphate tricalcique bêta* (**β-TCP**, $\beta\text{-}Ca_3(PO_4)_2$). Ce choix a été dicté par le fait que, même si ces deux matériaux font partie de la même famille (CaP), ils peuvent être utilisés comme matériaux modèles pour deux grandes classes de substituts osseux. Le DCPD, obtenu dans ce travail par la voie des ciments à basse température, présente une solubilité élevée en conditions physiologiques; il est de ce fait vraisemblablement sujet à la dissolution après implantation et peut donc être considéré comme "biosoluble". D'autre part, le β-TCP, obtenu par frittage, en étant beaucoup moins soluble, est censé être résorbé par l'activité cellulaire et peut être classifié, par conséquent, comme "biorésorbable".
Une autre partie de ce travail de thèse a donc été dédiée à l'étude des phénomènes de dégradation cellulaires (par **cellules ostéoclastiques** principalement). Pour cette raison, des tests de culture cellulaire ont été réalisés sur des échantillons de β-TCP lors d'un séjour dans le laboratoire du Prof. Aldo Boccaccini (FAU Erlangen-Nürnberg, Allemagne). Les matériaux ont été testés sous forme d'échantillons denses composés de β-TCP pur ou de β-TCP dopé avec 5 mol.% de magnésium. L'intérêt d'ajouter du magnésium était double: d'un côté, le dopage était censé modifier les propriétés du matériau (par exemple sa cinétique de dissolution) et d'un autre influer sur le comportement cellulaire.

Pour les essais de dissolution, des échantillons poreux de DCPD (60% de porosité) ont été obtenus par la voie des ciments, à température ambiante, selon la réaction de prise illustrée dans l'équation (1). Les échantillons poreux de β-TCP (79% de porosité), gracieusement fournis par le Prof. Marc Bohner (RMS Foundation, Bettlach, Suisse), ont été élaborés en calcinant un ciment apatitique émulsifié.

$$\begin{gathered} \beta - TCP \; + \; MCPM \; + \; H_2O \; \rightarrow \; DCPD \\ \beta - Ca_3\left(PO_4\right)_2 + \; Ca\left(H_2PO_4\right)_2 \cdot H_2O \; + \; 7H_2O \; \rightarrow \; 4CaHPO_4 \cdot 2H_2O \end{gathered} \quad (1)$$

Les tests de dissolution *in-vitro* ont été effectués dans des solutions tamponnées à base de TRIS et de PBS (Phosphate Buffered Saline) pour des périodes s'étalant de 30 minutes à 14 jours pour le DCPD et de 1 à 8 semaines pour le β-TCP. Des conditions statiques (agitation seule) ainsi que dynamiques (avec renouvellement périodique de la solution d'immersion) ont été appliquées pour la solution TRIS (conditions dénommées respectivement TRISs et TRISd); au contraire, le PBS a été utilisé uniquement en conditions dynamiques (PBSd). Les détails expérimentaux sont listés dans le Tableau 1. Pour suivre l'évolution de ces matériaux, les échantillons ont été caractérisés avant et après les tests de dissolution. Les propriétés physico-chimiques ont été évaluées par Diffraction aux Rayons X (DRX) et suivi de pH de la solution d'immersion; la microstructure a été observée par Microscope Electronique à Balayage (MEB) et tomographie aux rayons X (µ-CT). Les propriétés mécaniques, enfin,

ont été évaluées par micro-indentation sphérique instrumentée; cette technique a été choisie parce qu'elle permet de mesurer des propriétés (module de Young et dureté) à une échelle locale et de manière quasi non-destructive.

Tableau 1: Conditions choisies pour les tests de dissolution statiques et dynamiques

	Conditions statiques	**Conditions dynamiques**	
Liquide	Solution tampon TRIS (TRISs)	Solution tampon TRIS (TRISd)	Solution PBS (PBSd)
Renouvellement de la solution (quantité, taux, fréquence)	Non	100mL en 1min, chaque 24h	100mL en 1min, chaque 24h
pH de la solution	7.40 ± 0.15	7.40 ± 0.15	7.40 ± 0.10
Température	37°C	37°C	37°C
Agitation	Agitateur orbital, 50 rpm	Agitateur à pâles, 50 rpm	Agitateur à pâles, 50 rpm
Rapport volume de liquide/masse de l'échantillon	130 mL/g (DCPD) 430 mL/g (β-TCP)	130 mL/g (DCPD) 430 mL/g (β-TCP)	130 mL/g (DCPD) 430 mL/g (β-TCP)
Durée du test	30min - 14 jours (DCPD) 1 - 8 semaines (β-TCP)	1 jour - 14 jours (DCPD) 1 - 8 semaines (β-TCP)	30min*, 1 j - 14 jours (DCPD) 1 - 8 semaines (β-TCP)

** A noter que pour les essais à 30 minutes, les conditions statiques et dynamiques ont été considérées comme étant équivalentes (pas de renouvellement de la solution dans les deux cas); pour cette raison, les tests de 30 minutes ont tous été réalisés selon le protocole suivi pour les conditions statiques (PBS compris).*

Les résultats des **essais de dissolution des échantillons de DCPD** ont suggéré une forte influence du milieu et des conditions du protocole expérimental sur l'évolution des matériaux. Les Figures 1, 2 et 3 représentent schématiquement et qualitativement l'évolution des propriétés mécaniques et du poids des échantillons en fonction du temps d'immersion. L'apparition (↓) et la disparition (↑) des principales phases cristallines sont également présentées. De plus, pour le temps d'immersion le plus long (14 jours), des images obtenues par µ-CT et par MEB illustrent la microstructure des matériaux à deux échelles différentes.

L'apparition de nouvelles phases par précipitation (surtout en surface des échantillons) a été observée dans le PBSd avant le TRISd, mais leur croissance était ensuite plus rapide dans le TRISd que dans le PBSd. Le milieu a également influencé les précipités au niveau de leur composition chimique et de leur morphologie. En effet, des petits agrégats de plaquettes minces d'OCP (*phosphate octacalcique*, $Ca_8(HPO_4)_2(PO_4)_4 \cdot 5H_2O$) ont été observés dans le PBSd (Figure 1), alors que de l'OCP et de l'apatite ont été trouvés dans le TRIS, sous forme d'assemblages plus compacts de plaquettes et de précipités "spongieux" (Figure 2). Les observations µ-CT ont permis d'apprécier à quel point la microstructure des échantillons immergés, et surtout de leur surface, était complétement différente selon le milieu d'immersion.

Le renouvellement du milieu est également apparu comme un paramètre fondamental: en comparant TRISd et TRISs, l'évolution du matériau a été beaucoup plus marquée en conditions dynamiques.

En général, les changements qui ont eu lieu dans les échantillons ont démarré en surface et se sont répandus vers l'intérieur du matériau par la suite. Cela a entraîné la formation d'un gradient de propriétés entre la surface et le cœur de l'échantillon, qui s'est répercuté sur ses caractéristiques mécaniques, telles qu'évaluées par micro-indentation (Figure 4). Dans l'ensemble, une forte diminution de la dureté et du module de Young a été observée sur la surface des échantillons, alors que seulement des changements modérés ont été détectés à cœur. En corrélant toutes ces modifications en fonction du temps, il est assez clairement apparu que les changements de porosité,

de microstructure et de phases cristallines en présence ont influencé fortement les propriétés mécaniques des matériaux testés. Cette observation a prouvé à quel point les évolutions des propriétés chimiques, structurales et mécaniques sont liées entre elles et a confirmé la nécessité de considérer tous ces aspects lorsque l'évolution d'un matériau résorbable est étudiée.

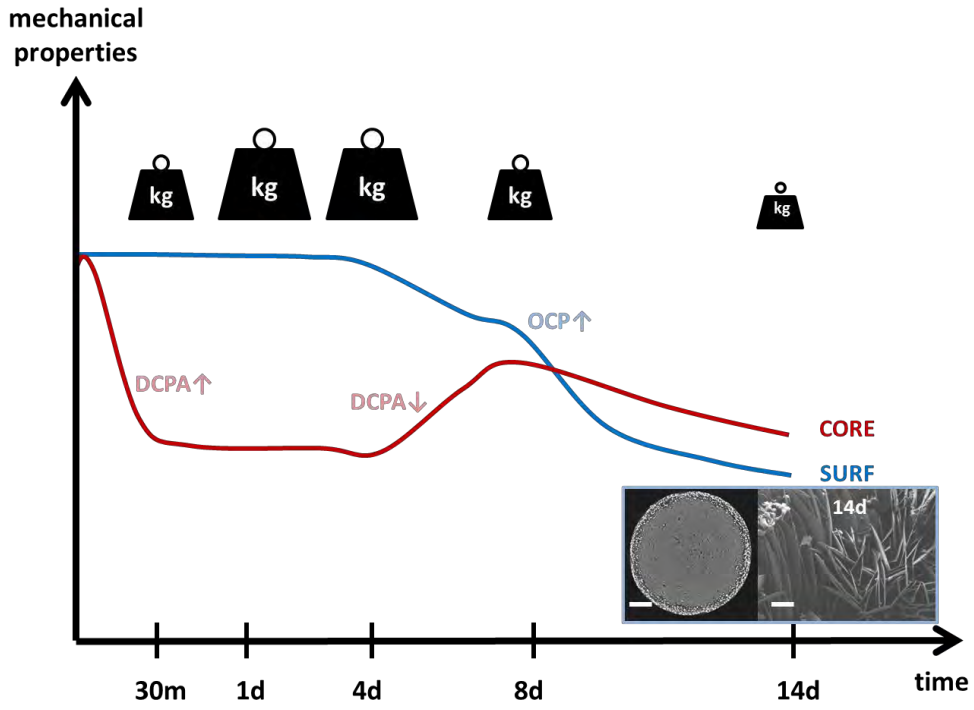

Figure 1: Représentation schématique des principaux changements observés après immersion des échantillons de DCPD dans du PBSd. Les petits poids représentent la masse des échantillons. Barre d'échelle de 1 mm et 5 µm pour les images µ-CT et MEB respectivement

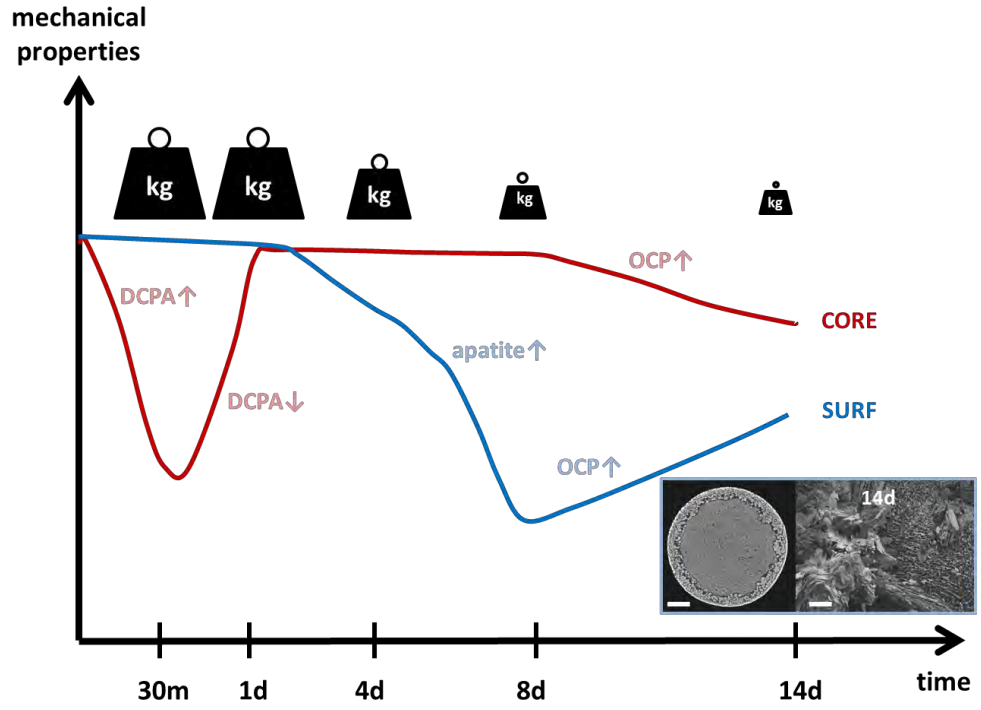

Figure 2: Représentation schématique des principaux changements observés après immersion des échantillons de DCPD dans du TRISd. Les petits poids représentent la masse des échantillons

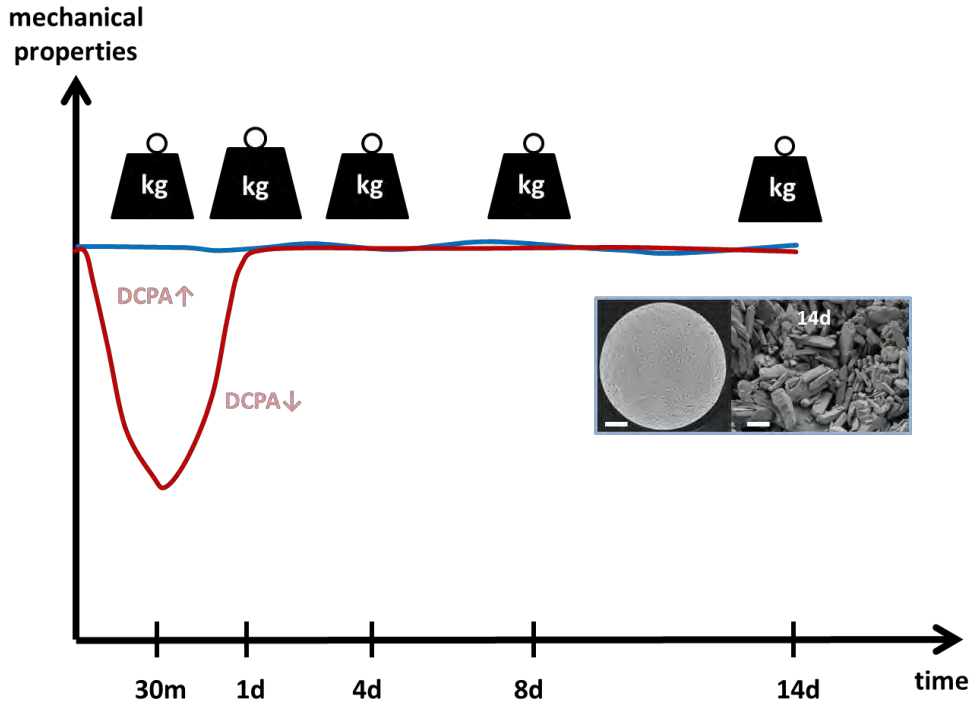

Figure 3: Représentation schématique des principaux changements observés après immersion des échantillons de DCPD dans le TRISs. Les petits poids représentent la masse des échantillons

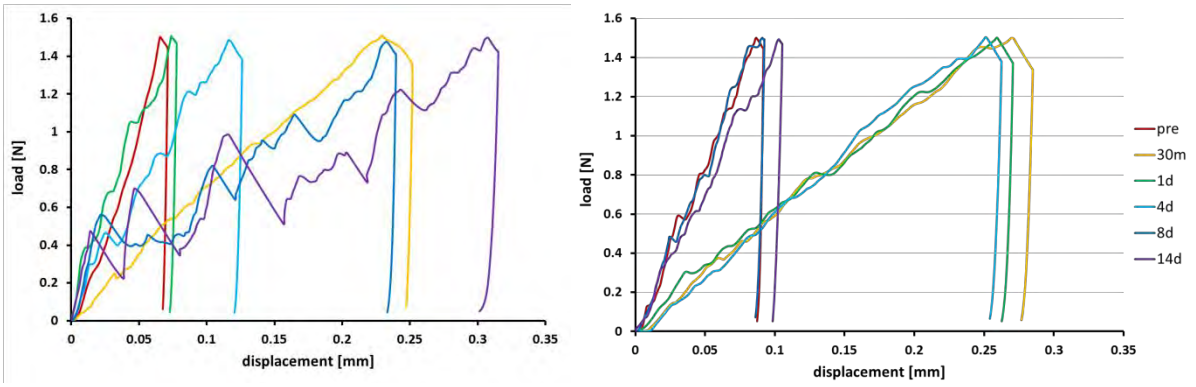

Figure 4: Exemple de courbes charge-déplacement obtenues lors des tests d'indentation à la surface (à gauche) et à cœur (à droite) des échantillons de DCPD immergés dans le PBSd

Pour ce qui concerne les **essais de dissolution des échantillons de β-TCP**, la forte influence de la composition de milieu et des conditions expérimentales a été confirmée. La plupart des changements détectés ont eu lieu en conditions dynamiques dans le TRIS (voir images µ-CT de la Figure 5). Contrairement à ce qui a été observé pour les échantillons de DCPD, dans le cas du β-TCP l'évolution du matériau n'a pas entraîné de précipitation de phases cristallines, mais a été plutôt causée par des changements microstructuraux liés à la dissolution du matériau. La diminution des propriétés mécaniques, notée surtout en surface des échantillons immergés en TRISd (Figure 6-Figure 7), parait liée à l'augmentation de porosité juste au-dessous de la surface. Cette observation apporte un regard nouveau sur la dégradation du β-TCP : ce matériau est en fait généralement considéré comme "bioresorbable" et non "biosoluble". Dans cette étude cependant, nous avons démontré comment, dans des conditions spécifiques (notamment avec une forte porosité des

échantillons et l'utilisation d'un milieu pauvre en ions et périodiquement renouvelé), cette céramique montre des caractéristiques propres aux matériaux "biosolubles".

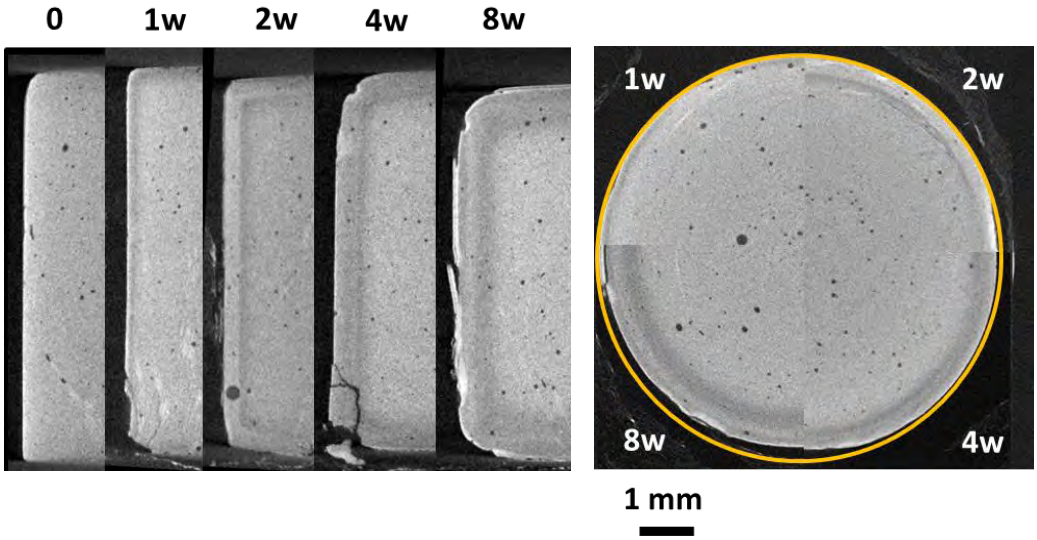

Figure 5: Images µ-CT frontales (à gauche) et transverse (à droite) des échantillons de β-TCP après différents temps d'immersion dans le TRISd. Le cercle jaune (section transverse) représente la circonférence d'un échantillon à temps zéro

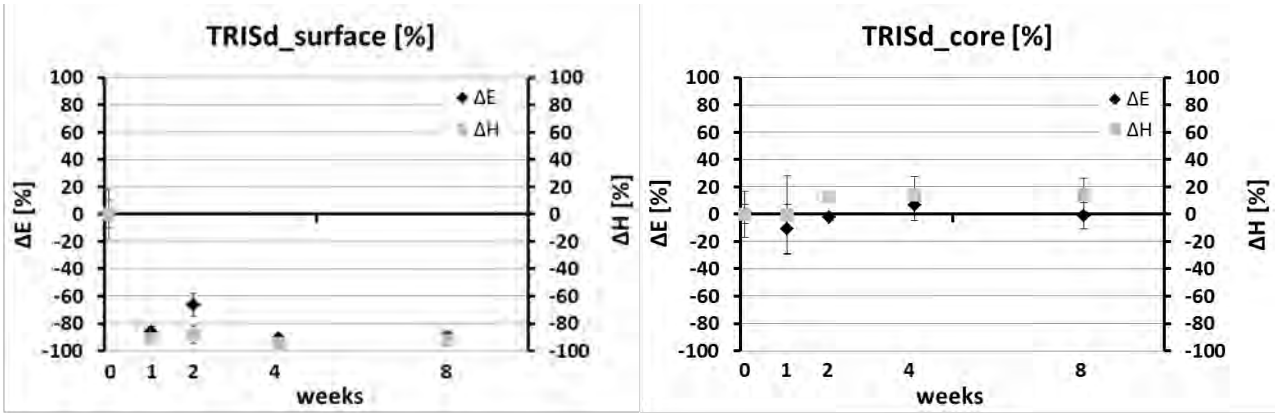

Figure 6: Variation (en pourcentage) de H et E à la surface (à gauche) et à cœur (à droite) des échantillons de β-TCP après différents temps d'immersion dans le TRISd

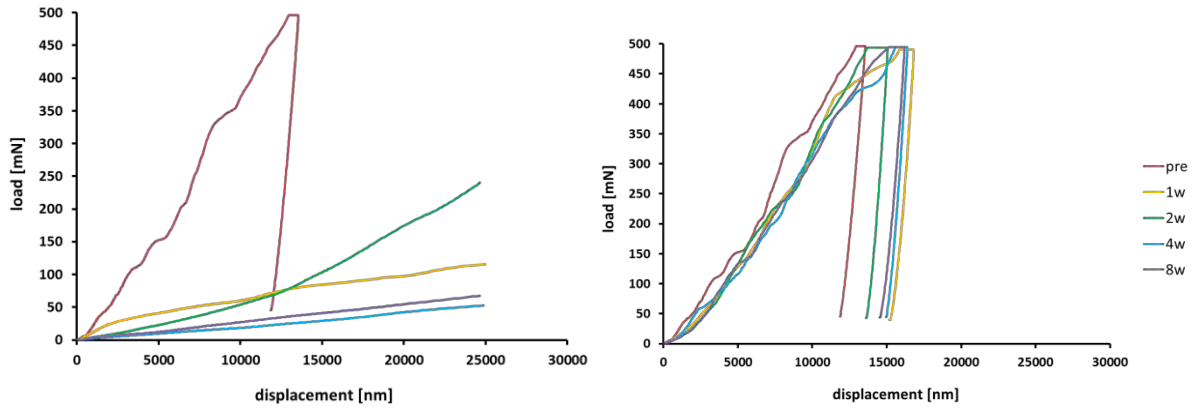

Figure 7: Exemple de courbes charge-déplacement représentatives obtenues pendant les tests d'indentation à la surface (à gauche) et à cœur (à droite) des échantillons de β-TCP immergés dans le TRISd.

Concernant la méthode choisie pour suivre l'évolution des propriétés mécaniques, la validité et l'intérêt de la **micro-indentation instrumentée** a été pleinement confirmée.
Une recherche bibliographique a montré que la majorité des études qui s'étaient focalisées sur l'évolution de substituts osseux résorbables n'incluait pas les aspects mécaniques ou bien utilisait seulement des essais courants qui fournissent une information uniquement sur le volume total de l'échantillon (principalement tests de compression et dans quelques cas de flexion 4-points). Cependant, ce travail a montré que la dégradation des échantillons n'était pas homogène et qu'un gradient de propriétés apparaissait entre le cœur et la surface de l'échantillon pendant le processus de dégradation. Des essais comme la compression ne sont pas adaptés pour détecter ces gradients, contrairement à la micro-indentation instrumentée, adaptée pour des caractérisations locales.
En effet, ceci a été confirmé en comparant les résultats des tests de compression et de micro-indentation effectués sur les échantillons de β-TCP. Grâce à l'utilisation de la micro-indentation instrumentée, cela a été possible de "découpler" les propriétés des différentes zones d'un même échantillon et d'évaluer ainsi l'influence de la couche poreuse externe sur les propriétés du matériau dégradé.
De plus, les essais mécaniques ont pu être réalisés sur le même échantillon avant et après immersion, grâce à la micro-indentation, qui est une technique quasi non-destructive. En conséquence, l'évolution de chaque échantillon a pu être suivie. Les résultats présentés ici ont aussi montré que les indentations réalisées avant immersion n'ont pas altéré significativement l'évolution des échantillons.
La technique de micro-indentation s'est avérée être suffisamment sensible pour détecter les tous premiers changements. Dans le cas d'une dégradation relativement lente, comme celle des échantillons poreux de β-TCP en TRISs, la micro-indentation a révélé une diminution des propriétés mécaniques alors que les autres techniques n'avaient pas encore montré de changement significatif.
Un autre avantage de la micro-indentation instrumentée est lié à la large gamme de géométrie que l'échantillon peut avoir. Quoique la surface doive être correctement préparée, la forme de l'échantillon peut être quelconque. Dans le futur, cette technique pourrait donc être appliquée pour des échantillons sous forme de disque, comme ceux utilisés dans ce travail pour les essais cellulaires, ainsi que pour des géométries bien plus complexes, comme celles d'explants.

En conclusion, même si certaines précautions doivent être respectées (surtout au niveau de la préparation de la surface des échantillons), la technique de la micro-indentation instrumentée peut s'avérer déterminante pour le suivi des propriétés mécaniques de matériaux dégradés.

Pour les **tests de culture cellulaire** (réalisés en collaboration avec le Prof. Aldo Boccaccini et le Dr. Rainer Detsch, FAU University, Erlangen, Germany), les poudres de β-TCP, pures et dopées au magnésium, ont été comprimées par pressage uniaxial puis isostatique, et frittées afin d'obtenir des échantillons denses (porosité < 9%). Des cellules souches RAW 264.7 ont tout d'abord été cultivées avec des facteurs de croissance (MCSF et RANKL) pour favoriser leur différenciation en ostéoclastes, puis transférées sur les échantillons. Après 2, 4 et 7 jours respectivement, les cellules et les échantillons ont été analysés. Pour les cellules, des marquages fluorescents et des essais « TRAP », ainsi que des essais de viabilité, ont été effectués. Les échantillons ont été observés au MEB après avoir enlevé les cellules qui étaient attachées sur leur surface. De plus, des tests de dissolution ont été effectués en parallèle dans le milieu de culture seul (RPMI) et dans une solution saline de référence (0.9% NaCl) afin d'identifier les modifications causées uniquement par la dissolution, et non liées à l'activité cellulaire.

Les essais cellulaires sur les échantillons de β-TCP pur et dopé ont confirmé la bonne cytocompatibilité des deux matériaux. Par contre, l'activité des ostéoclastes n'a pas été favorisée par le β-TCP. Parmi les différentes causes possibles, l'influence de la topographie des échantillons (notamment leur rugosité et leur taille de grains) sur l'activité des ostéoclastes offre une nouvelle

perspective d'étude qui serait intéressante à approfondir. Une autre explication, déjà avancée par des études précédentes, serait liée au relargage d'ions calcium provenant du β-TCP dans le milieu de culture: une concentration trop élevée de ces ions pourrait alors amoindrir l'activité des ostéoclastes. Finalement, le dopage du β-TCP au magnésium a semblé affecter principalement les propriétés intrinsèques du matériau, en diminuant notamment son taux de dissolution (Figure 8).

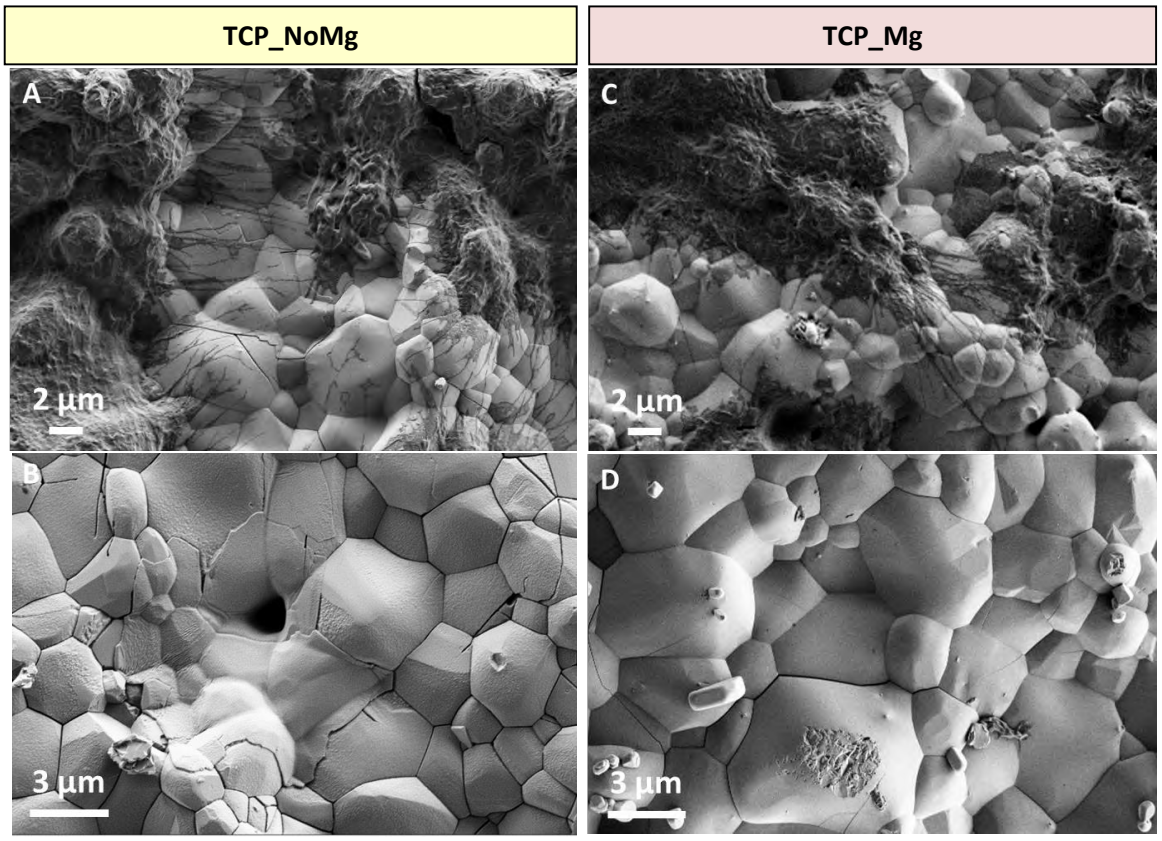

Figure 8: Micrographies électroniques (MEB) des échantillons de β-TCP pur (A-B) et dopé (C-D) avant (A-C) et après (B-D) avoir enlevé les es cellules ostéoclastiques (cultivées sur les échantillons pendant 4 jours)

En conclusion, cette étude s'est attachée à suivre de manière précise et complète l'évolution *in-vitro* de deux phosphates de calcium couramment utilisés dans la substitution et le comblement osseux, en soulignant l'importance du choix des conditions expérimentales d'étude. De plus, la micro-indentation s'est révélée être une technique appropriée pour l'évaluation des propriétés mécaniques de substituts osseux et, surtout, pour le suivi de leur évolution après immersion. Il a été prouvé que les changements physico-chimiques, microstructuraux et mécaniques sont très étroitement liés et que, en conséquence, ils devraient tous être pris en compte lorsque l'on étudie l'évolution d'un matériau résorbable.

Par la suite, il serait intéressant d'approfondir certains aspects de cette étude, et en particulier :

- mesurer la concentration des ions (calcium, ortophosphates, magnésium) dans les milieux collectés pendant les essais de dissolution et de culture cellulaire;
- comprendre l'influence de potentielles phases amorphes et des ions citrate présents dans les ciments brushitiques, grâce à l'utilisation de la spectroscopie infrarouge à transformée de Fourier;

- effectuer des tests avec des solutions plus proches des fluides physiologiques en terme de concentration d'ions. Des milieux contenant des protéines pourraient également être utilisés;
- réaliser des tests d'indentation supplémentaires en condition humides à différents temps d'immersion, pour mieux évaluer l'influence du protocole de séchage, de la présence d'humidité et comprendre s'il s'agit d'un paramètre significatif sur les propriétés mesurées;
- appliquer la méthode de l'identification inverse aux données collectées; en suivant la stratégie décrite dans l'étude de Clément [1], il serait alors possible d'extraire encore plus d'informations à partir des essais de micro-indentation instrumentée (notamment, la loi de comportement mécanique);
- évaluer l'influence du taux de porosité sur la dégradation du β-TCP ; à ce sujet, des essais préliminaires de frittage ont déjà été effectués afin de modifier la distribution de taille des pores du matériau de manière sélective (par exemple en faisant disparaître les pores de plus petites tailles tout en gardant les plus gros);
- réaliser des tests *in-situ*, comme par exemple:
    - o des suivis en DRX pendant les premiers jours d'immersion des échantillons de DCPD, pour enregistrer les tous premiers changements qui ont lieu dans le matériau,
    - o des indentations sur la surface des échantillons pendant qu'ils sont encore immergés,
    - o des essais d'indentation couplés avec des observations µ-CT pour suivre en temps réel les processus d'endommagement des échantillons dégradés de DCPD et de β-TCP,
- effectuer des essais de dissolution avec d'autres substituts osseux, comme les phosphates de calcium biphasiques,
- répéter les tests de culture cellulaire avec des échantillons caractérisés par une rugosité et une taille de grains sub-micrométrique, afin de mieux comprendre l'influence de la topographie du matériau sur l'activité des ostéoclastes. Des essais supplémentaires sur des échantillons de β-TCP dopés avec plus de magnésium, enfin, pourraient aider à identifier l'influence de ce dopage sur les propriétés du matériau.

1. Clement, P., *Détermination des proprietés mécaniques de céramiques poreuses par essais de micronindentation instrumenée sphérique.* Ph.D. Thesis, 2013.

ANNEX

Annex A refers to Chapter 2, Annex B to Chapter 3, Annex C to Chapter 4 and Annex D to Chapter 5.

ANNEX A

Optimization of DCPD samples production

The following graphs show the influence of grinding time on the granulometry of β-TCP powders used for the production of DCPD samples (Figure A.a.1). In particular, the values of the 10th, 50th and 90th percentiles are reported (Figure A.a.2).

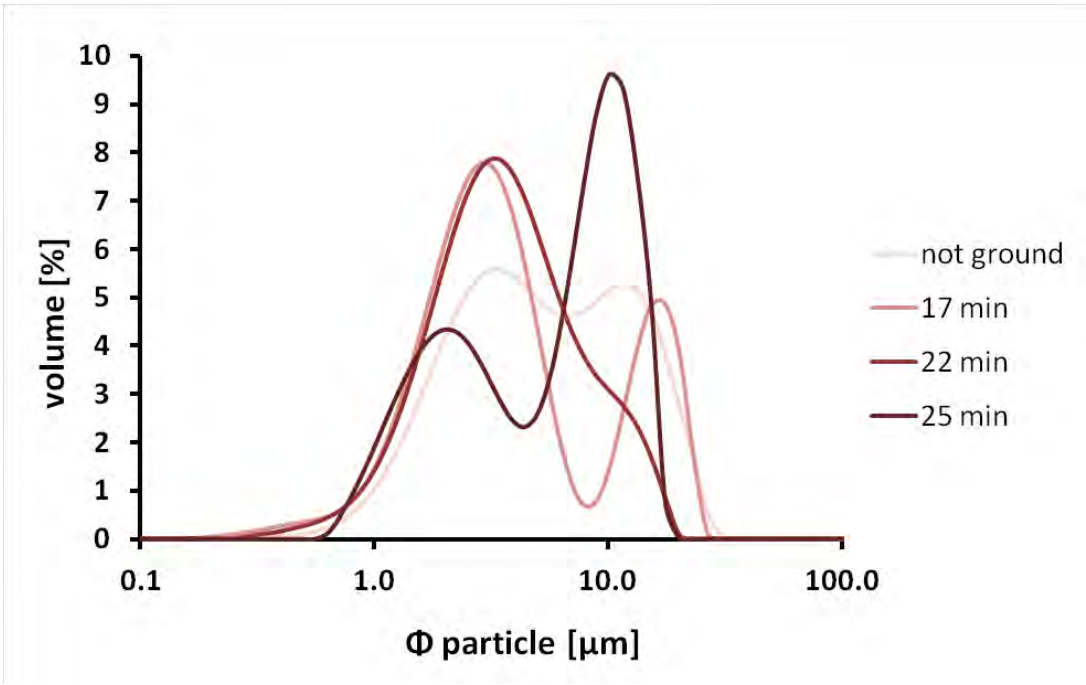

Figure A.a.1: particle size distribution of βTCP before and after grinding

Table A.a.1: particle size distribution of βTCP before and after grinding (dX = X% in volume of the particles is below this diameter)

sample	d 10	d 50	d 90
not ground	1.56	4.73	14.62
17 min	1.26	3.07	15.41
22 min	1.33	3.24	9.00
25 min	1.31	6.26	12.11

Figure A.a.2 displays the influence of the type and concentration of additive on the knife setting time of a brushite cement produced according to the reaction described in eq.1 of Chapter 2. Two different powder to liquid ratios (P:L), moreover, were investigated.

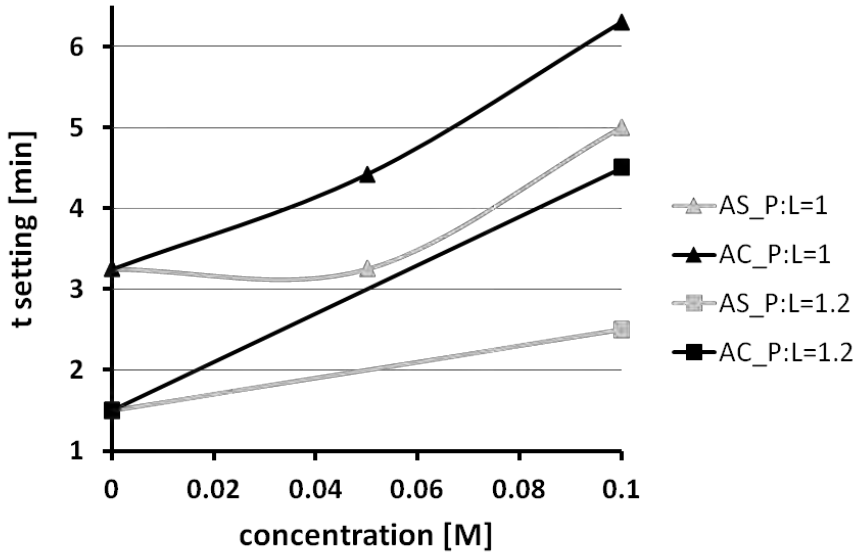

Figure A.a.2: Influence of concentration of citrates (AC) and sulphates (AS) on knife setting time

ANNEX B

X-ray diffraction of DCPD samples: additional data

Graphs reported here (A.b.1 to A.b.8) represent on three axes (2θ angle, time, and counts) the evolution of the crystalline phases found at the surface and in the core of the DCPD samples after different immersion times. Observing the pictures from the fore part to the rear one, it is possible to visualise the evolution during time of DCPD, MCPM, MCPA, and OCP as described in detail for each condition in paragraph 3.2.2.

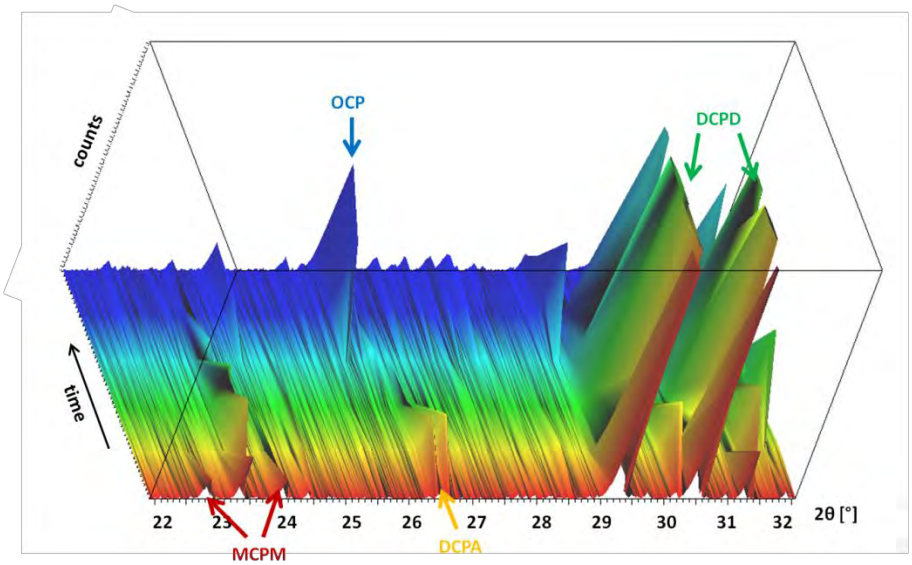

Figure A.b.1: Evolution during time (0-14d) of phases at the surface of DCPD samples after immersion in PBS. Range 2θ = 22°-32°

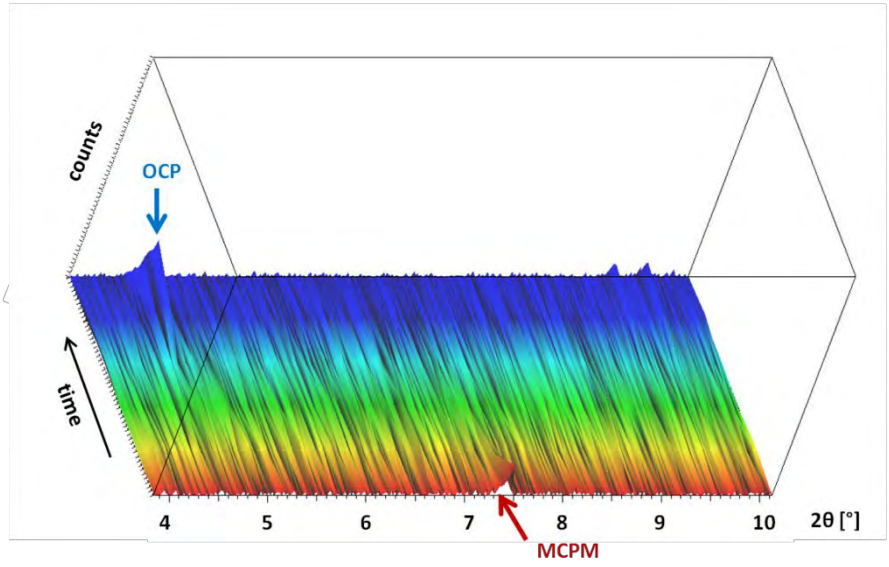

Figure A.b.2: Evolution during time (0-14d) of phases at the surface of DCPD samples after immersion in PBS. Range 2θ = 4°-10°

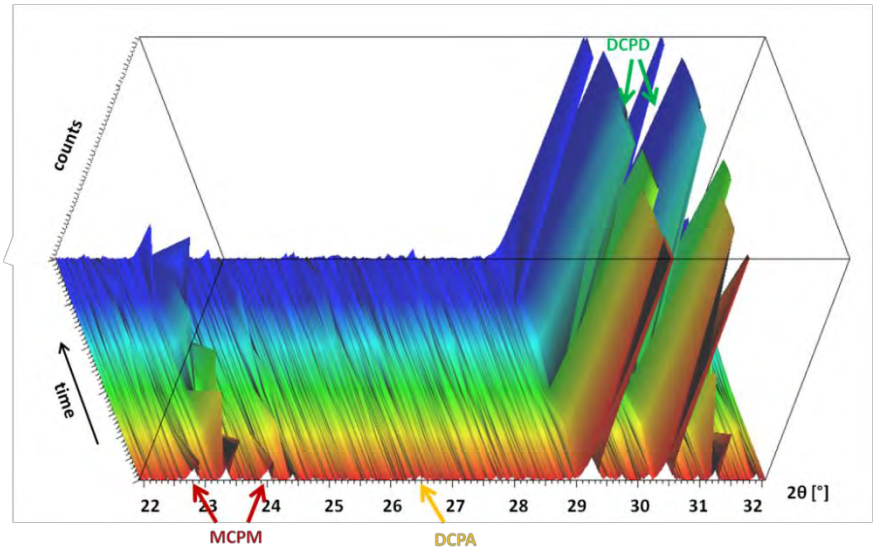

Figure A.b.3: Evolution during time (0-14d) of phases at the surface of DCPD samples after immersion in TRISs. Range 2θ =22°-32°

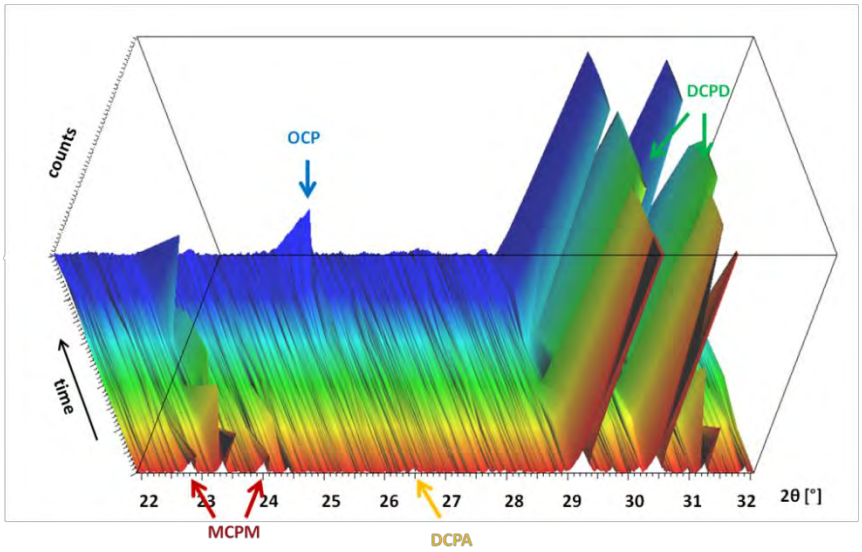

Figure A.b.4: Evolution during time (0-14d) of phases at the surface of DCPD samples after immersion in TRISd. Range 2θ =22°-32°

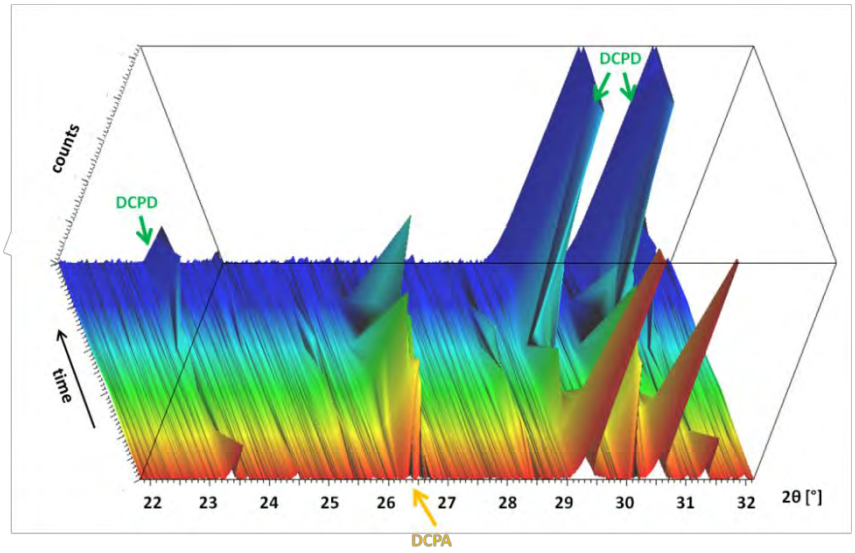

Figure A.b.5: Evolution during time (0-14d) of phases in the core of DCPD samples after immersion in PBS. Range 2θ =22°-32°

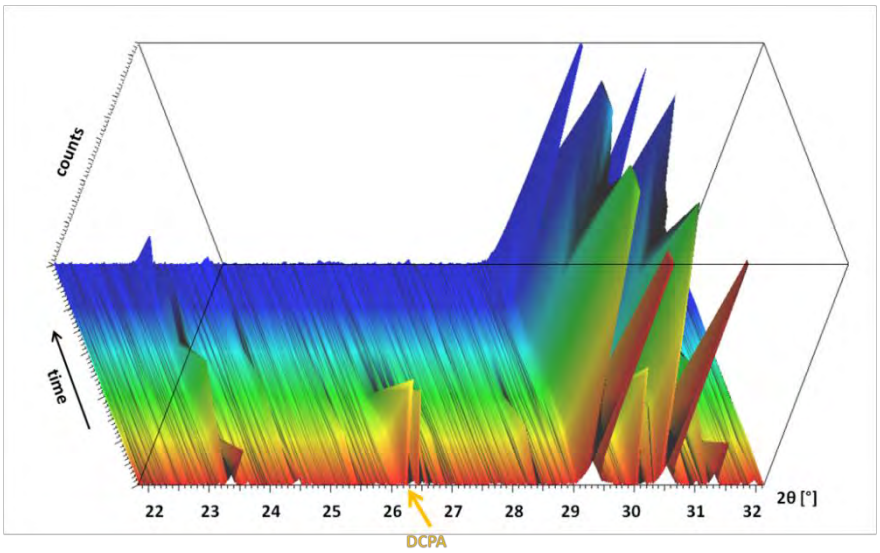

Figure A.b.6: Evolution during time (0-14d) of phases in the core of DCPD samples after immersion in TRISs. Range 2θ =22°-32°

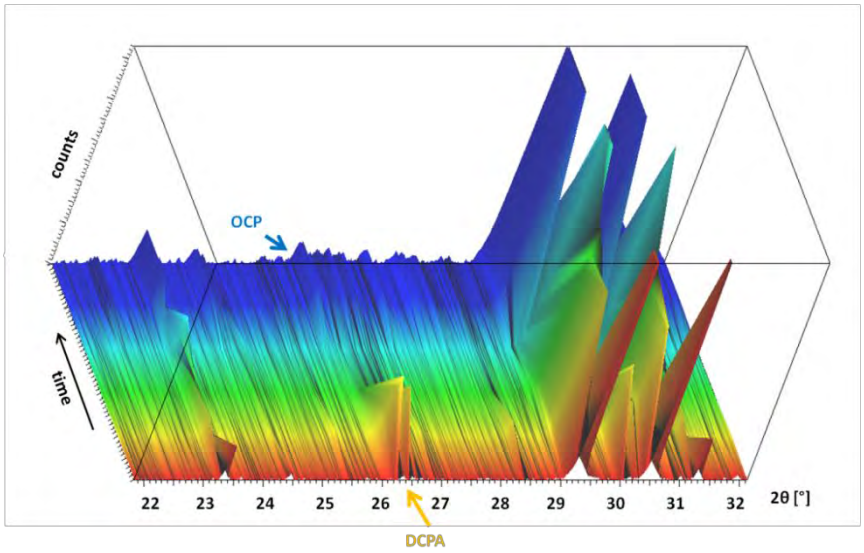

Figure A.b.7: Evolution during time (0-14d) of phases in the core of DCPD samples after immersion in TRISd. Range 2θ =22°-32°

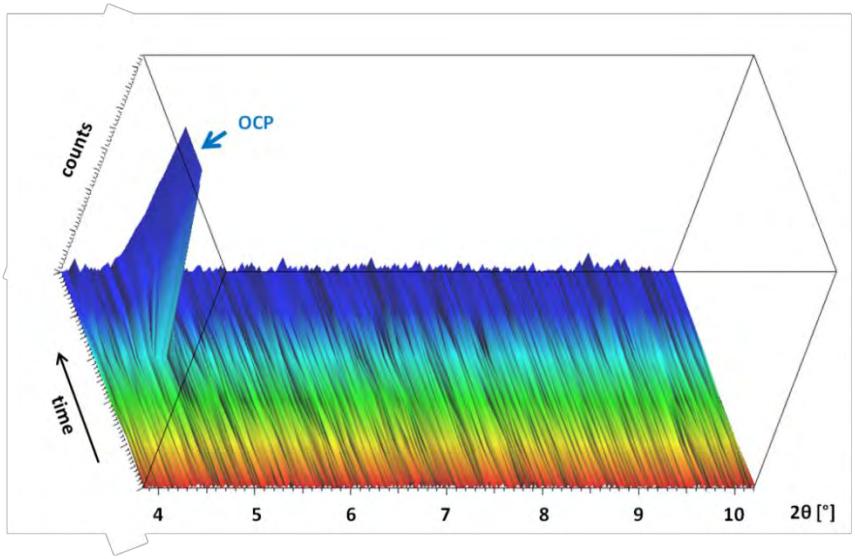

Figure A.b.8: Evolution during time (0-14d) of phases in the core of DCPD samples after immersion in TRISd. Range 2θ =4°-10°

Micro-computed tomography of DCPD samples: additional data

The images A.b.9 and A.b.10 report the X-Ray tomography images of DCPD samples immersed for 30 minutes in PBS and TRIS. It is worthy to underline that for this short time-point TRISs and TRISd were considered equivalent: the 30-minute test, thus, was performed only in static conditions.

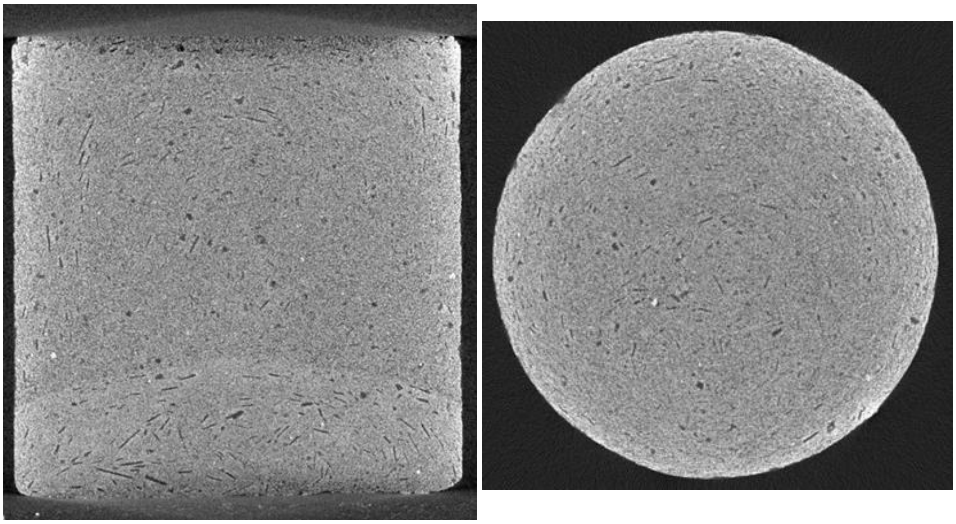

Figure A.b.9: Frontal (left) and transverse (right) µ-CT images of DCPD samples after 30 minutes of immersion in PBS

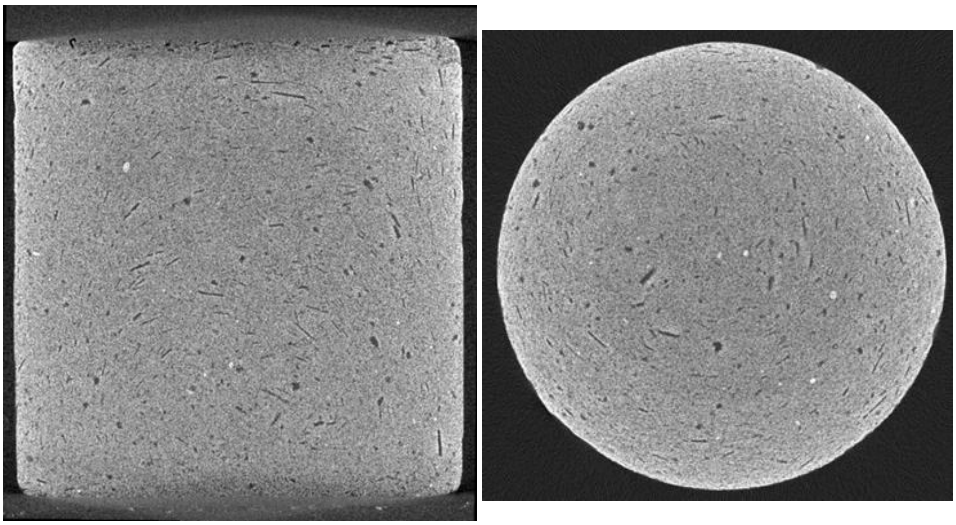

Figure A.b.10: Frontal (left) and transverse (right) µ-CT images of DCPD samples after 30 minutes of immersion in TRIS

Scanning electron microscopy of DCPD samples: additional data

The images from A.b.11 to A.b.14 show the SEM images of immersed DCPD samples which for sake of briefness were not reported in chapter 3. In particular samples after 30 minutes of immersion in PBSd are shown in Figure A.b.11, while all the following images reported the core of the specimens after 4 and 8 days of immersion in PBSd, TRISs and TRISd.

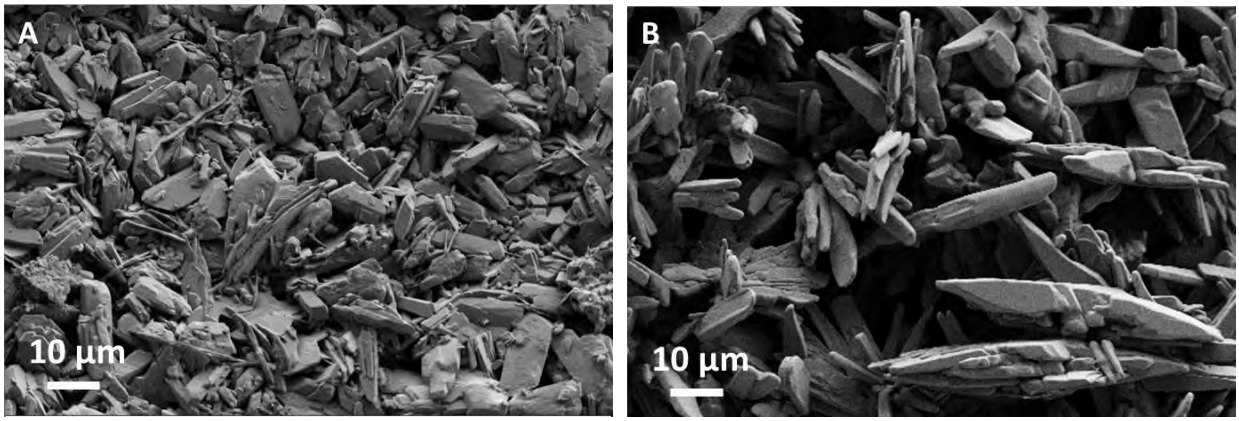

Figure A.b.11: SEM micrographs of surface (A) and core (B) of DCPD samples after immersion in PBSd for 30 minutes. Images of samples immersed in TRISs and TRISd are not reported, given that, compared to t0, even less changes took place in these solutions.

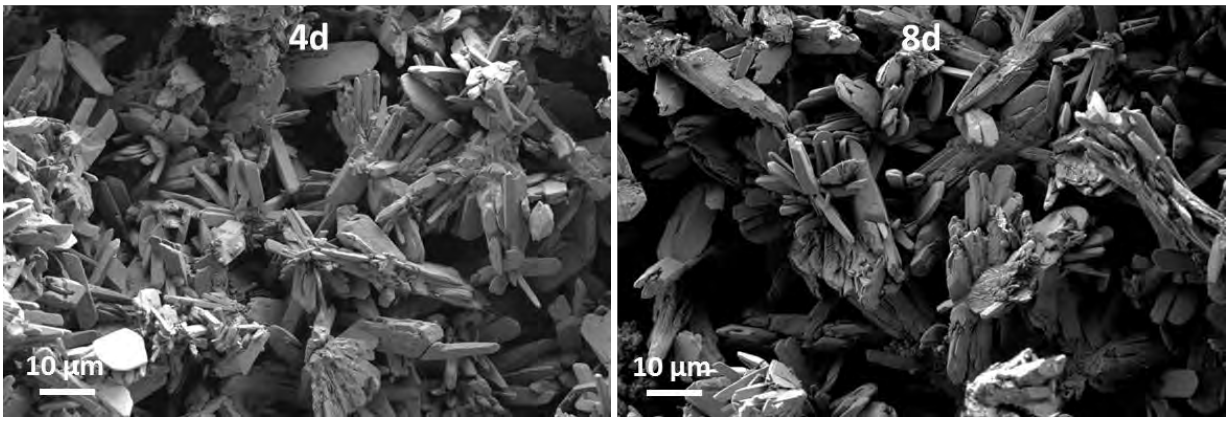

Figure A.b.12: SEM micrographs of the core of DCPD samples after immersion in PBSd for 4 and 8 days

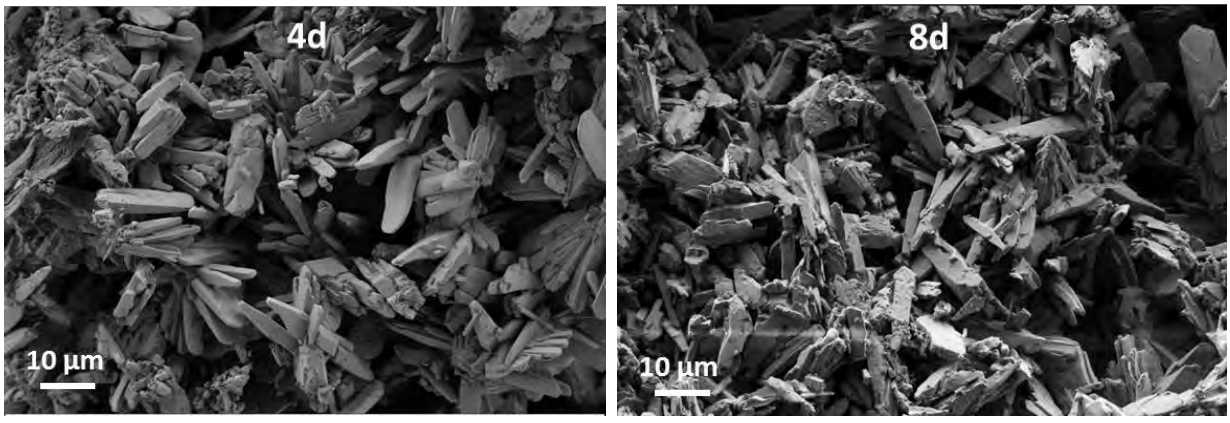

Figure A.b.13: SEM micrographs of the core of DCPD samples after immersion in TRISs for 4 and 8 days

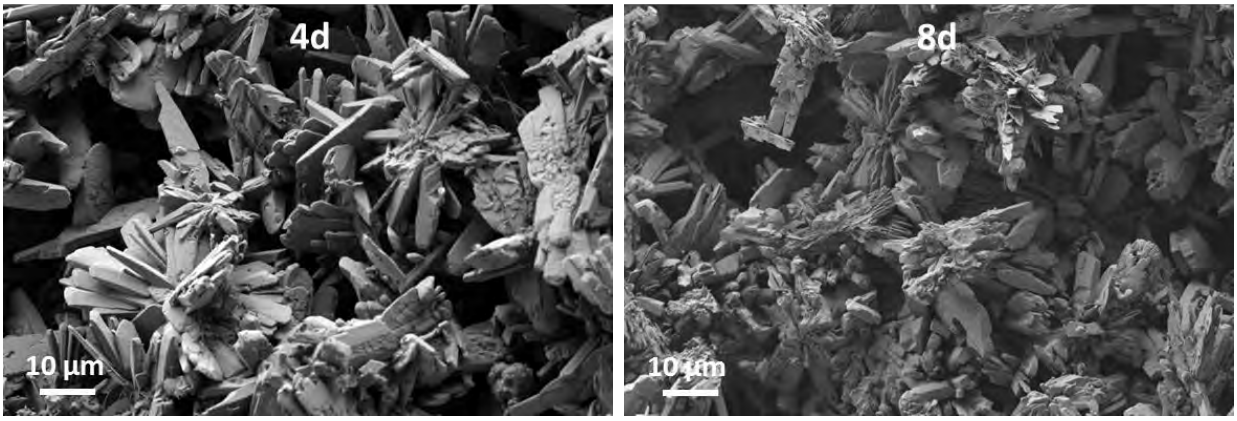

Figure A.b.14: SEM micrographs of the core of DCPD samples after immersion in TRISd for 4 and 8 days

Micro-indentation of DCPD samples: additional data

The three bars displayed in graphs from Figure A.b.15 to A.b.20 correspond to the values obtained at the surfaces of three different samples (denoted "surf a", "surf b" and "surf c" respectively). Thus, each bar represents the percentage variation of *H* or *E* of the very same sample after dissolution tests compared to the sample initial state (cf. Eq.1 of Chapter 3).

For the core, instead, the two bars (denoted "core a" and "core b") correspond to the percentage variation of *H* and *E* calculated in comparison with the values of reference samples at time zero (cf. Eq.1 of Chapter 3).

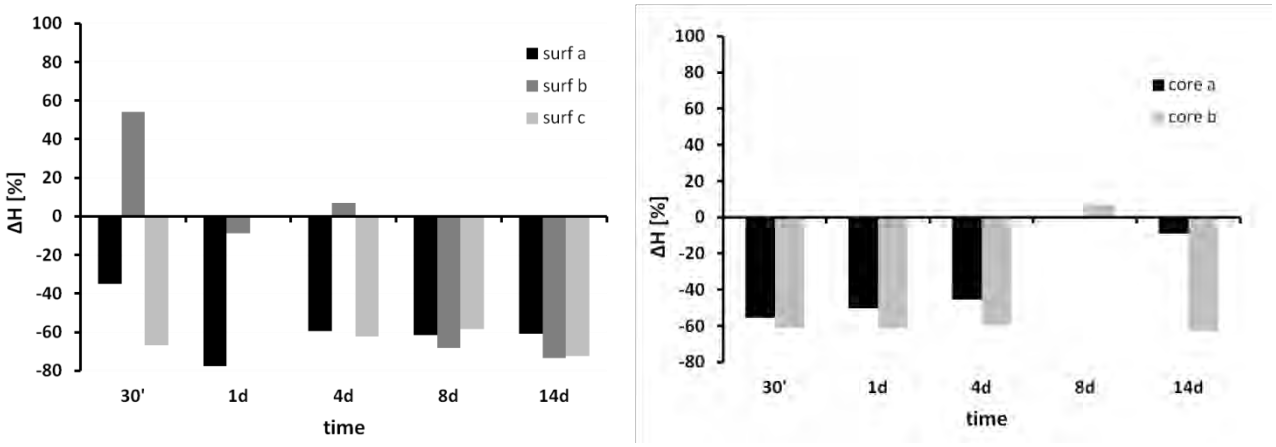

Figure A.b.15: Variation of hardness of DCPD samples at the surface (left) and in the core (right) after different immersion times in PBSd. Average values at t0: $H_{surface}$=9.2MPa, $E_{surface}$=1101MPa, H_{core}=6.1MPa, E_{core}=882MPa

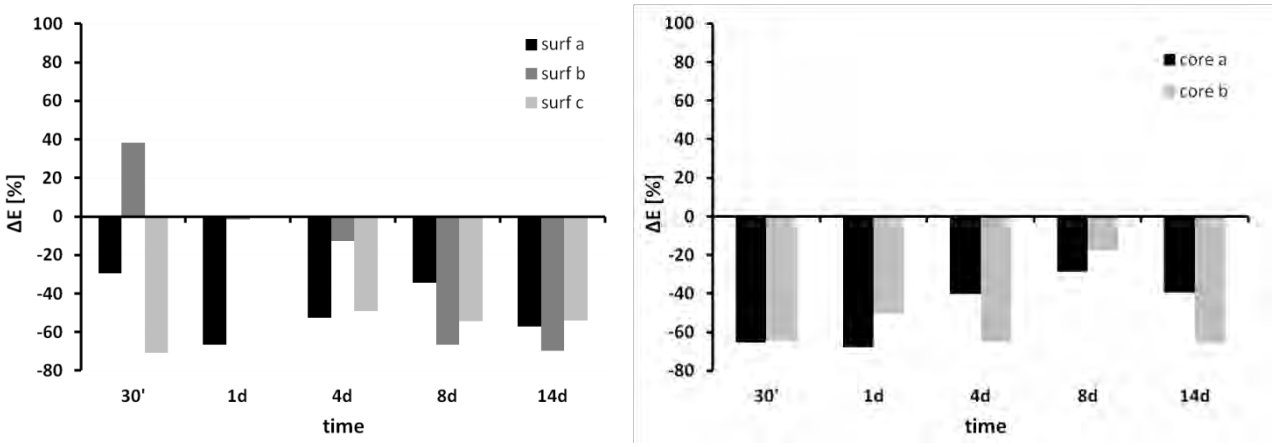

Figure A.b.16: Variation of Young's Modulus of DCPD samples at the surface (left) and in the core (right) after different immersion times in PBSd. Average values at t0: $H_{surface}$=9.2MPa, $E_{surface}$=1101MPa, H_{core}=6.1MPa, E_{core}=882MPa

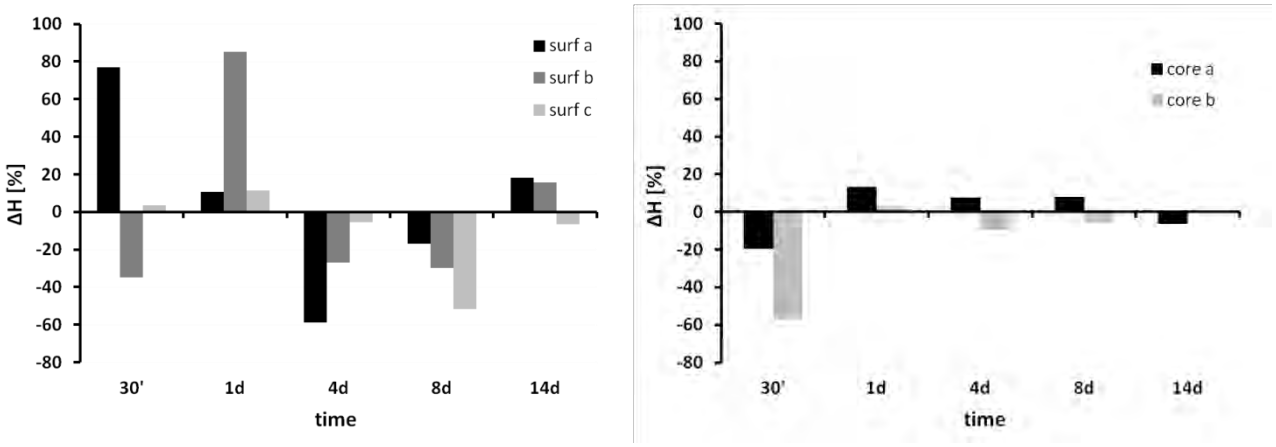

Figure A.b.17: Variation of hardness of DCPD samples at the surface (left) and in the core (right) after different immersion times in TRISs. Average values at t0: $H_{surface}$=9.2MPa, $E_{surface}$=1101MPa, H_{core}=6.1MPa, E_{core}=882MPa

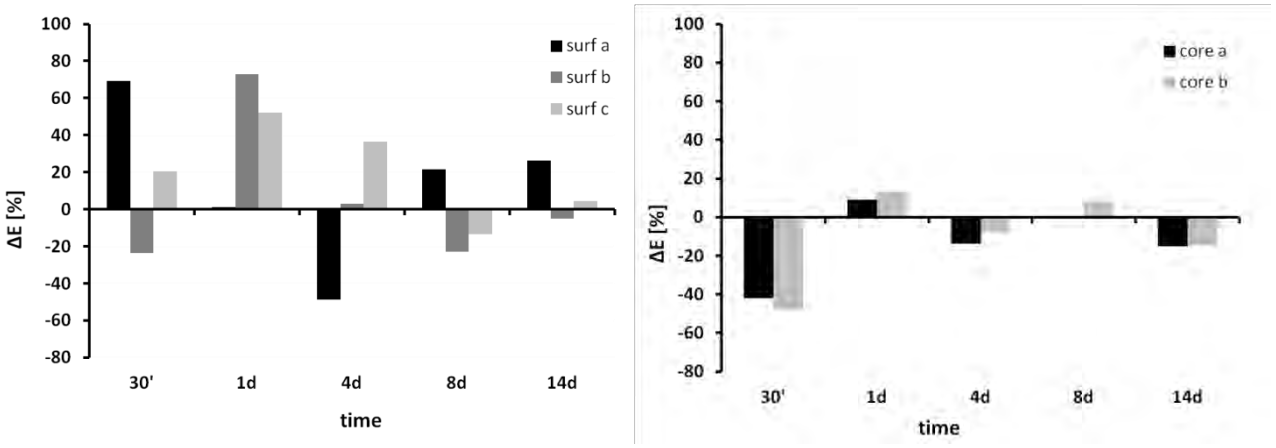

Figure A.b.18: Variation of Young's Modulus of DCPD samples at the surface (left) and in the core (right) after different immersion times in TRISs. Average values at t0: $H_{surface}$=9.2MPa, $E_{surface}$=1101MPa, H_{core}=6.1MPa, E_{core}=882MPa

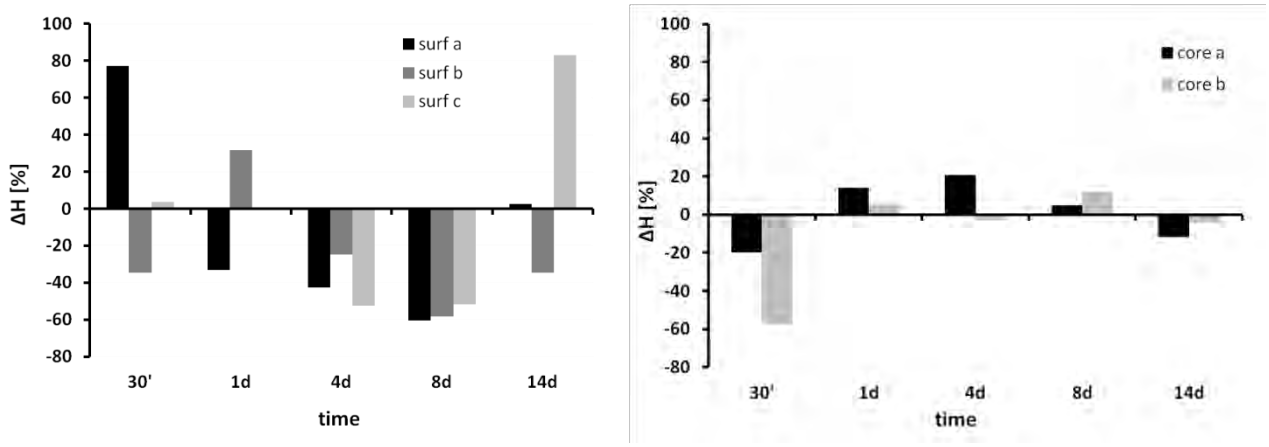

Figure A.b.19: Variation of hardness of DCPD samples at the surface (left) and in the core (right) after different immersion times in TRISd. Average values at t0: $H_{surface}$=9.2MPa, $E_{surface}$=1101MPa, H_{core}=6.1MPa, E_{core}=882MPa

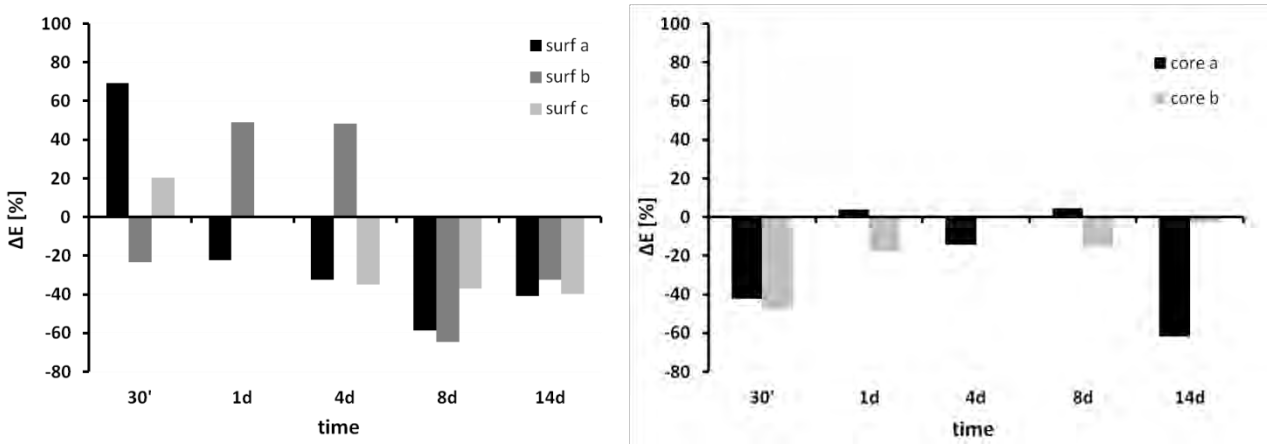

Figure A.b.20: Variation of Young's Modulus of DCPD samples at the surface (left) and in the core (right) after different immersion times in TRISd. Average values at t0: $H_{surface}$=9.2MPa, $E_{surface}$=1101MPa, H_{core}=6.1MPa, E_{core}=882MPa

<u>Preliminary experiment: *in-situ* XRD monitoring of the dissolution of a DCPD sample</u>

A batch reactor (Figure A.b.21), specially designed in MATEIS laboratory to investigate samples in aqueous solutions, was placed in the XRD machine on an X, Y and Z platform. A DCPD sample was cut and then dipped in TRIS solution with a liquid to cement ratio of 35.7 mL/g. Its crystalline composition was continuously assessed by *in-situ* XRD.

Acquisition parameters were adapted to the kinetics of the events occurring during the *ex-situ* dissolution tests: in the first hour, the 2θ range was limited and the step size was increased, to be able to monitor rapid changes. Then, longer scans were performed, to get more precise details about the possible evolutions. In detail, diffractograms were acquired for the first hour between $2\theta = 15°$ - 30° with 156 s per step and 0.05° as step size (resulting in a total acquisition time of 5 minutes per scan). Then, the parameters were changed and diffractograms were acquired between $2\theta = 4°$ - 36° with 184 s per step and 0.02° as step size (resulting in a total acquisition time of 30 minutes per scan). The experiment was run for more than 4 days at a temperature of 37 °C, to be as close as possible from the *ex-situ* experiments detailed in Chapter 3.

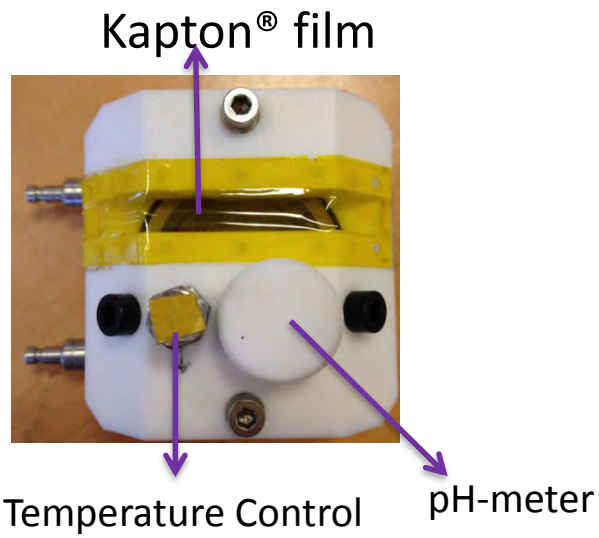

Figure A.b.21: Batch reactor designed for in-situ XRD analyses in liquid media

As shown on Figure A.b.22, no DCPA was detected between t0 and 24h (DCPA peaks would appear at 2θ=26.4°, 26.6° and 30.2°). The experiment was prolonged until more than 100 hours and till the end of this test, no significant evolution of the XRD pattern was noticed.

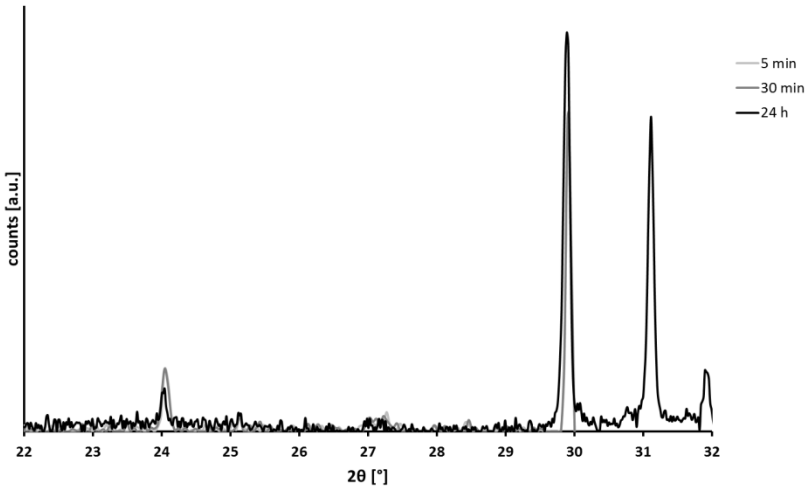

Figure A.b.22: in-situ XRD patterns of DCPD samples after 5, 30 minutes and 24 hours in TRISs

ANNEX C

X-ray diffraction of porous β-TCP samples: additional data

The following images report de XRD patterns at the core of porous β-TCP samples after immersion.

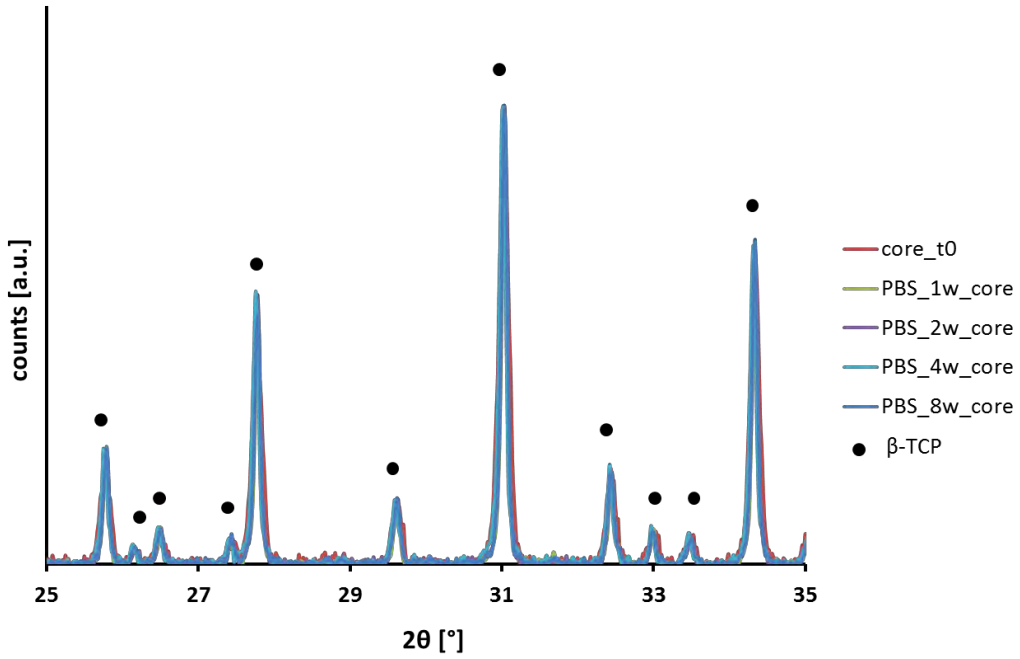

Figure A.c.1: XRD patterns of β-TCP samples in the core at time 0 and after 1-2-4-8 weeks in PBSd

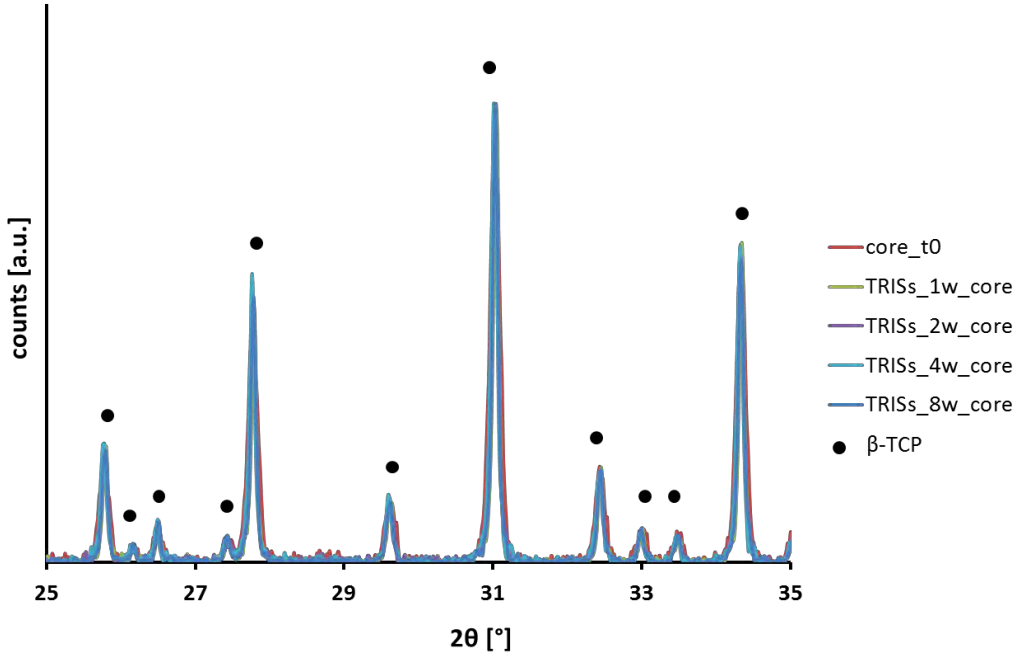

Figure A.c.2: XRD patterns of β-TCP samples in the core at time 0 and after 1-2-4-8 weeks in TRISs

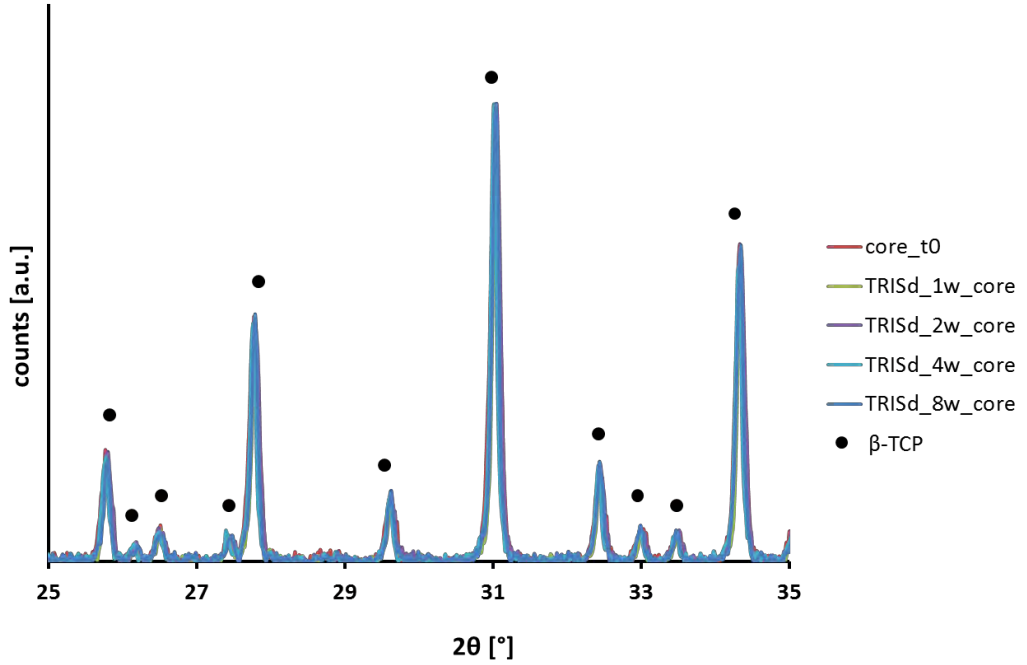

Figure A.c.3: XRD patterns of β-TCP samples in the core at time 0 and after 1-2-4-8 weeks in TRISd

pH: additional data

The evolution of the pH of TRISd solution where β-TCP porous samples were immersed is reported in Figure A.c.4. The dotted line represents the values measured in the reference medium.

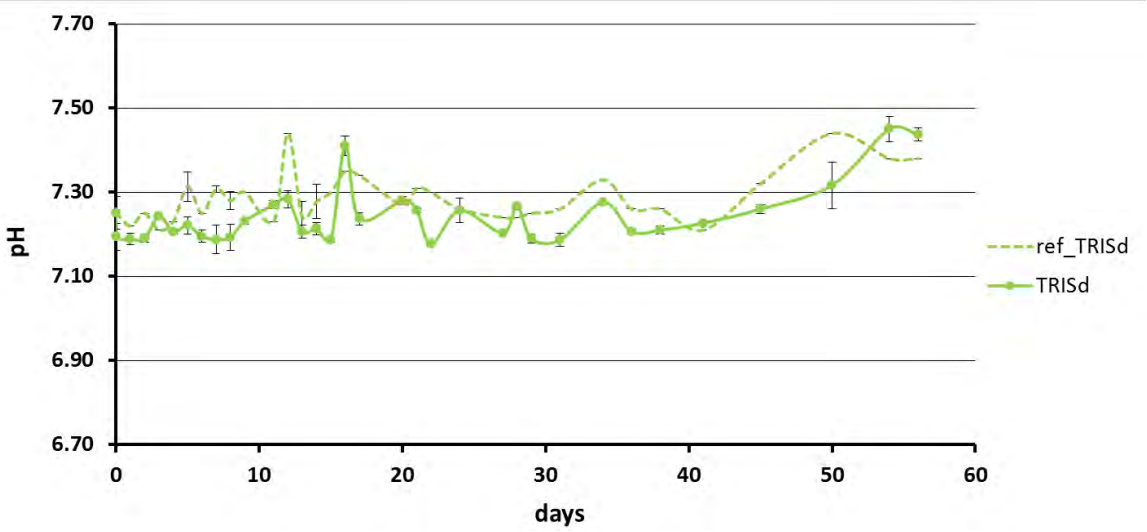

Figure A.c.4: Evolution of pH of TRISd solutions along all the duration of the tests

Micro-indentation of porous β-TCP samples: additional data

The following figures represent the percent variations of hardness and Young's modulus of the porous β-TCP samples after different times of immersion in PBSd, TRISs and TRISd. For each time-point, three samples were analysed at the surface (6 indentations per sample) and two in the core (9 indentations per sample).

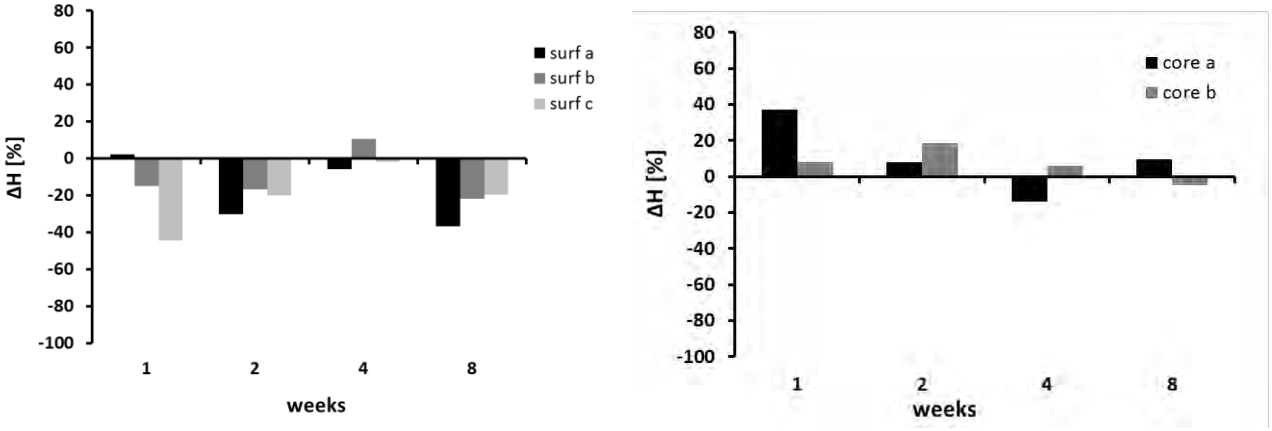

Figure A.c.5: Variation of hardness of β-TCP samples at the surface (left) and in the core (right) after different times of immersion in PBSd. Average values at t0: $H_{surface}$=5.0MPa, $E_{surface}$=788MPa, H_{core}=3.8MPa, E_{core}=986MPa

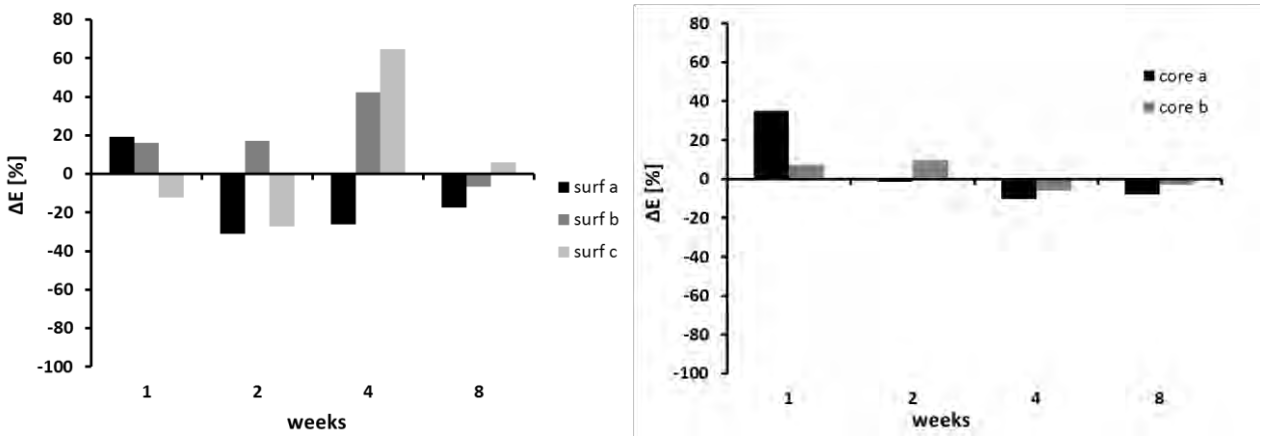

Figure A.c.6: Variation of Young's Modulus of β-TCP samples at the surface (left) and in the core (right) after different times of immersion in PBSd. Average values at t0: $H_{surface}$=5.0MPa, $E_{surface}$=788MPa, H_{core}=3.8MPa, E_{core}=986MPa

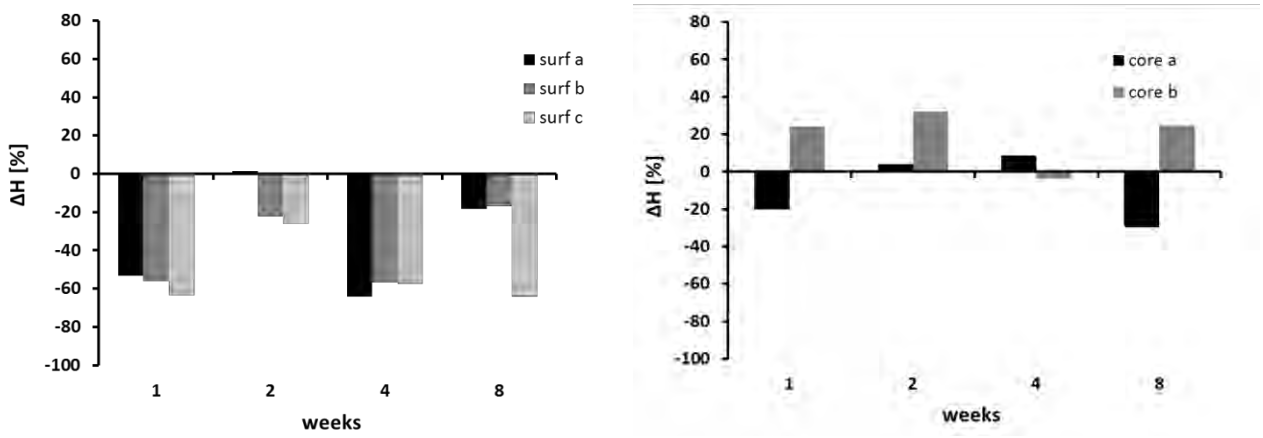

Figure A.c.7: Variation of hardness of β-TCP samples at the surface (left) and in the core (right) after different times of immersion in TRISs. Average values at t0: $H_{surface}$=5.0MPa, $E_{surface}$=788MPa, H_{core}=3.8MPa, E_{core}=986MPa

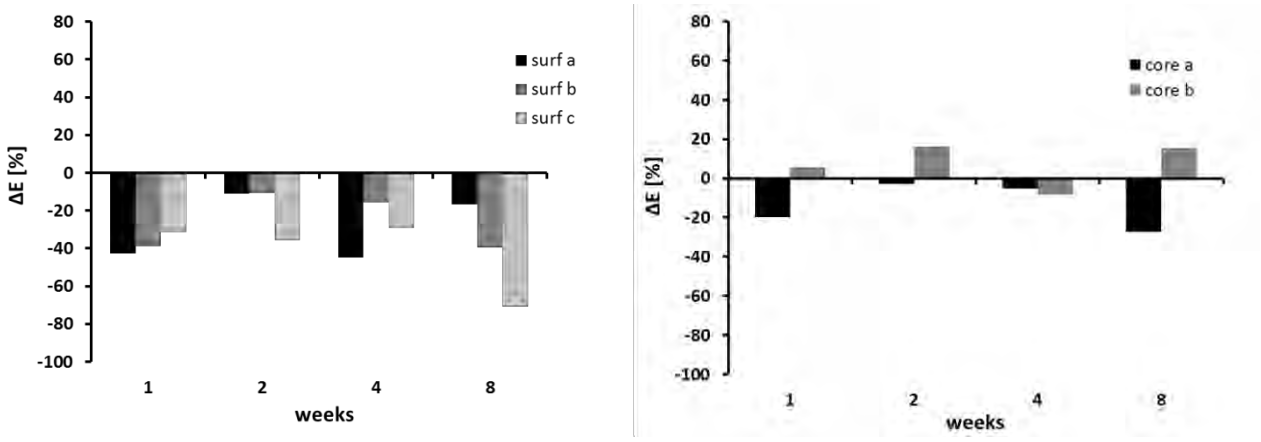

Figure A.c.8: Variation of Young's Modulus of β-TCP samples at the surface (left) and in the core (right) after different times of immersion in TRISs. Average values at t0: $H_{surface}$=5.0MPa, $E_{surface}$=788MPa, H_{core}=3.8MPa, E_{core}=986MPa

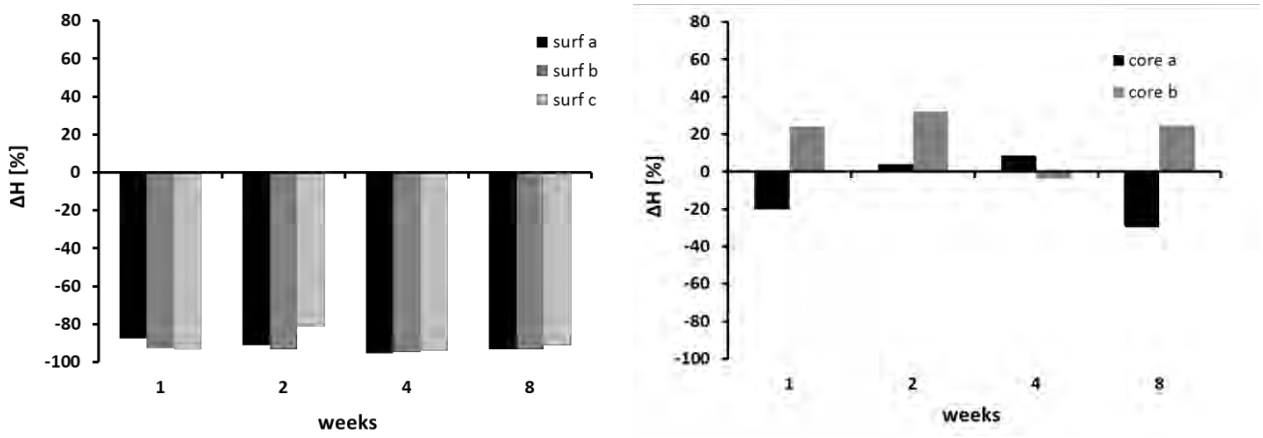

Figure A.c.9: Variation of hardness of β-TCP samples at the surface (left) and in the core (right) after different times of immersion in TRISd. Average values at t0: $H_{surface}$=5.0MPa, $E_{surface}$=788MPa, H_{core}=3.8MPa, E_{core}=986MPa

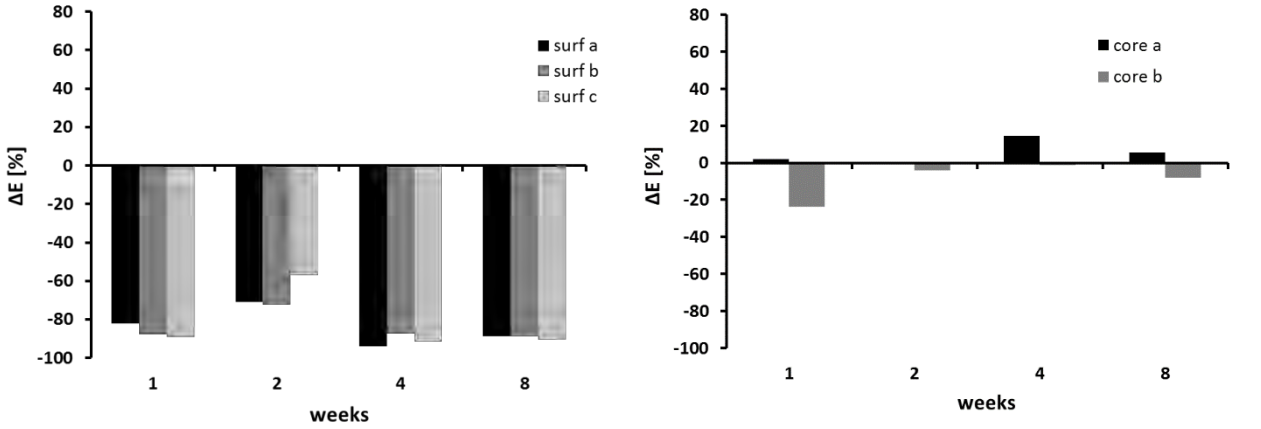

Figure A.c.10: Variation of Young's Modulus of β-TCP samples at the surface (left) and in the core (right) after different times of immersion in TRISd. Average values at t0: $H_{surface}$=5.0MPa, $E_{surface}$=788MPa, H_{core}=3.8MPa, E_{core}=986MPa

Figure A.c.11 reports the load-displacement curves of the additional micro-indentation tests performed along the diameter of two samples after immersion in TRISd (1 week and 2 weeks respectively).

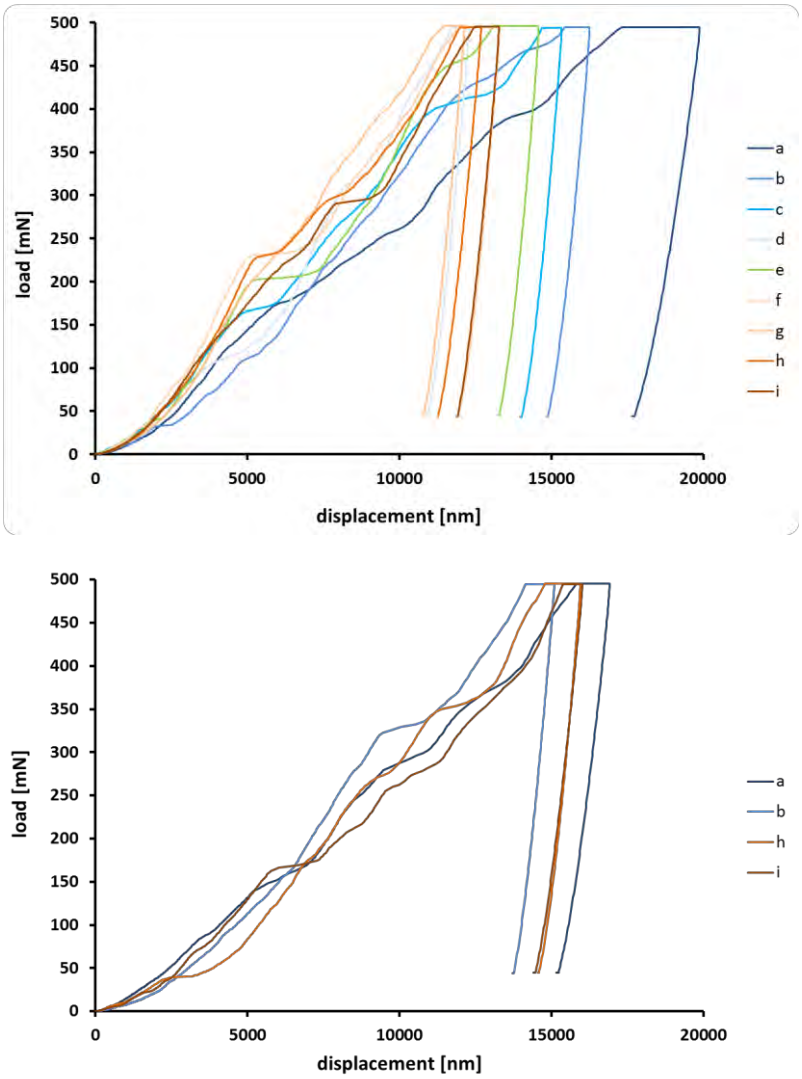

Figure A.c.11: Load-displacement curves obtained along the section of samples (cf. fig.42) immersed for 1w (up) and 2w (down) in TRISd

Micro-computed tomography of porous β-TCP samples: additional data

Figure A.c.12 shows a µ-CT image of a sample at time zero, which presented bright concentric circles.

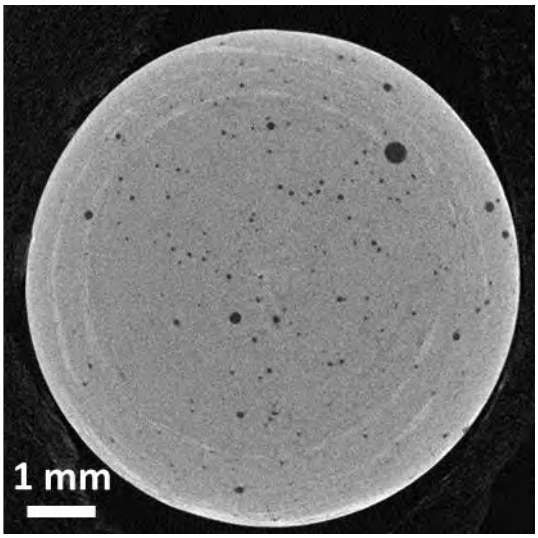

Figure A.c.12: transverse µ-CT image of a sample of β-TCP at t0 (resolution of 10 µm/voxel)

Influence of porosity on the degradation of β-TCP samples: preliminary test

Figure A.c.13 shows the variation of pore interconnection size as a function of the temperature of thermal treatments performed on β-TCP porous samples.

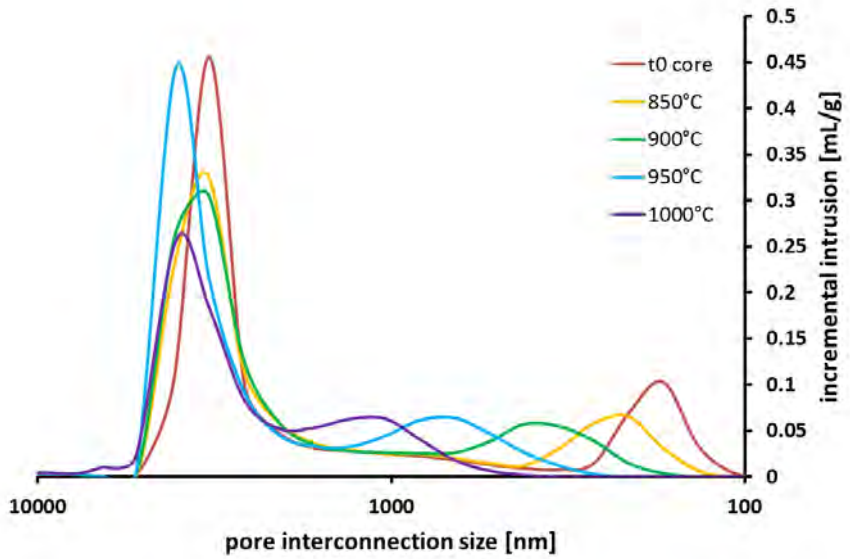

Figure A.c.13: Influence of sintering temperature on pore interconnection size distribution

ANNEX D

Cellular tests: preliminary study

Some preliminary tests were performed culturing directly monocytes on the surface of the materials. In particular RAW 264.7 cells were seeded on the surface of the samples and grow for:

- 2 days without any growth factor, in order to evaluate the cytocompatibility
- 21 days with MCSF and RANKL, in order to induce osteclastogenesis

Glass discs were used as a reference substrate. After the preset time-points, cells and samples were analysed by SEM, fluorescence, TRAP staining and WST essay.

Results at 2 days displayed a good cell viability for all materials (Figure A.d.1), with no significant differences between TCP_NoMg, TCP_Mg and reference substrates. Cells appeared homogeneously distributed all over the surface of the specimens (Figure A.d.2). In terms of morphology, cells were small (diameter <10 μm), round-shaped, well adherent on the surface, but not interconnected (Figure A.d.3). All these features, typical of monocytes, could be recognised on both pure and Mg-doped materials.

After 21 days, cells appeared on the average larger, well distributed on both types of β-TCP, but slightly less in number on TCP_Mg (Figure A.d.4); moreover, multinucleated cells were observed on all samples. A closer look to cells (Figure A.d.5) revealed that these were well adherent on the surface, often interconnected one with the other and of large diamensions, confirming that the fusion of some monocytes had taken place. However, TRAP-staining led to inconclusive results; clearly stained cells could not be found neither on TCP_NoMg nor on TCP_Mg (Figure A.d.6). After cell removal, in addition, no resorption pits could be observed on the surface of the specimens (Figure A.d.7); only slight signs of dissolution, mainly at grain boundaries, were noticed on TCP_NoMg.

Considering the results of these preliminary tests, it could be stated that the good biocompatibility of both pure and doped β-TCP was assessed; in fact, no problems of cytocompatibility on RAW 264.7 cells were noticed for both materials neither on a short (2 days) nor on a relatively long period (21 days). However, osteoclasts' activity was not supported by β-TCP. It could not be concluded if this was due to a low differentiation of precursor cells, or if it was due to a low activity of differentiated cells.
One of the possible causes, as hypotheised by Detsch et al. [1], could have been the calcium released by the β-TCP materials; a high enough extracellular concentration of calcium, in fact, would act as a signal of "no-need" to resorb and would therefore hinder osteoclasts' activity.
In order to avoid this problem, and to favour the differentiation of monocytes into osteoclasts, a second approach was followed for growing the cells for all the other tests described in chapter 5. As explained in chapter 2, in fact, monocytes were culture for 17 days with growth factors (MCSF and RANKL) in Petri dishes (in absence of any sample). Then potentially differentiated cells were scratched, centrifuged and seeded on the surface of the samples. In this way, avoiding a direct contact with β-TCP during all the differentiation process of monocytes, we tried to minimise the influence of calcium release on the presence of osteoclast-like cells.

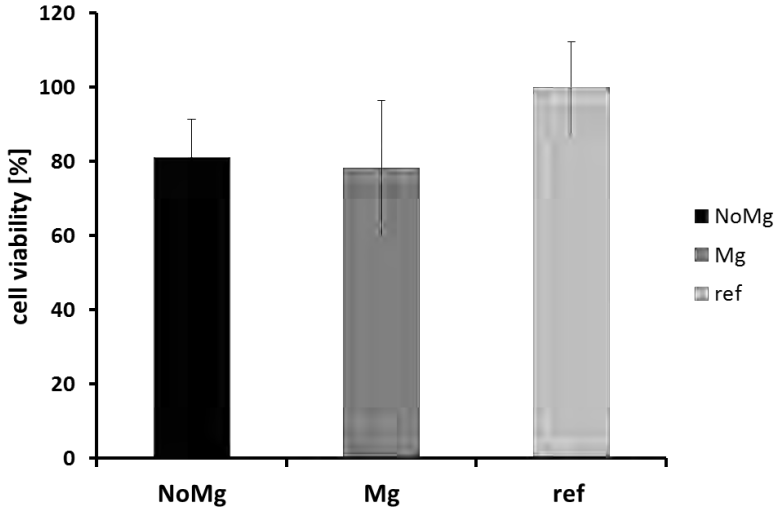

Figure A.d.1: Raw cell viability at 2 days. Asterisks point out statistically significant differences in comparison to values obtained for the reference glass discs

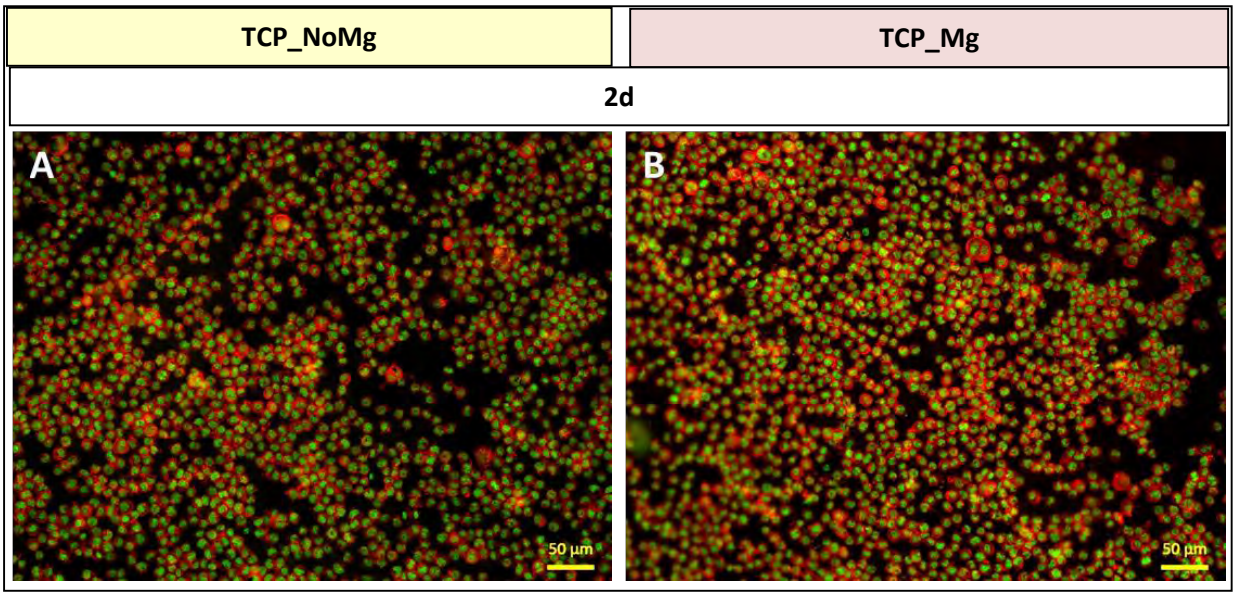

Figure A.d.2: Fluorescence images of cells cultured during 2 days on β-TCP samples with (B) and without (A) magnesium

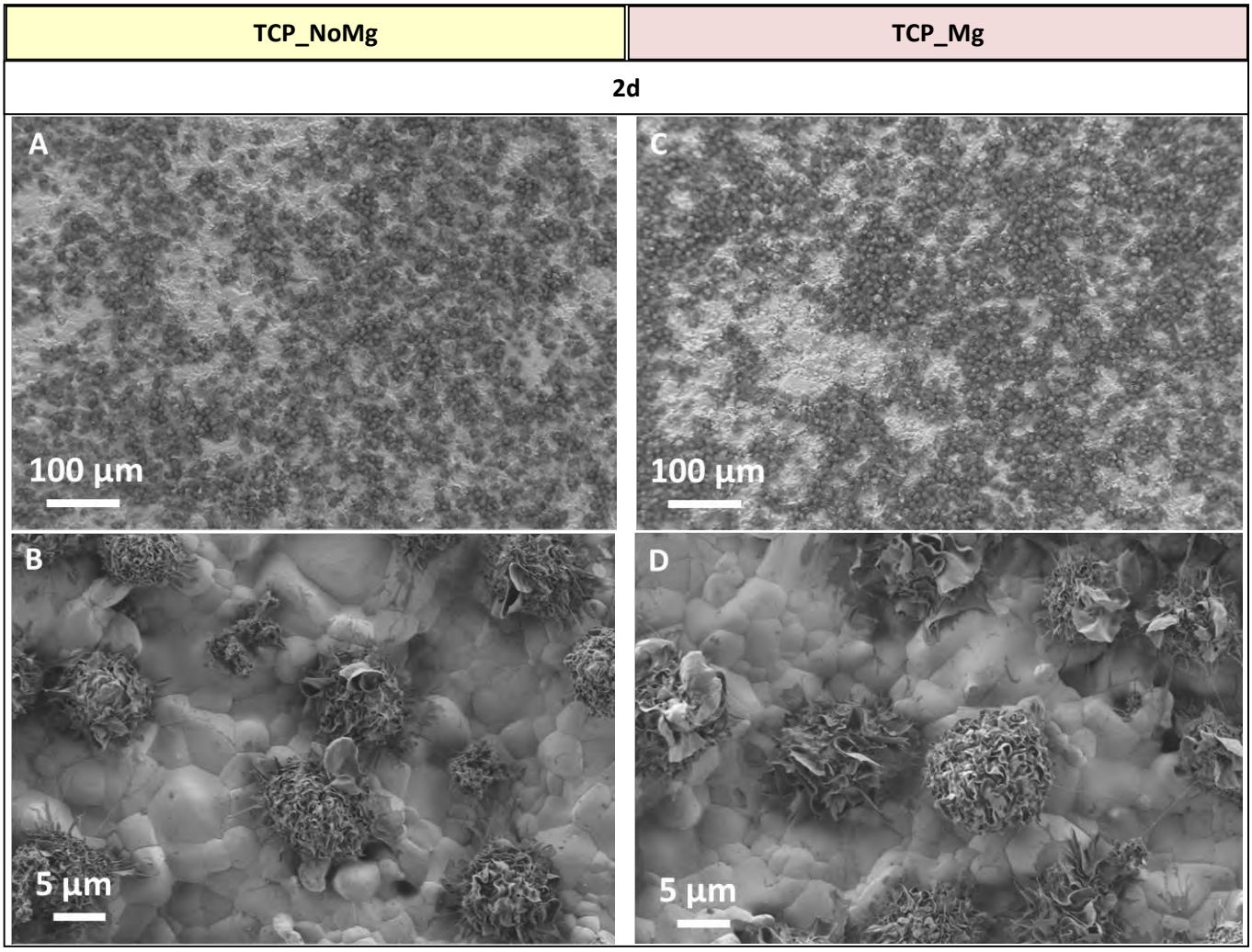

Figure A.d.3: SEM micrographs of cells on β-TCP samples with (C, D) and without (A, B) magnesium after 2 days of culture

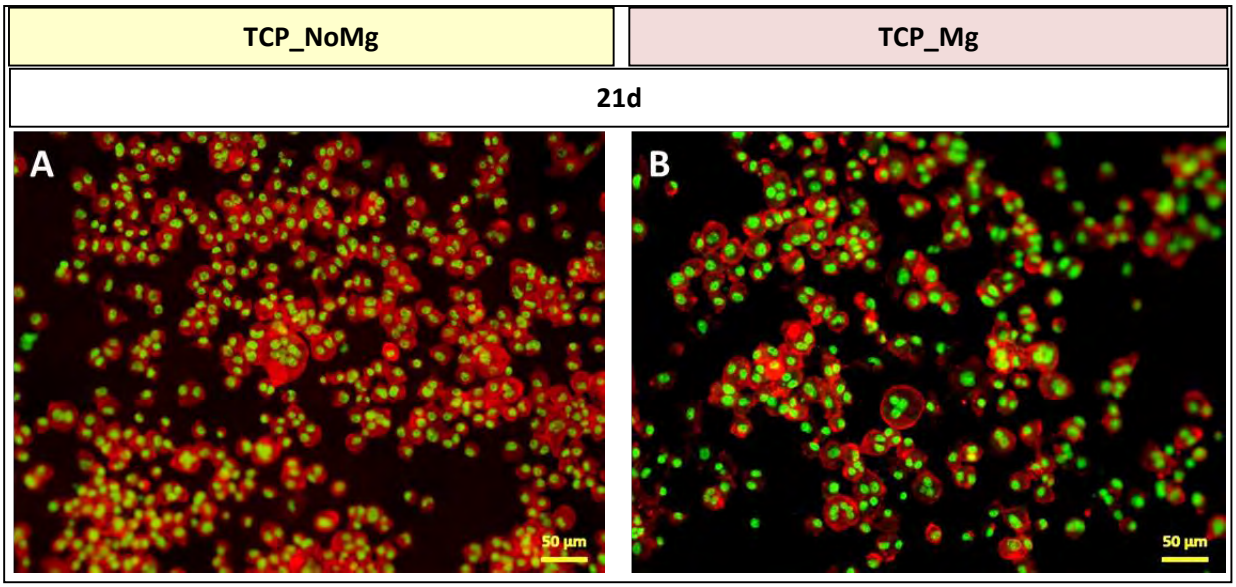

Figure A.d.4: Fluorescence images of cells cultured during 21 days on β-TCP samples with (B) and without (A) magnesium

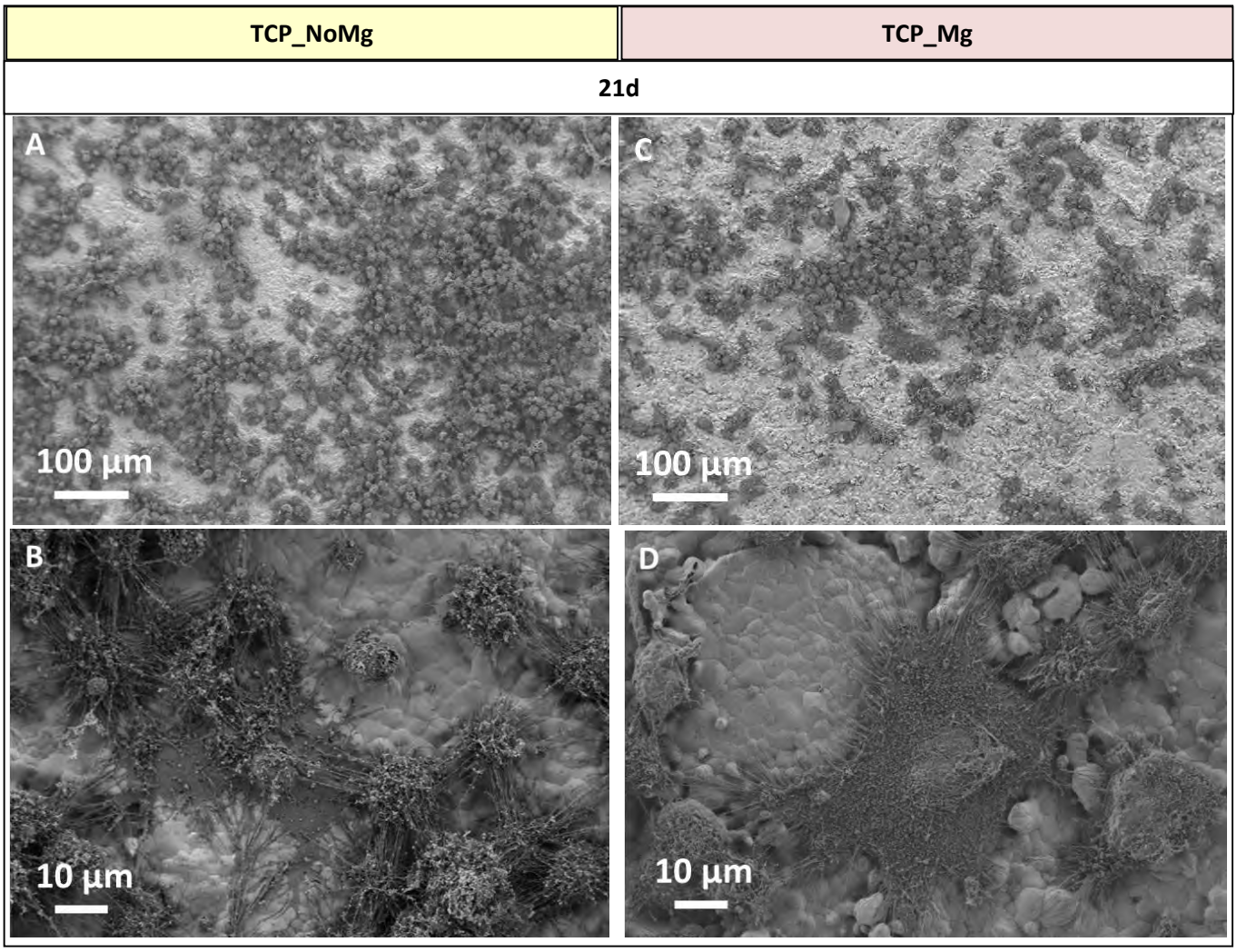

Figure A.d.5: SEM micrographs of cells on β-TCP samples with (C, D) and without (A, B) magnesium after 21 days of culture

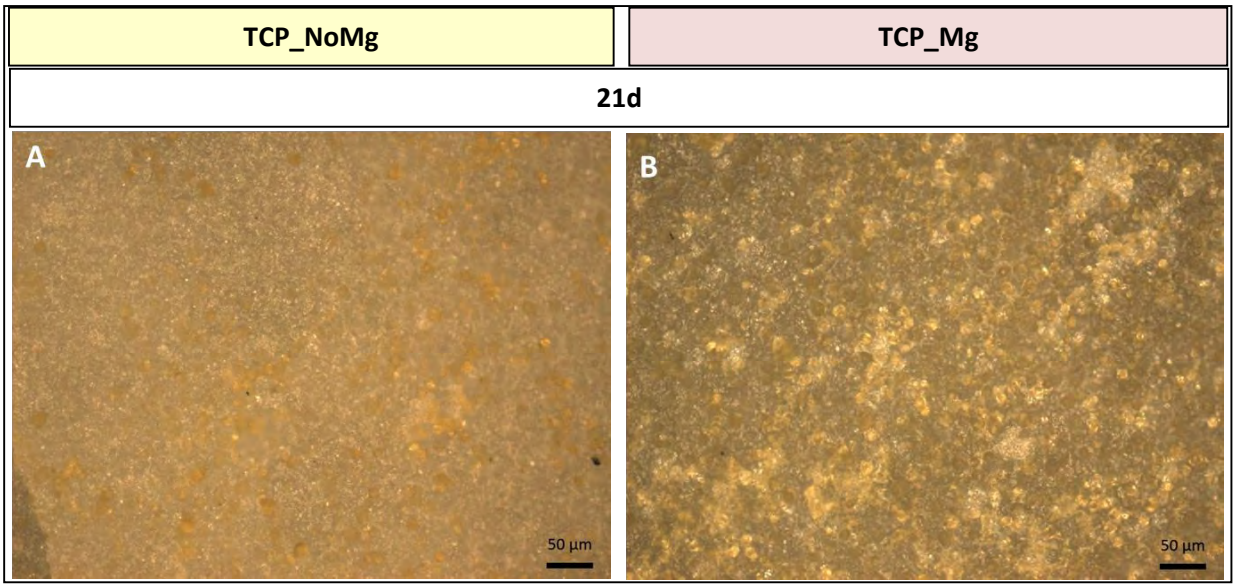

Figure A.d.6: Images of TRAP-stained cells cultured for 21 days on β-TCP samples with (B) and without (A) magnesium

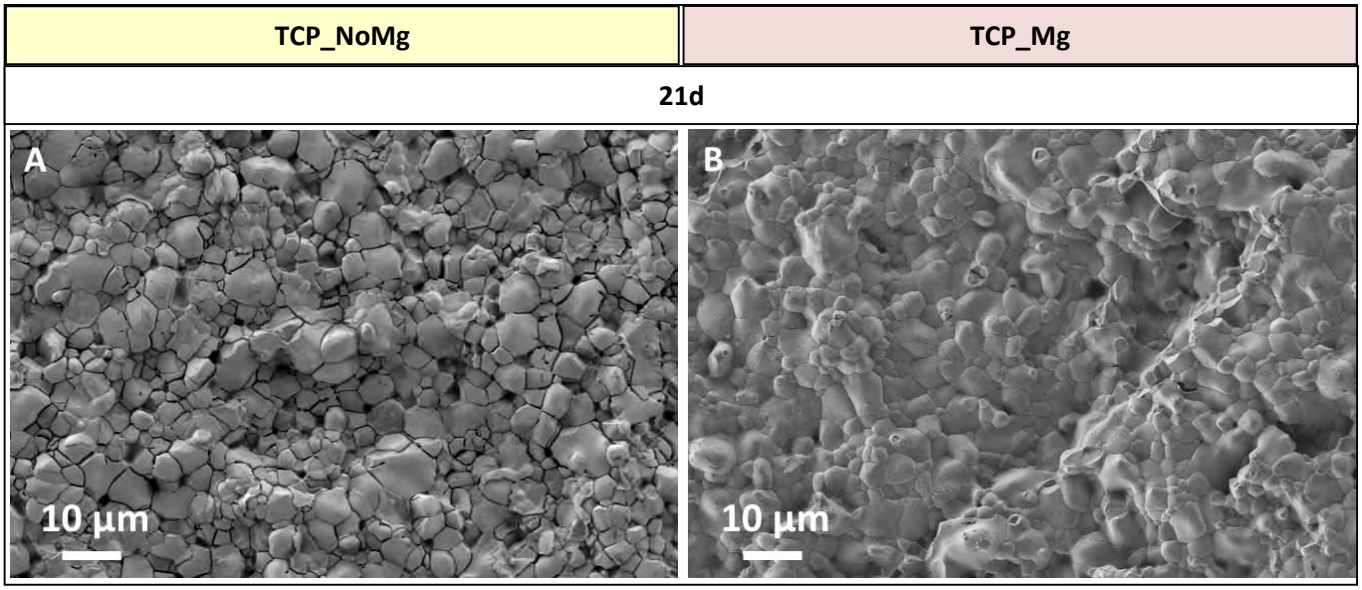

Figure A.d.7: SEM micrographs of samples once the cells were removed (after 21 days of culture) from β-TCP samples with (B) and without (A) magnesium

Cell viability and density: additional data

Graphs of cell density and viability after 4 days of culture; the protocol followed for differentiating the cells is described in chapter 2.

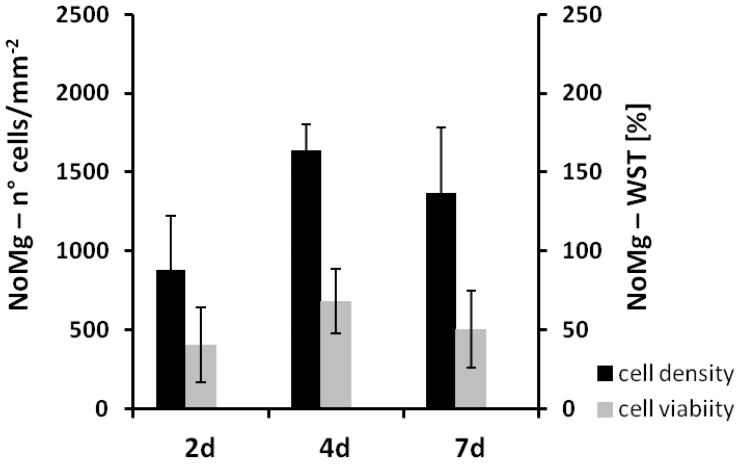

Figure A.d.8: Cell density and viability assessed on TCP_NoMg samples at different time-points

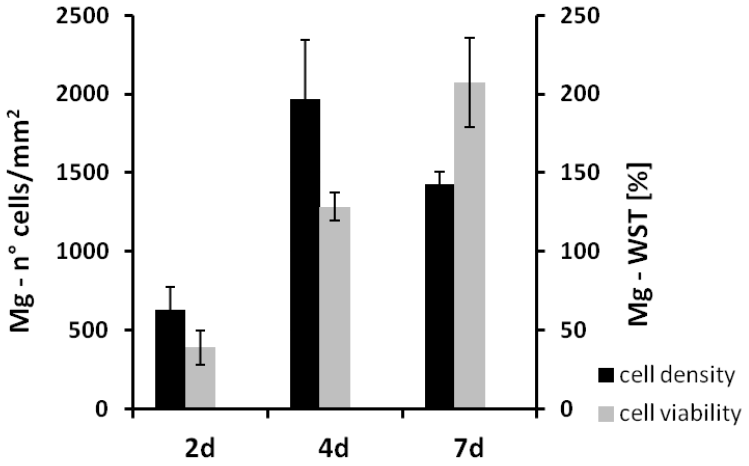

Figure A.d.9: Cell density and viability assessed on TCP_Mg samples at different time-points

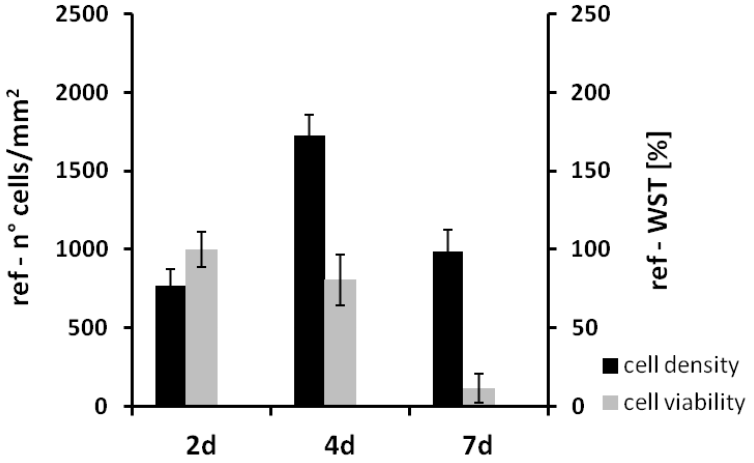

Figure A.d.10: Cell density and viability on the reference glass discs substrates at different time-points

Acellular tests: additional X-ray diffraction data

Figure A.d.11 reports the diffraction patterns of doped samples after 4 and 7 of immersion without cells in RPMI and NaCl.

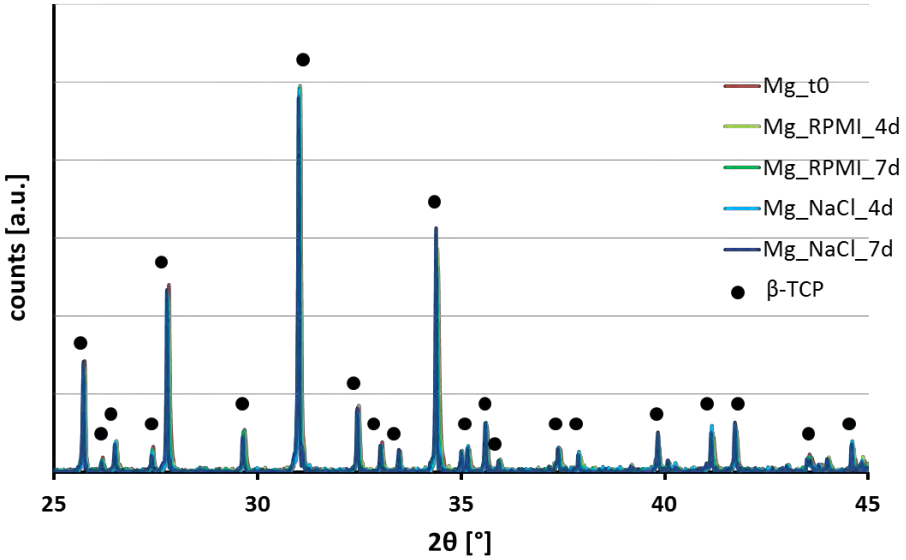

Figure A.d.11: XRD pattern of TCP_Mg samples after 4 and 7 days of immersion in RPMI (without cells) and NaCl

Acellular tests: additional X-ray diffraction data

Figure A.d.12 reports the micrographs of the surface doped and un-doped samples after 4 days of immersion in RPMI without cells.

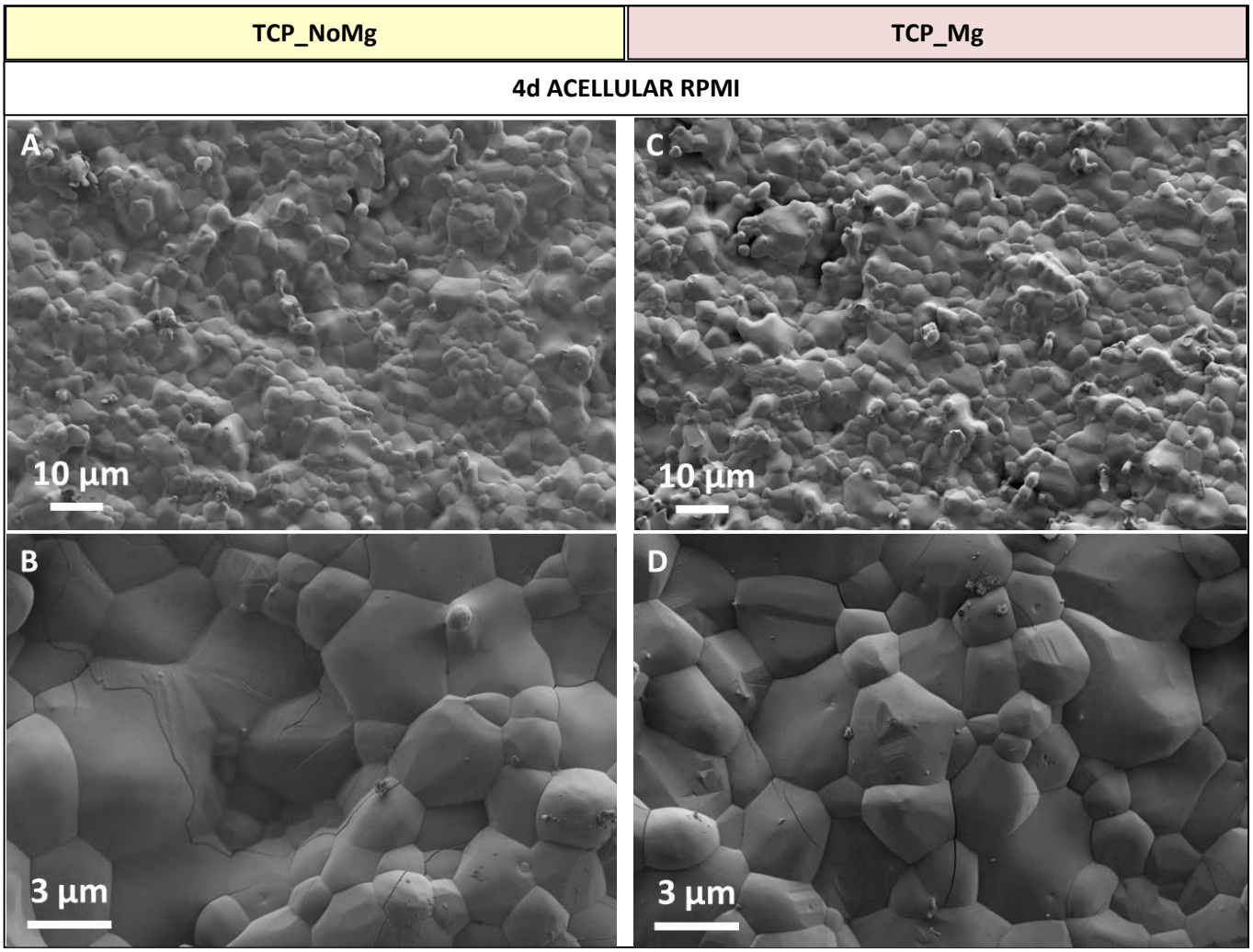

Figure A.d.12: SEM micrographs of β-TCP samples with (C, D) and without (A, B) magnesium after 4 days of immersion in RPMI without cells

1. Detsch, R., et al., *The resorption of nanocrystalline calcium phosphates by osteoclast-like cells.* Acta Biomaterialia, 2010. **6**: p. 3223–3233.

This work was funded by the European Commission funding under the 7th Framework Program (Marie Curie Initial Training Networks; grant number: 289958, Bioceramics for bone repair)

INSTITUT NATIONAL DES SCIENCES APPLIQUÉES LYON

FOLIO ADMINISTRATIF

THÈSE SOUTENUE DEVANT L'INSTITUT NATIONAL DES SCIENCES APPLIQUÉES DE LYON

NOM : GALLO

DATE de SOUTENANCE : 26 novembre 2015

Prénoms : Marta

TITRE : *In-vitro* degradation of calcium phosphate bone substitutes: coupled monitoring of the evolution of mechanical, microstructural and physico-chemical properties of DCPD and β-TCP samples

NATURE : Doctorat

Numéro d'ordre : 2015ISAL0107

Ecole doctorale : Matériaux de Lyon

Spécialité : Science des Matériaux

RESUME :
Ce travail de thèse a eu comme objectif la mise en place et la validation d'une méthodologie expérimentale pour le suivi de l'évolution *in-vitro* de substituts osseux à base de phosphates de calcium. Du phosphate dicalcique dihydraté (DCPD, $CaHPO_4 \cdot 2H_2O$) et du phosphate tricalcique bêta (β-TCP, β-$Ca_3(PO_4)_2$) ont été choisis comme matériaux modèles de deux grandes classes de substituts osseux: les "biosolubles" (sujets à dissolution après implantation) et les "biorésorbables" (sujets à résorption cellulaire après implantation).
Pour l'étude des phénomènes de dissolution et de reprécipitation observés lorsque les phosphates de calcium sont plongés en solution, ces matériaux ont été produits sous forme d'échantillons microporeux (60% de porosité pour le DCPD, 75% pour le β-TCP) et soumis à des tests de dissolution *in-vitro* en conditions statiques ou dynamiques (sans ou avec renouvellement du liquide) dans différentes solutions tamponnées à pH physiologique (TRIS et PBS) et pour des durées s'étalant entre 30 minutes et 2 mois. L'analyse des propriétés physico-chimiques, microstructurales et mécaniques des échantillons avant et après immersion a permis d'évaluer l'influence du type de milieu et des conditions de test choisies sur l'évolution des échantillons. Une attention particulière a été prêtée à la caractérisation mécanique: la technique de micro-indentation instrumentée sphérique a été préférée à autres essais plus conventionnels. Cette technique permet d'évaluer plusieurs paramètres tels que la dureté et le module de Young de façon quasi non-destructive et à une échelle locale. En conséquence, l'utilisation de la micro-indentation s'est avérée d'une grande aide pour le suivi des caractéristiques d'échantillons dégradés qui présentaient un gradient de propriétés entre la surface (où le processus de dégradation commence) et le cœur (sujet à des changements sur plus long terme).
La dernière partie de cette étude a été dédiée à l'étude du deuxième phénomène qui entraine la résorption de substituts osseux *in-vivo*, à savoir la résorption cellulaire. Pour cela des essais cellulaires avec des cellules précurseurs d'ostéoclastes ont été réalisés sur des échantillons denses de β-TCP pur ou dopé avec 5% molaire de magnésium. L'addition de cet élément est censée modifier les propriétés du matériau (notamment sa solubilité) et, par conséquence, modifier le comportement cellulaire. Les résultats des tests ont confirmé la cytocompatibilité des deux types de β-TCP, mais ont également mis en avant une difficulté d'activation des ostéoclastes. Deux des causes possibles seraient liée à la topographie de surface des échantillons et au relargage des ions calcium suite à la dissolution du matériau.

MOTS-CLÉS : phosphates de calcium, résorption *in-vitro*, micro-indentation instrumentée, ostéoclastes

Laboratoire (s) de recherche :

Université de Lyon
MATEIS – UMR CNRS 5510 – INSA de Lyon
7, Avenue Jean Capelle, 69621 Villeurbanne Cedex, France

Directeur de thèse: Jérôme CHEVALIER
Co-directeur de thèse: Solène TADIER
Encadrant : Sylvain MEILLE

Président de jury : Marc BOHNER

Composition du jury : J-M. Bouler (rapporteur), C. Combes (rapporteur), A. Boccaccini, M. Bohner, J. Chevalier, S. Meille, S. Tadier, R. Detsch (invité)